Doctoral Dissertation
Doctoral Program in Electronic Engineering (XXX cycle)

Development and characterization of nanostructured catalysts

By

Luisa DELMONDO
******

Supervisor(s):
Prof. F. C. Pirri, Supervisor
Doct. A. M. Chiodoni, Co-Supervisor

Doctoral Examination Committee:
Prof. A. Falqui , Referee, University of King Abdullah University of Science and Technology (KAUST)
Prof. V. Morandi, Referee, University of Turin
Prof. N. De Leo, Istituto Nazionale di Ricerca Metrologica (INRiM)
Prof. E. Tresso, Polytechnic of Turin
Prof. G. Cicero, Polytechnic of Turin

Politecnico di Torino
2018

Declaration

I hereby declare that, the contents and organization of this dissertation constitute my own original work and does not compromise in any way the rights of third parties, including those relating to the security of personal data.

Luisa DELMONDO
2018

I would like to dedicate this thesis to my loving parents

Acknowledgements

First of all, I would like to acknowledge the people that mostly have contributed to the success of my PhD: my parents and the man, the dj I love - Claudio.

My gratitude goes to Prof. Fabrizio Pirri for the opportunity given me to work onto these interesting research fields, to Dr. Angelica Chiodoni and Dr. Marzia Quaglio for their scientific support that they gave me and the constant help.

Thank you also to Francesco 3V, Beatrice, Giulio Cat, first my friends and then my colleagues, with which I spent hours talking about science [1, 2] during our coffee breaks [3] and lunches.

I wish to sincerely acknowledge the scientific contribution, measurements and characterizations of all people, researcher and technicians, of IIT (Center for sustainable Future Technologies CSFT@Polito) with whom I had the honor of working: Gian Paolo Salvador, Denis Perrone, Katarzyna Bejtka, José Alejandro Munoz-Tabares, Giulia Massaglia, Valentina Margaria, Valeria Agostino, Nadia Garino, Adriano Sacco, Angelica Chiodoni, Stefano Bianco, Micaela Castellino and Marzia Quaglio.

Last but not least, special thanks go to my friends outside the labs: my brother Gio, my sister-in-law Francesca, Bea, Chiara, Isa, Lele, Bobo, Boiler, Carlo, Edo, Caste, Maina, Geppo, Steve, Jhonny, Giulia, Don Calo, Miky, Davide, thank you for the laughs, for spending your time in listening and helping me with my complains, ups and downs and for all the pleasant moments spent together.

Abstract

The aim of this thesis work is focused on the development and characterization of nanostructured catalysts, in order to exploit them in two different reactions: the Oxygen Reduction Reaction (ORR) and the CO_2 Reduction Reaction (CO_2RR). The objective of this research is to find economical and ecological materials that could replace platinum as catalyst of the two reactions, while maintaining comparable performance.

Considering the ORR, the study is concentrated on the manganese oxide family (Mn_xO_y), structured in the form of nanofibers by electrospinning technique and subsequent thermal treatment. The aim is to demonstrate that the Mn_xO_y nanofibers own all the necessary properties, e.g. cheapness, efficiency and environmental-friendliness, revealing themselves as promising and innovative structures as catalysts for ORR. This material is studied in terms of morphology, composition and electrochemical activity by varying the final calcination temperature of the nanofibers. Thanks to this study, it is possible to describe the thermal evolution of the catalyst, comparing the electrochemical performance to a precise nanostructure and crystalline composition. The ceramic nanofibers, in fact, catalyze efficiently the ORR, granting a cheaper and more eco-friendly material than platinum, which is the most used today in energy production devices, as Microbial Fuel Cells (MFCs). The Mn_xO_y catalyst is also coupled with a conductive substrate in an MFC device, revealing its capability of successfully reduce oxygen after the direct integration onto the electrode, without changing its catalytic performance.

Considering the CO_2RR, the attention is focused on the titanium dioxide nanotubes (TiO$_2$ NTs) and copper oxide nanofibers (Cu$_x$O NWs) -based catalysts. Vertically oriented TiO$_2$ NTs are obtained by anodic oxidation of a titanium foil and studied, by their own, in terms of morphology and composition. Further they are coupled with a copper and a copper oxide layers, characterizing the electrochemical properties, catalytic performance and selectivity toward CO_2RR. As a competitive alternative to TiO$_2$ NTs, Cu$_x$O NWs are obtained by thermally oxidizing the copper foils at different temperatures and characterizing them in terms of morphology, composition catalytic activity and selectivity, analyzing both the liquid and gaseous byproducts. Lastly, the Cu$_x$O NWs are coupled with and titanium dioxide upper layer, exploiting the same in characterizations of the former substrate in order to be

comparable. All the studied substrate show some catalytic activity toward CO_2 reduction, but the highest efficiency is associated to the Cu_xO NWs, revealing formation of byproducts both in liquid and in gaseous form.

Dr. Frankenstein: *What a filthy job.*
Igor: *Could be worse.*
Dr. Frankenstein: *How?*
Igor: *Could be raining.*
[it starts to pour]
[M. Brooks, Young Frankenstein]

Contents

Nomenclature

Acronyms

$\mu - GC$ Micro gas chromatograph

A Anatase phase - TiO_2

CB Conduction band

CO_2RR Carbon dioxide reduction reaction

COD Chemical oxygen demand

CP Carbon paper

CV Cyclic voltammetry

EIS Electrochemical impedance spectroscopy

FE Faradaic efficiency

$FESEM$ Field emission scanning electron microscope

GDE Gas diffusion electrodes

$GHGs$ Greenhouse gases

HER Hydrogen evolution reaction

LSV Linear sweep voltammetry

MFC Microbial fuel cell

ND Nanodrop

NF Nanofiber

NHE Normal hydrogen electrode

NP Nanoparticle

NT Nanotube

NW	Nanowire
OER	Oxygen evolution reaction
ORR	Oxygen reduction reaction
PEC	Photo-electro-catalytic cell
PEM	Proton exchange membrane
PEO	Poly ethylene oxide
R	Rutile phase - TiO_2
RDE	Rotating disk electrode
RHE	Reversible hydrogen electrode
RRDE	Rotating ring disk electrode
SCMFC	Single chamber microbial fuel cell
SHE	Standard hydrogen electrode
TEM	Transmission electron microscope
VB	Valence band
XRD	X-ray diffraction

Chemical formulas

CO_2	Carbon dioxide
Cu_2O	Cuprous oxide
Cu_xO	Copper oxide, not stoichiometric
CuO	Cupric oxide
Mn_xO_y	Manganese oxide, not stoichiometric
TiO_2	Titanium dioxide

Greek Symbols

η	Solution viscosity

Roman Symbols

E_0	Vacuum level

Chapter 1

Introduction

Chapter abstract *In Chapter 1, a brief introduction on the world pollution problem will be discussed, Sec. 1.1. In order to reduce greenhouse effect, new electrochemical devices will be discussed in Sec. 1.2, pointing out their working principles. Moreover, among these electrochemical cells renewable energy sources may be used in order to produce energy or wastes (CO_2) to be converted into valuable products. In the end, the aim of this Ph.D. project will be explained, Sec. 1.3, with a short introduction of the following chapters.*

1.1 Pollution, greenhouse effect and renewable energies

Greenhouse gases (GHGs) are atmospheric gases that can absorb and emit radiation within the infrared range, thereby leading to the so-called **greenhouse effect**. In a certain concentration, they are able to maintain the Earth's surface temperature in a range suitable for life. In fact, without GHGs, the average temperature would be approximately -18°C, rather than present average of 15°C [4, 5]. Among the gases affecting the ambient temperature, some of them are called long-lived greenhouse gases (LLGHGs), such as carbon dioxide (CO_2), methane (CH_4), chlorofluorocarbons (CFCs) and nitrous oxide (N_2O), because of their chemical stability and ability to persist in the atmosphere even for centuries. Their emission in the atmosphere has a long-term influence on the global warming.

The most abundant GHGs in the atmosphere are water vapor (H_2O), CO_2, CH_4, N_2O, ozone (O_3), and CFCs, deriving from natural and anthropogenic sources. However, since the beginning of the industrial revolution, human activities increased of about 40% the atmospheric concentration of CO_2 from 280 ppm in 1750 to 410 ppm in 2017. The rapid increase of the carbon dioxide concentration in the atmosphere has motivated worldwide concerns and worries of global climate change from government, industrial and academic groups. Indeed, the CO_2 anthropogenic emissions come from deforestation, soil erosion, animal agriculture and, mostly,

combustion of carbon-based fossil fuels (as coal, oil and natural gas). For these reasons, during the last decades, different worldwide agreements were signed in order to mitigate the global warming effects.

In 1997, the **Kyoto Protocol** was adopted in Kyoto (Japan), aiming to attain a reduction of global GHG emissions at least 5% by 2012, less than the observed levels in 1990. As a result, the European Union (EU) issued a global reduction aim of GHG levels by 8%. A more recent treaty is the Paris Agreement, in the framework of the World Climate Summit, held in Paris (France) in 2015. Negotiations between 196 parties resulted in the adoption of the agreement starting from 2020. It will become legally binding only if at least 55 counties, which together produce at least 55% of the global GHG emissions, ratify the agreement [6]. The expected key result of this agreement was highlighted by the statement:

> *Holding the increase in the global average temperature to well below 2°C above pre-industrial levels and to pursue efforts to limit the temperature increase to 1.5°C above pre-industrial levels, recognizing that this would significantly reduce the risks and impacts of climate change.*

This is also called *zero net anthropogenic GHG emissions*, to be reached by 2050, in order to limit global warming below 2.7°C by 2100. In Fig.1.1 is represented the global temperature change since 1850 up to 2016, highlighting the limit of 1.5°C.

In order to mitigate the rapid global warming and reduce the climate change caused by huge anthropogenic CO_2 emissions, different strategies have been proposed and implemented in the last years [7, 8]. According to the International Energy Agency (IEA) report, the strategies to reduce CO_2 emissions include [9]:

(i) improving the efficiency of actual energy production;

(ii) implementing Carbon Capture and Storage (CCS) technologies;

(iii) utilizing renewable energy sources and material recycling.

CCS technologies could potentially reduce CO_2 emissions by 9–50% in industrial sectors by 2050, if compared to the present level, and could mitigate global climate change by 15–55% in 2100 [10].
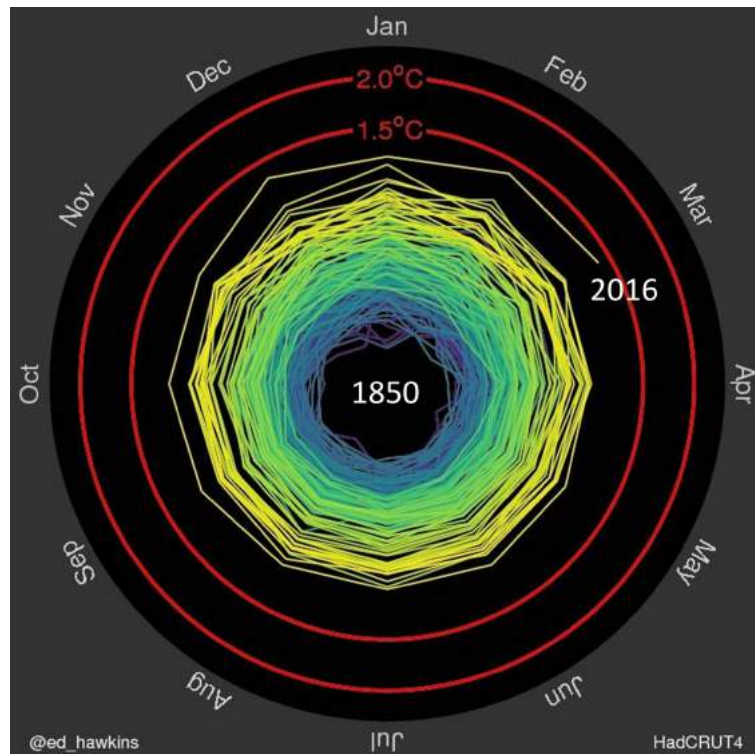
Fig. 1.1 Spiral representation of the global temperature change between 1850 and 2016. Data: HadCRUT4.4 from January 1850 (interior part) – March 2016 (exterior part), relative to the mean of 1850-1900, http://blogs.reading.ac.uk/climate-lab-book/files/2016/05/spiral_optimized.gif

1.1.1   Energy share

Actually, in our modern society, not renewable sources are still very important, pointed out in the estimated energy share in Fig.1.2, where fossil fuels occupy almost 79% and renewable energies less than 20%. In this framework, improving the energy production efficiency, could be only a temporary measure, while the development and improvement of the *renewables* will be the real challenge. On the total share, the *traditional biomass* accounts for about 9%, comprising cooking and heating in remote and rural areas of developing countries, while *modern renewables* occupy only a slight 10%, even if they are considered the real future in energy production [11]. Even though the use of renewable energy is rising rapidly, the share of renewables in the global energy consumption is not growing as quickly. In fact, in developed countries, energy demand growth is slow and the energy source change takes time because of the large amount of existing infrastructures. In developing countries, energy demand growth is rapid and fossil fuels still play a significant part in meeting this rising demand. In general, it would be promising a shift away from traditional biomass and fossil fuels in favor of modern and more-efficient renewable sources, increasing their overall energy shares. The modern renewable energy sources are among of the best solutions for the rising energy demand and

global pollution, especially CO_2, although they are facing different political and policy challenges, economic structures, financial needs, availability, and other factors that delay their affirmation. In fact, one of the most significant obstacles for their wide adoption is that they are relatively dilute, even if the potential energy coming from them is order of magnitude higher than the actual global energy usage (15 TW), as showed in Fig.1.3. Unlike fossil fuels or similars, which could be concentrated in big power plants, renewable sources are distributed across the territory, in small production stations, such as solar panels.
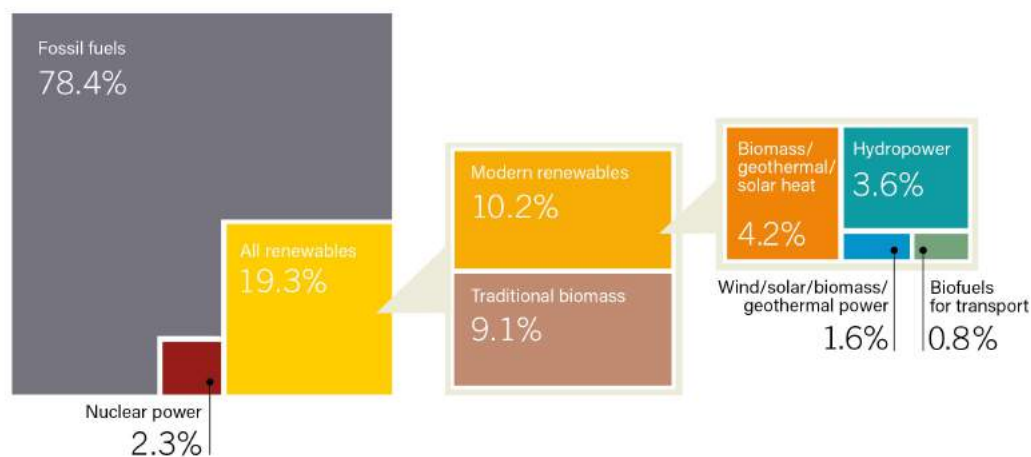
Fig. 1.2 Estimated fossil fuels and renewable energy share of the total energy consumption. Source: REN21 *Renewables, 2017 Global Status Report*

If the renewable energy use will be doubled, the cost for pollution remediation would be reduced of at least a factor of four, together with a reduction of the CO_2 emissions and environmental damage. In order to reach climate goals, at least a 36% share of modern renewables are needed, coupled with a strong decrease of fossil fuels use. The renewables global potential is very high, as depicted in Fig.1.3, if compared to the global energy needs. Doubling at least their share would avoid up to 12 gigatonnes (Gt) of additional carbon dioxide emissions per year by 2030 compared to the present days, while energy efficiency measures would avoid a further 8 Gt.

New technologies and a more efficient renewable energy harvesting represent two of main key points of government roadmaps, the target of actual scientific research.

Fig. 1.3 Renewable energy potential, divided between sources, compared with the actual global energy usage. Source:REN21 *Renewables, 2016 Global Status Report*

1.1.2 CO$_2$ concentration

Reaching 400 ppm is a stark reminder that the world is still not on a track to limit CO$_2$ emissions and therefore climate impacts, passing this mark should motivate us to advocate for focused efforts to reduce emissions across the globe.

ANNMARIE ELDERING
NASA's Orbiting Carbon Observatory-2 satellite mission

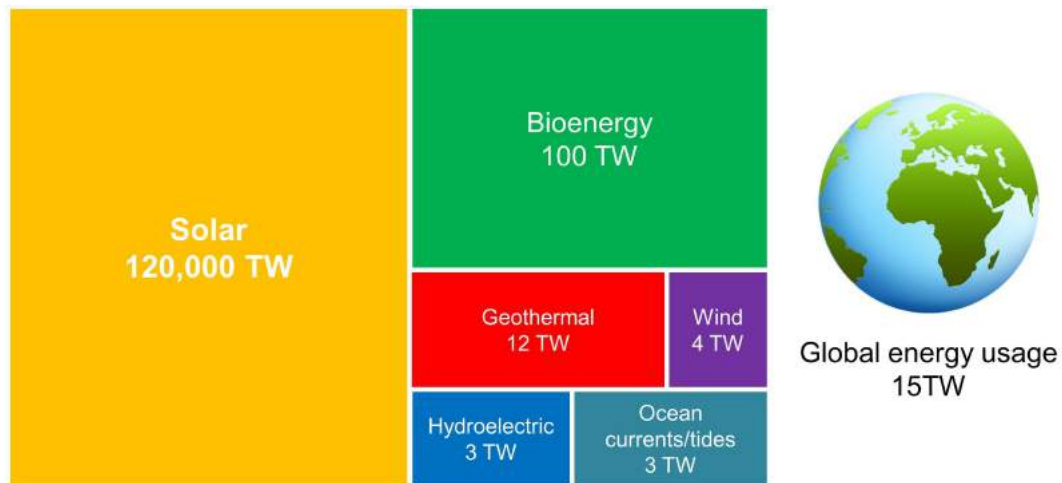During, 2017, the CO$_2$ concentration just breached 410 ppm, and unfortunately, its increase does not slow down (Fig.1.4). To find a time when the planet's air was consistently above this level, one have to look back to 16 million years ago, Miocene, when Earth was a very different place and its climate totally dissimilar from what we expect today. For future years, the models predict that the greenhouse gases concentrations will continue to rise if the world will continue to make the use of fossil fuel resources, as present days. This will lead to a continuous increase of the Earth's average surface temperature. Based on a range of emission scenarios, the average surface temperatures could rise among 2°C and 6°C by the end of this century. In fact, at the current growth rate, the CO$_2$ concentration will reach 500ppm in the next 50 years, causing effects on weather, sea level, animals and humans.

Recently, the Intergovernmental Panel on Climate Change (IPCC) concluded and published a report, RCP [12], were possible scenarios for Earth depending on the global adopted politics are summarized, as showed in Fig.1.5. In the most pessimistic scenario, RCP8.5, the carbon dioxide concentration will reach more than 1000 ppm, due to population booms, technology stagnation and rising emissions. That would give an atmosphere as in Jurassic period, when dinosaurs roamed, and would cause a temperature rise above 5°C. In the second next-most-pessimistic scenario, RCP6, CO$_2$ emissions peak would be around the year 2080 and then would decline, leading
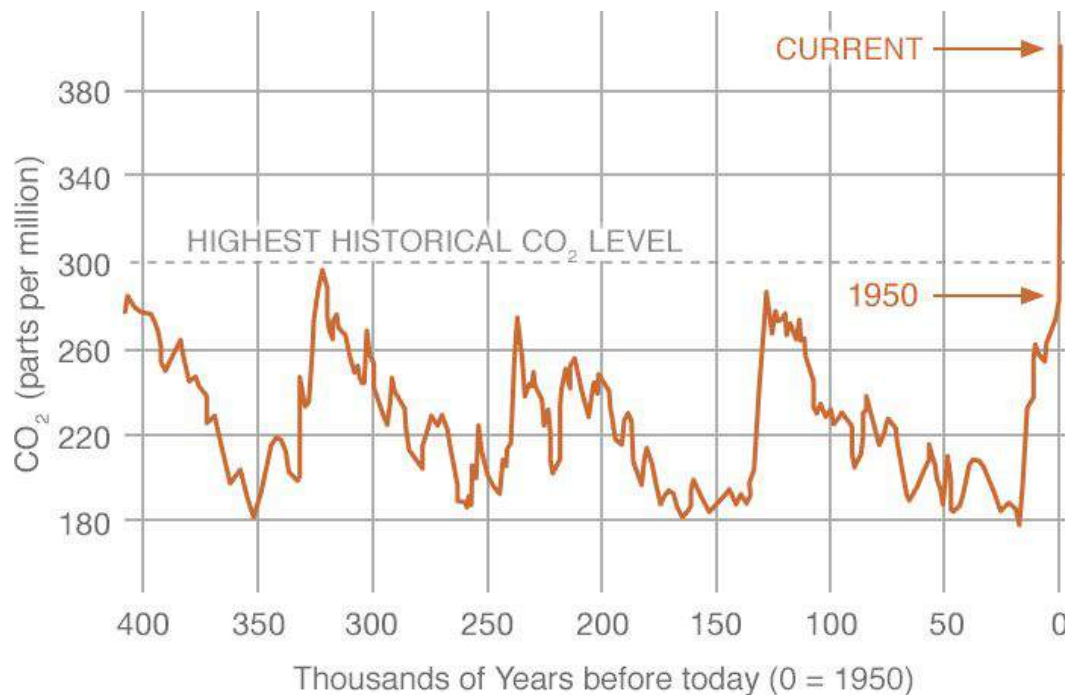
Fig. 1.4 CO_2 concentration over 400,000 years up to 2012, Source: NASA, Global Climate Change. https://climate.nasa.gov/climate_resources/24/

to a concentration between 700-1000 ppm and a probable temperature increases of more than 3°C. In the most optimistic scenario, RCP2.6, the emissions peak should be now (2010-2020), then a decline would start, with humans consuming more carbon than the worldwide production by 2070. The CO_2 atmospheric concentration would go below 400 ppm in a hundred of years, with a temperature increase kept under 1°C in the long term.

Looking deep in these scenarios, it is clear that the *business-as-usual* cannot be afforded anymore, continuing to consume more and more fossil fuels. The more optimistic scenarios, however, imply the development and use of new, sustainable, environmental-friendly technologies such as fuel cells, solar panels, and wind energy replacing much of today's fossil fuel combustion.

Fig. 1.5 Real CO_2 emissions, until 2016, plotted against the IPCC's projections. On the right side are reported the expected temperature increases by 2100 for each projection. Source: Global carbon project, http://www.globalcarbonproject.org/

1.2 Devices for pollution reduction

As already stated, environment needs a diversification of the energy sources, with a strong reduction of the exploitation of fossil fuels, and the use of renewable energy sources such as wind, solar and hydroelectric power. This is happening in the electricity 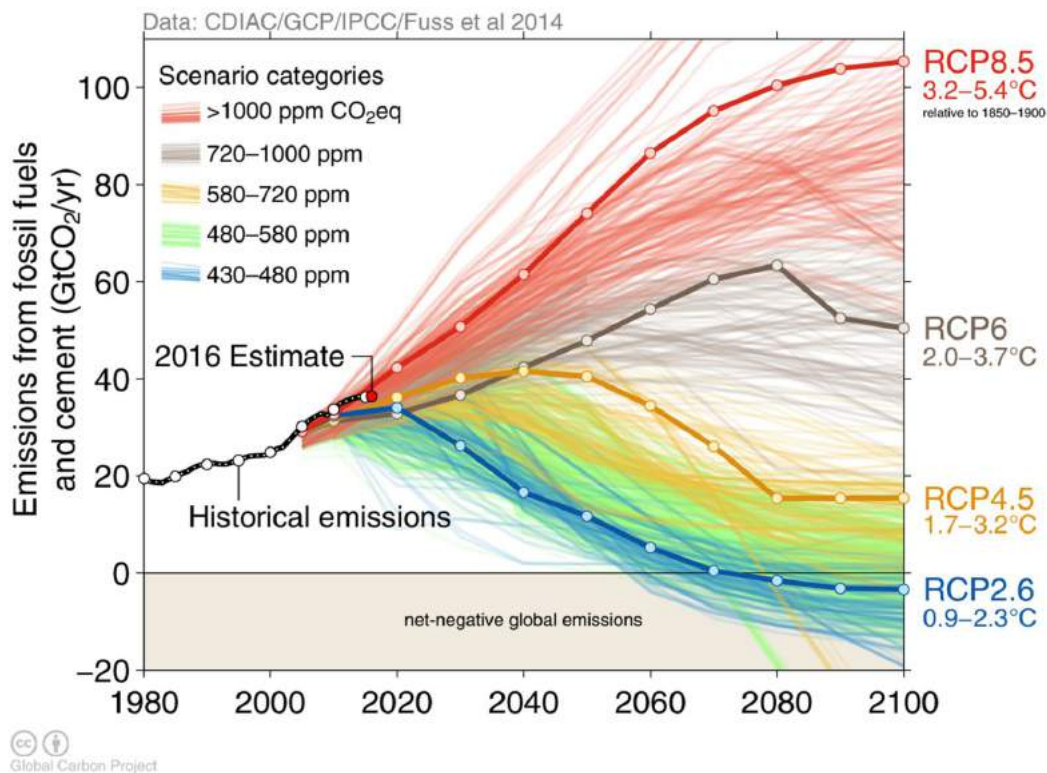sector, that accounts for about 12% of the global energy demand [13], while it is harder in transportation and chemical industry. In the first case, huge impact is given by commercial transportation (e.g. marine, aviation, rail, and heavy-duty road vehicles) where electrification, and so renewable sources, is very challenging [14], and this means that chemical fuels are more fitting for this sector. In the same way, strong interest in the development of sustainable pathways is present in the production of industrial chemicals, where fossil fuels derivatives are fundamental. Therefore, a fossil fuel–free and sustainable production is globally needed for chemicals [15, 16], as hydrogen, hydrogen peroxide, ethylene, propylene, methanol and ammonia.

In Fig.1.6 a possible sustainable pathway is reported in order to produce *green* fuels and chemicals as hydrogen, hydrocarbons and ammonia. This approach works thanks to the replacement or co-working with the traditional way of energy produc-
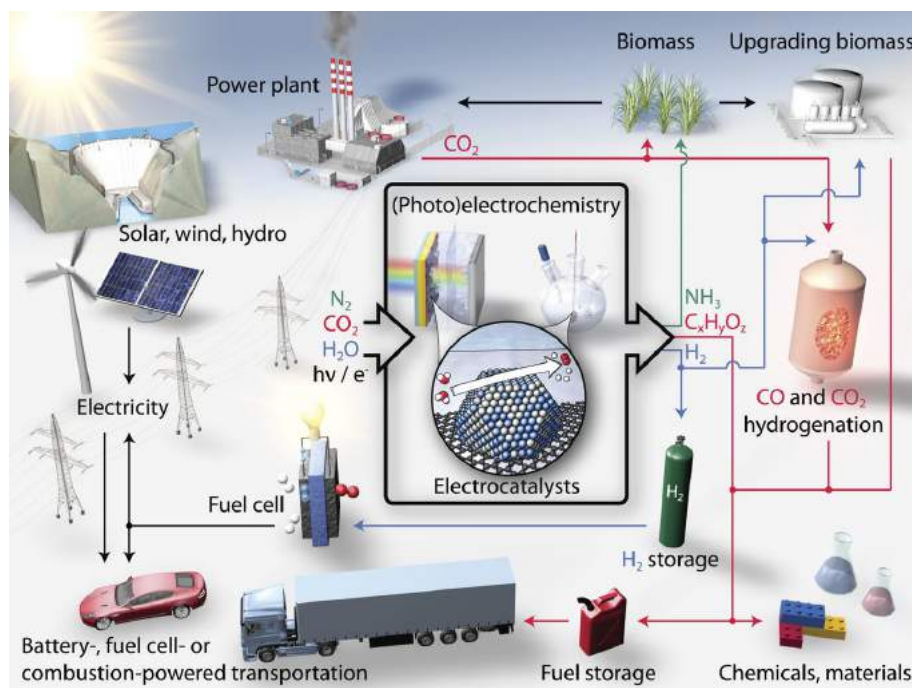
Fig. 1.6 Schematic of a sustainable energy landscape based on photo/electro/catalysis. From [14]. Reprinted with permission from AAAS.

tion. In fact, Earth is an unlimited source of water, carbon dioxide and nitrogen, that can be used potentially as building blocks for the aforementioned products by employing suitable electrocatalysts or photo-electrocatalysts coupled to renewable energy sources. As first example, water-splitting reactors have gained much attention as a sustainable source of hydrogen [17, 18]. In fact, hydrogen is an energy carrier that can be employed as green energy in fuel cells. In this case, H_2 can be oxidized together with an Oxygen Reduction Reaction (ORR), converting the potential chemical energy into electricity [19, 20]. On the other side, hydrogen peroxide can be a result of the Oxygen Evolution Reaction (OER) [21] and can be used as chemical in the bleaching and water treatment industries. Moreover, atmospheric carbon dioxide can be captured or instantaneously converted becoming an important carbon source for fuels, commodity chemicals, fine chemicals, and precursors to polymers and plastics via its electroreduction [22]. In the same way, the nitrogen electroreduction into ammonia would allow for the production of green fertilizers and locally at the point of use and application and at the required concentration, eliminating distribution costs [23].

The crucial key point is the development of electrocatalysts or photo- electrocatalysts with a suitable efficiency and selectivity for the chemical transformation involved, together with devices and reactors appropriate for the energy source employed in the reaction. More in general, it will be indicated as *electrode*, the whole material consisting in a *substrate* and a *catalyst*, placed above. The substrate should be conductive, ensuring an efficient electron transfer from the external circuit toward

the catalyst and, in some cases, permeable to gases, such as oxygen. The catalyst layer is where the electrochemical reactions take place, so, it should be in intimate contact with the reactants (liquid or gas), with the electrolyte and with the current collector, the substrate. Effective contact between the catalyst and the reactants is maintained thanks to the high surface area of the catalyst itself, obtained with nanostructuration that ensures a number of catalytic sites, in order to reach high performance.

1.2.1   Reactors for O_2 reduction

Several types of modern renewables systems, such as Proton Exchange Membrane (PEM) fuel cells, Metal-air batteries and Microbial Fuel Cells (MFCs), exploit the Oxygen Reduction Reaction (ORR) at the cathode.

Proton Exchange Membrane (PEM) fuel cells are nowadays considered clean energy-converting devices thanks to their high efficiency, high energy density, and low or zero pollutant emissions. In this fuel cell, Hydrogen (or liquid fuels) Oxidation Reaction (HOR) occurs at the anode, while at the cathode Oxygen Reduction Reaction (ORR) takes place, both catalyzed by suitable materials. At the actual state-of-the-art, the most practical and used electrocatalysts are Pt-based nanoparticles [24], even though their cost, sensitivity to contaminants, intolerance toward methanol oxidation and Pt dissolution [25].

In general, the conversion from chemical energy into electrical energy in a PEM fuel cell occurs by a direct electrochemical reaction, without combustion. In Fig.1.7, it is reported a schematic representation of the fuel cell, that can be divided in three main sections: anode, cathode and polymer electrolyte. In the anodic side the fuel (e.g. hydrogen) and oxidant are supplied to device from an external source, while at the cathode, the oxygen is supplied. In between, a membrane electrode assembly (MEA), consisting of a polymer electrolyte, is placed in order to conduct protons, from the anode to the cathode, and to separate the two incoming gases in the device. During its operation, the hydrogen is decomposed into positively charged protons and negatively charged electrons. Both of them flow from the anode toward the cathode, but the protons flow through the polymer electrolyte membrane, while the electrons through an external load, creating an electrical current. At the cathodic side, the electrons recombine with protons and oxygen, forming water as reaction byproduct flowing out of the fuel cell.

Platinum-based catalysts are nowadays the most efficient option for the hydrogen molecule splitting, which is relatively easy. On the other side, oxygen molecule splitting is harder, and, also in this case, Pt is one of the best options for the oxygen reduction reaction. It has to be remarked that the PEM fuel cell is a complex system whose performance depend on the successful operation of all its components. In fact, research focuses on different topics such as flow field design, electrode catalysts, membrane as well as on parameters such as temperature and humidity.

A second example are **metal–air batteries**, where electricity is generated through a redox reaction between a metal and the oxygen present in air. In Fig.1.8 is pre-
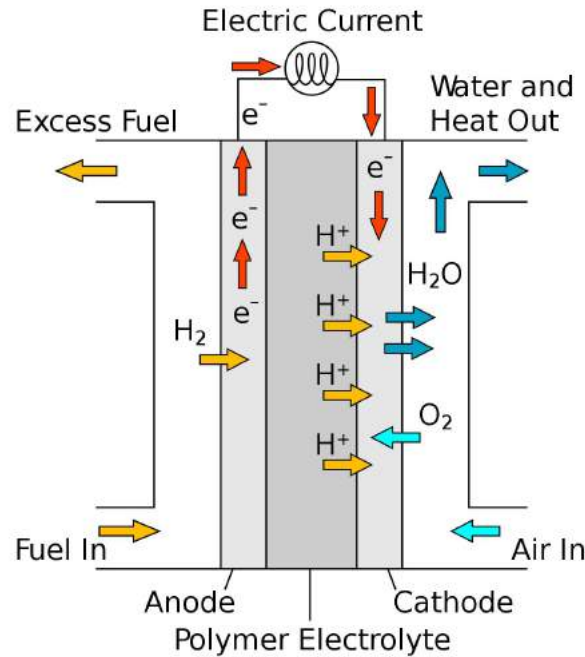
Fig. 1.7 Scheme of the working principle of a PEM fuel cell. Source: Wikipedia, Proton exchange membrane fuel cell, https://en.wikipedia.org/wiki/Proton_exchange_membrane_fuel_cell.

sented a schematic illustration of this kind of battery, featured with an open cell structure, which allows a continuous supply of oxygen (the cathode active material). Considering the metal as the 'fuel' of the cell, these devices can be considered similar to a fuel cell. They are characterized by a notably high energy density [26], being the oxygen not stored in the cell, while the metallic anode has an high ratio of valence electrons compared to the atomic nuclei [27]. Some examples of metal-air batteries are the $Zn-MnO_2$ (Zn-Mn), the rechargeable lead-acid, nickel–metal hydride (Ni–MH) and lithium-ion batteries [28]. In particular, the Li–air battery is able to release a very high theoretical specific energy (11.7 kWh/Kg), close to the one of the most energy-dense liquids such as gasoline [29, 30].

The most actual electrically rechargeable metal–air batteries still remain at research and development level [30, 31]. In 1996, Abraham and Jiang reported for the first time a $Li-O_2$ battery, composed by a lithium anode, a carbon composite as cathode and a conductive organic polymer electrolyte membrane (composed of Li^+ ions) [29]. As for fuel cells, the cathode engineering is one of the major obstacles due to the intrinsic low-kinetic reactions, high overpotentials and poor reversibility of oxygen chemistry [32]. The air cathode is one of the main factors affecting the battery performance, being complex in design and, in some cases, expensive. In this framework, researchers investigated the cathode reaction mechanism, developing more efficient catalytic materials for ORR and making the electrode structures more
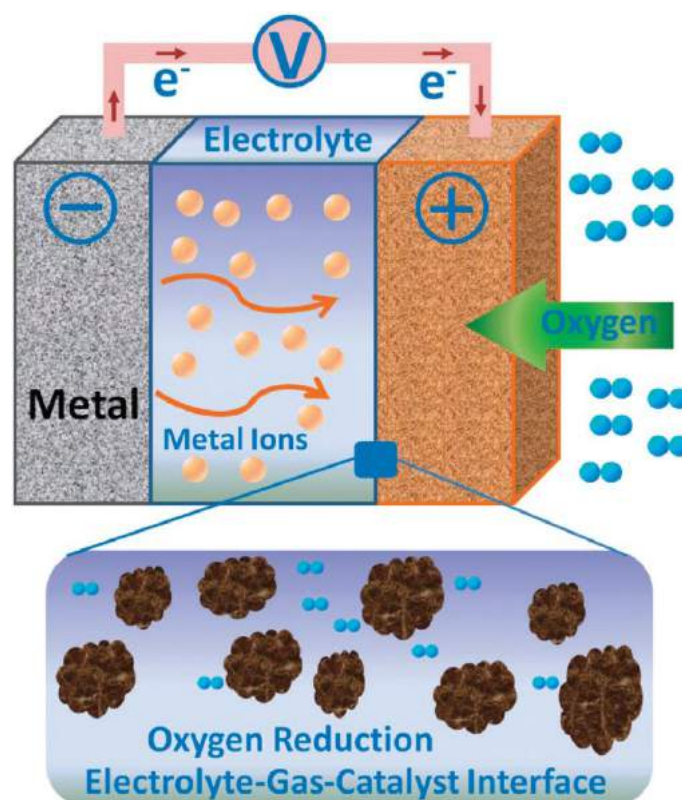
Fig. 1.8 Scheme of a metal-air battery. At the cathode/electrolyte interface is pointed out where the ORR takes place. Reproduced from [26] with permission of The Royal Society of Chemistry (RSC).

efficient in order to facilitate the mass/charge transport and the interface interaction [30, 31, 33, 34].

A further example is represented by **Microbial Fuel Cells (MFCs)**, a more recent approach for the bioelectricity generation from biomass thanks to bacteria respiration. MFCs is considered as a promising technology for researcher, thanks to its capability of energy production starting from wastes, thus providing a more green alternative to the other fuel cells by coupling electricity production with wastewater treatment.

In general, in MFCs depicted in Fig.1.9, microorganisms degrade (oxidize) organic matter at the anode of the device, producing electrons that induce the development of a potential difference between the anode and the cathode, which acts as driving force for the bioelectrogenic activity [36, 37]. At the cathode occurs the reduction process between the protons (coming from the Proton Exchange Membrane, PEM), the electrons (coming from the external load) and the Terminal Electron Acceptor (TEA). Oxygen is the most abundant and readily available electron acceptor for biological systems for its high reduction potential (+0.816 V) and, therefore, is the most widely used. The involved bacteria can exogenously transfer electrons, called exoelectrogens, and they can be used to produce power in MFCs. An
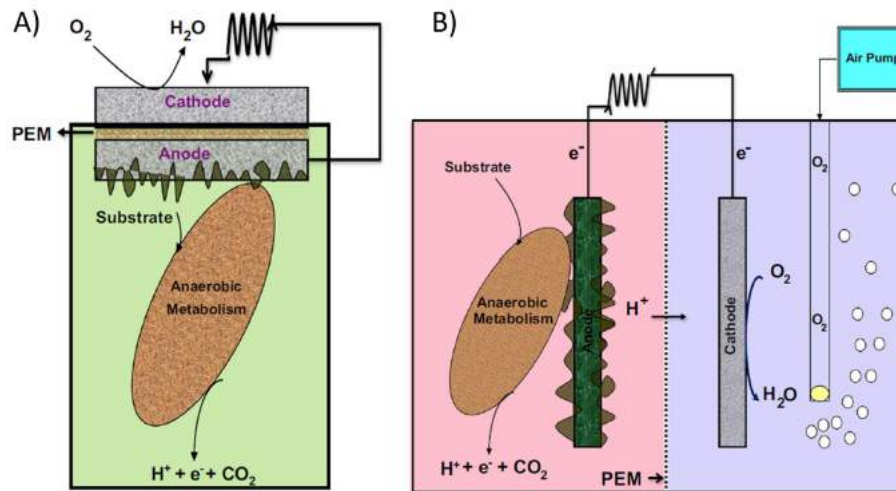
Fig. 1.9 Scheme of two microbial fuel cells: A) open air cathode, B) traditional two chambers cell. Reprinted from [35] with permission from Elsevier.

oxygen contamination in the anode chamber would inhibit the electron generation, so the system must be designed to keep the two electrodes separated. This can be achieved by placing a PEM that allows charge transfer between the electrodes giving the opportunity to get two types of cells: open air cathode (Fig.1.9A) and two chambers configuration (Fig.1.9B). In both cases the anolyte (anode electrolyte) surrounds the bacteria, isolated by the PEM. In the first case A, however, the cathode is directly in contact with the oxygen source, the air, while, in the second one B, the oxygen is bubbled in the catholyte (cathode electrolyte). The two electrodes are connected by a wire with a load, the device being powered. In principle, the membrane is permeable to protons, produced at the anode, that can migrate toward the cathodic side, where they can combine with electrons, via the wire connection, and oxygen to form water as a byproduct.

In recent years, MFCs have gained considerable interest due to their ability to harvest power from a wide range of substrates (anolyte fuel) which include biomass, real-field wastewater, synthetic medium, etc. as electron donor [37–41]. MFCs can be specifically designed to harvest bioelectricity from the aquatic eco-system where the water wastes are considered as a potential source to convert the organic rich sediment into energy [42]. Considering plant-based MFCs, the solar radiation can be exploited to generate bioelectricity thanks to the integration of living plant with electrodes [42]. Besides power generation, MFCs can be used also as efficient bio-electro-chemical system for waste remediation [43–45].

1.2.2   Reactors for CO_2 reduction

As already mentioned, the urgency to exploit renewable energy sources and to produce green fuels and chemicals, has pushed the research towards systems able to exploit CO_2 as valuable resource. Since the initial studies on CO_2 Reduction

Reaction (CO_2RR), no standard experimental methods have been established for the electrochemical reduction investigation, as already stated by Jaramillo et al. [46]. However, reactor should contain a small as possible amount of electrolyte with a large surface area of the working electrode, as a general recommendation. In order to identify and evaluate the reduction reaction byproducts, current and voltage have to be measured with highly sensitive instruments.
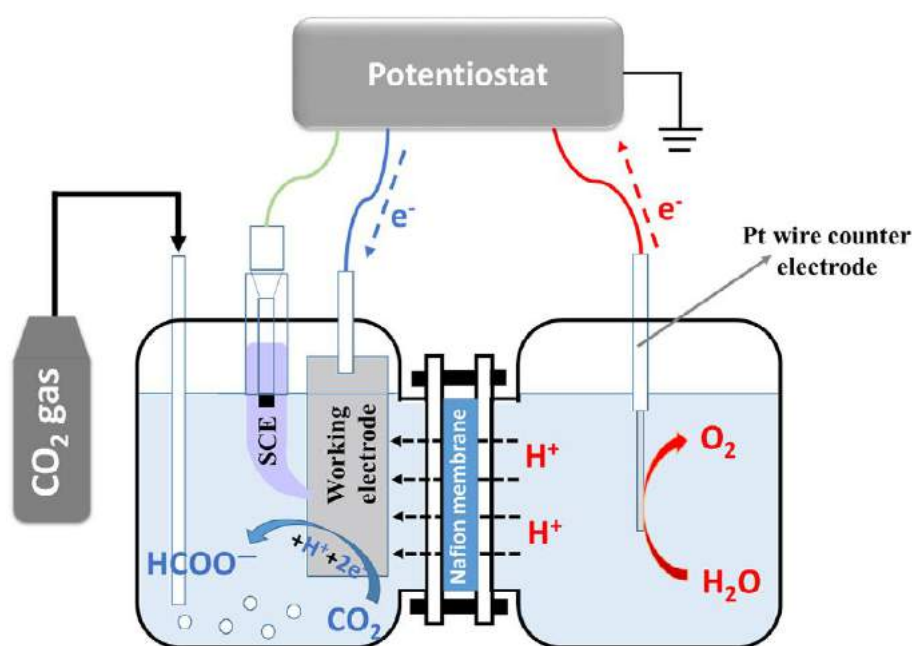

Fig. 1.10 Scheme of an H-type reactor in a 3 electrode cell, used for the electrochemical reduction of CO_2 onto a copper surface. Reprinted from [47] with permission from Elsevier.

In general, reactors can be divided in two different categories: flow and batch reactors. Compared to the second case, the first type has an enhanced capability of mass transfer of CO_2. Studies were devoted to the the use of conventional H-cells (see Fig.1.10) or more complicated setups, with the aim of a uniform electric field distribution between the working and the counter electrode. Electrochemical cells can be built and operated in three different modes [48]:

(i) **Semi-half discontinuous cells**. One side of the cell membrane, the counter electrode side, is in contact with a liquid electrolyte, while the working electrode is placed on the other side of the membrane, kept in touch with the gas phase, containing high-purity CO_2.

(ii) **Discontinuous cells**. The electrochemical cell is first flushed with a stream of CO_2, then closed, and after applied a voltage drop onto the cell.

(iii) **Semi-half continuous cells**. It has a similar design to the semi-half discontinuous cell, with the difference of having a continuous flow of CO_2 through the cell.

All the three listed cells have been proven to be efficient in a **photoelectrocatalytic cell (PEC)**, converting CO_2 into valuable fuels or long-chain hydrocarbons [48, 49]. In Fig.1.11 is presented a scheme of a PEC device, where the CO_2 is transformed into fuels due to the photo-electro-catalyst placed onto the electrode (in yellow), e.g. nanostructured titania as utilized by Centi and co-workers [49–51]. At the counter electrode side (green electrode), the water molecule is oxidized forming oxygen, protons and electrons.
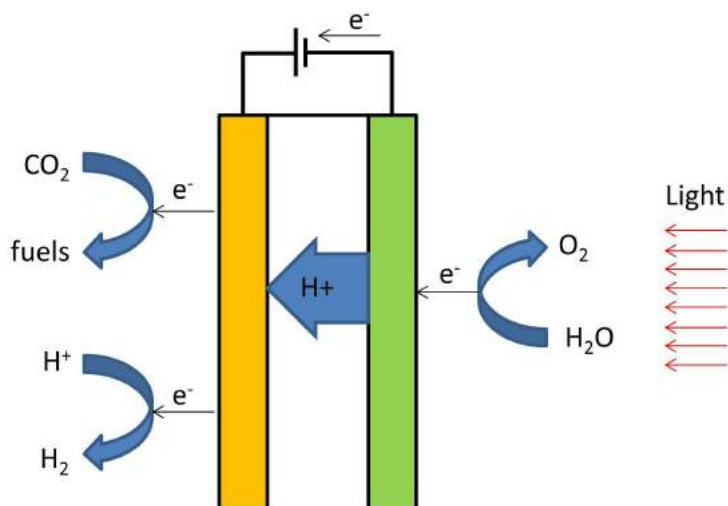

Fig. 1.11 Scheme of a photo-electro-catalytic cell (PEC).

In order to commercialize a CO_2 electroreduction device, engineers and researchers should design a continuous system on a large scale. This would include both the electrode design and the electrolyte choice. As an example, Gas Diffusion Electrodes (GDEs) have shown good performance by improving the oxygen transfer capability, even though some drawbacks arose. Some of these include the lack of electrode stability and the deficiency of the potential for electrochemical reactions in the pores of GDE [52–54]. Concerning the electrolyte, the most commonly used is based on $KHCO_3$ solution, but, a more eco-friendly choice would be the use of industrial waste waters as electrolytes. If this would come true, the chemical costs of CO_2 electroreduction could be greatly reduced, solving, at the same time, the waste disposal of some plants, together with the production of fuels and chemicals.

1.3 Aim of the work

This Ph.D. thesis investigates different metal oxide nanostructures as catalysts used in electrochemical cell cathodes: manganese oxide (Mn_xO_y) nanofibers, titanium dioxide (TiO_2) nanotube-based and copper oxide (Cu_xO) nanowire-based catalysts.

The Mn_xO_y nanofibers are presented as catalysts for Oxygen Reduction Reaction (ORR) in Microbial Fuel Cells (MFCs). They can be fabricated starting from

environmental friendly, biocompatible and biodegradable precursors, by means of the electrospinning technique. This leads to and ease and reproducible nanostructuration with an high surface area. The study of the thermal evolution of the nanofibers, from the precursors to the oxide, gives the possibility to modulate the morphological and structural properties of the catalysts, also providing a thermal evolution model, and leading to the selection of the optimal Mn_xO_y for ORR. The final integration with a conductive substrate will be the key point of this study, in order to fabricate a complete cathode. A new and valuable approach is proposed and followed in this work: it consist in the direct integration of the catalyst onto carbon-based substrate that can improve the final device efficiency, the Microbial Fuel Cell (MFC).

The catalysts considered in the present days for CO_2 Reduction Reaction (CO_2RR), are studied both as single materials or as a core-shell configuration, in order to take advantage of the catalytic properties fo both the materials. The TiO_2 nanotube-based, proposed as CO_2 Reduction Reaction (CO_2RR) catalyst, are developed and fabricated directly growing the NTs array onto the Ti foil by anodic oxidation thus obtaining a complete cathode, and coupling this material with copper or copper oxide. The key point of this material development relays in the simple integration method of the nanotube array with the upper layer: a combination of sputtering and thermal oxidation techniques. The nanostructuration and composition of both bare and Cu-Cu_xO-supported TiO_2 NTs are studied in order to define their role in the CO_2RR studied in an electrochemical test cell.

The Cu_xO nanowire-based catalysts, in the end, are also studied for CO_2RR, developing the NWs carpet directly onto the bare Cu foils and, also in this case, obtaining a complete cathode. The growth of copper oxide nanowires is obtained from a simple thermal annealing and, as for the TiO_2 NTs, they are studied in terms of composition, morphology and CO_2RR catalytic activity by changing the process parameters. A preliminary study of integration between Cu_xO NWs and TiO_2 will be presented, by proposing a simple method that couples Ti evaporation with thermal annealing. As stated for the TiO_2 NTs, nanostructuration and composition are studied in order to define their role in the CO_2 Reduction Reaction (CO_2RR) studied in an electrochemical test cell.

The manuscript is divided in 6 chapters: Chapter 1 provides an introduction on energy demand, pollution problems, energy production devices and describes the objectives and the structure of this work; Chapter 2 presents the detailed description of the two reduction reactions investigated in this work, i.e. ORR and CO_2RR, focusing the attention on the reduction process and the different catalyst proposed in literature. Chapter 3 focuses on the synthesis method used and developed in this thesis: electrospinning, anodic oxidation and thermal annealing. The experimental part starts with Chapter 4 were the manganese oxide nanofibers are presented, giving a detailed description of their synthesis, morphology, composition and electrochemical behavior, also considering their integration in MFC. Chapter 5 describes the development and characterization of the TiO_2 NTs and Cu_xO NWs -based catalyst with the target of producing valuable byproducts from CO_2 reduction. Finally, Chapter 6 provides the concluding remarks and outlooks of this Ph.D. thesis.

This work is the result of a collaboration among the *Center for Sustainable Futures Technologies* (CSFT, ITT@PoliTo) of Istituto Italiano di Tecnologia, the *Applied Science and Technology Department* of Politecnico di Torino and *Electronics and Telecommunications Department* of Politecnico di Torino.

Chapter 2

Nanostructured catalysts based on transition metals oxides

Chapter abstract   *In Chapter 2, a brief introduction to the state of the art on the metal-oxide catalysts will be given. At first, a brief definition of catalyst is proposed, in Sec. 2.1, declaring the targets of a good catalyst material. In Sec. 2.2, the concept of nanostructuration and nanomaterials will be defined shortly. The catalytic mechanisms and state-of-the-art of ORR and CO_2RR will be discussed in Sec. 2.3 and Sec. 2.4, respectively. For both reactions, it will be listed the principal metal and metal-oxide catalysts proposed in literature, highlighting advantages and drawbacks.*

2.1   Definition of a catalyst

Catalysis is a chemical phenomenon in which a reaction is accelerated by a foreign material, called *catalysts* [55]. An optimal catalyst should enhance the rate of a reaction without changing the position of the thermodynamic equilibrium state. Most of the catalysts are in solid or liquid form, but they can also be gases. The catalytic reaction, in general, is a cyclic process, where the reactant or reactants form a complex with the catalyst and subsequently a pathway is opened for the transformation of the reactants into the products. The catalytic material should be released and a second cycle can proceed. Unfortunately, catalysts do not have infinite life due to side reactions and products, that lead to the catalyst deactivation.

A reaction is called *homogeneously catalyzed*, if the catalyst and reactants or their solution form a common physical phase. Typical homogeneous catalysts are metal salts of organometallic complexes, organic acids and carbonyls of Co, Rh and Fe. On the contrary, *heterogeneous catalysis* occurs when the catalyst and reactants form separate physical phases. Typical heterogeneous catalysts are inorganic solids such as oxides, metals, metal salts, sulfides and organic materials such as enzymes. A catalytic process consists in the reactant molecules coordination, the ligands, to the central atoms, where the ligands themselves could be molecular species, in the

case of homogeneous catalysis, or surface neighboring atoms of the solid matrix, in the case of heterogeneous catalysis.

More in general, a catalysts should undergo several characteristics:

(i) Unchanged in chemical composition and mass during working conditions;

(ii) Long life, without surface poisoning or alteration;

(iii) Low cost of the material that constitutes it and of the production process;

(iv) Nanostructured, in order to optimize the catalytic efficiency. Nano-dimensions should enable the possibility of having an higher surface area, increasing the catalytic activity due to the fact that more catalytic sites are available at the same time.

However, a catalyst should not be confused with a catalyst electrode, which indicates a material consisting in a substrate and a catalyst, placed above. The substrate should be the conductive backbone, ensuring an efficient electron transfer from an external circuit (e.g. in a fuel cell) toward the catalyst and, in some cases, permeable to gases, such as oxygen. The catalyst is electrochemically active part and it should be in intimate contact with the reactants (liquid or gas), the electrolyte and the current collector, thus the substrate. Strong contact between the catalyst and the reactants is maintained thanks to the high surface area of the catalyst itself, obtained with nanostructuration that ensures a number of catalytic sites, in order to reach high performance.

2.2   Definition of nanostructuration

In the science history, *Nanotechnology*, was the first term that appeared referring to a class of measurable values around 10^{-9} of know physical objects such as 10^{-9} m = 1 nm (nanometer), 10^{-9} s = 1 ns (nanosecond), ... [56] Nanotechnology covers a variety of technologies connected to atomic, ionic or chemical transport, where distances strongly contribute to the interactions between the nanostructures. *Nanotechnology*, as well as, *Nanoscience*, is based on the combination of different disciplines: physics, chemistry, mathematics, biology and so on. These are the fundamentals of the *science of nanomaterials*, with which one can obtain information about composition and properties of nanomaterials or nanoparticles. Since the first nanostructure definition as the range from 1 nm to 1000 nm [57–59], lots of paper published set the upper value up to 100 nm.

It is quite obvious to say that the difference of nanoparticles from others nanomaterials is determined by their specific characteristics, physical or chemical [56]. In fact, a nanoparticle shape can vary strongly, depending on the nature of the atoms that form it. The molecules, so the electron interactions, determine the atomic structure of the nanostructure, its geometry and activity or reactivity towards specific reactions. More importantly, nanomaterials are able to show completely different properties from their correspondent bulk ones.
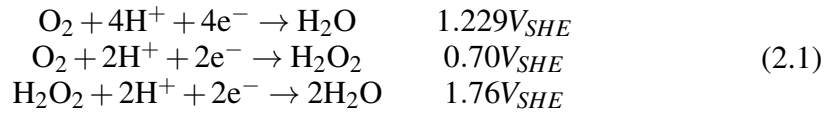
2.3   ORR catalysts state-of-the-art

Oxygen (O_2) is one of the most abundant element on Earth and Oxygen Reduction Reaction (ORR) is also one of the most important reactions in different processes (e.g. biological respiration and energy conversion in fuel cells). The reaction, in aqueous media, mostly occurs with two different pathways: the **4-electron reduction pathway** from O_2 to H_2O and the **2-electron reduction pathway** from O_2 to hydrogen peroxide (H_2O_2).
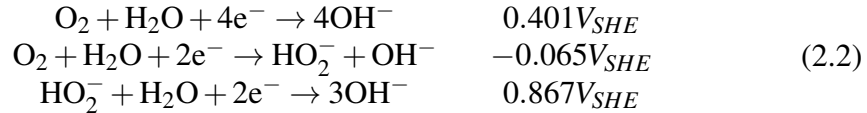
Generally, in fuel cells such as Microbial Fuel Cells (MFCs), the ORR occurs at the cathode, as described in Sec. 1.2.1. Without a proper catalyst at this electrode, the cell would be practically unusable, due to the low ORR kinetics. Pt is the best known ORR catalyst, but, due to its high cost, it is practically unusable for commercially viable fuel cells. In the last decades, extensive research has focused on alternative electro-catalysts [60], including metals [61], carbon [62], conductive polymers [63] and metal oxides [64]. It has to be highlighted that all the aforementioned materials, and the nets ones, are electrocatalysts, meaning that the reduction reaction activated by an external bias.

2.3.1   ORR mechanism

The ORR mechanism is rather complicated and involves several intermediates, mainly depending on the nature of the used catalyst, electrode material and electrolyte. In Eq.2.1 are reported the ORR reactions in case of acid aqueous electrolytes [65, 66] with their thermodynamic electrode potentials at standard conditions versus SHE (Standard Hydrogen Electrode):

$$\begin{aligned}
O_2 + 4H^+ + 4e^- &\rightarrow H_2O & 1.229 V_{SHE} \\
O_2 + 2H^+ + 2e^- &\rightarrow H_2O_2 & 0.70 V_{SHE} \\
H_2O_2 + 2H^+ + 2e^- &\rightarrow 2H_2O & 1.76 V_{SHE}
\end{aligned} \tag{2.1}$$

In Eq.2.2 are reported the ORR reactions in case of alkaline aqueous electrolyte [65, 66], with their thermodynamic electrode potentials at standard conditions:

$$\begin{aligned}
O_2 + H_2O + 4e^- &\rightarrow 4OH^- & 0.401 V_{SHE} \\
O_2 + H_2O + 2e^- &\rightarrow HO_2^- + OH^- & -0.065 V_{SHE} \\
HO_2^- + H_2O + 2e^- &\rightarrow 3OH^- & 0.867 V_{SHE}
\end{aligned} \tag{2.2}$$

Generally speaking, the ORR reduction can be divided in two reduction processes [67]. The first one is the 4-electron direct pathway or full reduction, which is the desired mechanism in fuel cells application [68, 69]. The second one is the 2-electron pathway, that is mostly used in industry for hydrogen peroxide production [70]. The full reduction is in general the most interesting and investigated pathway, thanks to the high chemical stability of water, compared to the hydrogen peroxide, which is highly reactive [71].

Fig. 2.1 schematically summarizes the two different pathways already mentioned. In case of partial reduction (Fig. 2.1A), the O_2 is firstly adsorbed on the catalyst surface, resulting in a H_2O_2 adsorbed molecule after the addiction of two hydrogens. This hydrogen peroxide may desorb resulting in a free H_2O_2 molecule or further reduce into two water molecules. The full reduction (Fig. 2.1B), instead, begins with a dissociative adsorption of oxygen on the catalyst surface. A first electron transfer takes place resulting in the formation of *OOH after hydrogen addiction. Afterwards, a second electron transfer occurs by a further hydrogen addiction. Depending on this last addiction, two types of O_2 reduction may occur, establishing how the reaction goes on. If the second hydrogen addition takes place at the oxygen adsorbed to the catalyst (mechanism A in Eq. 2.3), the resulting products are two water molecules. If the second hydrogen addition takes place at the oxygen already bound to the first hydrogen (mechanism B in Eq. 2.4), the product is a single water molecule that desorbs from the catalyst. From literature the mechanism A is thermodynamically favored, being also the more realistic mechanism [69].
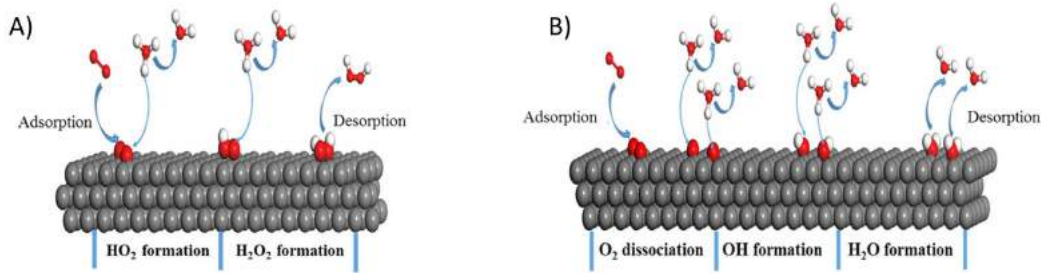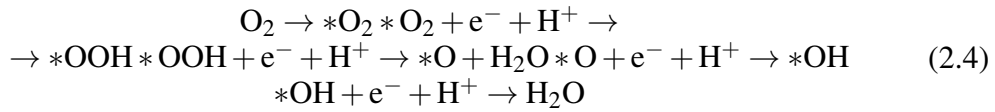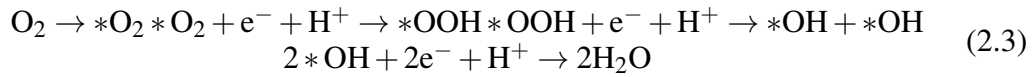
$$O_2 \rightarrow *O_2 \, *O_2 + e^- + H^+ \rightarrow *OOH \, *OOH + e^- + H^+ \rightarrow *OH + *OH$$
$$2*OH + 2e^- + H^+ \rightarrow 2H_2O \tag{2.3}$$

$$O_2 \rightarrow *O_2 \, *O_2 + e^- + H^+ \rightarrow$$
$$\rightarrow *OOH \, *OOH + e^- + H^+ \rightarrow *O + H_2O \, *O + e^- + H^+ \rightarrow *OH \tag{2.4}$$
$$*OH + e^- + H^+ \rightarrow H_2O$$

Fig. 2.1 Schematic representation of the ORR mechanism: A) 2–electron pathway, B) 4–electron pathway. Reprinted by [67] with permission from Elsevier.

In the last decades, due to its applications in fuel cells and industry fields, the number of publications about ORR rose drastically, as shown in Fig. 2.2.
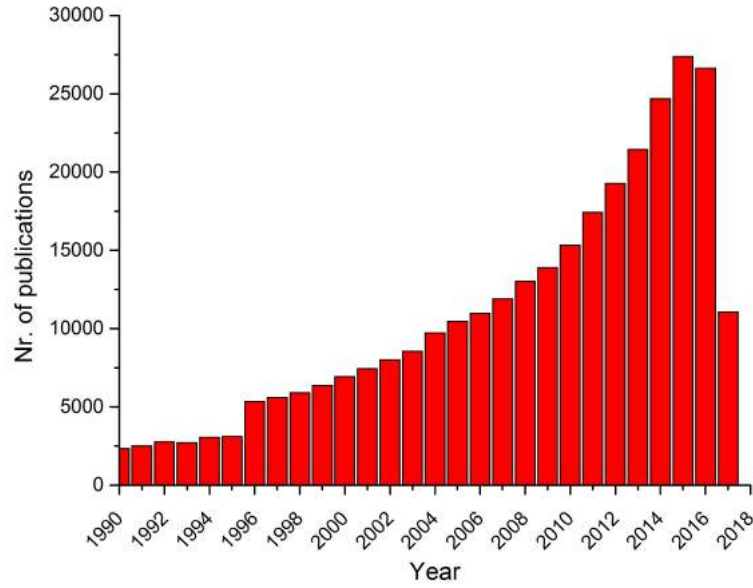
Fig. 2.2 Number of publication per year on Oxygen Reduction reaction (1990-2017), source Scopus.

2.3.2   Kinetics of ORR

In order to have a good reaction rate, the ORR should occur at potentials as close as possible to the thermodynamic electrode potential. The current-overpotential relationship is given by the following equation [66]:

$$I_c = i^o_{O_2} \left(e^{\frac{n_{\alpha O} \alpha_o F \eta_c}{RT}} - e^{\frac{n_{\alpha O}(1-\alpha_o)F\eta_c}{RT}} \right) \tag{2.5}$$

where:

- I_c is the ORR current density;
- $i^o_{O_2}$ is the exchange current density;
- $n_{\alpha O}$ is the number of electron transfered;
- α_o is the transfer coefficient;
- η_c is the ORR overpotential;
- F is the Faraday constant;
- R is the gas constant;
- T is the temperature in Kelvin.

High current at low overpotential can be obtained when $i^o_{O_2}$ is large and/or $\frac{RT}{n_{\alpha O}\alpha_O F \eta_c}$ is small.

It has to be highlighted that the exchange current density is an important kinetic parameter that represents the electrochemical reaction rate at equilibrium [24].

Considering $O + ne^- \leftrightarrow R$ as a general electrochemical reaction, both forward and backward reaction may occur at the equilibrium, where the current density is zero [66]. In fact, the current density of the forward reaction is equal to the one of the backward reaction and it's called exchange current density. Its intensity tells how rapidly my occur the considered electrochemical reaction.

The exchange current density of a given electrochemical reaction depends not only on the reaction but also on the electrode surface on which is occurring the reaction. The ORR, in fact, has an exchange current density on a Pt electrode [72] much higher than on an Au one. This means that Pt has a stronger catalytic activity on ORR with respect to Au. It is easy to deduce that different electrode materials or catalysts can have a strong effect on ORR kinetics, giving different exchange current densities.

Generally the exchange current density is expressed in A/cm^2, being strongly dependent on the effective electrode surface area. In fact, the electroactive area is different from the geometrical area.

2.3.3   Techniques Used in Electrocatalytic ORR

There are many techniques to evaluate the catalytic efficiency of a selected material. Among them the ones discussed in this thesis are Cyclic Voltammetry (CV) and Rotating Ring Disk Electrode (RRDE).

Cyclic Voltammetry (CV)   provides qualitative information about the electrochemical activity of a catalysts. CV is carried out by cycling the potential between two fixed values (one high and one low), acquiring the resulting current. The resulting plot of current as a function of the voltage is called *voltammogram*. The sweeping rate, otherwise the sweep of the potential, is linear and generally used between 1 mV/s and 1000 mV/s. During a measurement the potential is swept to cause the reduction (or oxidation) of some given electrochemical active species, causing the rise or lowering of the current. The anodic current increases with the potential due to the oxidation reaction speedup. On the contrary, the cathodic current becomes lower as the potential goes lower: similarly as before, the potential lowering causes the reduction reaction speedup. When the potential reaches the standard potential E^0, the oxidized and reduced species concentrations become equal at the electrode surface/electrolyte interface. The highest current is obtained when the potential reaches a value at which all the electrochemically active species (reduced or oxidized forms) are consumed at the electrode surface. This formal potential, E^f, is given by the equation:

$$E^f = E^0 - 2.303\frac{mRT}{nF}pH \tag{2.6}$$

where m is the number of proton exchanged in the reaction, n is the number of electron exchanged, F is the Faraday constant, R is the gas constant, T is the

temperature in Kelvin and *pH* refers to the pH of the electrolyte used. Increasing (or lowering) the potential above E^f, the current starts to decline due to the double-layer thickness growth (due to the presence of ions in the electrochemical solution), resulting in a lowering of concentration gradient of the active species. In this case it can be clearly seen an anodic (or a cathodic) peak in the voltammogram. When the potential reaches one of the two limits, it reverses direction and starts to scan in the backward direction. If the considered electrochemical reaction is thermodynamically reversible, the positions of the cathodic or anodic peaks do not change with the potential scan rate (υ), and the current peak height i_p is defined as:

$$i_p = (2.69 \cdot 10^5) n^{3/2} A D^{1/2} \upsilon^{1/2} C \tag{2.7}$$

where *n* is the number of electrons per reactant molecule, *A* is the electrode area (expressed in cm^2), *D* is the diffusion coefficient and C is the bulk concentration of the reactant [66].
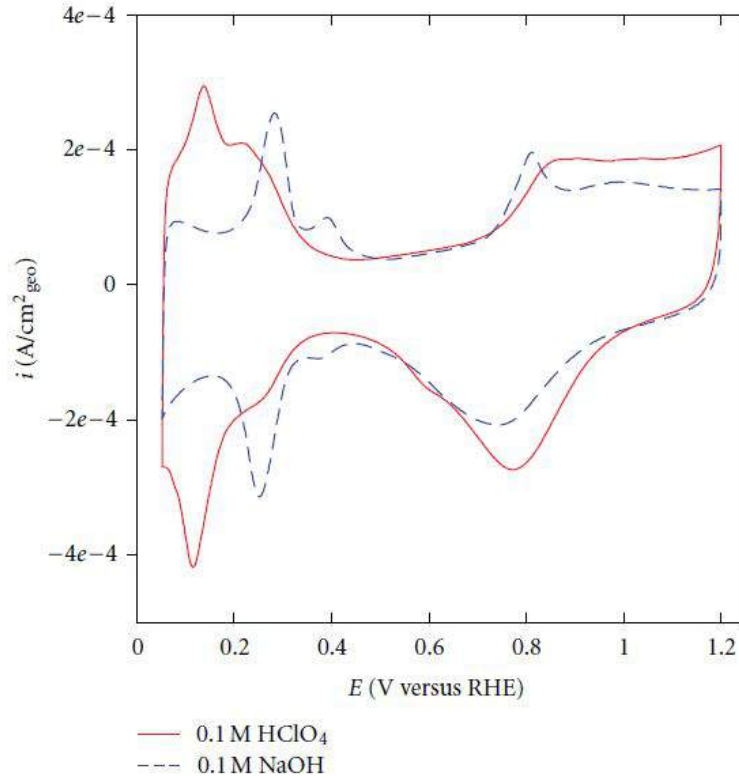

Fig. 2.3 Cyclic Voltammetry of 30% Pt nanoparticles supported on carbon in 0.1M NaOH (blue curve) and 0.1M HClO$_4$ (red curve) electrolytes. Reproduced from [73], DOI:10.1155/2012/491604.

Fig. 2.3 shows an example of cyclic voltammetry on 30% Pt/C in 0.1M NaOH and 0.1M HClO$_4$ electrolytes for the oxygen reduction. It can be observed that the catalyst shows the typical hydrogen underpotential deposition/stripping region under

0.5 V vs RHE (Reference Hydrogen Electrode) in both of the electrolytes considered. Above 0.7 V vs RHE the oxide formation on Pt occurs. This phenomenon is caused by the water molecules oxidation (water activation) in the acidic media [74] and by the specific adsorption of hydroxide anions from the supporting electrolyte in the alkaline media [75, 76]. Comparing the two electrolytes, the onset potential of the Pt-OH formation is similar for both. However, in alkaline conditions, the oxide formation current shows a more peaked shape if compared to the acidic media. The potential of Pt-OH formation is 0.775 V in NaOH whereas in $HClO_4$ is slightly shifted to 0.810 V.

Rotating Ring Disk Electrode (RRDE)   method is used to study the O_2 reduction catalyzed by a specific material. On the disk electrode, 2-electron and 4-electron pathway ORR may occur, while on the ring electrode, H_2O_2 is further oxidized to H_2O [77]. In Fig. 2.4 is reported a scheme of the arrangement of the two electrodes in a RRDE setup, where a coaxial ring electrode is added outside the disk electrode. During the product formation, the disk electrode is kept in continuous rotation in order to sweep away the products, detected by the outer ring electrode. E_R, potential of the ring, is at a value high enough to have the immediate reaction of the products. The measured I_R, current at the ring, reveals the amount of products formed at the disk. In general, if an oxidation occurs on the disk electrode, a reduction have to occur at the ring electrode, and conversely.
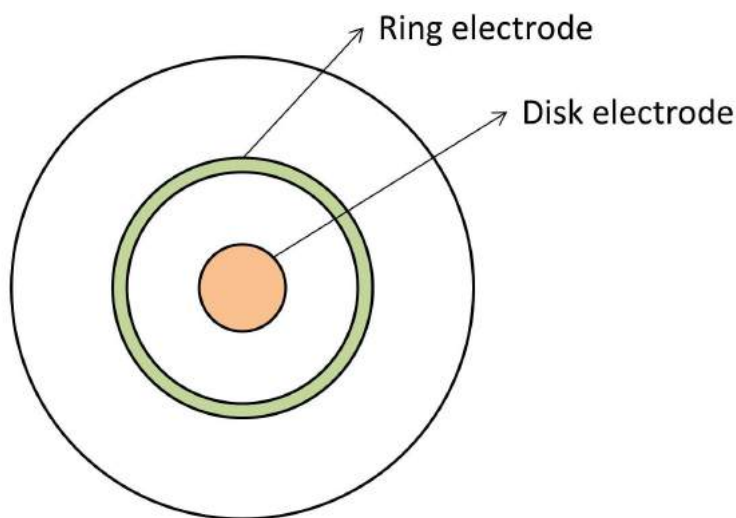

Fig. 2.4 Schematic representation of the ring and disk electrode in a RRDE setup.

The 2-electron reduction current (I_{2e^-}) is given by:

$$I_{2e^-} = I_R/N \tag{2.8}$$

where I_{2e^-} is the 2-electron ORR on the disk electrode, I_R is the oxygen reduction current on the ring electrode and N is the collecting coefficient number. The ORR current (I_D) on disk electrode can be expressed as:

$$I_D = I_{2e^-} + I_{4e^-} \tag{2.9}$$

where I_{4e^-} is the 4-electron ORR current. The subsequent equation is used to calculate the average electron number (n_{e^-}) involved in ORR:

$$\frac{I_D}{n_{e^-}} = \frac{I_{2e^-}}{2} + \frac{I_{4e^-}}{4} \tag{2.10}$$

By rearranging Eq. 2.10, the number of exchanged electrons n_{e^-} is:

$$n_{e^-} = \frac{4I_D}{I_D + I_R/N} \tag{2.11}$$

In the same way, it can be obtained the number of peroxide species, obtained $OH_2^-\%$ as:

$$OH_2^-\% = 200 \cdot \frac{I_R/N}{I_D + I_R/N} \tag{2.12}$$

In the case of a good-performing catalyst, n_{e^-} should be as close as possible to the value of 4. This means that the 4-electron pathway reduction is favored, leading to the production of water instead of hydrogen peroxide.

2.3.4   ORR materials

In order to have a good ORR catalyst, oxygen must tightly bond to the catalyst surface when the reaction takes place. The final dissociation products, however, must have bonds weak enough in order to desorb from the surface and, so, not poison the catalyst surface [55, 78, 79]. In literature, generally, *volcano plots* are used to express the correlation between the catalytic activity with the binding energy. In this section, some ORR catalysts will be described, focusing on the composition, nanostructuration and catalytic activity of the proposed materials.

Metal catalysts

In Fig. 2.5 is reported a volcano plot that shows the oxygen binding energy (ΔE_O) as a function of the catalytic activity for different metals. As already evidenced, **platinum (Pt)** is one of the best ORR catalysts and occupies the most optimal position, showing the highest catalytic activity among other metals (Pt > Pd > Ir > Rh). However, Pt

is not at the volcano peak, meaning that there are good opportunities for new ORR catalyst design and synthesis.
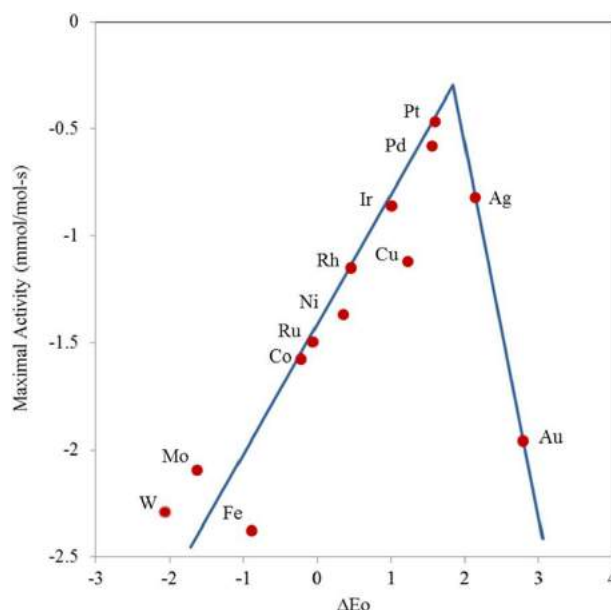

Fig. 2.5 Volcano plot showing relationship between oxygen binding energy and maximal activity calculated using Sabatier Analysis for different metals. Reprinted by [67], with permission from Elsevier.

The adsorption energy of O_2 and dissociation energy of O–O bond are strongly influenced by the electronic structure of the Pt catalyst (so the Pt d-band vacancy) and by its interatomic distance [80]. Moreover, the high cost of Pt, together with the aging effect in fuel-cell reactions reduce it applicability in scalable devices [81, 82]. In fact, the formation of highly stable Pt–OH and Pt–O species on catalyst surface acts as a limiting factors in the efficiency of energy conversion, slowing the ORR kinetics [83].

Current state-of-the-art of Pt catalysts is based on its nanostructuration in order to increase the active surface area (nanoparticles, nanowires) or on its alloying with a suitable metal (noble or transition one).

Pt nanoparticles (NPs) supported on various carbon supports. Unfortunately, the main drawback of these materials is the fact that Pt NPs show a large number of defect on the surface, which are less catalytically active. In fact, they slow down the ORR kinetic and decrease the durability of the catalyst because of irreversible surface atoms oxidation [84, 85]. In this framework, a good way to face this problem relies on the control of the shape of NPs. Sánchez et al. [86], in 2010, studied the catalytic activity of Pt NPs with different crystallographic arrangements at room temperature: tetrahedral-octahedral, cubic, spherical, hexagonal. They demonstrated that the hexagonal Pt NPs, with (100) and (111) preferential surface facets, exhibited an ORR enhanced activity if compared to other configuration. Therefore, they proved

the fundamental importance of the Pt NPs shape control and not only of the NP size and composition.

Yang and co-workers proposed Pd@Pt core shell NPs supported on carbon (Pd@Pt/C NPs) for ORR [87]. Cyclic voltammetry on different concentration samples showed the best electrocatalytic behavior for Pd70@Pt30/C at room temperature in acidic solutions. They could be able to extend the catalyst life and to enhance the ORR activity of the Pt/C NPs by lowering OH_{ads} bonds on Pt sites.

Particular interest gained also one dimensional Pt nanostructures such as **Pt nanowires (Pt NWs)** [88] and **Pt nanotubes (Pt NTs)** [89]. In particular, 1D structures, as showed in Fig. 2.6, improve the electron transport on the catalyst and increase the surface area without introducing new surface defects [90]. Yu and co-workers were able to produce ultrathin Pt NWs (see Fig. 2.6A), maximizing the surface area-to-volume ratio and decreasing the amount of supporting material, not catalytically active, in the inner part of the wire. In this way, they were able to obtain an active surface area 4 times greater than the analogous not supported Pt NTs and 7 times higher than the commercial supported Pt NPs [91]. Fig. 2.6 shows Pt NTs and PtPd NTs synthesized by Yan and co-workers. They obtained active NTs mass 1.4 and 2.1 times higher than that of Pt/C and platinum black, respectively, demonstrating an improved ORR kinetics thanks to the nanostructuration.
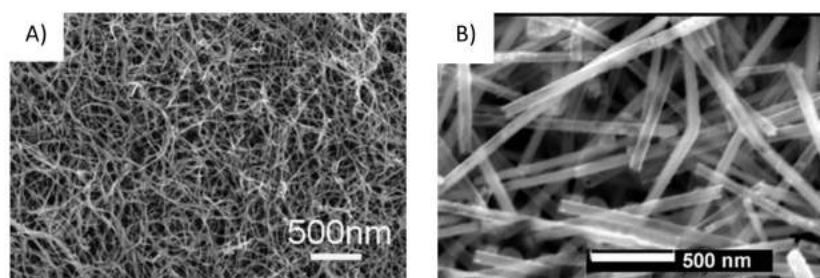

Fig. 2.6 Pt 1D nanostructurtes: A) TEM image of the Pt NWs. Reproduced from [88], with permission from john Wiley & Sons Inc. B) SEM image of Pt NTs. Reproduced from [89], with permission from john Wiley & Sons Inc..

Regarding **Pt alloys**, researchers calculated [71] and experimentally demonstrated [92] that PtM (M=Fe, Co, Ni, Y, Pd, etc.) alloys have an higher ORR activity than pure Pt. This can be explained by the change in the Pt electronic structure and interatomic distance. During Pt alloying, the lattice contracts, leading to a more favorable Pt-Pt distance for the dissociative adsorption of O_2. In Fig. 2.7 is shown a volcano plot of Pt-based metal alloys with higher kinetic current densities than pure Pt. These materials, in fact, tune the stability of these critical intermediates during ORR, thanks to Pt electronic structure modification.

Thanks to noble metals resistance to oxidation and robustness in acidic environments [93], they are good candidates for Pt alloying. The main drawback is the fact that they suffer of poor stability in fuel cells due to Ostwald ripening [94].

In recent years, Zhang et al. have established, for the first time, a one-pot solution synthesis method to produce a platinum-on-iridium catalyst NPs [95]. This synthesis
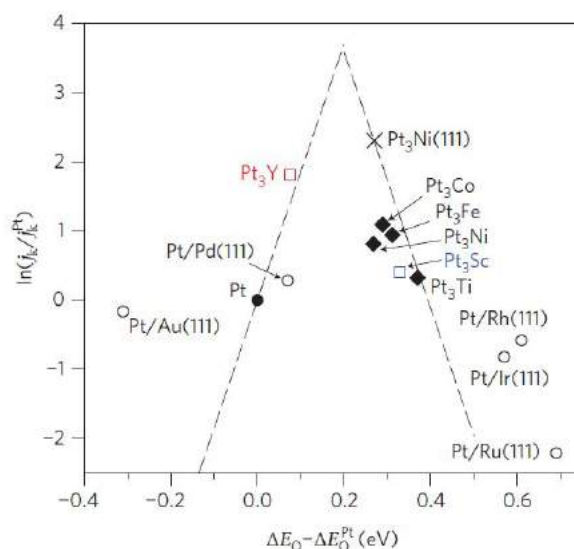
Fig. 2.7 Volcano plot showing relationship between oxygen binding energy and maximal activity calculated for Pt and Pt alloys. Reprinted by permission from Macmillan Publisher Ltd, [92] (DOI: 10.1038/NCHEM.367)

resulted in a uniform dispersion of 15nm particles as seen in Fig. 2.8A with a 2 : 1 Ir:Pt molar ratio. The ElectroChemical Surface Area (ECSA) is increased thanks to the nanodendritic nature of these NPs. Comparing these NPS with platinum and 1 : 1 M Ir:Pt mixture, the ORR activity is very high. This can be related to the increased number of corners and edge sites in this nanodendritic morphology [96]. Rotating Disk Electrode (RDE) measurements in Fig.2.8B show the great performances of the 2 : 1 Pt/Ir catalyst with a mass activity of 0.12 A mg_{Pt}^{-1} vs. a reversible hydrogen electrode (RHE) in a 0.5 M H_2SO_4 solution.

The use of these high-performing Pt-alloys means less platinum required for each catalyst. However, the reduction reaction is exploited by means of other expensive noble metals. Therefore, researchers arise a desire to alloying Pt-free or non-precious metals.
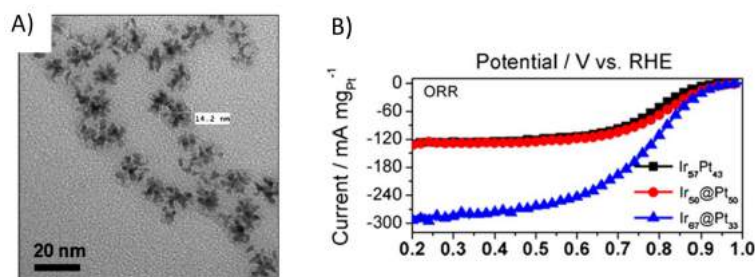
Fig. 2.8 A) TEM image of Ir nanodendrites. B) ORR curves whose current is normalized to the mass of Pt and mass activity of ORR at 0.85 V. Reprinted from [95], with permission from Elsevier.

Based on Fig.2.5, **Palladium (Pd)** is the second most active metal for ORR, followed by **Gold (Au)** and **Silver (Ag)**. The binary alloy for ORR, such as Pd–M systems (where M is 1/4 of Co, Ni, Fe, Cu, W and Mo), shows good stability and activity, especially for annealed catalysts [97]. In recent years, carbon-supported Pd-Cu catalysts (PdCu/C), have gained great attention thanks to the ease of control of the nanostructuration and composition. Kariuki and co-workers [98] developed PdCu/C alloy nanoparticles (5–10 nm) heat treated at 500°C, showing higher ORR activity with the 1 : 1 Pd–Cu composition than with the 1 : 3 composition. In a similar way, nanotubular PdCu catalyst (NM-PdCu) was synthesized by Xu et al. [99], showing very high ORR activity if compared to Pt/C and Pd/C commercial catalysts. Researchers demonstrated the advantage of the nanostructured catalyst, providing good transport channels for electrons and medium molecules.

Non-noble metal catalysts

Several **non-noble metal-based catalysts** has been studied and developed in order to overcome the problems related to the Pt long term-stability, cost and abundance. The suitable materials have to withstand the working conditions in order to have a long lifetime in a fuel cell, such as an MFC.

In particular, **organometallic complexes** have gained much attention in ORR catalysis as reliable catalysts. Examples are metal–N_4 (M–N_4) chelates as cobalt phthalocyanines (CoPc) [100], transition metal porphyrins (tetraphenyl porphyrins, TPP) and phthalocyanines (Pc). Researchers also demonstrated that thermally treating those macrocycles increased their ORR-current densities of many orders of magnitude [101] if compared to the not-annealed ones. During thermal treatment, in fact, the nitrogen transformation, together with the type of metal chosen, strongly influences the ORR catalysis. For example, Fe-N_4 complexes are preferable to their Co-counterparts as ORR catalysts, thanks to their ability of favoring the direct $4e^-$ process [102], while Co-N_4 ones mostly favor $2e^-$ route.

The new mono-nuclear Fe(II)Pc (**2**) and ball-type homo-dinuclear Fe(II)–Fe(II) phthalocyanine (**3**) were synthesized from the corresponding molecule (**1**), in Fig. 2.9, whereas ball-type hetero-dinuclear Fe(II)–Co(II) phthalocyanine (**4**) was synthesized from (**2**). Improved ORR catalysis was shown, in particular due an higher binding ability with O_2 through m-peroxo iron species (Fe–O–O–Fe), followed by a $4e^-$ path. The RRDE measurements showed a very large number of electrons exchanged, during the ORR reaction, up to 3.9 in the range[-0.30, 0.40] V vs SCE [103].

Other class of materials are **metal oxides (MOs)** and **transition metal oxides (TMOs)**, that still do not exhibit sufficient catalytic activity toward ORR if compared to Pt, but these oxides are potentially superior to Pt thanks to their chemical stability. Possible materials are manganese oxides (MnO_x) based catalysts, the use of which is justified by their environmental friendliness, low cost, abundance and significant catalytic activity in alkaline media [104]. The catalytic properties of the manganese oxides nanostructures are influenced by the crystallographic structure and morphology. If the morphological influence is excluded, the catalytic activity follows the order $\alpha- > \beta- > \gamma$ - MnO_2. Different kind of MnO_x in the form of
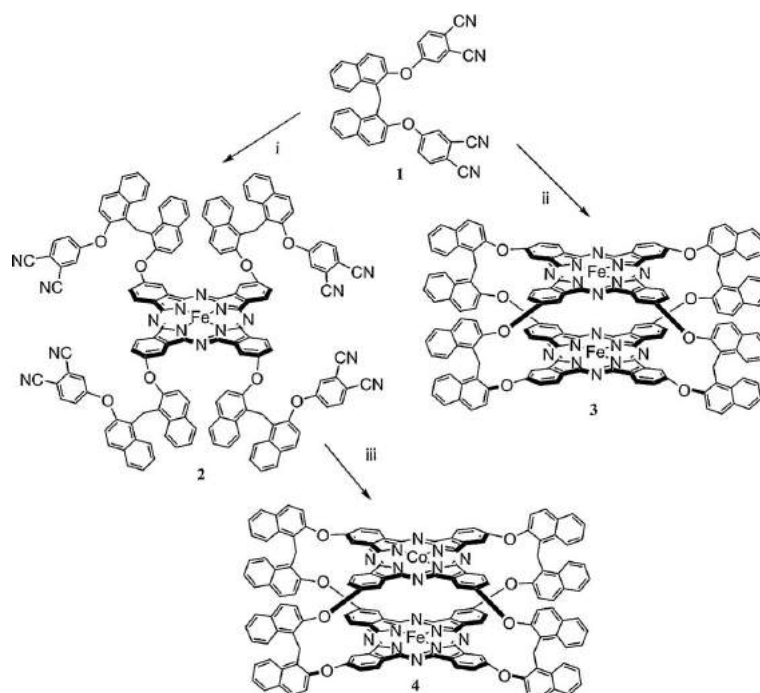
Fig. 2.9 Graphical scheme of **1** Fe(OAc)$_2$ and **2**, **3**, **4** Fe(II)-based phthalocyanine. Reprinted from the Lancet, [103], with permission from Elsevier.

bulk, particles, nanospheres and nanowires generate different OR potential and so current densities, as show in Fig. 2.10. By changing the structural properties it is possible to achieve almost a 4e$^-$ transfer for α-MnO$_2$ nanowires [105]. In a similar way, conductivity can be improved, as described in the same paper, by the creation of a new nanocomposite made by Ni nanoparticles, uniformly deposited onto α-MnO$_2$ nanowires in a carbon matrix (MnO$_2$-NWs@Ni-NPs/C). The onset potential for ORR is 0.08 V (vs. Ag/AgCl) and a specific current of 33.5 mA mg^{-1}, resulting in a possible application as ORR electro-catalyst.

A part from MnO$_2$, other manganese oxides can be listed and among them it can be also found: MnO, Mn$_2$O$_3$, Mn$_3$O$_4$ and Mn$_5$O$_8$. Depending on the stoichiometry of these binary oxides, the number of electrons exchanged can vary significantly, due to the variation of the manganese valence state. In fact, by changing the catalyst the number of electrons my vary from 3.94 up to 3.75 in case of pure α-MnO$_2$ [106], α-Mn$_2$O$_3$ [107], Mn$_3$O$_4$ [107] and Mn$_5$O$_8$ [107]. However, when supported onto carbon materials or powders, their ORR catalytic activity may change strongly, reducing the associated number of electrons to 2.3, 1.5, 1.5 [108] for MnO$_2$/C, Mn$_2$O$_3$/C, Mn$_3$O$_4$/C, respectively. This means that, these materials produce mostly peroxide species, instead of exploiting a 4-electro pathway as the former materials. Due to this lack of literature and study upon the manganese oxide integration with carbon electrode, this thesis will be mostly focused on the production and study of an efficient ORR electrode based on manganese oxide, see Chap. 4.
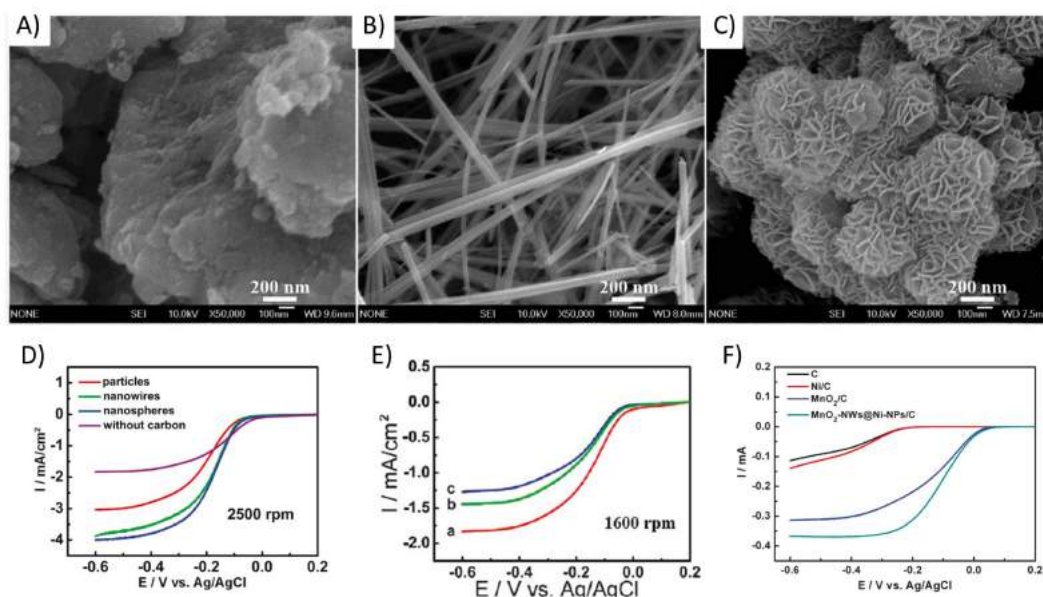
Fig. 2.10 Upper panels, SEM images of: (A) α - MnO_2 bulk particles, (B) nanowires, (C) flowerlike nanospheres. Lower panels: (D) Comparison of the LSVs of neat $\alpha - MnO_2$ nanowires, bulk particles/carbon, nanowires/carbon and nanospheres/carbon, (E) Comparison of the voltammetry curves for α-MnO_2 (red), β-MnO_2 (green), and γ-MnO_2 (blue) nanowires detected at the rotation rate of 1600 rpm, (F) LSV curves of C, Ni/C, MnO_2/C and MnO_2-NWs@Ni-NPs/C obtained at a rotation rate of 900 rpm and a potential scan rate of 1 mVs^{-1}. Reprinted (adapted) with permission from [105]. Copyright (2009) American Chemical Society.

Similar to the manganese oxides, MnOOH together with carbon materials exhibits ORR catalytic activity [109, 110], depending on chemical morphology, structure, composition and synthesis method of MnOOH. In particular, Chen and co-workers showed that the catalytic activity depends on the MnOOH amount (9–36 wt%) [111]. With higher content of MnOOH (over 72 wt%), the amorphous structure amount increases and the exchanged electrons in ORR decrease, as the current.

It is also possible to synthesize ORR **metal oxides catalysts from group IV and V**, that show high stability both in alkaline and in acid electrolytes. Their main drawback is related to their insulating behavior that reduces the adsorption rate of oxygen at the catalyst surface. Researchers overcame this problem by: forming complex oxide layer containing active sites [112], doping with nitrogen [113], introducing surface oxygen defects [114] or partially oxidizing carbonitrides [115].

Other new catalysts

The main drawback of inorganic ORR catalysts is the rate of reduction reaction at the surface of the material, being not competitive with respect to Pt. In nature, this

problem has been overcome with enzyme-based catalysts, where ORR may occur at very low overpotentials [116]. The $4e^-$ pathway can be so exploited by groups of enzymes: *cytochrome c oxidases* (CcOs) [117] and *multicopper oxidases* (MCOs) [118]. Interesting studies came not only from MOCs, but also from *laccase* and *bilirubin oxidase*, as ORR catalysts, proving the ability of these materials to reduce the overpotential and enhance the catalytic activity. In fact, Mano et al. compared the overpotential of a Pt cathode in 0.5 M H_2SO_4 with bilirubin oxidase, electrically connected (*wired*) to the electrode by a redox polymer [119]. They showed that the enzyme overpotential was significantly lower than the one of the Pt cathode, see Fig. 2.11. Moreover, the diffusion-limited currents reached with the *wired* enzymes were about twice as high as those reached with the bare Pt cathode.
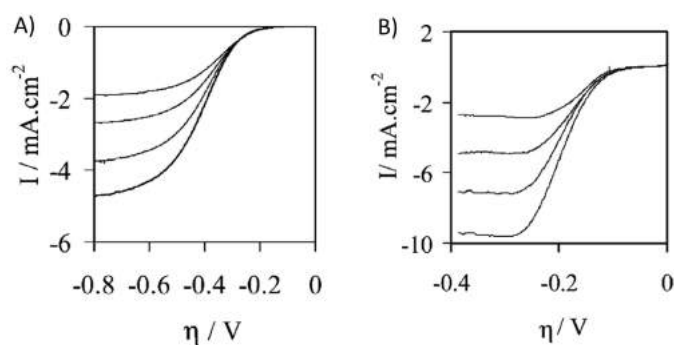
Fig. 2.11 Dependence of the current density on the overvoltage for (A) polished Pt and (B) *wired* bilirubin oxidase on polished vitreous carbon in a pH 7.2 saline, at 500, 1000, 2000, and 4000 rpm (from top to bottom curves) under 1 atm O_2 at 37°C. Scan rate: 5 mV/s. Reprinted (adapted) with permission from [119]. Copyright (2003) American Chemical Society.

For this reason, novel bio-inspired catalysts could be rival to the traditional Pt-based, even if they show many drawbacks [120] as:

  (i) low current density per volume of catalyst because of the big size of the biological molecules;

 (ii) sensitivity to pH and temperature;

(iii) long-term stability and durability due to the presence of organic matter.

Therefore, there is the need of new bio-inspired catalysts, correlating peculiar characteristic of the low overpotential with high surface active sites density of the bio-inspired enzyme materials. Therefore CcOs, with binuclear centers, give new interest on the development of bio-inspired catalysts based on alloys, metal clusters, and multi-nuclear complexes. In fact, Fea_3/Cu_B, lab synthesized, can be a possible choice in ORR catalysis for its preferential $4e^-$ pathway [120]. One example can be a recently developed CcO models attached, with a covalent bond, to a self-assembled- monolayer (SAM) on a Au electrode, having all the essential features of

the CcO's ORR sites [121]. Collman and co-workers showed a 96% selectivity for $4e^-$ reduction pathway, compared to the >99% selectivity of the bare CcOs.

2.4   CO$_2$RR catalysts state-of-the-art

Carbon dioxide, CO$_2$, is one of the major responsible of the greenhouse effect, as already mentioned in Chap.1. It's a fundamental molecule for the plants growth and a sub-product of many industrial processes. In particular, mankind activities are the cause of the actual CO$_2$ imbalance, that led to the global warming issue. Therefore, *CO$_2$ economy* became an important topic that comprises 'carbon capture storage & utilization' (CCSU). For this reason, several governments chose to invest substantial resources and sums of money in order to reduce CO$_2$ production and convert it into useful materials at the same time [122].

CO$_2$ reduction into sustainable fuels may occur in different ways:

  (i) Photoreduction, activated by solar light;

 (ii) Electroreduction, activated by an external bias;

(iii) Photo-electroreduction, activated by a combination of an external bias and solar light.

2.4.1   Reduction of CO$_2$

In general, there are two ways to chemically reduce CO$_2$: the first one is the reduction to valuable products such as carbon monoxide (CO), methane (CH$_4$), formic acid (HCOOH) and oxalic acid (H$_2$C$_2$O$_4$), while the second one is the reduction with other organic materials, to produce new ones. In the following sections, the attention will focus on the first type of reactions, also reported in Table 2.1 [123]. It can be noticed that, as ORR, CO$_2$RR is a multi-electron reduction reaction, involving a number of different surface-bond reaction intermediates [124, 125, 46]. They depend on the different experimental condition, leading to different reaction mechanisms of CO, therefore to a variety of different products.

In the case of CO$_2$RR in aqueous solution, a widely accepted mechanism is [122, 126, 127]:

$$CO_2 + e^- \rightarrow CO_2^{\bullet-} \tag{2.13}$$

$$CO_{2\,(ads)}^{\bullet-} + H_2O \rightarrow HCO_{2\,(ads)}^{\bullet} + OH^- \tag{2.14}$$

$$HCO_{2\,(ads)}^{\bullet} + e^- \rightarrow HCO_2^- \tag{2.15}$$
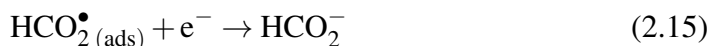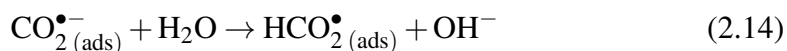
Reaction	E0 vs. SHE [V]
$2H^+ + 2e^- = H_2$	0
$CO_{2\ (g)} + 4H^+ 4e^- = C_{(s)} + 2H_2O_{(l)}$	0.210
$CO_{2\ (g)} + 2H^+ + 2e^- = HCOOH_{(l)}$	-0.672
$CO_{2\ (g)} + 2H_2O_{(l)} + 2e^- = HCOO^-_{(aq)} + OH^-$	-1.078
$CO_{2\ (g)} + 2H^+ + 2e^- = CO_{(g)} + H_2O_{(l)}$	-0.106
$CO_{2\ (g)} + 2H_2O_{(l)} + 2e^- = CO_{(g)} + 2OH^-$	-0.934
$CO_{2\ (g)} + 4H^+ + 4e^- = CH_2O_{(l)} + H_2O_{(l)}$	-0.070
$CO_{2\ (g)} + 3H_2O_{(l)} + 4e^- = CH_2O_{(l)} + 4OH^-$	-0.898
$CO_{2\ (g)} + 6H^+ + 6e^- = CH_3OH_{(l)} + H_2O_{(l)}$	0.016
$CO_{2\ (g)} + 5H_2O_{(l)} + 6e^- = CH_3OH_{(l)} + 6OH^-$	-0.812
$CO_{2\ (g)} + 8H^+ + 8e^- = CH_{4\ (g)} + 2H_2O_{(l)}$	0.169
$CO_{2\ (g)} + 6H_2O_{(l)} + 8e^- = CH_{4\ (g)} + 8OH^-$	-0.659
$2CO_{2\ (g)} + 2H^+ + 2e^- = H_2C_2O_{4\ (aq)}$	-0.500
$2CO_{2\ (g)} + 2e^- = C_2O^{2-}_{4\ (aq)}$	-0.590
$2CO_{2\ (g)} + 12H^+ + 12e^- = CH_2CH_{2\ (g)} + 4H_2O_{(l)}$	0.064
$2CO_{2\ (g)} + 8H_2O_{(l)} + 12e^- = CH_2CH_{2\ (g)} + 12OH^-$	-0.764
$2CO_{2\ (g)} + 12H^+ + 12e^- = CH_3CH_2OH_{(l)} + 3H_2O_{(l)}$	0.084
$2CO_{2\ (g)} + 9H_2O_{(l)} + 12e^- = CH_3CH_2OH_{(l)} + 3H_2O_{(l)} + 12OH^-$	-0.744

Table 2.1 Selected standard potential for CO_2 in acqueous solution (V vs. SHE) at 1 atm and 25°, calculated according to the standards Gibbs energies of the reactants in the reaction. Adapted from [123].

$$CO^{\bullet-}_2 + BH + e^- \rightarrow HCO^-_2 + B^- \qquad (2.16)$$
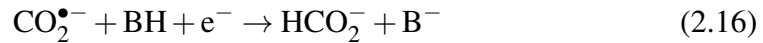
where BH represents the substances that provide protons to the reaction. As an example, Chaplin and Wragg [128] proposed a mechanism for CO_2 reduction in the case of acid system, as depicted in Fig. 2.12.

CO_2 surface adsorption is described with reaction route A, where carbon dioxide reacts with the electrolytes producing chemical species in a transition state.

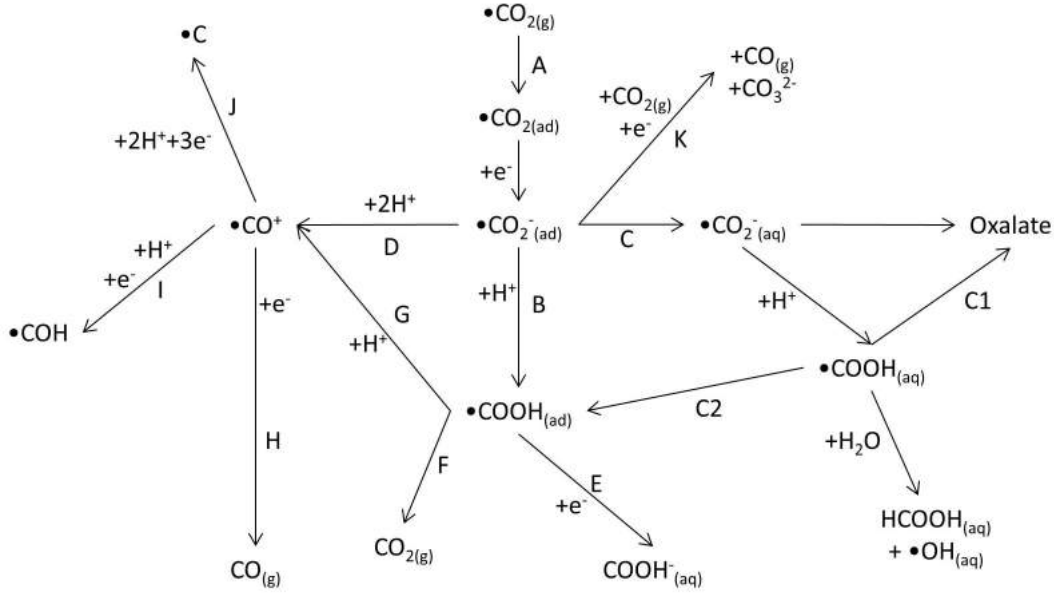$$CO_{2\ (g)} \rightarrow CO_{2\ (ad)} \qquad (2.17)$$

or

$$CO_{2\ (g)} + e^- \rightarrow CO^-_{2\ (g)} \qquad (2.18)$$
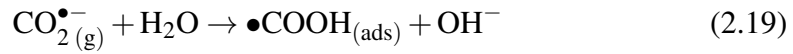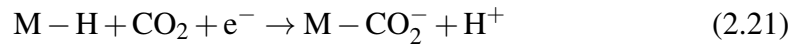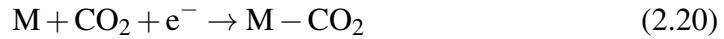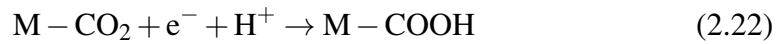
then follows

Fig. 2.12 Schematic representation of the CO$_2$ reaction routes proposed in the case of an acid system. With kind permission from Springer Science + Business Media: [128].

$$CO_{2\,(g)}^{\bullet-} + H_2O \rightarrow \bullet COOH_{(ads)} + OH^- \qquad (2.19)$$

When CO$_2$ is adsorbed on a metallic catalyst (represented with M in the equations), the activation energy of the CO$_2$RR can be reduced:

$$M + CO_2 + e^- \rightarrow M - CO_2 \qquad (2.20)$$

$$M - H + CO_2 + e^- \rightarrow M - CO_2^- + H^+ \qquad (2.21)$$

Reaction route B describes CO$_2$ after its protonation, then generating MCOOH. The process can be expressed as:

$$M - CO_2 + e^- + H^+ \rightarrow M - COOH \qquad (2.22)$$

Considering electrodes on which CO$_2$ can be easily abdorbed and released, CO$_2^{\bullet-}$ can be generated (route C) [129]. When the pH of the electrolyte is very low, the reaction follows route B and D, having an ease of reaction of CO$_2$ with H$^+$ [130]. The generated products can be re-absorbed on the metal electrode, reacting again to form formic acid (HCOOH). In the case of non-aqueous solvents, $\bullet$COOH generate oxalate ($\bullet$C$_2$O$_4^{2-}$) by following route C1. On the other side, route D, describes how the oxygen atom is removed from M $-$ CO$_2^-$:
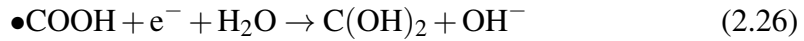
$$M - CO_2 + e^- + H_2O \rightarrow MCO^+ + 2OH^- \qquad (2.23)$$

or

$$M - CO_2 + e^- + H^+ \rightarrow MCO^+ + 2H_2O \qquad (2.24)$$
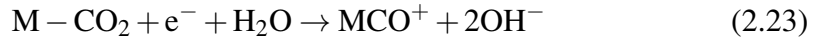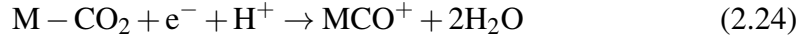
Formic acid (HCOOH) is released into the solution, undergoing to the following process:

$$\bullet COOH + e^- \rightarrow COOH^-_{(ads)} \qquad (2.25)$$

or in the form of hydrate:

$$\bullet COOH + e^- + H_2O \rightarrow C(OH)_2 + OH^- \qquad (2.26)$$

and

$$C(OH)_2 \rightarrow HCOOH \qquad (2.27)$$
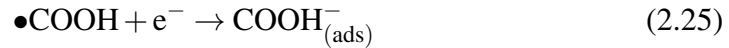
Further reaction are described in routes H, I, J, followed by Cu, Rh and many transition metals [131, 132]. In route H, M-CO$^+$ reacts with an electron, generating carbon monoxide (CO). On the other side, M-CO$^+$ can react both with and electron and with a proton to form M-CHO, behind the generation of CH_2CO, CH_3CHO, C_2H_4 and many others. Lastly, route J, describes the generation of $\bullet C$, that, reacting with protons and electrons, generates C_2H_2 and CH_4. This last route can easily occur at low temperatures, even if I is its competitive reaction.

2.4.2   Competitive reaction

In the same potential range of CO_2RR, Hydrogen Evolution Reaction (HER) occurs, due to the hydrolysis of water[133]. In the case of a reaction at pH = 14 and ambient temperature (25°), the two possible reactions are:

$$CO_{2\,(aq)} + H_2O + 2e^- \rightarrow HCOO^- + OH^- \qquad E_0 = -1.02V_{SHE} \qquad (2.28)$$

$$2H_2O + 2e^- \rightarrow H_2 + 2OH^- \qquad E_0 = -0.83V_{SHE} \qquad (2.29)$$
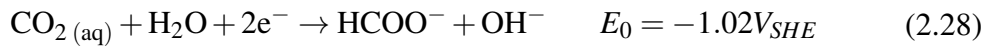
Considering cathode potentials between -0.8V and -1.8V vs. SHE, the reaction in Eq.2.28 is considered to be a kinetically 'slow' process. Moreover, the reaction kinetics of Eq. 2.28 is considered independent on pH (2 < pH < 8), but for pH>6 a strong limiting mass transfer may occur, as shown in Fig.2.13. In this figure, in

fact, is reported the influence of pH of the electrolyte reduction of CO$_2$, H$_2$O, and relative materials. It can be clearly noticed that, when the pH value is less than 8, CO$_2$ can steadily exist in solution, but for pH lower than 7, the HER is more likely to occur. According these considerations, only in a very limited range (7 < pH < 8) can the CO$_2$RR can have an advantage. In addiction, the reaction in Eq.2.29 is thermodynamically favored with respect to the first one in almost all the pH range at the considered temperature [134]. This difference between the two reactions leads to the selectivity of CO$_2$RR towards formate/formic acid observed in many papers.
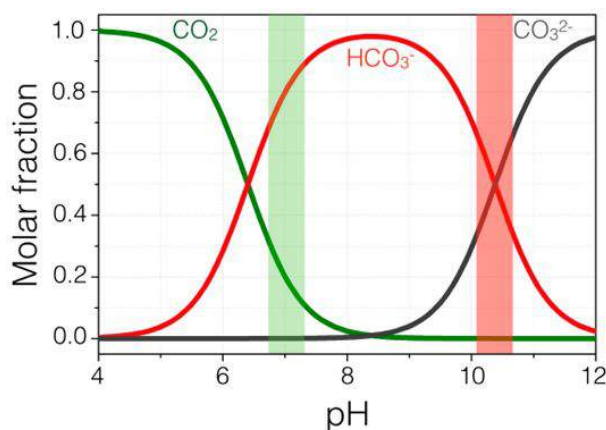
Fig. 2.13 Electrolyte pH determining the equilibrium concentrations of carbon dioxide–bicarbonate–carbonate system. Reprinted with permission from [134]. Copyright 2015 American Chemical Society.

Many researchers found that the increase of the reduction rate of the carbon dioxide may lead to a lowering of the hydrogen evolution reaction [135–138]. This can be achieved by increasing the pressure, that leads to an increase of the solubility of the CO$_2$.

In general, CO$_2$RR must take place at low potential with high efficiency and selectivity at high current densities in order to compete successfully with alternative processes.A stable catalyst should be found, with high overpotential for hydrogen evolution, affinity for CO$_2$, that allows further H$^+$ transfer steps selectively toward the formation of valuable products.

2.4.3   Faradaic efficiency

In a electrochemical reaction system, the utilization efficiency of electricity is measured by two popular indexes: η for the current efficiency and f for the faradaic efficiency.

In general, η can be considered as the instantaneous current efficiency ($i_{r,t}/i_{total,t}$) or the overall current efficiency ($Q_{r,t}/Q_{total,t}$). $i_{r,t}$ and $i_{total,t}$ are the currents of the rth process and all processes that occur simultaneously at an electrode at a time t, respectively. $Q_{r,t} = \int_0^T i_{r,t}dt$ and $Q_{total,t} = \int_0^T i_{total,t}dt$ are the charges of the rth

process and all ones at an electrode overall a period of time T, respectively. Moreover, η will be 100% when only one process is occurring. Considering a desirable CO_2RR, η for the formation of target products should be the highest, having HER completely inhibited.

The faradaic efficiency f of a specific product of CO_2RR describes the efficiency with which electrons are transferred in the reaction. It is calculated from the number of electrons consumed in the process by using the equation:

$$f = \frac{mnF}{\int_0^t i_{r,t} dt} \qquad (2.30)$$

where m is the number of moles of product harvested, n is the number of electrons required for the selected reaction, F is the Faraday constant ($9.6485 \cdot 10^4 C/mol$), and $i_{r,t}$ is the circuit current. If we focus on the product selectivity, f will be given. In general, the faradaic efficiency may be affected by:

  (i) Catalyst element [139] and chemical composition [140];

 (ii) Morphology of catalysts [141];

(iii) Reaction conditions [142].

2.4.4 CO_2RR materials

CO_2RR can be carried out by means of chemical methods [143], photocatalytic [144] and electrocatalytic reduction [145]. In recent years, unfortunately, the high costs of CO_2 capture, separation, purification, and transportation to user sites, the limitations in market size and investment incentives together with the insufficient socioeconomic driving forces are some of the major disadvantages associated to CO_2RR [146]. In spite of such challenges, CO_2 capture, conversion, and utilization is still recognized as a feasible and promising research in energy and environmental field.

In general, a catalytic material is evaluated on the basis of the onset potential of reduction and the faradaic efficiency, while its stability (or durability) is determined depending on the variations in catalyst behavior during working time [147]. Focusing the attention to these parameters, in this section, some CO_2RR catalysts will be described.

Metal catalysts

First studies of electroreduction of CO_2 on **Platinum (Pt)** was studied by Eggins and McNeill in different electrolytes: water, dimethyl sulfoxide (DMSO), acetonitrile (CH_3CN), and propylene carbonate (PC) [149]. Years after, Brisard et al. analyzed the CO_2RR mechanism on polycrystalline Pt in acidic media by applying differential
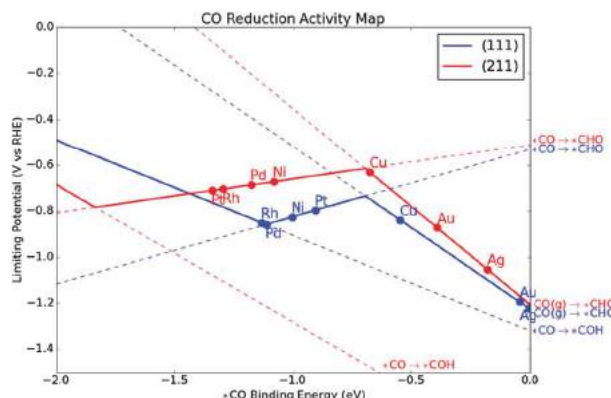
Fig. 2.14 Limiting potential activity map to hydrocarbons shown with the (111) and (211) facets on the same axes for different materials. Bold lines highlight the limiting potential for the blue (111) and red (211) facets. Reproduced from [148], with permission of the Royal Society of Chemistry.

electrochemical mass spectrometry and demonstrating that methanol was the main reaction product [150]. High pressure CO$_2$ reduction was also performed on Pt electrodes, resulting in a faradaic efficiency of 46% and finding CH$_4$ and CH$_3$CH$_2$OH as major products [151]. The selectivity toward methane, as a product, was enhanced by increasing the carbon dioxide pressure, leading to a decrease in the hydrogen evolution. Maximum selectivity (100%) toward paraformaldeide was reached on Pt NPs were supported on either calcia-stabilized zirconia (Pt/CSZ) or MnO$_2$ (Pt/MnO$_2$) by employing high-temperature conditions ($300 - 900°C$) [152]. Latter studies lowered the temperatures to $300 - 450°C$, unfortunately, remaining with a CO$_2$ conversion efficiency of 8%.

As showed in Fig.2.14, platinum do not show the maximum activity toward CO$_2$RR, as copper, nickel or palladium. Several studies using metallic **Copper (Cu)** electrodes reported its good performance and its good selectivity toward CH$_4$ (in aqueous KHCO$_3$). By using Cu electrodes it is possible to produce not only low-chain hydrocarbons such as CH$_4$, CO, HCOOH, alcohols and esters, but also some relatively high-chain hydrocarbons such as paraffins and olefins [124, 153]. Since early stages of CO$_2$RR, copper is considered a promising electrode material as it offers intermediate hydrogen overvoltage and produces more reduced form of CO, as mentioned before. With more negative potentials the hydrogen evolution is more and more suppressed [145]. In general, the products faradaic efficiencies strongly depend on temperature, type and concentration of electrolytes, electrode potential, pH, crystal structure, crystal orientation and the purity of the Cu. Hori et al. [154] demonstrated that a small temperature increase ($0 - 40°$), with a 99.999% Cu sheet electrode, caused a strong modification of the faradaic efficiencies. The methane production dropped rapidly from 65% up to nearly zero, while ethylene increased up to 20%.

It is interesting to notice that the ability to convert CO$_2$ was harmed greatly by a significant promotion of the HER, having a nanostructured Cu surface. For

this reason, Reske et al. investigated the catalytic behavior of Cu nanoparticles (Cu NPs) having different particle sizes (2–15 nm) [155], studying the so-called "catalytic particle size effect" [156], that is the variation of the catalytic activities and selectivities by varying the size and shape of the catalytically active species, in this case metal nanoparticles. They found a significant increase of H_2 selectivity on Cu NPs if compared to the bulk material (Fig.2.15). It appears clear that H_2 and CO formation is suppressed on the nanostructured material, while the hydrocarbons selectivity is enhanced.
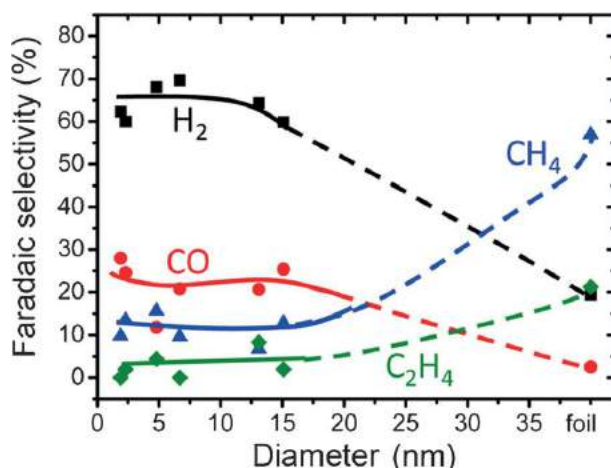
Fig. 2.15 Faradic selectivity of reaction products during CO_2 electroreduction on Cu NPs of different dimensions, compared to the bulk condition. Conditions: 0.1M of $KHCO_3$, E=1.1 V vs. RHE at 25°C. Reproduced with permission from [155]. Copyright 2014 of American Chemical Society.

Other types of nanostructured metallic electroctrodes can be used for CO_2RR, such as **Gold (Au)** and **Silver (Ag)**, however, at present, the research is moving toward metallic complexes, alloys, oxides and organic catalysts.

Metal oxides catalysts

In Fig.2.16 are showed the band gaps of the most common metal oxide catalysts used in recent literature compared to the CO_2 redox potentials. These semiconductors can be used both as photocatalysts such as Fe_2O_3, being low cost and having suitable band gap energies for visible light absorption, and as electrocatalysts [157]. In particular, Fe_2O_3 together with WO_3 and SnO_2 possess conduction band edge values below the methanol and methane potential and the use of an external electrical bias is a requirement needed to achieve the wanted reduction reaction.

In an attempt to enhance the electrochemical reduction of CO_2, oxidized Cu surfaces have been applied since 1991 for the CO_2 reduction into CH_3OH at various **Copper oxides (Cu_xO)** electrodes operating at ambient temperature [158]. More recently, Cu_2O-catalyzed carbon clothes were prepared by Chang et al. [159] starting from Cu_2O cubes. The gas chromatography (GC/FID) analysis of the CO_2RR process
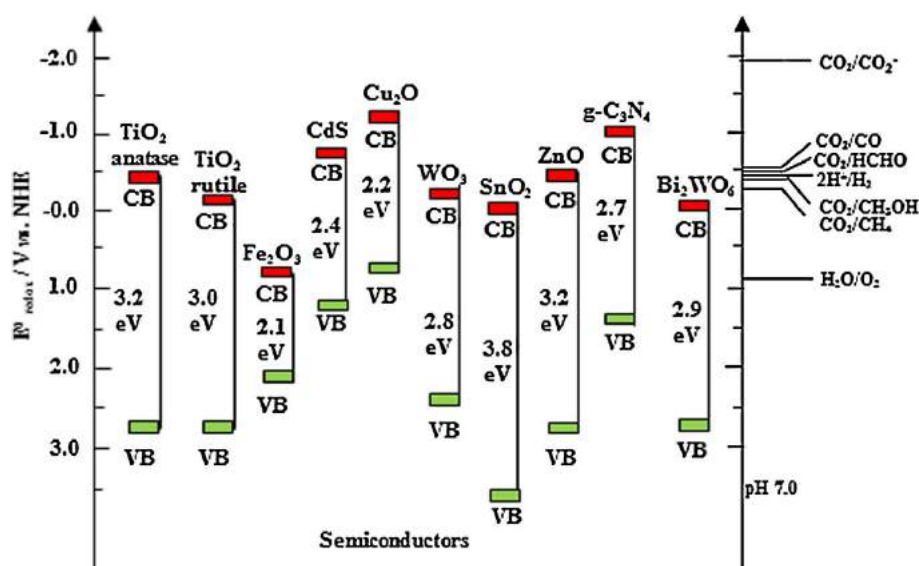
Fig. 2.16 Band gap of some metal oxide catalysts with respect to the CO$_2$ redox potentials of different chemical species measured at pH 7. Reproduced from [157], with permission of Elsevier.

confirmed that the CH$_3$OH was the main reaction product, together with a very good electrochemical stability for the potential range 0 to -1.70 V (vs. SCE). In 2012, a simple Cu foil, thermally oxidized in air, was prepared by Li et al. [160], resulting in a Cu$_2$O layer. The researches linked the catalytic activity to the thickness of the Cu$_2$O layer, exhibiting a good electrochemical stability. In particular, the Cu$_2$O electrodes ($\geq 3\mu m$ thick) showed 480 times larger surface roughnesses than a polycrystalline Cu electrode. Moreover the oxidized sample needed 0.50 V less overpotential to reduce carbon dioxide, having as main products CO and HCCOH.

Moreover, Fe$_2$O$_3$ has been reported by Fox and Dulay [161] to exhibit lower photoactivity compared to TiO$_2$ and ZnO due to material corrosion. In particular, **Titanium oxide (TiO$_2$)** appears to be corrosion resistant and chemically stable [162] and also showed a catalytic activity toward CO$_2$, especially in the case of metal oxides deposited on the Ti surface [163–165]. First studies of Monnier and co-workers reported the cathodic behavior of TiO$_2$, TiO$_2$/Ru and TiO$_2$/Pt thin film electrodes[166, 167]. The samples were prepared thanks to thermal deposition on Ti rods and the electrochemical reduction of CO$_2$ revealed the formation of electrochemically detectable species on the TiO$_2$/Pt surface. Moreover, if a metal oxide is placed on a TiO$_2$ substrate, the catalytic performance can be improved. This is the case of the study of the electrochemical reduction of CO$_2$ on a bare RuO$_2$-coated diamond electrode [165] and TiO$_2$-supported. The second configuration showed an higher faradaic efficiency for the reduction of CO$_2$ to methanol under identical conditions, leading to the conclusion that the titanium oxide may enhance the catalytic efficiency. Based on this research, Qu et al. [164] loaded RuO$_2$ onto TiO$_2$ nanotubes or nanoparticles, placed onto a Pt electrode for the electrocatalytic reduction of CO$_2$. Compared with RuO$_2$ coated or with RuO$_2$-TiO$_2$ nanoparticles

electrode, the one with RuO_2-TiO_2 nanotubes exhibited an higher electrocatalytic activity toward CH_3OH, with a current efficiency of 60.5%. This suggests that the tube nanostructuration is important in achieving both an high efficiency and an high selectivity for CO_2RR.

Another important catalyst is **Tin oxide (SnO_x)**, thanks to the ability of tin to selectively convert CO_2 to formate and formic acid [168]. In particular, Chen and Kanan [169] were able to prepare a thin-film catalyst by simultaneously electrodepositing Sn^0 and SnO_x on a titanium electrode. The Sn^0/SnO_x catalyst showed eight times higher partial current density and four times higher faradaic efficiency for CO_2 reduction, compared to a bare Sn electrode coated with native oxide. Researchers suggested that metal/metal oxide structure is a promising catalysts for sustainable fuel synthesis favoring the CO_2 reduction pathway. Based on this findings, Wu et al. [170], developed Sn nanoparticles, covered with a variable thickness of SnO_x layer. They found that the current showed a negligible dependence on the thickness of the oxide surface, while the selectivity towards the CO and formate formation showed a strong relationship with the oxide thickness. The highest faradaic efficiency was found for $\sim$3.5 nm SnO_x thickness toward formate formation at -1.2V. In general, they deduced that the decrease of the selectivity towards CO_2RR with increasing thickness of the SnO_x layer can be attributed to the enhancement of HER.

Perovskite-type catalysts

Perovskite-type oxides are a class of compounds with the general formula ABO_3. They are a very important family of materials and exhibit properties suitable for several applications, especially related to the photocatalytic reduction of CO_2 [171]. In Fig.2.17 are showed the band gap energy levels of some perovskite oxides, having a quite large gap (more than 3 eV). However, these crystalline structures offer an excellent framework in which band gap values can be tuned to enable the absorption of visible-light and band edge potentials to fulfill the needs of specific photocatalytic CO_2RR.

A first example can be **sodium niobate**, $NaNbO_3$. Li et al. reported a study of photocatalytic properties variation upon the change of the crystal structure (particularly crystallographic symmetry) of the perovskite oxide. They synthesized cubic $NaNbO_3$ (c-$NaNbO_3$) and orthorhombic $NaNbO_3$ (o-$NaNbO_3$), and studied the CO_2 photoreduction in the gas phase. Researchers observed that c-$NaNbO_3$ showed nearly twice the photoactivity of o-$NaNbO_3$ maybe due to the differences in the electronic structure of the two phases [172].

A second perovskite example is **strontium titanate**, $SrTiO_3$, that shows good CO_2 reduction activity if properly doped with a metal. In fact, $SrTiO_3$ shows an adsorption spectra in the UV range, having a large band gap of 3.3eV. He and co-workers were able to shift the adsorption spectra in the visible range by doping the crystal with chromium (Cr^{3+}) [173]. The doping of Cr^{3+} at Sr site in the nanocrystals results in the photoreduction of CO_2 due to the oxygen vacancies created. Methane is the first product obtained, with a good production yield.
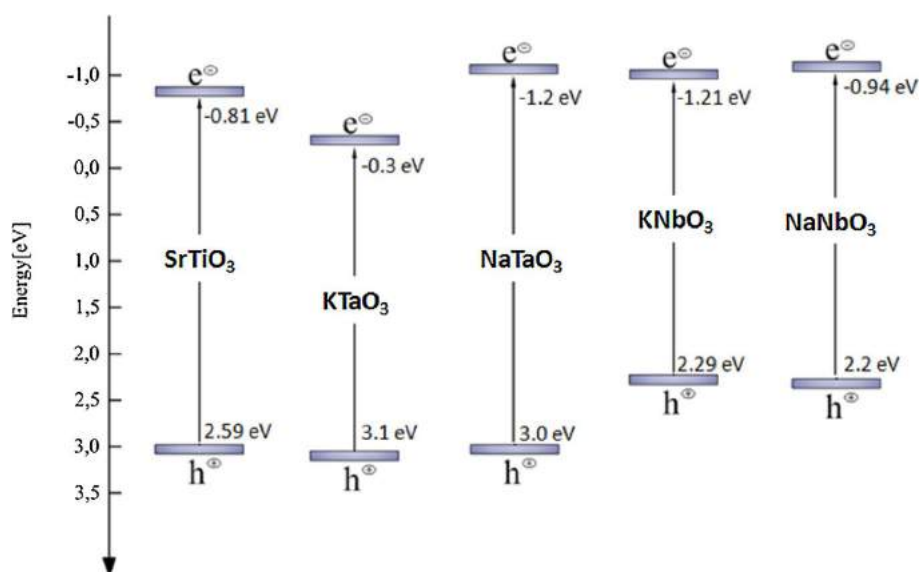
Fig. 2.17 Band structures of SrTiO$_3$, KTaO$_3$, NaTaO$_3$, KNbO$_3$ and NaNbO$_3$. Reproduced from [171], with permission of Elsevier.

Moreover, Jiao et al. synthesized Cr-doped SrTiO$_3$/TiO$_2$ nanotube arrays, by using a simple hydrothermal method and well-aligned titania nanotube arrays [174]. They demonstrated that the doped heterostructure exhibited higher photoelectro-chemical and photocatalytic activities than pure TiO$_2$ nanotube arrays and pure SrTiO$_3$/TiO$_2$ heterostructure nanotube arrays under visible light irradiation. The chromium element reduces the band gap, by lifting up the valence band of the stron-tium titanate. Researchers demonstrated also that the direct coupling of Cr-doped SrTiO$_3$ to TiO$_2$ can both enhance the visible light response and reduce the charge carriers recombination at the heterostructure surface.

Other catalysts

Besides the metals and metal oxides mentioned above, organic molecules can be also employed as catalysts for CO$_2$ reduction, such as conducting polymers, ammines, ionic liquids, enzymes.

Conducting polymer electrodes have also been developed for the heterogeneous electro-catalysis of CO$_2$RR. As an example, Pickup and co-workers developed two nitrogen-rich polymers based on pyridine and benzimidazole units, producing large catalytic current in acetonitrile solution containing only 1% water [175]. The first polymer exhibited a stable electrochemical behavior, while the second one gave large catalytic currents for CO$_2$RR. On the other hand, Koleli et al. developed a polyaniline (PAN) electrode [176], used in a methanol solution. The main reduction products were formic acid and acetic acid, with maximum faradaic efficiencies found of 12% and 78%, respectively.

Enzymes can be also used as catalyst as CO_2RR. In this field, Addo et al. proposed a study on understanding the role of carbonic anhydrase to efficiently facilitate CO_2 uptake. They took into account three oxido-reductase enzymes for CO_2 reduction to methanol as product reaction: formate, aldehyde, and alcohol dehydrogenase [177]. They found that the dehydrogenases alone can achieve CO_2 reduction, but the process can be accelerated by adding carbonic anhydrase. This study was a proof of concept, the pathway should be optimized so that all the enzyme cascade reduction rates can be equal to minimize product inhibition and maximize the methanol output.

A final example of CO_2RR catalyst is based on metal clusters, in particular gold, that always exhibited good catalytic properties toward this reduction. Kauffman et al. synthesized **Au$_{25}$ cluster** that showed reversible interaction with carbon dioxide [178]. They were able to reduce CO_2 to CO in aqueous media with approximately 100% efficiency.They also demonstrated that the peak of CO_2 conversion occurred at -1 V (vs RHE) with a rate 7-700 times higher than that for larger Au catalysts and 10-100 times higher than those for current state-of-the-art processes.

Chapter 3

Material synthesis and characterization techniques

Chapter abstract *In Chapter 3 all the synthesis techniques used in this Ph.D. study are described. In particular, in Sec. 3.1, the electrospinning technique is deeply analyzed, starting from the principles of nanofibers formation up to a description of the tools dedicated. In Sec. 3.2.1, the anodic oxidation of titanium is presented, while in Sec. 3.2.2, the thermal oxidation of copper is described. For both the materials a physical/chemical principles are presented, being the basis of these nanostructuration techniques. In the end of the chapter, in Sec. 3.3, the main characterization techniques used by myself are mentioned.*

3.1 Electrospinning technique

3.1.1 Nanofibers: definition

The International Standards Organization (ISO) considers nanomaterials, those materials that range between 1 nm to 100 nm in, at least, one dimension. Nanofibers (NFs) are fibers whose diameter is less than 100 nm, considering them as artificial or natural, with a circular shape and high aspect ratio (much longer than wide). In industry, however, NFs are generally considered to be fibers below 1 μm in diameter. Fig. 3.1A shows a comparison between a human hair (with dimension ranging from 100 μm to 50 μm), pollen (with dimension ranging from 10 μm to 100 μm) and a mat of nanofibers. This comparison clearly shows the dimension scale in which this material is placed. Decreasing the diameter of the nanofibers, a greater surface area can be obtained. Fig. 3.1B highlights the trend of the surface area to fiber diameter dependence.

There are traditional techniques to produce fibers, mostly micrometric, starting from polymer-based solutions obtained by non-electrospinning techniques. They were developed to improve industrial production and they include: solution blowing
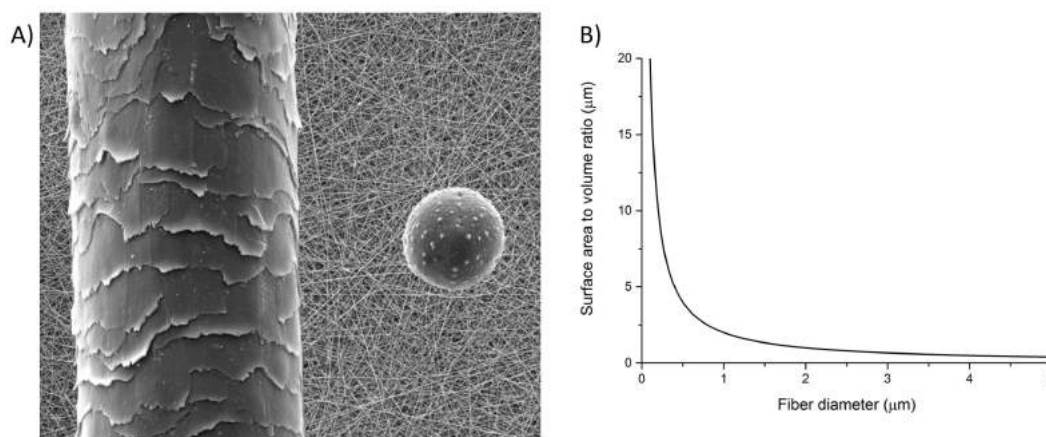
Fig. 3.1 A) FESEM image comparing a human hair (on the left), pollen (on the right side) and electrospun nanofibers. B) Representation of the correlation between the surface area of a nanofiber mat and its fiber diameter. http://www.elmarco.com/gallery/nanofibers/

[179], centrifugal spinning and template synthesis [180, 181]. The electrospinning (described in the following sections) is the only technique able to produce NFs at the nanoscale.

3.1.2 Electrospinning history

In XVI century Sir William Gilbert noticed for the first time the electrostatic attraction. When he brought near to a water-covered needle, an electrically charged piece of amber, he observed the droplet deformation into a cone. Further, he also described how to eject small droplets from the tip of the water cone [182]. This was the first known experiment of **electrospray**.

Only many years later, in 1887, C.V. Boys described his experiment of "electrical spinning", that is nowadays known as **electrospinning**. His setup was made by "a small dish, insulated and connected with an electrical machine", with which he could obtain fibers from the dish edge starting from natural polymers (e.g. beeswax) [183].

The first patents on electrospinning came out in 1902 thanks to J.F. Cooley and W.J. Morton (U.S. Patent 692,631 and U.S. Patent 705,691 respectively). Between 1934 and 1944 Anton Formhals presented several patents of fiber fabrication (U.S. Patents 2116942, 2160962 and 2187306) by electrospinning starting from a polymeric blend system [184].

Twenty years later, around 1965, Sir Geoffrey Ingram Taylor set the theoretical basis behind the initial phases of the droplet formation under the effect of an electrostatic field [185–187]. After these studies the initial droplet was named **Taylor cone** in his honor. In these years, Taylor developed the "leaky dielectric model" for conductive fluids together with J. R. Melcher. They explained the behavior of a droplet under a steady electric field and they noticed a characteristic cone-shape

of the deformed droplet. The critical angle to have a stable cone is $\phi = 49.3°$ (see Fig. 3.2), over which the droplet is broken because the electric field overcomes the drop surface tension. This is defined also as the critical voltage, concept developed by Taylor.
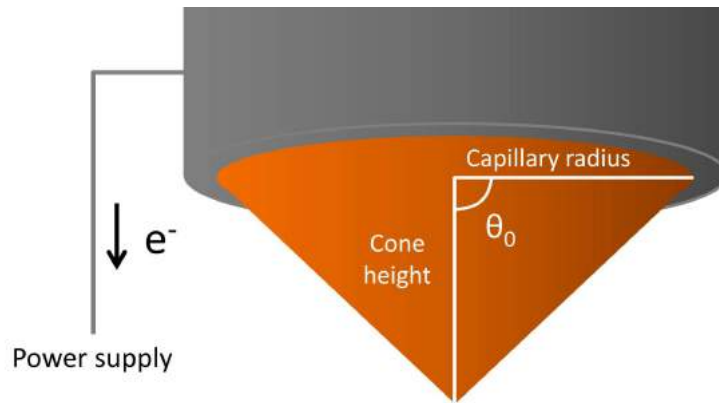
Fig. 3.2 Schematic representation of the definition of the Taylor cone.

In 1971, Baumgarten [188] was able to electrospin acrylic fibers with diameters ranging from $0.05\mu m$ to $1.1\mu m$, thanks to Taylor's studies. In fact, he reached the critical value of his solution, obtaining a fluid stream of nanofibers instead of droplets. Indeed, he could reach the critical voltage value, as defined by Taylor, where the charges repulsion forces overcome the viscoelastic forces of the fluid.

Since the 80s and especially in recent years, electrospinning has gained attention thanks to the growing interest in nanotechnologies. In fact, sub-micrometric and nanometric fibers can be easily fabricated with a single process. Since 1995, researchers pointed the attention not only on new polymeric solution, but also on new theoretical and computational studies. They focused, in fact, on the mathematical laws behind the electrospinning process. The Taylor cone shape and the fluid jet emission were described by Reznik and co-workers [189]. The growth rate of the several instabilities, during electrospinning, was studied by Hohman et al. [190]. More precisely, they described the most important instability in electrospinning, defining it as the **bending instability** (or whipping) [191–195].

Since 2000, a number of theoretical and experimental papers have been published on the electrospinning technique. Scopus search engine datas, reported in Fig. 3.3, in fact, clearly show the rising interest in this field in recent years.
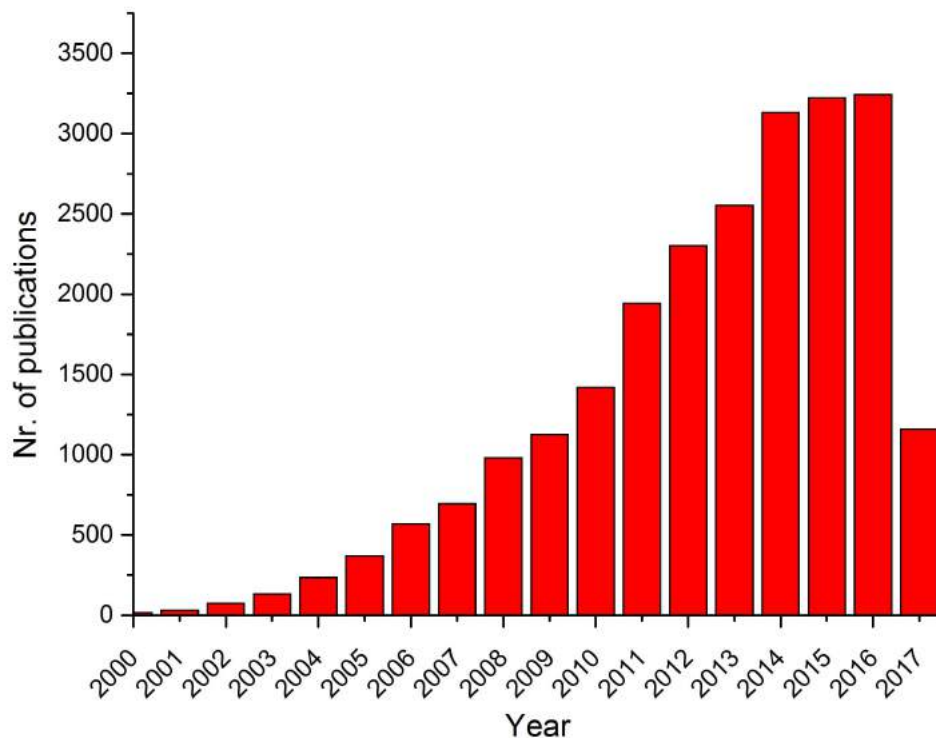
Fig. 3.3 Number of publication per year on electrospinning (2000-2017), source Scopus.

3.1.3 Electrospinning process

As already pointed out in the previous paragraphs, the electrospinning is a recent and peculiar technique that allows the production of fibers down to the nanometric scale starting from a polymeric solution. The nanofiber formation occurs thanks to the Columbic interaction among the several charged elements of the solution itself. The electrostatic forces generated, through an high voltage setup, make the uniaxial stretching of the viscoelastic solution. The nanofibers produced have not only thinner diameter but also larger surface area than the ones produced with conventional spinning processes.

The electrospinning process, moreover, offers the possibility of application on a large variety of materials, among which one may comprise natural and synthetic polymers. Besides, metallic, ceramic and carbon nanofibers can be produced, starting from different electrospinned polymeric mats and further processing them properly (e.g. calcination, pyrolysis, ...).

Generally electrospinning is conducted at room temperature and with atmospheric pressure. In Fig. 3.4(A) is shown a schematic representation of an electrospinning setup, which can be divided into three major components [184]:
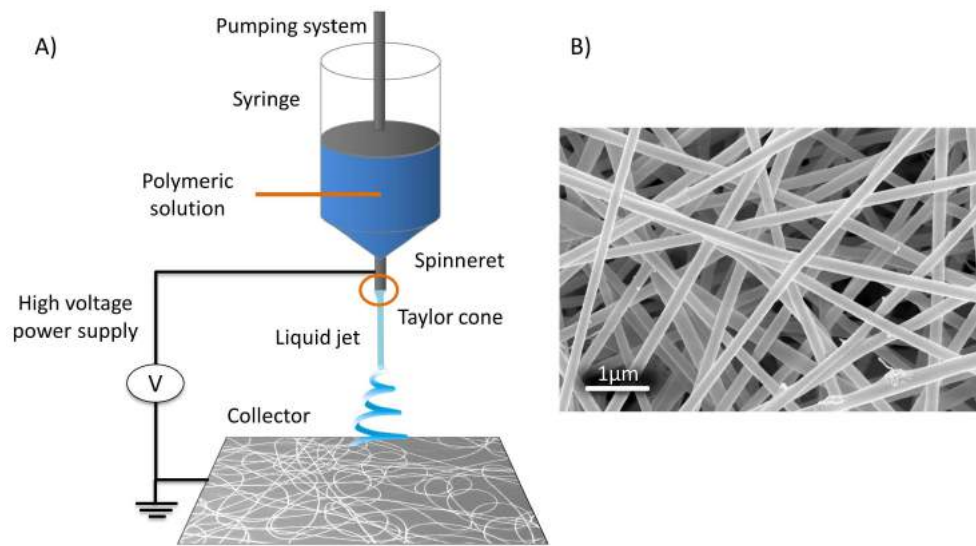
Fig. 3.4 Schematic representation of the electrospinning setup (A) and example of a Field Emission Scanning Electron Microscope (FESEM) image of the no woven mat of nanofibers (B). Specifically, the NFs mat was obtained in laboratory from a polymeric water-based solution of PEO (Poly Ethylene Oxide).

  (i) an high voltage power system. It is connected to the spinneret and injects the charge in the polymeric solution loaded in a syringe. The solution is afterward accelerated to the collector at an opposite polarity.

 (ii) a spinneret. It constitutes one of the two electrodes of the setup, which is at high voltage.

(iii) a grounded collector. It can be also called grounded counter-electrode. During the flight, the jet opens and the nanofibers are formed due to the solvent evaporation. They are so collected with random configuration on the plane of the counter electrode, as showed in Fig. 3.4B. Other types of collectors can be used in the same electrospinning setup, such as rotating drum, disk collector, ring collector placed in parallel, parallel wires electrodes, patterned electrodes, rotating tube collector with knife-edge electrodes below and many others [196, 197]. Each counter electrode shape and configuration ensures a different nanofibers collection. As an example, it may induce a preferential orientation of the fibers in one direction.

The voltage drop is so applied between the spinneret and the collector. The ratio between the applied voltage and the distance between the two electrodes defines, as one can easily deduce, the electric field intensity. This gap is generally called working distance (generally between 0 mm - 150 mm).

The spinneret is directly connected to a syringe, by means of a plastic pipe, in which a polymeric solution is loaded. Thanks to a pumping system, the solution flow in the needle at a constant velocity called flow rate (generally between 0.1 ml/h -

99.9 ml/h). During the electrospinning process, the surface tension of the solution holds the solution itself at the end of the capillary needle. The application of an high potential drop deforms the hemispherical shape of the solution droplet due to the electric charge accumulation and mutual repulsion. The droplet thus assumes a conical shape known as Taylor cone. When the electric field overcomes a critical value, eventually, the polymeric jet is ejected from the tip of the cone. During the flight toward the collector, the solvent evaporates, leaving only the polymeric part behind [198–200]. Moreover, the jet is electrically stable only at the tip of spinneret, after it is subject to charge instabilities. These instability starts open the jet into nanofibers, which are collected on the counter electrode.

3.1.4 Physics of the nanofibers formation

During the electrospinning process, the fiber formation can be divided in four different steps [201–206], each one dominated by a specific physical phenomenon:

(i) Droplet deformation and onset of jetting;

(ii) Linear path of the jet;

(iii) Bending part of the jet and instabilities;

(iv) Deposition on the collector.

In the following subsections, all the formation steps will be further described, considering the electrospinning setup previously described in Sec. 3.1.3, as the theoretical model.

Droplet deformation and onset of jetting

Without the application of an electric field, the polymeric solution exiting the tip of the needle assumes an hemispherical shape, due to the surface tension and viscoelastic stresses of the solution itself. Applying a voltage between the needle and the planar counter electrode, the solution droplet becomes electrically charged and is deformed because of the interaction of the external electric field (see Fig. 3.5, upper images).

By increasing the external electric field, the droplet elongates its shape, reaching a conical shape, where surface tension and Coulombic interactions are balanced. Close to the critical potential, the droplet assumes the cone-like shape with a characteristic half-angle of the cone, which is determined to be of the order around 30° - 38° (see Fig. 3.5, upper images) [205]. Moreover, the droplet should reach, from predictions, the conical shape near to the critical electric field value with a half-angle of the cone at 49.3° at the tip of the deformed droplet. Experimentally it can be found half - angles significantly smaller than this value (see Fig. 3.5, lower images). Taylor, in fact, has shown that a viscous fluid exists in equilibrium in an applied electric field when it has the form of a cone with a semi-vertical angle of 49.3°.
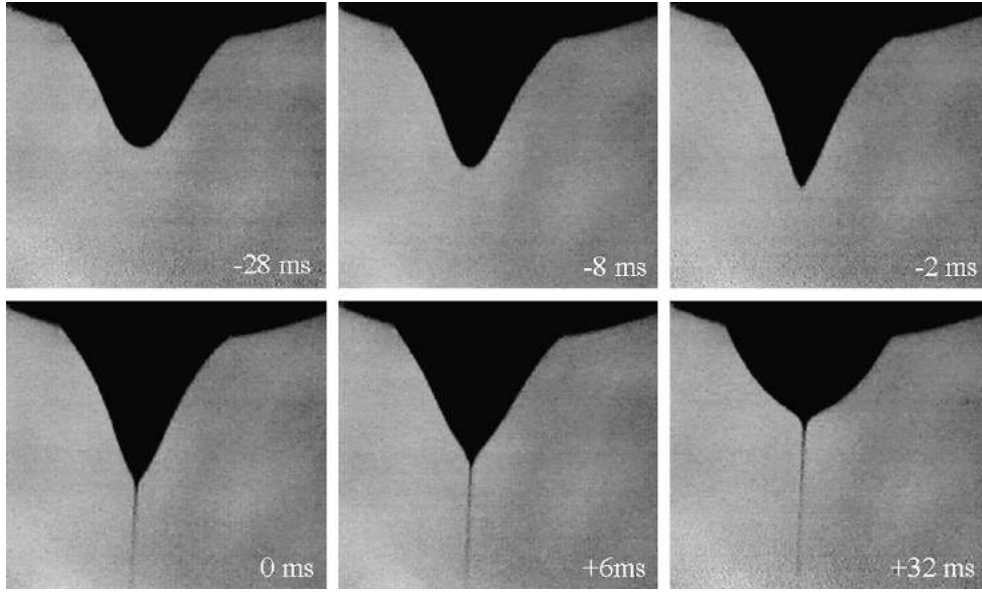
Fig. 3.5 Droplet deformation due to the interaction of an external electric field. In the six frames are showed the same droplet before, during and after reaching of the critical potential. Reprinted from [206], with permission from Elsevier.

Furthermore, Taylor showed that the critical voltage V_c (expressed in kV) at which the maximum jet fluid instability develops is given by:

$$V_c^2 = 4\frac{H^2}{L^2}\left(ln\frac{2L}{R} - 1.5\right)(0.117\pi R\gamma) \tag{3.1}$$

where:

- H is the working distance;
- L is the length of the plastic capillary tube that connects the needle and the syringe in which is loaded the polymeric solution;
- R is the radius of the capillary tube;
- γ is the surface tension of the polymeric solution

On the contrary, the minimum electro-spraying voltage of a suspended conducting drop in air medium was calculated, under the hypothesis of hemispherical shape, to be:

$$V_{spray} = 300\sqrt{20\pi r\gamma} \tag{3.2}$$

where r is the droplet radius.

If the dielectric medium between the 2 electrodes is not air, but it is a fluid not conductive and immiscible with the electrospinned solution, the droplet distortion

will be grater than the one depicted in Fig. 3.5. The electric field is so increased, lowering the the critical voltage required in order to have the jet emission. For example, electrospinning in vacuum conditions will lower the critical potential.

It has to be highlighted that the fluid circulation in the deformed droplet is directed to the apex of the cone due to the presence of tangential electrical shear stresses. However, when the fluid cone is subjected to high electric fields, its shape is strongly modified. The cone becomes, in fact, more and more concave close to the tip with rising electric fields until it vanishes. The droplet is therefore pushed inside the needle due to the strong fluid circulation at the apex of the cone. This phenomenon is due to the direct connection between the droplet shape and the applied electric field. For the cone calculations, Taylor assumed the droplet shape as a spheroid, resulting from the ellipsoid rotation around his major axis. Many years after, Yarin et al. [207] assumed the droplet shape as an hyperboloid of revolution, when an external electric filed is applied. These two geometric objects can be represented by the following formulae:

$$x^2 + \frac{y^2}{a^2} + \frac{z^2}{b^2} = 0 \qquad (3.3)$$

b > a for a spheroid with a prolate geometry and

$$x^2 + \frac{y^2}{a^2} - \frac{z^2}{b^2} = 0 \qquad (3.4)$$

for an hyperboloid of revolution

The Fig. 3.6 represents the geometry of the cone (points B, C, and D) expressed in polar coordinates (z,ρ) at the apex of the needle tip. The tip is also assumed to be at a distance a_0 from the flat equipotential surface at $z = 0$. This position does not correspond to the working distance, which is much higher (in the orders of *cm*). The value of a_0 suggests the distance within witch are present the distortions induced by the electric filed. The a_0 magnitude is of the order of $1\mu m$.
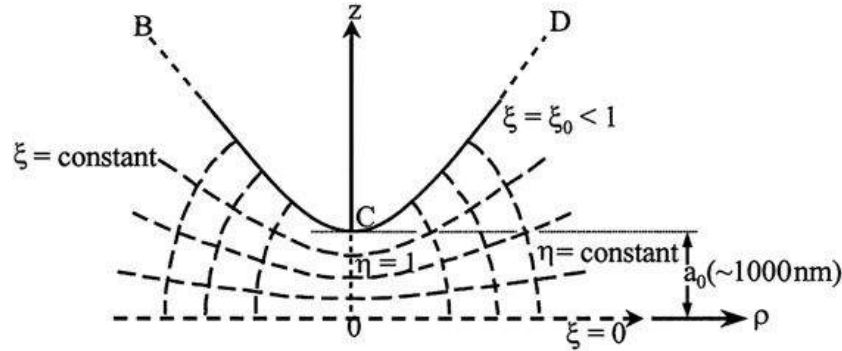
Fig. 3.6 Representation of the mathematical model of the droplet shape (curve BCD) immersed in the electric field, in cylindrical coordinates. The tip of the droplet C is at a distance a_0 from the flat equipotential surface. Reprinted from [206], with permission from Elsevier.

From calculations, the droplet shape parameters ξ_0 can be defined as a function of the electrical potential. It thus defines that the maximum potential, able to ensure a stationary state and shape, corresponds to a factor $\xi_0 = 0.834$, being ξ_0 the critical hyperboloid. The envelope cone for this studied hyperboloid is characterized by an half angle of $33.5°$.

Linear path of the jet and bending instabilities

When the jet is originated from the deformed droplet, as showed at the time zero in Fig. 3.5, it undergoes a straight path. It is, in fact, accelerated toward the collector from the Coulomb forces. These forces, indeed, generate longitudinal stresses along the jet axis, ensuring the formation of a linear path and the thinning of the jet. The force, longitudinally applied on the fluid, is the main parameter that controls the jet straight path. Moreover, the jet is elongated along its axis due to the applied electric field and to the Coulomb repulsion between all the equally charged segments of the jet [190, 208, 209].

The jet is stable up to a certain distance from the needle, depending on the applied electric field. After this, the jet undergoes a stress relaxation effect, where the Coulomb interaction between the charges in the fluid become predominant. This induces a jet chaotic motion toward the counter electrode. Besides, the stretching effect, caused by the electrostatic forces, is neutralized by the viscoelastic stresses.

The polymeric jet can be modeled as a linear distribution of charged elements, connected by a viscous medium, where one end is anchored at the jet origin, and the other end can freely move in a 3D space. The free end describes the deviation of the jet from the straight path, so, the bending instabilities. They are originated from the interactions among the electric filed, the surface tension, the Coulomb repulsion between the jet charges. In fact, the jet charge transport is induced when the electric field is applied and, consequently, they interact, causing the formation loops of circular shape in the jet. This phenomenon leads to the onset of the so-called instabilities.

The electrostatic forces, between the single elements of the jet, induce the establishment of repulsion forces with radial distribution. In a particular way, the repulsion forces cause the splitting of the primary jet into several sub-jets, called **Bending (whipping) instabilities** [199, 210]. This can occur in self-similar way on a smaller and smaller dimensions scale, by decreasing the jet diameter. Thanks to this phenomenon, the fibers diameter is reduced from micrometric to the nanometric scale. Fig. 3.7 is a schematic representation of the onset of the bending instabilities with different orders, starting from a straight jet.
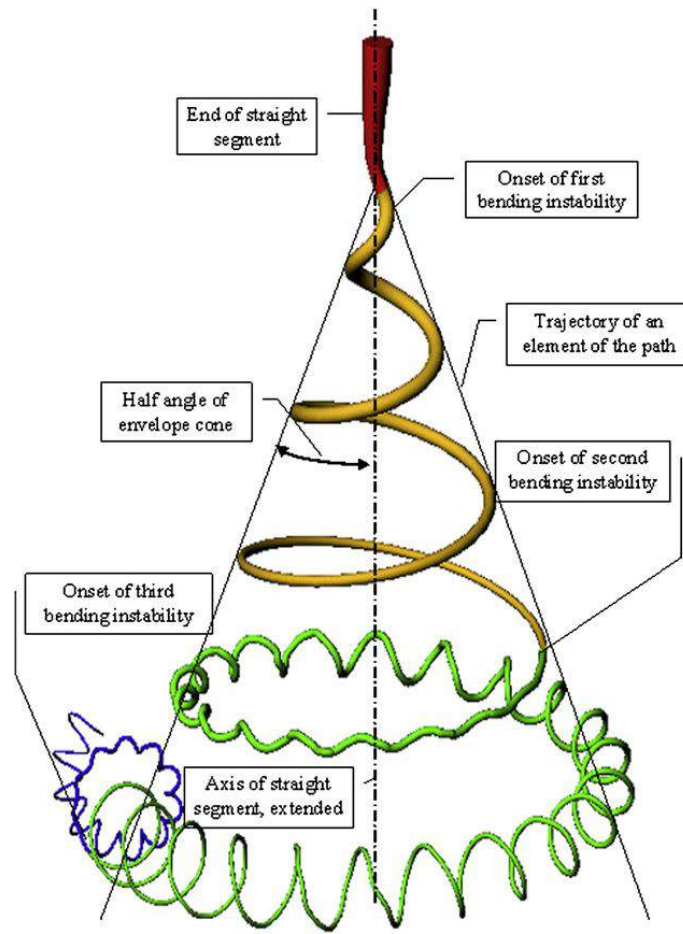
Fig. 3.7 Schematic representation of the whipping instabilities starting from a straight polymeric jet. Reprinted from [206], with permission from Elsevier.

The fluid jet diameter, due to the whipping instabilities, can be expressed as:

$$r_0{}^3 = \frac{4\varepsilon\dot{m}_0}{\kappa\pi\sigma\rho} \tag{3.5}$$

where r_0 is the radius, ε is the fluid permittivity, $\dot{m}_0$ is the mass flow rate, κ is a parameter related with the electric currents and dimensionless, σ is electric conductivity and ρ is the density of the electrospun material.
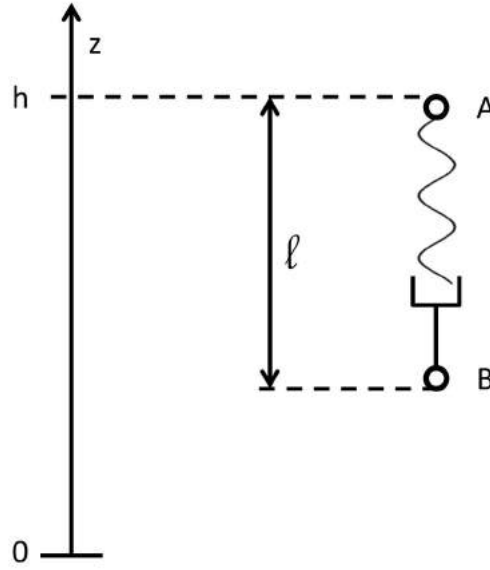
Fig. 3.8 Viscoelastic dumbbell model (spring, beads, dashpot) representing the polymeric jet linear path.

Concerning the linear path of the jet, a viscoelastic dumbbell model can be defined to calculate the linear path length as a function of the external field.

The viscoelastic model (in Fig. 3.8) could be described as the connection, in series, of a spring, having elastic modulus G, with a dumper having viscosity μ. According to this model, the total deformation $\frac{d\Sigma}{dt}$ can be expressed as written in the following formula:

$$\frac{d\Sigma}{dt} = G\frac{dl}{dt} - \sigma\frac{G}{\mu} \tag{3.6}$$

Where, the fluid viscous deformation is function of the viscoelastic relaxation time $\tau = \mu/G$, represented by the second equation term. It follows that the force that acts on the jet during the linear path is defined by the a sum of three terms. The first one is related to the external applied electric field $-\frac{eU_0}{h}$, being h the working distance, e the electron charge and U_0 the electric potential energy. The second term, instead, arises from the Coulomb repulsion forces $-\frac{e^2}{l^2}$, present between all the jet charged elements. The last term is related to the resulting force acting on the droplet B (in Fig. 3.8), applied on an area πa^2, section of the droplet. The total momentum balance acting on B can thus be defined as:

$$m\frac{dv}{dt} = -\frac{e^2}{l^2} - \frac{eU_0}{h} + \pi a^2\sigma \tag{3.7}$$
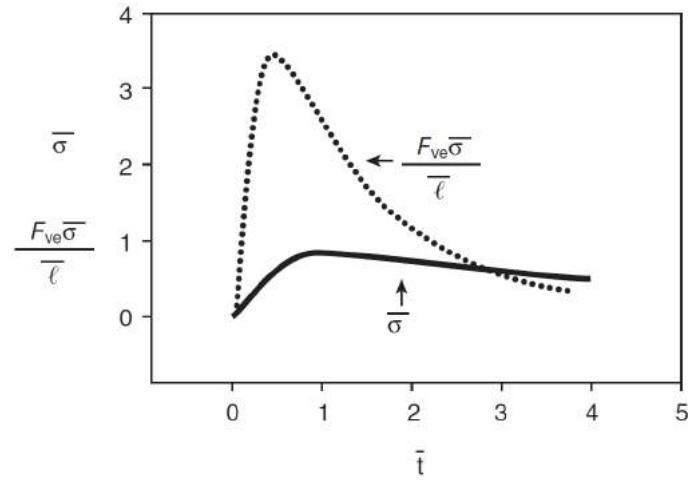
Fig. 3.9 Dependence of longitudinal stress and force on reduced time scale, as discussed in detail in the text above. Reprinted from [211], with the permission of AIP Publishing.

The main results of a numerical evaluation [211] of this expression are given in Fig. 3.9 and 3.10.
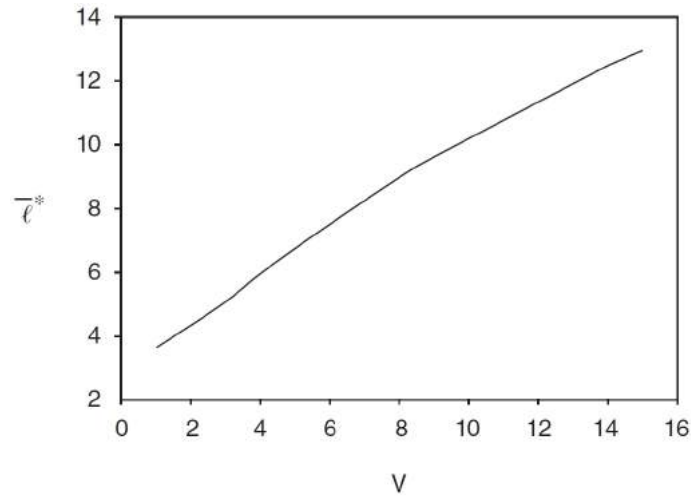
Fig. 3.10 Length of linear path of the jet as function of the applied voltage, for details see text. Reprinted from [211], with the permission of AIP Publishing.

In particular, Fig. 3.9 shows the variation of the viscoelastic stress during time as long as the jet is deformed in time as given relative to the relaxation time introduced above. In addition, the longitudinal force F_{ve} acting on the jet is given in the same plot. The stress, at first, increases with time as the segment is stretched, when a maximum is passed, it begins to decrease. The reason of the decrease is the onset of the viscoelastic relaxation process characteristic of the model. The longitudinal force acting on the jet also passes through a maximum at a time corresponding roughly to

the relaxation time, and then decreases very strongly. The stress passes through its maximum in the same time scale, although at a somewhat later time.
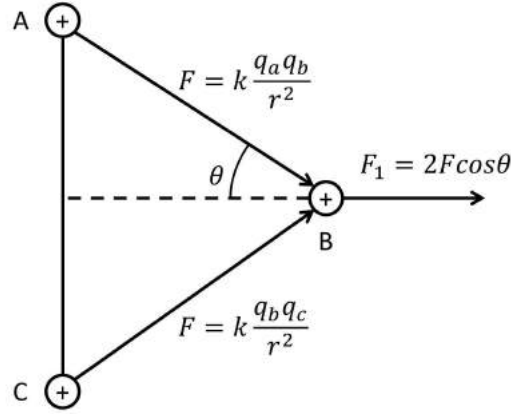
Fig. 3.11 Schematic representation of the electrostatic forces applied on the charge B from 2 separated charges A and C. Reprinted from [211], with the permission of AIP Publishing.

The linear jet is stable for sufficiently high values of force and stress. However, after a maximum, it decays rather strongly, where the jet they become so small that instabilities, i.e. the bending instability, become dominant. This causes the linear jet to deviate from the original path along the z-direction, bending along the x and y directions: this will happen at a length $\bar{l}^*$. Fig. 3.10 shows the length $\bar{l}^*$, as a function of the voltage, at which the jet leaves the linear path along the z-direction. In fact, the length depends strongly on the applied voltage. The characteristic length is usually interpreted as the length of the linear part of the jet observed experimentally.

It follows that the jet is expected to become controlled by instabilities as the longitudinal force/stress become sufficiently small, as indicated previously. Bending causes deviations from the path oriented purely along the z-axis causing the jet to follow a spiraling or looping trajectory. In order to explain this, Reneker and co-workers considered three equal and positive charges to explain the onset of the beginning instabilities. Two of them are assumed on the jet axis, while the third one is perpendicularly displaced [210, 212], as represented in the Fig. 3.11. In this figure, A and C charges apply on B, two forces equal in magnitude, but having different directions. The resulting force magnitude can be defined as:

$$F = k\frac{q_a q_b}{r^2} = k\frac{q_b q_c}{r^2} \tag{3.8}$$

Where q_a, q_b and q_c are the charge intensities, r is the A-B and C-B distance and k is the Coulomb's constant.

The resulting force on the charge B is $F_1 = 2F\cos\theta$, that induces a lateral movement of the charge, as depicted in Fig. 3.11. Moreover, the force F_1 induces an instability already predicted by the Earnshaw's theorem. It states, indeed, that a point charge collection cannot be maintained in an equilibrium state only by the

interaction of the electrostatic forces between the charges [213, 214]. For this reason, the F_1 should be considered as one of the main cause of jet instabilities.

Based on Reneker's descriptions on the electrospinning process, the instabilities might be reduced by controlling the electric filed distribution. The nanofibers distribution on the collector can be so manged.

In conclusion of this theoretical analysis, some points have to be highlighted. First of all, the viscoelastic stresses reduce with time, during the jet deformation. In fact, the jet becomes more and more deformed, forming secondary jets from the primary one due to the presence of the repulsion forces.

Furthermore, the linear path length increases linearly as the applied voltage increases, as long as forces and stress are sufficiently high, up to a threshold value, after which, they decrease strongly. This behavior makes the jet so thin that instabilities become dominant, as the whipping ones.

Finally, one should point out that more phenomena could be observed during an electrospinning process. One of these is the **jet branching** [206, 215] sometimes observed during nanofibers formation. It is characterized both by isolated and by regular arrangements of the branches, very small jets protruding perpendicular from the main jet. The branching phenomena is related to the presence of static undulations on the surface of a charged jet that interacts with the electric field. The assumption that has to be done is that, near the highest peaks of these static undulations, shape perturbations enhance the curvature radius rapidly, forming branches. In this way, the branches were obtained, starting from the undulations of the jet.

Deposition on the substrate

The conclusive process of the electrospinning process is the deposition of the solidified nanofibers on the substrate located at the counter electrode. Here, nonwovens can be defined as fabrics that are neither woven nor knit, e.g. felt, in random configuration of a plane (see Fig. 3.4B). During the elongation and thinning of the nanofibers within the deposition process, the solvent evaporates, strongly contributing to jet thinning and to the final diameter of the solidified nanofibers on the counter electrode. In general, the mat of nanofibers assumes circular shape if the spinneret is fixed or elliptical shape if the spinneret is put in movement along one direction (e.g. right-left) during the deposition step.

The flight time that a jet section experiences, during the electrospinning, from the cone apex until it is deposited on the substrate is estimated to be about $10^{-1}s$. This is an extremely high value, and it corresponds to the rapid and sudden reduction of the jet diameter from around $100\mu m$ down to $100nm$. It has to be noticed that molecules of the chain tend to become highly oriented along the jet during electrospinning, possibly showing a crystal morphology [205].

Generally, electrospun nanofibers are deposited in very short times, starting from solution based on high boiling points solvents, e.g. de-ionized water. Combining this with the use of high solvent concentrations or polymers with glass-transition tem-

peratures close to or below the room temperature, could lead to partial coalescence effect, depending on the relative humidity during deposition. Coalescence occurs both when two soft fibers within the mat come in close contact and when two such nanofibers cross each other. This effect is caused by the not complete evaporation of the solvent during the nanofibers flight. This process thus causes the formation of junction points between the nanofibers [216].

As already mentioned, the counter electrode is conductive, and connected to the ground potential to keep stable the potential drop between the needle and the collector. Much effort has been dedicated to the investigation of the relationship between the counter electrodes setup and the resulting nanofibers properties, in terms of morphology and physics. Thus, different types of collectors were developed such as: plane plate collector, simple mesh collector, rotating drum collector, disc collector, rotating wheel with edge, parallel bars, multifilament thread, ... [196].

Plane plate collector   is depicted in the electrospinning setup drawing in Fig. 3.4, usually covered by an aluminum foil during tests. This counter electrode collects nanofibers in the form of a no woven mat due to its planar arrangement. In the following paragraphs, different kind of collectors will be shown, each one able to obtain a different nanofibers arrangement.

Rotating drum collector   can organize nanofibers in parallel thanks to its rotation as depicted in Fig. 3.12A. The collector has a cylindrical shape and rotates around its axis at very high speed (up to thousands rpm - round per minute). When tangential velocity, proportional with angular velocity and the cylinder radius, is enough high to ensure the full evaporation of the solvent during the jet flight, the nanofibers assume a circular shape (as showed in Fig. 3.13A). On the other hand, if the tangential velocity is not sufficient, the nanofibers distribution tend to form a random mat (as showed in Fig. 3.13B). Lastly, having a too high tangential speed, leads to a not continuously collection of fibers because the take-up speed breaks the fiber. This kind of collector needs a fine tuning of the rotating speed, depending on the starting polymeric solution [217, 218].
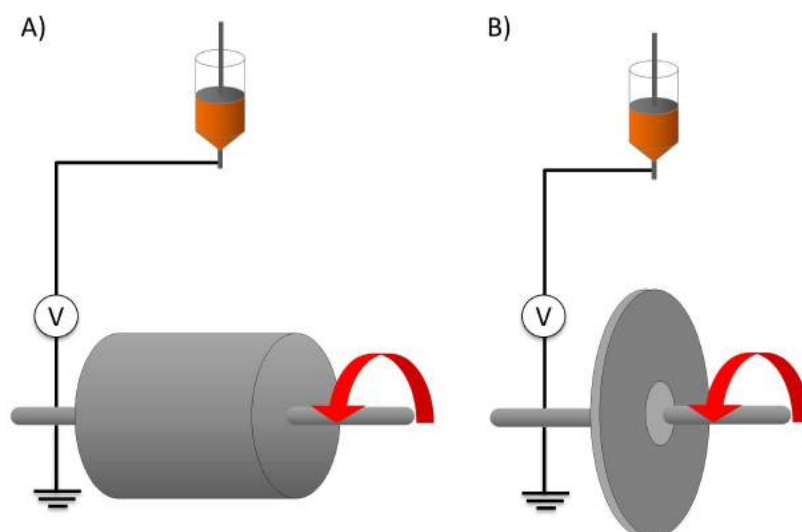
Fig. 3.12 Schematic representation of two electrospinning collectors: A) rotating drum and B) disk collector.
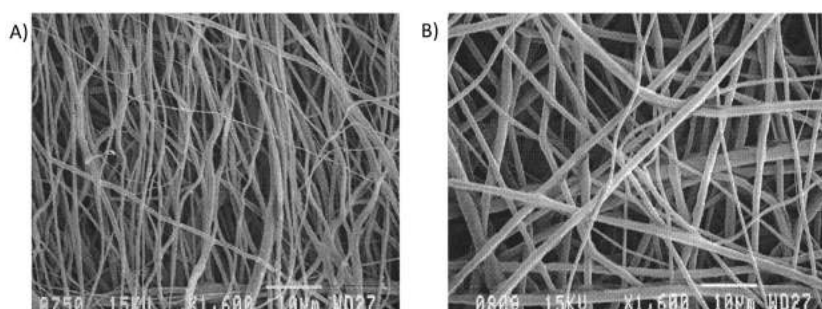
Fig. 3.13 FESEM of electrospun nanofiber with rotating drum of 1/7 w/v PGA in HFIPA as: A) aligned fibers at 1000 rpm, B) random fiber orientation at 100 rpm. Reprinted from [217], from Taylor & Francis

Disk collector is employed to obtain uniaxial aligned nanofibers, being a variation of the drum collector. This counter electrode is thinner than the drum collector (as depicted in Fig. 3.12B) and, consequently, it collects nanofibers only on its edge of the rotating disk. Therefore, the resulting fibers are more aligned than the ones obtained with the drum collector [219–222]. During electrospinning, the jet follows the usual cone-shaped path caused by the charge instabilities, but, at a certain distance, the loops section decreases, ans so the jet cone shrinks. It appears, so, an inverted cone whose apex lays on the disk. The reason is that the electric field is concentrated on the disk edge and it gathers the polymeric jet on this region. The disk rotation, also, induces a tangential force acting on the fibers. Thus the nanofibers are deposited only on the edge of the disk and, at the same time, they are stretched are reduced in diameter due to the tangential force. The fibers alignment quality results

to be much better than the one obtained with the drum, but the throughput is much lower.

3.1.5   Process parameters

As evident from the presented examples in the previous sections, the electrospinning process is governed by many parameter that have to be investigated and understood to analyze the whole process. In fact, the morphology of the final nanofibers mat strongly depends on them [184, 215, 223–225]. The parameters can be broadly divided in four main categories:

  (i) Solution parameters. They include the properties related to the polymeric solution to be electrospinned, as viscosity, concentration and polymer molecular weight;

 (ii) Processing parameters. They are variables strictly correlated to the electrospinning process, as voltage, flow rate and working distance;

(iii) Ambient parameters. They are parameters related to the room environment, such as room temperature and humidity;

(iv) Substrate parameters. They are properties related to the substrate selected as collector, like conductivity, roughness, porosity, selected curvature.

Solution parameters

The solution parameters, as viscosity, concentration and polymer molecular weight, strongly bear upon the morphology of the nanofibers mat. Lots of studies have shown how these solution parameters influence the formation of nanofibers or the defects arise [192, 206, 219].

Polymer concentration   There is a direct connection among the polymeric solution viscosity and the polymer concentration. In fact, the viscosity increases with the concentration of the polymer. There is a threshold solution concentration for the electrospinning process, below which beads can be formed instead of fibers. However, above the optimal concentration, the formation of continuous mat is prohibited because of the inability to maintain the flow of the solution at the tip of the needle resulting in the formation of larger fibers. In Fig. 3.14 are showed two FESEM images of PEO-based (Poly Ethylene Oxide) nanofibers, in which the concentration of the starting solution was varied. By increasing the polymer concentration from $3wt\%$ to $5wt\%$, the mean fiber diameter increases from $160nm$ to $210nm$. Researchers have attempted to find a relationship between solution concentration and fiber diameter and they found a power law relationship [226, 227].
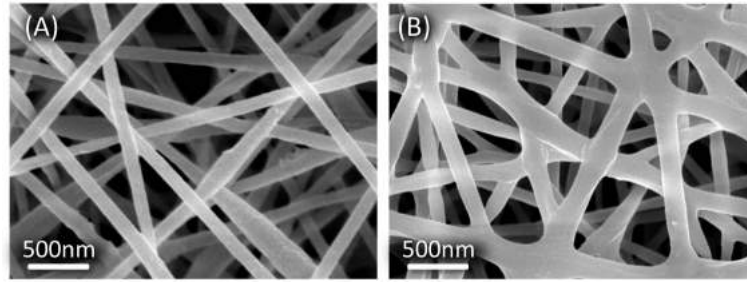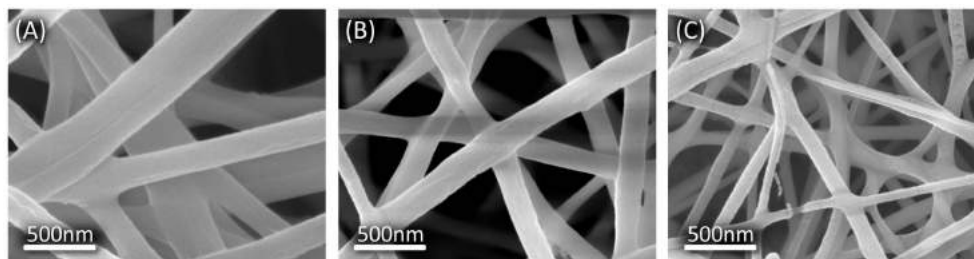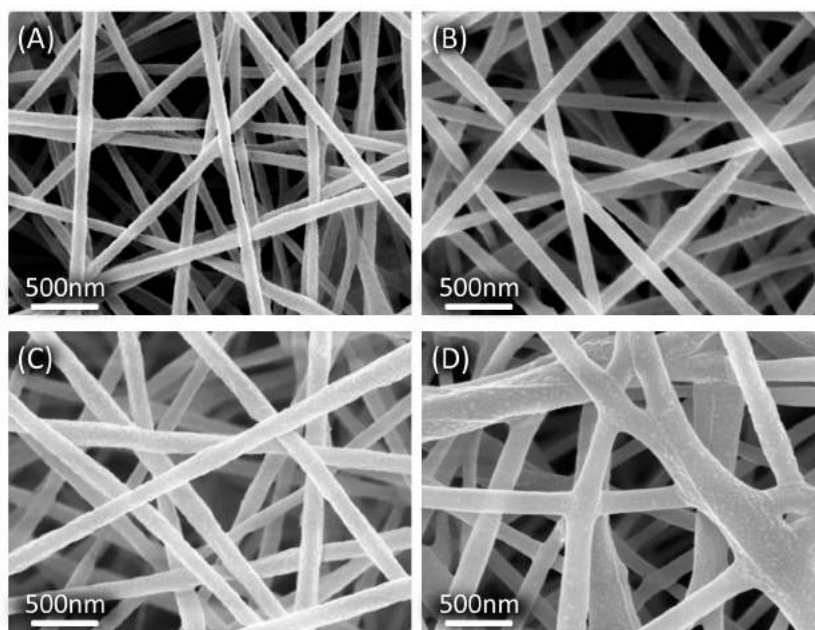
Fig. 3.14 FESEM images of nanofibers obtained from a water-based solution of PEO 600kDa (Poly Ethylene Oxide) at different polymer concentrations. A) 3$wt\%$PEO with mean fiber diameter of 160nm. B) 5$wt\%$PEO with mean fiber diameter of 210nm.

Solution viscosity   is defined from literature as the measure of its resistance to gradual deformation by shear stress or tensile stress. It arises from the collisions between neighboring particles in a fluid, having different velocities. When a fluid is pumped in a small tube, the particles composing it move quicker in the inner part of the tube and slower near its walls. This means that some stress is present due to the resistance between the particles in order to keep the fluid moving and the stress is directly proportional to the viscosity of the fluid. The formation of the mat of nanofibers is thus ensured if the solution viscosity is kept into the range [205, 212, 228]:

$$(0.02 \leq \eta \leq 300) \, Pa \cdot s \tag{3.9}$$

The Eq. 3.9 indicate the presence of two distinct regimes. At low viscosity values ($\eta \leq 0.1 Pa \cdot s$), the solution surface tension is higher than the viscoelastic forces, breaking the polymeric jet into the droplets. This regime is defined as **electrospray** [205, 212]. On the other hand, at higher viscosity values ($\eta \geq 2 Pa \cdot s$), the formation of nanofibers is ensured thanks to a stable electrospinning process. In this case the viscosity is sufficient to have a polymeric continuous flow toward the counter electrode, with the formation of a dried mat. The viscosity increase, caused by the increase of polymer concentration, ensures the formation of a uniform nanofibers mat, without the presence of defects, such as beads [212]. The beads in the mat are due to the interaction between surface tension, charge density and viscoelastic forces, inducing a modification of the section of the fiber [193, 212, 229].

Polymer molecular weight   has a strong effect on the solutions rheological properties, such as viscosity and surface tension, affecting the electrospun fiber morphology. Generally, polymer solutions with high molecular weight are used during electrospinning providing the desired viscosity for the fiber generation and giving fibers with larger average diameters [230–232]. On the other hand, solution with too low molecular weight tend to form beads instead of fibers. Polymer molecular weight reflects the number of entanglements of the chains in a solution, thus the solution

viscosity. Entanglements of the chain play an important role in the processing of electrospinning.

Processing parameters

The electrospinning parameters influence the mat of nanofibers in terms of diameter of the fibers, then the surface area and porosity distributions of the mat. Therefore, it is quite important to study the influence of these parameters on the diameters distribution.

Voltage is a crucial element for the electrospinnning of a solution. Only after the attainment of a proper threshold voltage, a continuous polymeric jet is originated, in which a current, due to the applied voltage, flows. Therefore, an increment of current causes an increase of net charge distribution in the jet leading to a reduction of the nanofibers diameter [231, 233, 234].

Working distance is a fundamental value to be controlled in order to ensure the solvent complete evaporation. It has been observed that, in general, both too low and too high working distances generate defects in the deposited mat. Defining the electric field intensity as the ratio between voltage and working distance, a strong variation in the fibers morphology can be clearly noticed. Fig. 3.15 shows the variation of the PEO based nanofibers with increasing electric field. The decrease of the nanofibers diameter, as previously explained, is related to the increase of the applied voltage [231, 233, 234], while a decrease of the working distance may lead to solvent evaporation problems. In most cases, higher voltages cause greater elongation of the solution due to the stronger culombic forces in the jet as well as a stronger electric field. These effects are responsible of the reduction in the fiber diameter and also of the rapid evaporation of the solvent from the fibers.

Fig. 3.15 FESEM images of nanofibers obtained from a water-based solution of $5wt\%$ PEO 1000kDa (Poly Ethylene Oxide) at different electric field intensities. A) $0.95kV/cm$ with mean fiber diameter of $195nm$. B) $1kV/cm$ with mean fiber diameter of $171nm$. C) $> 1.1kV/cm$ with mean fiber diameter of $168nm$.

Flow rate   is the rate at which the polymeric solution is pushed through the needle, replenishing the Taylor's cone and determining also the linear path length [205]. Low flow rate values lead to the formation of the Taylor's cone inside the needle, and so an electrospinning process intermittent. On the other side, when the flow rate becomes too high, a continuous charged polymeric jet is formed, having a resulting mat characterized by the presence of many defects, such as beads or by a broader diameter distribution. Experimental results, moreover, underline and demonstrate that higher flow rates lead to bigger nanofibers [205, 235, 236]. Fig. 3.16 shows clearly this trend applied on a PEO-based solution. The nanofibers diameter increases with the flow rate until a point in which the solvent cannot evaporate completely during the deposition. In this last case, (Fig. 3.16D) the fibers result as joined in many points, tending to weld one with the others.

Fig. 3.16 FESEM images of nanofibers obtained from a water-based solution of 5wt% PEO 600kDa (Poly Ethylene Oxide) at different flow rates. A) 0.1 ml/h with mean fiber diameter of 140 nm. B) 0.2 ml/h with mean fiber diameter of 160 nm. C) 0.3 ml/h with mean fiber diameter of 180 nm. D) 0.5 ml/h with mean fiber diameter of 280 nm.

Ambient parameters

Temperature   affects the electrospinning process as well as the other solution and processing parameters. Mit-Uppatham et al. (2004) [237] have investigated the effect of temperature on the electrospinning process ranging from 25 to 60 °C and they found that with increasing temperature, the fibers diameter decreased. They attributed this diameter reduction to the viscosity decrease of the polymer solutions at increased temperatures, being an inverse relationship among them [192].

Humidity   variation during the electropinning process has been studied and shows that increasing values of humidity bring to the appearance of circular pores of small dimension on the surface of the fibers. When the humidity is further increased, the pores coalesce [238]. Moreover, it has been found that at very low humidity percentages lead to a faster evaporation of the solvent, having a volatile solvent that may dry rapidly. Sometimes, if the evaporation rate is fast, compared to the removal of the solvent from the needle tip, problems with electrospinning may occur, such as the needle tip clogging [188]. It has also been proposed that high humidity levels could help the discharge of the electrospun fibers [239].

3.1.6 Applications

Electrospun nanofibers are characterized by large surface area to volume ratio and many beneficial properties based on the surface and chemical properties. Fig. 3.17 highlights some of the main practical application of nanofibers [219, 240].
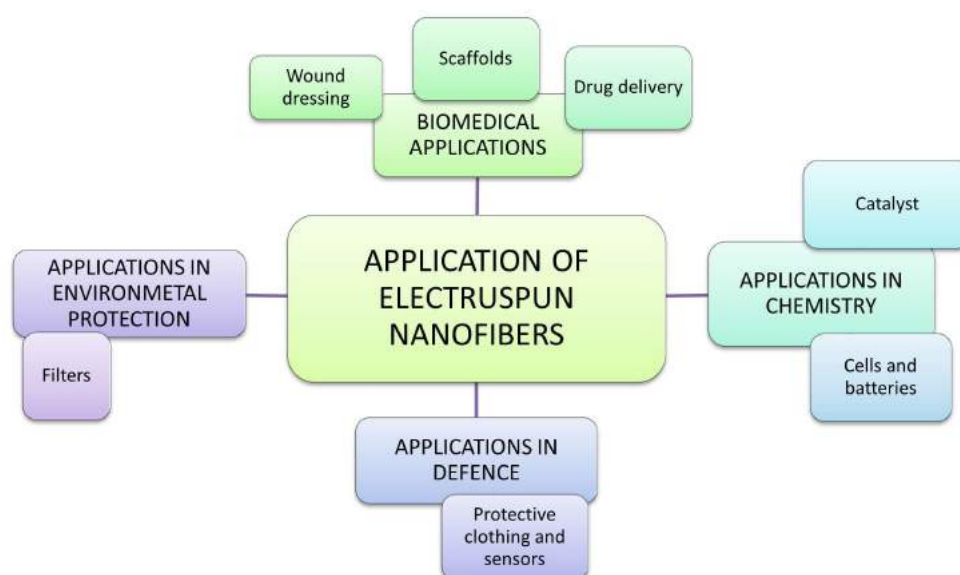
Fig. 3.17 Schematic illustration of the most important applications of electrospun nanofibers.

Biomedical applications

Wound dressing   is an essential step for a rapid healing of an affected part and, moreover, offers protection against infection due to micro-organisms. Traditional wound dressing materials are made of hydrocolloids, hydrogels and alginate salts and silver nanoparticles, also reported to have efficient antimicrobial potential. Nowadays, nanofibers decorated with nanoparticles have gained attention thanks to their activity against micro-organisms. Lee at al., in 2014 [241], demonstrated that the silver nanoparticles contained in chitosan (CS) nanofibers could be prepared

by the electrospinning technique. This study demonstrated that the chitosan was inactive against the tested micro-organisms, wherein silver nanoparticles loaded chitosan nanofibers exhibited significant activity by restricting the respiration of micro-organism.

Scaffolds   are engineered materials created to obtain desirable cellular interactions to contribute to the formation of new functional tissues for medical purposes. Experiments to grow cells and tissues in laboratory are an intense field of research for human welfare. The polymers for scaffold materials are chosen by their hydrophobic and hydrophilic nature, drug adhesion and release tendency as well as the type of mat structure. High surface area and short diffusion length of nanofibers increased their use as scaffold material by higher rate of drug release than the bulk material. Nanofibers are reported to possess control over the drug release and hence improved efficiency towards the sustained discharge of drug rather than the burst release. An example of protein drug-loaded nanofibrous scaffold prepared, consisted of Polyurethane (PU)/cellulose acetate (CA)/zein composite nanofibers mats loaded with streptomycin, an antimicrobial drug [242]. These electrospun nanofibers showed efficient antibacterial activity as well as good attachment and proliferation of cells thanks to the loaded zein protein. Composite fibers allowed the growth of cells inside the nanofibers mat as it was on the surface in neat PU fibers. Presence of hydrophilic zein protein improves the cell attachment and cellulose acetate enhances the cell growth, while, the drug compound inhibits the growth of bacteria on the nanofibers. Furthermore, in scaffolds, it is necessary to achieve a sustained release of the desired drug as well as better therapeutic usage. Micro-adhesive properties are needed for the scaffolds. Recently, a novel scaffold for oral applications was reported in 2015 using electrospinning technique [243]. The release mechanism proved that the initial burst followed by sustained release of drug as a result of dissolution of surface moieties followed by layer by layer. These nanofibrous mats also exhibited very good antimicrobial activity with low toxicity.

Drug delivery   refers to approaches and systems to transport a pharmaceutical compound in the body in order to safely achieve its desired therapeutic effect. Zong et al.[244] carried out in-vitro studies on the delivery pattern of an antibiotic drug loaded into an electrospinned nanofibrous mat. They produced mefoxin-loaded PDLLA (poly-DL-lactide) nanofibers by optimizing the instrumental parameters such as electric field, concentration, salt addition and feeding rate. The as-prepared nanofibred membrane was treated in buffer solution for in vitro drug release study and the complete release was confirmed at 48 h [245]. Recently, several new drugs are designed to cure cancer disease efficiently. Common cancer treatments have many limitations such as clinical toxicity in radiotherapy, toxicity to healthy cells by overdose of drugs in chemotherapy and limited distribution of drugs in blood vessels. In this connection, nanofibers extend its role in cancer therapy by easily carrying drugs and releasing them. Shaobing Zhouand co-workers developed a new device with core-shell nanofibers as implant material for safe and effective cancer treatment. It is an excellent work in which the folate-conjugated PEG/PCL

(polyethylene glycol/polycaprolactone) copolymer layered micelle with drug loaded nanofibers prepared by co-axial electrospinning technique. Core and shell of the nanofibers were micelle/PVA (polyvinyl alcohol) and gelatin solution respectively. These nanofibrous mats with the micelle examined for therapeutic action revealed efficient killing of tumor cells, with minimal loading of drug and reduced frequency of drug administration and thereby improved the survival of affected people [246].

Applications in chemistry

Catalyst , in the form of nanomaterials, have attracted great interest thanks to the large surface area and the capability of high catalyst loading. Nanofibred catalysts are able to substitute nanoparticles thanks to the capability of overcoming the limitations of catalyst recovery. Among the several hundreds of reports on nanofibers, significant numbers of them are related to their applications as catalysts. Nanofibers of poly(ethyleneimine)/poly(vinylalcohol) (PEI/PVA) immobilized with gold nanoparticles were prepared and utilized as a catalyst for organic reduction reaction [247]. Researchers found that immobilized Au NPs showed an excellent catalytic activity and re-usability for the transformation of 4-nitrophenol to 4-aminophenol. Moreover, nonporous substrates can be covered with nanofibers in order to increase their surface area, and thus enhance the reactivity. As an example, carbon nanofibers loaded with iron nanoparticles showed higher conversion of hydrocarbons when compared with active carbon and alumina. The catalytic activity is enhanced, while the dimension scale is reduced, as in the case of nanofibers [248].

Fuel cells contain, as already stated, three principal part: anode, electrolyte and the cathode. Breitwieser et al. [249], have developed a fuel cell membrane thanks to electrospinning technique by direct membrane deposition (DMD). In this paper, poly(vinylidene fluoride-co-hexafluoropropylene) (PVDF-HFP) nanofibers are directly electrospun onto gas diffusion electrodes, in order to use them as electrolyte in the cell. Nafion exchange membrane is deposited onto the nanofibers though the inkjet printing and other PVDF-HFP are electrospun. This method requires no additional production steps and both deposition methods can be combined within one production line to further simplify mass production.

Batteries are characterized by three primary functional components, such as anode, cathode and electrolyte, as already discussed in the first chapter. Jayaraman et al. reported a novel $TiNb_2O_7$ nanofibrous material as anode material for fuel cell application [250]. They were able to construct an excellent Li-ion battery, having both electrode and electrolyte material made of electrospun nanofibers. Newly fabricated device has delivered the reversible capacity of 116 mAh/g at current density of 150 mA/g for the applied potential of 2.4 V and 278 Wh/kg. Depending on the nature of conductive polymeric materials, the ionic mobility was enhanced/declined and hence influenced the charge/discharge capacity as well as the storage capacity. Another example of electrospinning-based batteries comes from Kim and Kim [251]. They

elaborated electrospun Cu/Sn/C composite nanofibers using dual nozzle electrospinning method followed by carbonization. These composite fibers were tested for the capacity of both Li-ion and Na-ion. Stable reversible performance reveals that the capacities of 490 mAh/g and 220 mAh/g for Li-ion (600 cycle) and Na-ion (200 cycles) respectively.

Applications in defense

Protective clothing   made with nanofibers, with surface pores, are used as catalyst for the degradation of organic compound such as dyes, pesticides and chemical warfare stimulants (CWS). Ramaseshan and co-workers published a set of papers [252] for the degradation of CWS using b-cyclodextrin (b-CD) and magnesium oxide (MgO) nanofibers with different composites. They compared the effectiveness of nanoparticles, charcoal and nanocomposite membranes on CWS degradation and they found that the nanofibers were about 2 times more reactive than the charcoal.

Sensors   are electronic devices that detect and respond to some kind of input from the physical environment. The high surface area offered from nanofibers, with respect to films, ensure their good performance in this field. A novel β-phase PVDF (Polyvinylidene fluoride) nanofibrous membrane decorated with multi-walled carbon nanotubes (MWCNTs) and platinum nanoparticles (Pt NPs) was fabricated by electrospinning technique [253]. These nanofibers on glass carbon electrode were applied as a potential material for H_2O_2, glucose bio-sensor and oxygen reduction reaction (ORR) catalyst. Electrochemical data indicated that the PVDF-MWCNT-Pt-NP nanofibrous membrane performs good electro-sensing activity towards H_2O_2 and glucose. The prepared biosensor based on hybrid nanofibrous membrane shows linear range, low detection limit, high selectivity, and long-term stability.

Applications in environmental protection

Electrospun nanofibers with surface functionalization with active groups are responsible for the removal of pollutants in waste water and drinking water by adsorption such pollutants on their surface. Nanofibers, in fact, exhibit different adsorption behavior based on the nature of functional groups on their surface. Removal of chromium (VI) and fluoride ions using alumina/PVP NFs was reported in recent years[254]. The study revealed that the maximum removal of chromium (VI) and fluoride was observed at pH 5 and 7 with adsorption capacity of 6.8 mg/g and 1.2 mg/g respectively during contact time of 1 h.

3.2 1D metals oxides

Nanowire (NW) and Nanotube (NT) structures possess significant and useful properties together with high surface-to-volume ratios thanks to their one dimensional (1D) feature.

Considering titanium dioxide (TiO_2, titania), the use both of chemical dissolution and of field-assisted oxidation, permits the formation of highly ordered and self-assembled nanostructures. Several studies have demonstrated the good performance of TiO_2 nanotube arrays when compared to colloidal TiO_2 in different applications: photocatalysis [255], sensing [256], photoelectrolysis [257], dye-sensitized solar cells [258], drug delivery and other biomedical applications [259], Li-ion batteries [260] and supercapacitors [261]. This nanostructured titania can be produced by different methods including templating through nanoporous alumina [262], sol-gel transcription processes [263] and hydrothermal techniques [264]. However the only technique that guarantees an efficient control on the NTs dimensions is the **anodic oxidation** of titanium in fluoride-based electrolytes [265–271].

Copper has two natural oxides, cuprous oxide (Cu_2O) and cupric oxide (CuO), being both semiconductors with band gaps of about 2.2 eV and 1.2 eV [272], respectively. Both of them are p-type semiconductor with a narrow band gap that has been reported as a candidate material for photothermal and photoconductive applications [273]. Their band gaps make them good candidates for photovoltaic devices [274], catalysts [275], sensors [276], stable electron sources [277] and optoelectronic devices [278]. Copper oxide NWs are particularly desirable due to their large surface areas, size confinement on electrical, transport and mechanical properties [279]. Nanowires and nanowhiskers of Cu_xO can be synthesized by using precursors [280], hydrothermal decomposition route [281], self-catalytic growth processes [282] and solvothermal route [283]. Few studies on the growth of CuO NWs by **thermal annealing** of copper foils in oxygen atmosphere [272, 284–286] have also been reported. If compared to complex chemical methods, thermal annealing of copper provides a simple, convenient and fast method for synthesizing copper oxide nanowires, enhancing absorption of photons in photovoltaic devices which results in greater efficiency, thanks to their high surface area.

In order to keep the description brief and slim, anodic and thermal oxidation will be the only techniques described in Sec. 3.2.1 and 3.2.2, being also the techniques experimentally used in this thesis.

3.2.1 TiO$_2$ anodic oxidation

Thanks to anodic oxidation process in aqueous electrolytes, on top of Al and other metals (as Ti, Zr, Nb, W, Ta) a compact oxide layer can be grown up to some hundreds of nanometers of thickness [287]. Among these materials, Al is the most investigated due to its capability of self-organization of aluminum oxide pores. In fact, since 1953 [288], both flat and compact oxide and regular and porous oxide

could be grown from Al anodization in alkaline electrolytes and in acidic electrolytes, respectively.

In the case of Ti anodization, researchers gave significant effort in order to study TiO_2 as material of unique properties in different applications. This oxide, in fact, is strongly affected in terms of morphology and structure by the electrochemical conditions (as the anodization voltage) and the solution parameters (as pH, water and fluorine species concentration).

It is possible to distinguish four different generation of TiO_2 nanotubes [289]:

- First synthesis generation. TiO_2 NTs arrays are obtained in HF-based electrolytes, strongly acidic, with a maximum nanotube length of 500 nm [290].
- Second synthesis generation. The nanotube array length is increased to about 7 μm by using buffered neutral electrodes, containing NaF or NH_4F instead of HF [266].
- Third synthesis generation. The electrolytes are characterized by a very small water content, mostly constituted of non-aqueous, polar organic electrolyte such as formamide, dimethylsulfoxide, ethylene glycol or diethylene glycol. Thanks to this optimization, the TiO_2 length achieves 1000 μm [265].
- Fourth synthesis generation. It is thought to be the one characterized by non-fluoride-based electrolytes during the anodization process.

TiO_2 nanotube array formation

Anodic oxidation of titanium is usually performed by applying a potential difference between an anode or working electrode (WE, e.g. Ti foil) and a cathode or counter electrode (CE, e.g. Pt foil) immersed in a fluorine-based electrolytic solution and with a little water content, as drawn in Fig. 3.18. This electrolyte used in the third generation of TiO_2 NTs, is the the one considered in this work.
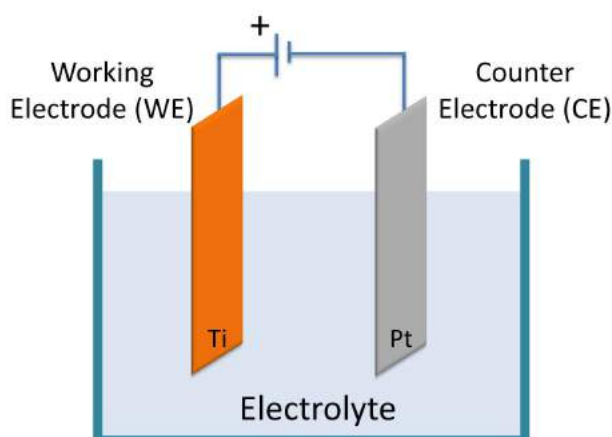
Fig. 3.18 Schematic representation of the anodic oxidation setup.

During the formation of NTs, the Ti surface starts to be oxidized, releasing Ti^{4+} ions and electrons in the solution:

$$2Ti \rightarrow 2Ti^{4+} + 8e^- \tag{3.10}$$

It follows the deposition of an oxide layer deposition onto the metallic surface due to the interaction of the Ti^{4+} ions with the O^{2-} or OH^- ions in water. The formation of the hydrated anodic and oxide layers can be described by the Eq. 3.11 and 3.12:

$$Ti^{4+} + 4OH^- \rightarrow Ti(OH)_4 \tag{3.11}$$

$$Ti^{4+} + 2O^{2-} \rightarrow TiO_2 \tag{3.12}$$

The titania layer is formed thanks to a condensation reaction from the hydrated anodic layer:

$$Ti(OH)_4 \rightarrow TiO_2 + 2H_2O \tag{3.13}$$

At the cathodic side, the Hydrogen Evolution Reaction (HER) takes place (see Eq. 3.14), while the entire process can be expressed as in Eq. 3.15:

$$8H^+ + 8e^- \rightarrow 4H_2 \tag{3.14}$$

$$Ti + 2H_2O \rightarrow TiO_2 + 2H_2 \tag{3.15}$$
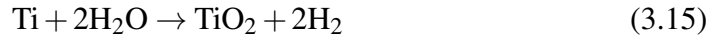
Due to the presence of the fluorine ions, the hydrated and oxide layers are attacked: the mobile F ions react with the Ti^{4+} ions under the application of the external electric field (see Eq. 3.16 and 3.17). This is called field-assisted dissolution and occurs at the interface between the oxide (or hydrated layer) and the electrolyte, creating small pits, as showed in Fig. 3.19a-c.

$$TiO_2 + 6F^- + 4H^- \rightarrow TiF_6^{2-} + 2H_2O \tag{3.16}$$

$$Ti(OH)_4 + 6F^- \rightarrow TiF_6^{2-} + 4HO^- \tag{3.17}$$
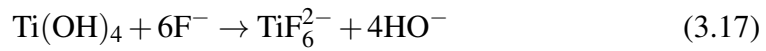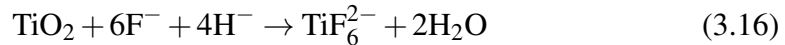
The locally etched pits act as seed for the formation of the pores, that will be converted in a uniform distributed array on the whole surface (Fig. 3.19d). The pores starts to grow at their bottom, moving inward the oxide layer, as showed in Fig. 3.19b-c. The ionic species (F^-, O^{2-}, OH^-) migrate from the electrolyte toward the metal/oxide interface. At the same time, Ti-O bond is weakened, due to the polarization, assisting the dissolution of the cations. Ti^{4+} ions move from the metal
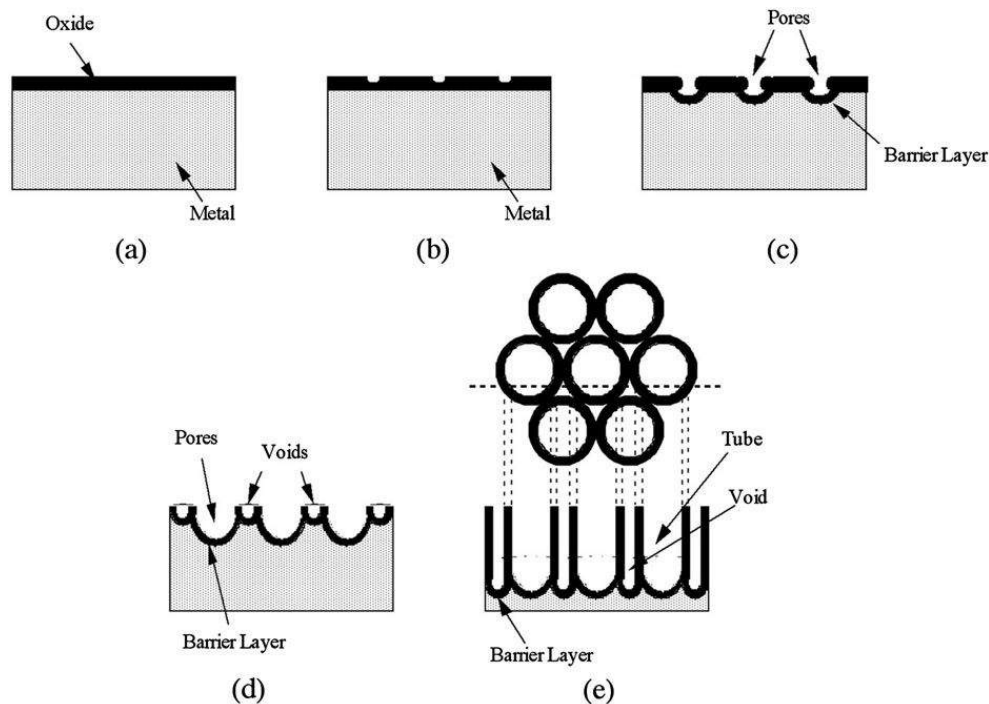
Fig. 3.19 Schematic representation of the TiO$_2$ NTs formation process at constant anodization voltage: (a) oxide layer formation, (b) pit formation on the oxide layer, (c) growth of the pits, (d) metallic part between the pores undergoes oxidation and field-assisted dissolution, (e) fully developed NTs with a corresponding top view. Reproduced from [291] with permission of the PCCP Owners Societies.

toward the oxide/electrolyte interface, reacting with fluorine as showed in Eq. 3.18. The O^{2-} anions migrate toward the metal/oxide interface and further interact with the metal.

$$Ti^{4+} + 6F^- \rightarrow TiF_6^{2-} \tag{3.18}$$

The oxide growth might then be controlled by acquiring the current density–time (j-t) curve. In Fig. 3.21 is shown a typical j–t curve for two different conditions, one that leads to compact oxide (CO) formation, while the other to porous oxide (PO). In the first case, the current decreases rapidly, as the compact TiO$_2$ thickness rises. In the case of PO, the curve of the density of current shows three characteristic stages:

- (I) - The curve follows the fluoride-free case, forming, in the initial stages, a compact oxide;
- (II) - A current increase occurs, leading to the formation of irregular nanoscaled pores onto the TiO$_2$ compact oxide just formed. In this stage, the current increases together with the relative area;
- (III) - The current follows a second drop forming a regular nanotube or nanopore layer.
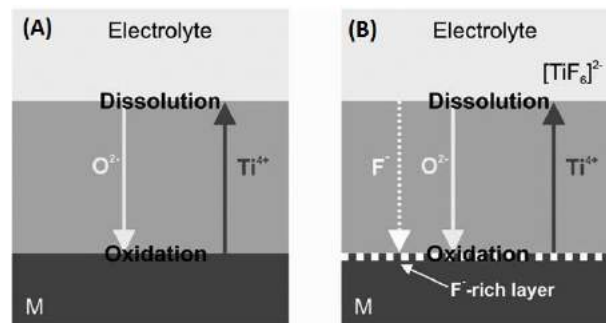
Fig. 3.20 Schematic drawing showing field aided transport of mobile ions through the oxide layers in the absence (A) and presence (B) of fluoride ions. Adapted from [292] with permission of John Wiley & Sons.
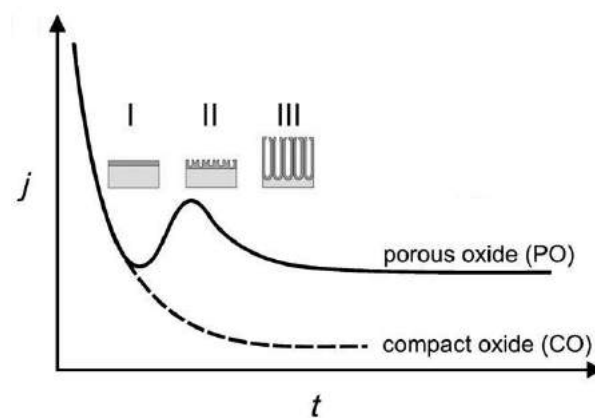
Fig. 3.21 Current density–time (j–t) characteristics after a voltage step in the absence and presence of fluoride ions in the electrolyte. Either compact oxide (fluoride free) or porous/tubular metal oxide formation (containing fluoride) forms by different morphological stages (I–III). Adapted from [292] with permission of John Wiley & Sons.

During the anodization process, the expected expansion factor, during the metal to oxide conversion, is given by calculating the ratio of the oxide volume to the consumed metal volume, called Pilling– Bedworth ratio (PBR) [293]. Theoretical calculations give 2.43 [294] as ratio of titanium oxide, while the observed expansion factor is about 3 [292]. The volume ratio difference can be ascribed to an increase of the length of the tubes caused by a plastic flow. This concept was used to explain the growth of allumina (Al_2O_3) during anodic oxidation [295]. In this case, the flow of the oxide is assumed to be originated from the plasticity of the barrier layer generated by the ionic movement in the high electric field together with the compressive stresses induced by the volume expansion. The result is the extending the tube lengths due to a force that pushes the oxide toward the pore walls. In general, observations on TiO_2 nanotubes volume expansion factors suggest a similar mechanism for their growth.

3.2.2 Cu_xO thermal oxidation

Thermal annealing of copper foils and wire is one of the most fast and convenient ways in order to synthesize CuO nanowires (NWs), when compared to complex chemical methods [280, 296]. Researchers have studied the NWs growth under different conditions of oxygen flow rate, annealing temperature and annealing time [297], but the CuO NWs growth starts to be understood only recently [285].

In the past, vapor–liquid–solid (VLS) catalyst-assisted growth [298] and the vapor–solid (VS) growth [299] were used as theories to describe the growth of this 1D nanostructures. In the VLS process, the NWs growth begins by the vapor condensation of the material at the tip of a droplet. The adoption of this mechanism is based on the 1D structure in which a round droplet is usually found near the tip of the wire. However, no foreign droplets were found in the electron microscope images of the copper oxide nanowires, indicating that VLS mechanism is not applicable here [284]. Considering the VS mechanism, it should be highlighted that CuO is stable up to temperatures of $1100°C$ at atmospheric pressure, vapor pressure of Cu and CuO at temperatures up to $800°C$ is very small and Cu_2O sublimes with vapor pressure of 10^{-4} Torr at $600°C$. Formation of Cu_2O during nanowires growth has been reported [300] and therefore, VS mechanism of growth could occur by evaporation of Cu_2O. However, if Cu_2O evaporation occurs, oxide should be deposited onto the furnace walls, together with a reduction of the Cu foil mass, which were not observed.

Cu_xO nanowires formation

In 2011, Yuan et al. [285] proposed a stress-driven mechanism on NWs formation, in analogy to the Sn whiskers formation [297, 301]. With this model, the growth is caused by the local compressive stress accumulated at the oxides interfaces causing an outward diffusion of Cu cations along CuO grain boundaries, resulting in CuO NWs growth on CuO grains. In order to better understand this mechanism, inFig. 3.22 is presented an example of CuO NWs trough an SEM cross-section image. A structure, composed by three-layers, can be clearly identified in Fig. 3.22A: a 3 μm-thick bottom layer, directly above the Cu substrate, an intermediate thin layer with a thickness of about 600 nm, and a top oxide NW layer. Researchers identified the different layers as Cu_2O as bottom layer and CuO as the intermediate and top layers. Fig. 3.22b is a magnified view from the 3-layered structure, revealing that CuO NWs appear to grow directly on the intermediate layer grains.

During the initial stages of copper oxidation, the metal oxide may grow in all directions, forming two thermodinamically stable oxides: Cu_2O and CuO as bottom and top layers, respectively. In order further oxidize copper, O_2 is chemisorbed onto the CuO surface, attracting electrons from a Cu lattice. This process generates an electron-hole pair in order to maintain the net charge equal to zero. As a second step, the chemisorbed oxygen is fully ionized, producing another hole and a Cu^{2+} ion that enters into the surface to interact with the O_2, forming another hole and a vacancy in the cation sub-lattice. It can be deduced that, Cu ions and electron-hole pairs are generated at the CuO/O_2 interface, where new CuO molecules are
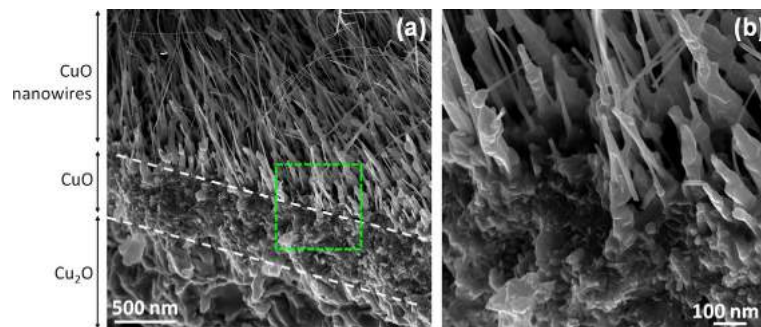
Fig. 3.22 SEM cross-section image of the tree-layered structure of an oxidized Cu substrate, showing: (a) the Cu_2O and CuO layers and the growth of CuO NWs on the CuO layer; (b) magnification of NW root region marked by the dashed square. Reprinted from [285] with permission from Elsevier.

formed by consuming the oxygen [302]. Then, the produced cation vacancies and holes migrate through the 2 oxide layers, until they reach the Cu/Cu_2O interface and they are annihilated. In a similar way, the Cu_2O is formed at the Cu_2O/CuO interface, creating new cation vacancies and holes, that will migrate toward the Cu/Cu_2O interface to be annihilated. Studies [285] demonstrated that the thickness of the copper oxide layer grows following a parabolic law, suggesting also that the oxidation is diffusion-controlled.
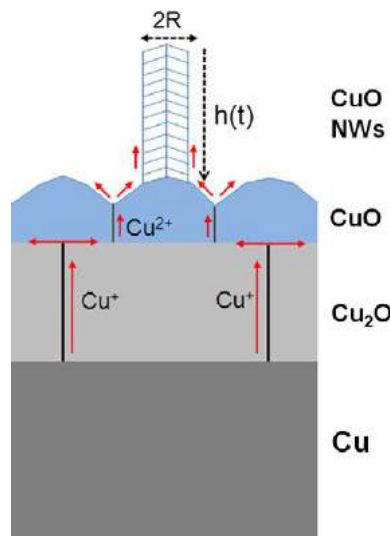
Fig. 3.23 Schematic representation of CuO NWs growth. Reprinted from [285] with permission from Elsevier.

Since the 2 copper oxides have different primitive cell volumes (77.83 $\mathring{A}^3$ and 81.16 $\mathring{A}^3$ for Cu_2O and CuO, respectively), they both grow by cations outward diffusion and, at the same time, generate stresses at their interface. This acts as driving force for the outward diffusion of Cu atoms together with the Cu^{2+} diffusion

due to the chemical potential gradient, also induced by the stress. The volume shrinkage, related to the conversion of CuO into Cu_2O, leads to the accumulation of compressive stresses at this interface region that can be attributed to the NWs formation driving force, requiring effective relaxation of the compressive stresses via CuO grain boundary diffusion. In Fig. 3.23 is presented an image that summarizes the Cu^{2+} ion diffusion during the oxidation process, while the oxygen diffuses in the opposite direction [303].

In general, the routes for particle diffusion can be a grain boundary, a defective region or the lattice itself. At temperatures below 500°C, the grain boundary diffusion is the prevailing route for the diffusion of the copper ions. Between 600° and 800°C both lattice diffusion and grain boundary diffusion are important, and at temperatures above 800°C lattice diffusion is the main transport mechanism for the particles [301].

For the intermediate range of the oxidation temperature (400–600°C), under which oxide NWs growth occurs, the atoms flux occurs mainly along CuO grain boundaries toward the CuO layer outer surface, which is stress-free. Via surface diffusion, the Cu cations reach the top of the CuO grains to be then incorporated in the NWs by reacting with vapor oxygen. As long as the compressive stress at the Cu_2O/CuO layer is kept, the outward diffusion flux goes on and acts as a continual source for NWs growth.
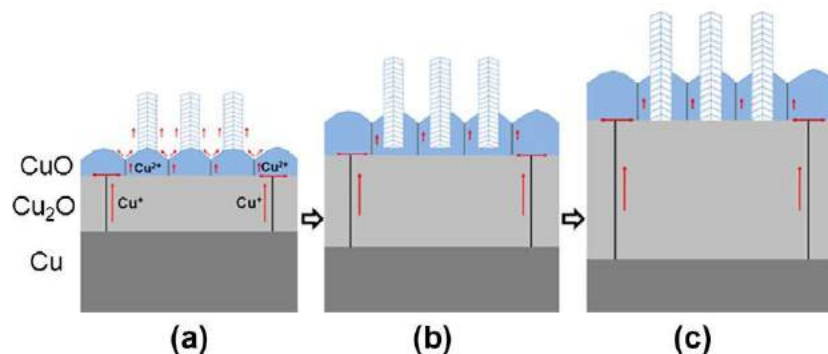
Fig. 3.24 Scheme of the CuO NWs grow: (a) Initial growth on the CuO grains outer surface; (b) initial burying the NWs root; (c) direct contact between the NWs roots and the Cu_2O layer. Adapted from [285] with permission from Elsevier.

It has to be highlighted that, during the NWs formation, the two underneath layers continue to grow in thickness, as depicted in Fig. 3.24. This may lead to a burying of the CuO NWs for prolonged oxidations and/or higher oxidation temperatures, Fig. 3.24a and b. Moreover, the nanowires may get in contact with the Cu_2O layer due to a complete consuming of the above CuO layer [285], Fig. 3.24c. Furthermore, many studies demonstrated than the CuO NWs formation occurs within a temperature range from 250°C to 700°C [284, 303–305]. In fact, the grain boundary diffusion must be possible and more efficient than the lattice diffusion. Thus, for oxidation at low temperature (<250°C), the grain boundary diffusion is not effective, while, for higher temperatures (>700°C) lattice diffusion becomes more favorable than grain boundary diffusion, leading to uniform growth of CuO grains.

3.3 Characterization and deposition techniques

I was in charge of the following characterization techniques, while the ones present in appendix (App. A) were done from colleagues that I gratefully thank.

3.3.1 Rheometer

The measurement were performed in order to evaluate the viscosity of the electro-spinning solutions by means of a rheometric analyses (MCR Rheometer series Anton Paar). This kind of rheometer controls the applied shear rate and measuring the resulting viscosity of the sample. The liquid sample is placed between two horizontal plates, where typically the upper plate is rotated and the torque on the cone measured. The known response of the torsion bar and the degree of twist give the shear stress, while the rotational speed and cone dimensions give the applied shear rate. The measure temperature was set at 25°C, while the shear rate was varied between 0.1 s^{-1} and 1000 s^{-1} for all the measures.

3.3.2 ThermoGravimetric Analysis - TGA

The decomposition behaviors of PEO and PEO/manganese acetate solutions were performed by means of ThermoGravimetric Analysis (TGA) using a TG209 F1 Libra from Netzsch.

In general, TGA analysis is used as a method of thermal analysis in which the sample mass is measured over time as the temperature changes. This measurement could provide information about physical phenomena, such as phase transitions, absorption, desorption, chemisorptions, thermal decomposition and solid-gas reactions. A typical thermogravimetric analyzer consists of a furnace with a programmable control temperature, over which a precision balance is located. The temperature is increased at constant rate to observe a targeted thermal reaction. The thermal reaction may occur under a variety of atmospheres including: ambient air, vacuum and inert gas (e.g. nitrogen). The data collected from the occurred thermal reaction are plotted as mass or percentage of initial mass as a function of temperature or time.

I performed all the tests between 25°C and 800°C under air flux, at a constant scan rate of 10°C/min in order to study the oxidation phenomena of the manganese oxide precursor. As described in Sec. 4.2.3, all the analyzed samples are studied after the water removal and placing them in an allumina crucible.

3.3.3 Field Emission Scanning Electron Microscopy - FESEM

The samples morphology was analyzed by means of Field Emission Scanning Electron Microscopy (FESEM, ZEISS, Auriga and Supra 40). All the FESEM images were collected with a dedicated secondary electron detector placed inside the

column, called in-lens detector, at 5 kV and using a beam current of about 330 pA (aperture size 30 μm), unless otherwise indicated in the caption of the image.

In the case of uncalcined samples of PEO/manganese acetate in Chap. 4, a Pt coating of about 10 nm was needed. This was performed with a metal sputter coater, as described in the following section (Sec. 3.3.4). TFor all the other samples (manganese oxide, titanium oxide or copper oxide), since their conductivity was sufficient to perform the FESEM characterizations, no metallic coating was used, in order to preserve their original morphology.

The Energy Dispersive X-Ray (EDX) spectra and maps were collected thanks to an Oxford Energy Dispersive X-ray detector equipped onto the FESEM. In case of titanium-based samples, the voltage applied was 10 kV and aperture size was 30 μm, in order to detect Ti K$_\alpha$ line. On the other side, in case of copper-based samples, the voltage applied was risen to 17 kV and aperture size was 30 μm, in order to detect Cu K$_\alpha$ line. Also in this case no kind of metallic coating was used onto the analyzed samples. For this reason, low number of iterations were used during the EDX maps acquisition (5 at maximum) in order to limit the samples drifting due to superficial charge accumulation.

3.3.4   Sputter coater

Metals were deposited by means of a sputter coater (Quorum Technologies, Q150T ES), with an ultimate vacuum of about $1 \cdot 10^{-4}$ mbar. Sputter deposition is a kind of physical vapor deposition (PVD) method of thin film deposition by sputtering.

For FESEM imaging sessions, platinum was deposited by means of a deposition current of 30 mA for 30 s. Metallic copper was deposited with a deposition current set at 30 mA and deposition time of 128 s.

Chapter 4

ORR catalysts Mn$_x$O$_y$ NFs

Chapter abstract *In Chapter 4 are analyzed the manganese oxide nanofibers as ORR catalyst. In Sec. 4.1 are listed the materials used in this chapter, while in Sec. 4.2 are presented the initial study on the electrospinning solution and deposition conditions. The thermal and morphological characterization are described in Sec. 4.3, by proposing a possible thermal evolution of the NFs. The final test in device of manganese oxide NFs, as catalyst at the cathode, is proposed in Sec. 4.4. In the end of the chapter, in Sec. 4.5, a preliminary study on a different type of nanostructure, the nanodrop, is described together with a test in device. Part of the work described in this chapter, in Sec. 4.2 and 4.3, is also published by the author in the papers [306] and [307].*

4.1   Materials

Manganese (II) acetate tetrahydrate (Mn(CH$_3$COO)$_2$·4H$_2$O), polyethylene oxide (PEO, M$_w$= 600 kDa and 1000 kDa), ethanol, 2-propanol, Nafion solution (5 wt% in water and aliphatic alcohols), potassium hydroxide, carbon cement and Pt/C paste were purchased from Sigma-Aldrich and processed without any further purification. Silicon wafers (p type <100>, 1-30 Ωcm) were supplied by MEMC. De-ionized water (Di-water) was used as solvent. Commercial carbon paper (CP) was purchased by Fuel Cell Earth LLC (USA), while titanium wires from Goodfellow (Cambridge Limited). The catalyst layer, based on a mixture of platinum (Pt 0.5 mg/cm^2), was purchased from Sigma Aldrich.

4.2 Mn_xO_y nanofibers synthesis

4.2.1 Solution

The starting polymer, PEO, was selected both because it is biocompatible and biodegradable and generally, because it is more environmental friendly than other common templating agents used to produce nanofibers. Indeed, it needs only water as solvent, differently from what is used for a widespread list of polymers, such as polyvinyl pirrolidone (PVP) [308, 309] and polyacrylonitrile (PAN) [310, 311].

As stated in Cap. 3.1.5, the fluid's viscosity influences strongly the behavior of a polymeric solution pushed inside a tube. In order to ensure the formation of the mat of nanofibers starting from an electrospun polymeric solution, the viscosity of the solution must be kept into the following range [205, 212, 228]:

$$(0.02 \leq \eta \leq 300) \, Pa \cdot s \qquad (4.1)$$

In particular, at low viscosity values ($\eta \leq 0.1 Pa \cdot s$), the surface tension overcomes the viscoelastic forces and consequently the polymeric jet is broken up into droplets with different diameters and in different concentrations (electrospray) [205, 212].

Given these constrain, a careful screening of the PEO solution experimental parameters has been done. In Fig. 4.1 is showed the viscosity for different water-based solutions of PEO as a function of: concentration, molecular weight and presence of the ceramic precursor (manganese acetate). It is easy to notice that by increasing the molecular weight, the viscosity rises of almost one order of magnitude (for more characterization details see Sec. 3.3.1). In fact, considering the 3wt% concentration, for PEO of M_w= 600 kDa, η is 0.5 Pa·s, while is 1.7 Pa·s in the case of PEO of M_w= 1000 kDa. It has to be highlighted that, for the first solution, the viscosity value is quite close to the electrospraying regime, therefore a stable nanofibers formation during the electrospinning process is quite difficult with the appearance of droplets on the mat. At higher polymer concentrations (5wt%), η rises from 6.8 Pa·s to 44.9 Pa·s by increasing M_w. Considering the highest viscosity obtained, the solution gave rise to nanofiber of not uniform diameter and branching phenomena, as showed in Fig. 3.15C.

On the other side, by increasing the polymer concentration, the viscosity rises of more than one order of magnitude. Considering the PEO with lower M_w, η rises from 0.5 Pa·s to 6.8 Pa·s, giving the possibility of having a more stable solution during the electrospinning process, as showed in Fig. 3.16A-C, with no presence of beads, branching or drops. For these reasons, the 5wt% PEO (M_w=600 kDa) was selected as the optimal PEO solution, to obtain, after the addition of the manganese acetate, the desired ceramic nanofibers. It has to be noticed that the addition of the salt slightly lowered the initial viscosity from 6.8 Pa·s up to 1.96 Pa·s, nevertheless maintaining the possibility of having a stable electrospinning process.
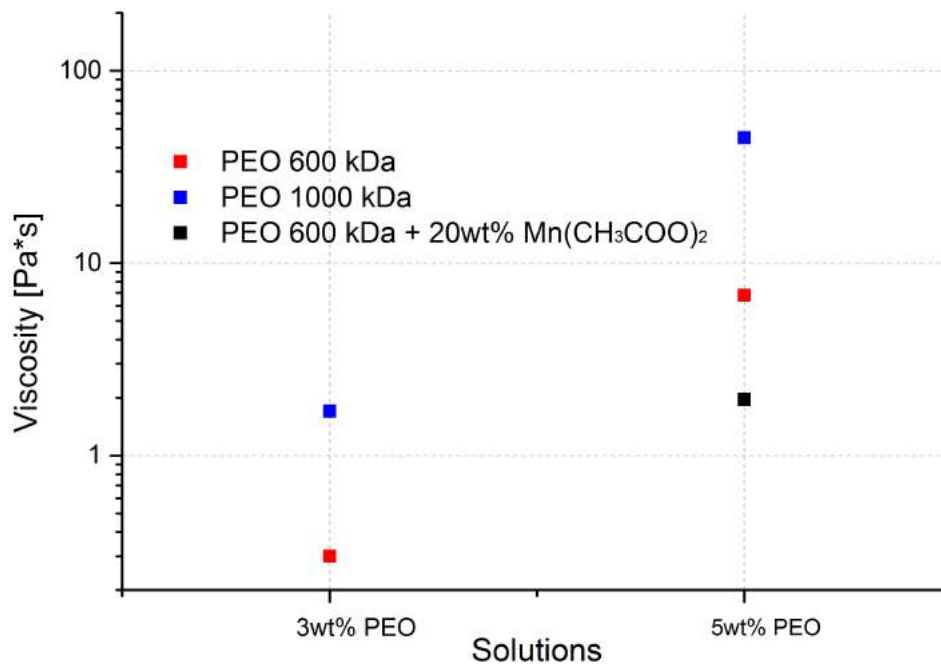
Fig. 4.1 Comparison of the viscosities of the PEO-based solutions for two different polymer concentrations.

4.2.2   Deposition by electrospinning

The solution used to obtain the manganese oxide nanofibers was firstly made with a 9 ml of aqueous PEO solution (5 wt%) made by mixing PEO powder and Di-water [306, 307]. Afterwards, 3 ml of 20 wt% aqueous manganese acetate solution were added to the polymeric solution and stirred for 24 h, at room temperature. The PEO/manganese acetate solution (named "5%PEO+MnAc"), thus prepared, was loaded in a 6 ml syringe, connected to a stainless steel needle (18 Gauge × 15 mm) and mounted into the electrospinning apparatus. During electrospinning, a voltage of about 14.5 kV was applied between the needle and the planar collector plate, covered with a substrate and placed at a distance of 10 cm. Monocrystalline silicon wafer was selected as substrates, in order to easily perform structural, compositional and morphological analyses on the mats.

4.2.3   Thermal analysis

Thermo-Gravimetric Analysis (TGA) was performed on 5 wt% PEO water-based solution, analyzed after the initial complete removal of the water content by means of a vacuum pump (name of the sample: "5%PEO-dried"), on manganese acetate salt, analyzed without any further treatment (name of the sample: "MnAc"), and on 5wt%PEO+manganese acetate solution, analyzed after its drying (name of the

sample: "5%PEO+MnAc-dried"), in order to study their thermal behavior [307]. For more instrument details see Sec. 3.3.2.
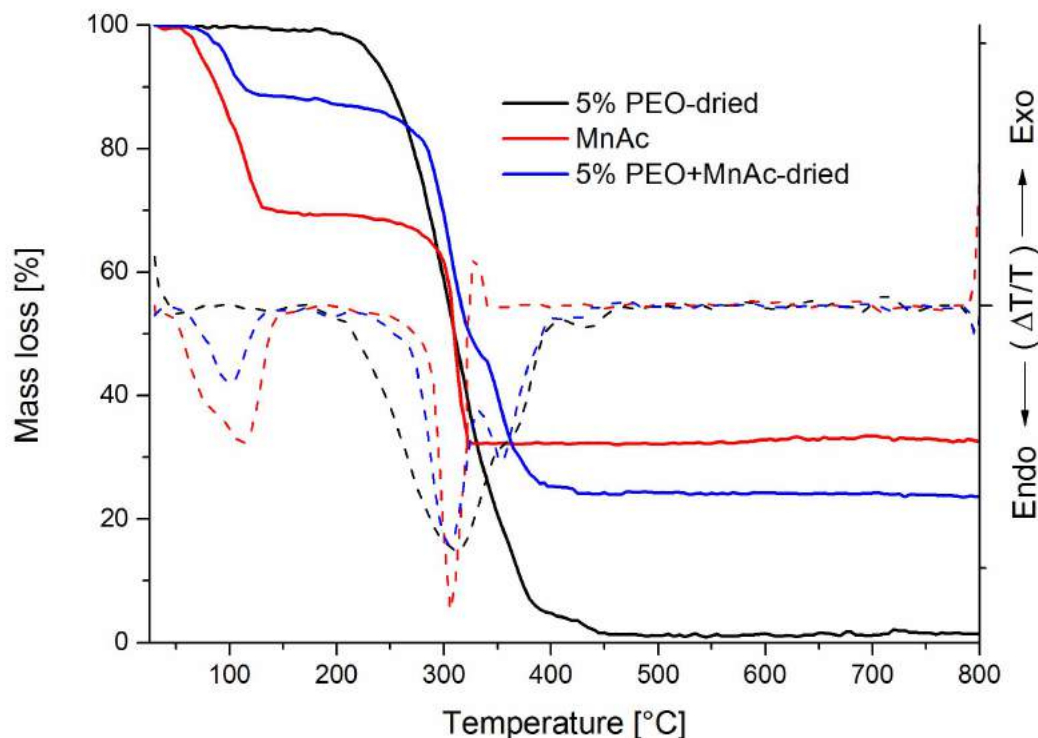
Fig. 4.2 TGA curves for the different samples are reported as straight curves (left axis): dried solution of 5% PEO 600kDa (black curve), manganese acetate salt (red curve) and dried solution of PEO/manganese acetate (blue curve). First derivatives of the TGA curves are reported as dashed curves (right axis) with the same color code. Reprinted from [307].

In Fig. 4.2 the results of the TG analysis of 5%PEO-dried, MnAc and 5%PEO+MnAc-dried are reported. In order to put in evidence the key temperatures for each material and component, the derivatives of the TGA curves are calculated and reported as dotted lines in Fig.4.2. The 5%PEO-dried black curves in Fig. 4.2 clearly show the almost complete degradation of the polymer within 450°C. The red curves show the thermal evolution of the MnAc, highlighting different decomposition steps. The first occurs at around 100°C, and corresponds to a weight loss of 30%, in which the acetate salt completely loses the coordinated water molecules. A second step occurs at around 300°C, corresponding to the transformation of manganese acetate into manganese oxyacetate (MnOCH$_3$COO) and/or manganese hydroxyacetate (Mn(OH)CH$_3$COO), as suggested in the literature [312, 313]. A final exothermic process follows at around 320°C: starting from 350°C, all the acetate component is completely degraded and the manganese oxyacectate or hydroacetate is entirely transformed into manganese oxide [313], leaving a black/brown residue in the TGA alumina crucible.

The thermal evolution of the 5%PEO+MnAc-dried, represented by the blue curves in Fig. 4.2, appears similar to the MnAc one (red curve). In fact, the corresponding degradation steps take place almost at the same temperatures range. As already said, at around 100°C, the acetate component loses the coordinated water molecules. The second step occurs between 250°C and 400°C and corresponds to the mixed thermal decomposition of PEO and manganese acetate. As showed in the blue curve, starting from 400°C, all the PEO component is completely degraded, leaving the manganese oxide only, with black/brown residue in the TGA alumina crucible.

On the basis of the thermogravimetric analyses the so prepared nanofibred samples were calcined by means of a vertical furnace (Carbolite, VST 12/300/3216) for 3 h in air, with a heating rate of 2.5°C/min to ensure the complete decomposition of the PEO and the manganese acetate oxidation. The final calcination temperature were selected to be 475°C, 600°C and 725°C, in order to study the morphology and composition of different obtained Mn$_x$O$_y$ ceramic nanofibers.

4.3 Mn$_x$O$_y$ NFs characterizations

4.3.1 Compositional characterization

In order to investigate the crystallization process and composition of the as-electrospun 5%PEO+MnAc nanofibers as a function of the temperature [307], in-situ X-ray diffraction was carried out in a reaction chamber (for more details refer to App. A.2). This study is of particular relevance, because it defines a correlation between the morphological and electrochemical behavior of the calcined nanofibers, with the specific manganese oxide crystalline phase. Fig. 4.3 shows the XRD spectra acquired during the calcination in air, and collected starting from ambient temperature up to 725°C, at steps of 50°C. The selection of the calcination temperatures was done on the basis of the TGA characterization.

As a first comment, the spectrum at 25°C shows two main peaks at 19.20° and 23.41°, related to the initial PEO component [314], that disappear in the curve collected at 75°C, being the PEO melting point at 65°C.

Starting from 125°C it can be clearly noticed the appearance of four main peaks, at about 36.1°, 32.2°, 59.7° and 28.8° (in order of decreasing intensity), corresponding to the (211), (103), (224) and (112) planes of Mn$_3$O$_4$ (Hausmannite, JCPDS 00-024-0734), respectively. The broadness of these peaks witnesses the very small crystal size. By increasing the temperature, such peaks become sharper and more defined, giving evidence of a crystal size increase. The Mn$_3$O$_4$ phase remains almost the single present crystalline phase up to 525°C.

Between 575°C and 625°C, the formation of a second phase starts to appear to the detriment of Mn$_3$O$_4$, that progressively disappears as the temperature arises. This second phase is identified as Mn$_2$O$_3$, as shown by the presence of five main peaks at 32.7°, 55.1°, 23.2°, 38.1°, and 65.5° (in order of decreasing intensity)
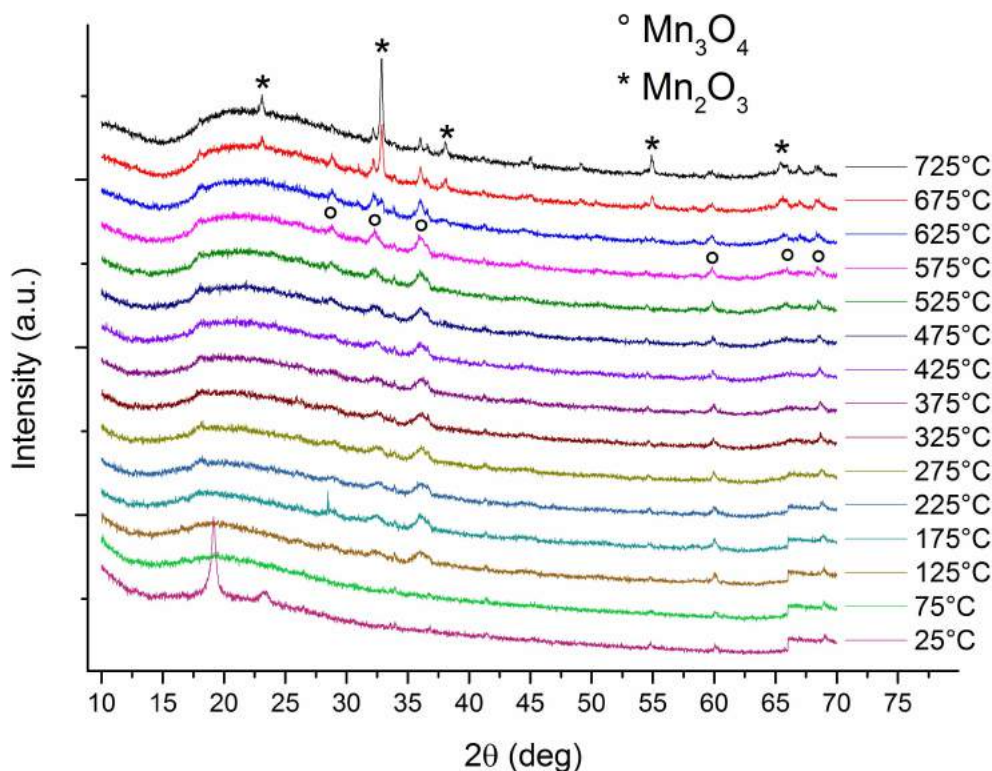
Fig. 4.3 In-situ XRD spectra collected with the reactor chamber from 25°C to 725°C, at steps of 50°C. Reprinted from [307].

corresponding to the (222), (440), (211), (400) and (622) planes of Mn$_2$O$_3$ (Bixbyite, JCPDS 00-041-1442), respectively. The Mn$_2$O$_3$ phase is characterized by very sharp peaks, putting evidence of the formation of bigger crystals, as better discussed in the next paragraph.

4.3.2   Morphological characterization

Morphological characterizations were performed on the electrospun nanofibers before the calcination step, in order to verify the quality of the obtained mat [306, 307]. FESEM images of the as-electrospun nanofibers at two different magnifications are reported in Fig. 4.4A and B (for more instrument details see Sec. 3.3.3). They show fibers with a smooth surface and with diameters ranging from 120 to 200 nm.

Both Scanning and Transmission Electron microscopies were carried out on three samples calcined in air in a tubular oven at the three selected temperatures: 475°C, 600°C and 725°C. Based on the TGA and on the in-situ XRD spectra, it turns out that at 475°C there is the formation of pure Mn$_3$O$_4$, at 600°C 600°C there is the co-presence of Mn$_3$O$_4$ and Mn$_2$O$_3$, while at 725°C the sample is nearly nearly pure Mn$_2$O$_3$.
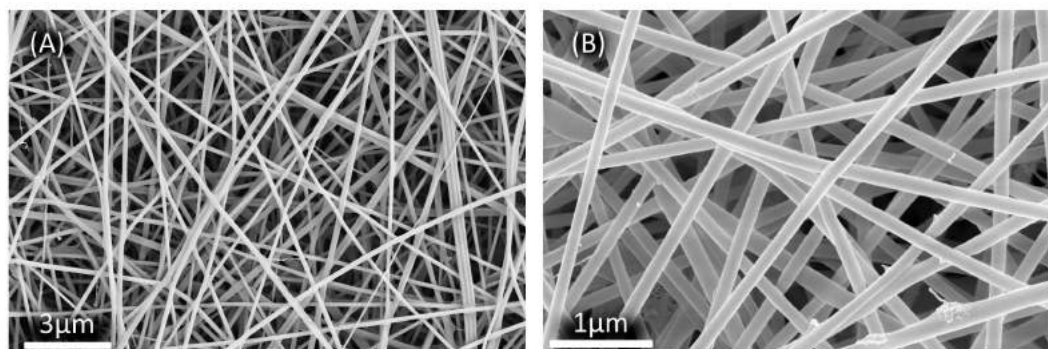
Fig. 4.4 FESEM images of the nanofibers after the electrospinning step at two different magnifications. Reprinted from [306] with permission of Elsevier.

In Fig. 4.5 the FESEM images of the calcined nanofibers at different magnifications are presented. Fig. 4.5A and D show the nanofibers calcined at 475°C, Fig. 4.5B and E show the nanofibers calcined at 600°C, while and Fig. 4.5C and F show the nanofibers calcined at 725°C.

As a general comment, it turns out that the calcination temperature strongly influences not only the nanocrystals shape and size, as already discussed for the in-situ XRD characterization, but also the fiber shape. In fact, by looking at Fig. 4.5, it appears clear that the nanofibers are able to retain a 1D shape in a quite large range of temperatures (from ambient temperature up to 525°C). Nevertheless, when Mn$_2$O$_3$ starts to nucleate, above 575°C, the crystals are bigger than those of the initial nucleation of Mn$_3$O$_4$. When the final calcination temperature is reached, the Mn$_2$O$_3$ crystals are so big that the nanostructuration into fibers is not anymore retained, leaving a nanostructured film of manganese oxide. These findings are in line with what observed in the in-situ XRD spectra.

In Fig. 4.6, the TEM images and the electron diffraction patterns of the nanofibers calcined at the three different temperatures are presented. Fig. 4.6A and D, Fig. 4.6B and E and Fig. 4.6C and F show the nanofibers treated at 475°C, 600°C and 725°C, respectively. The insets of Fig. 4.6A-C are the electron diffraction pattern, collected at the same conditions for the three samples. The insets of Fig. 4.6D-F represent the Fast Fourier Transform (FFT) of the squared white regions in the same figures (for more details refer to App. A.1).

At 475°C (Fig. 4.5D, 4.6A and D), the manganese oxide nanofibers are constituted by very small crystals (in the range of 5-10 nm) of pure Mn$_3$O$_4$. The rings in the electron diffraction pattern in the inset of Fig. 4.6A show a randomly oriented pattern of many small crystals. At 600°C (Fig. 4.5E, 4.6B and E), the nanofibers are slightly discontinuous and are characterized by bigger crystals (in the range of 10-20 nm). The electron diffraction pattern still evidences the presence of rings, but in this case there are some intense spots that indicate the co-presence of small and big crystals, in agreement with in-situ XRD. When the calcination temperature reaches 725°C (Fig. 4.5F), the shape of the nanofibers is no more retained, and they are mostly composed by Mn$_2$O$_3$, with big crystals (in the range of 40-200 nm)
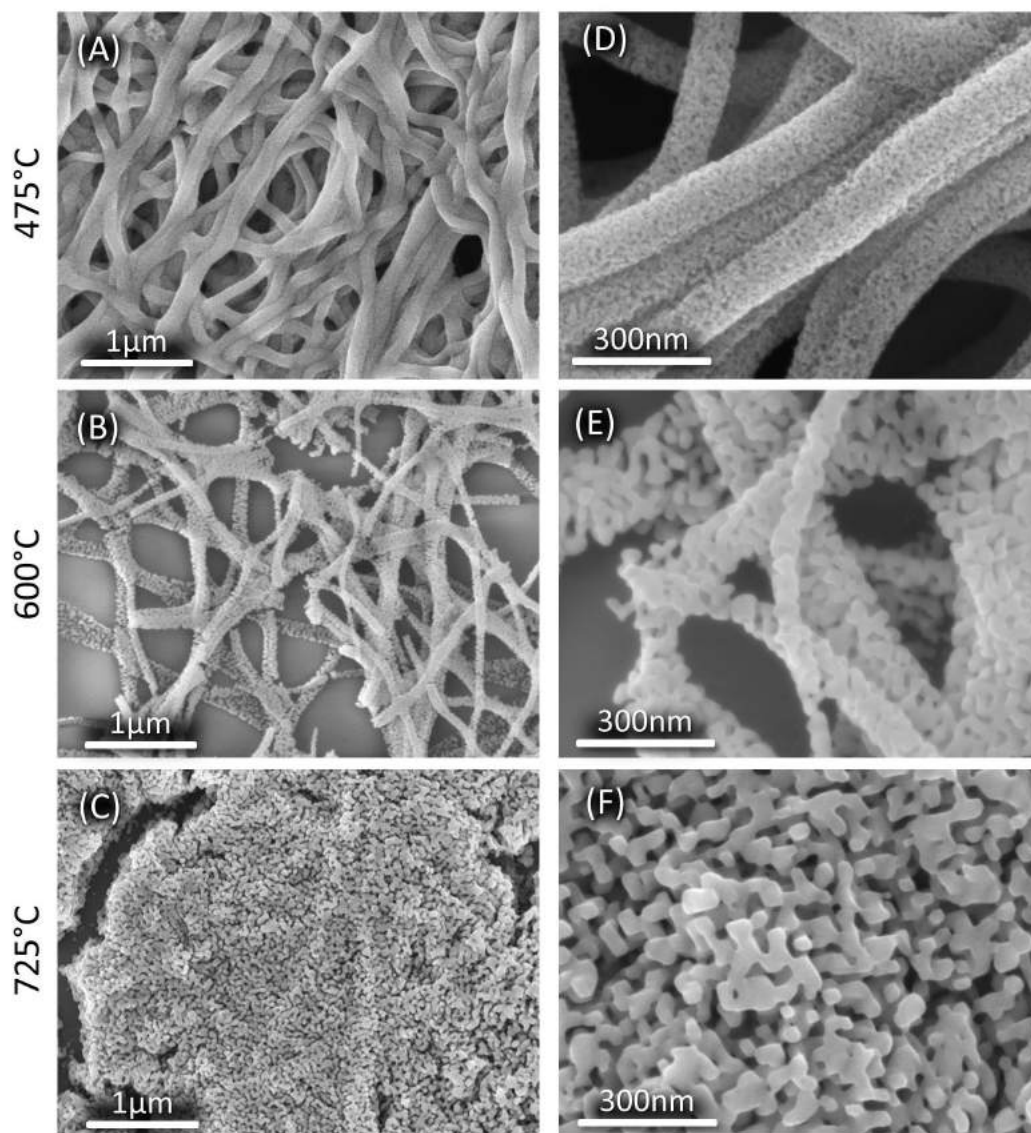
Fig. 4.5 FESEM images of the calcined nanofibers at different magnifications. The manganese oxide nanofibers are calcined at different final temperatures: (A) and (D) at 475°C, (B) and (E) at 600°C, (C) and (F) at 725°C. Adapted from [307].

in a dendritic arrangement (see Fig. 4.5F). In Fig.4.6C it is reported, for sake of comparison, a small part of the fibers in which, beside the main big Mn_2O_3 crystals, there are also smaller Mn_3O_4 crystals. The high-magnification of one of the big crystals (Fig. 4.6F) show that they are monocrystalline, in agreement with XRD.
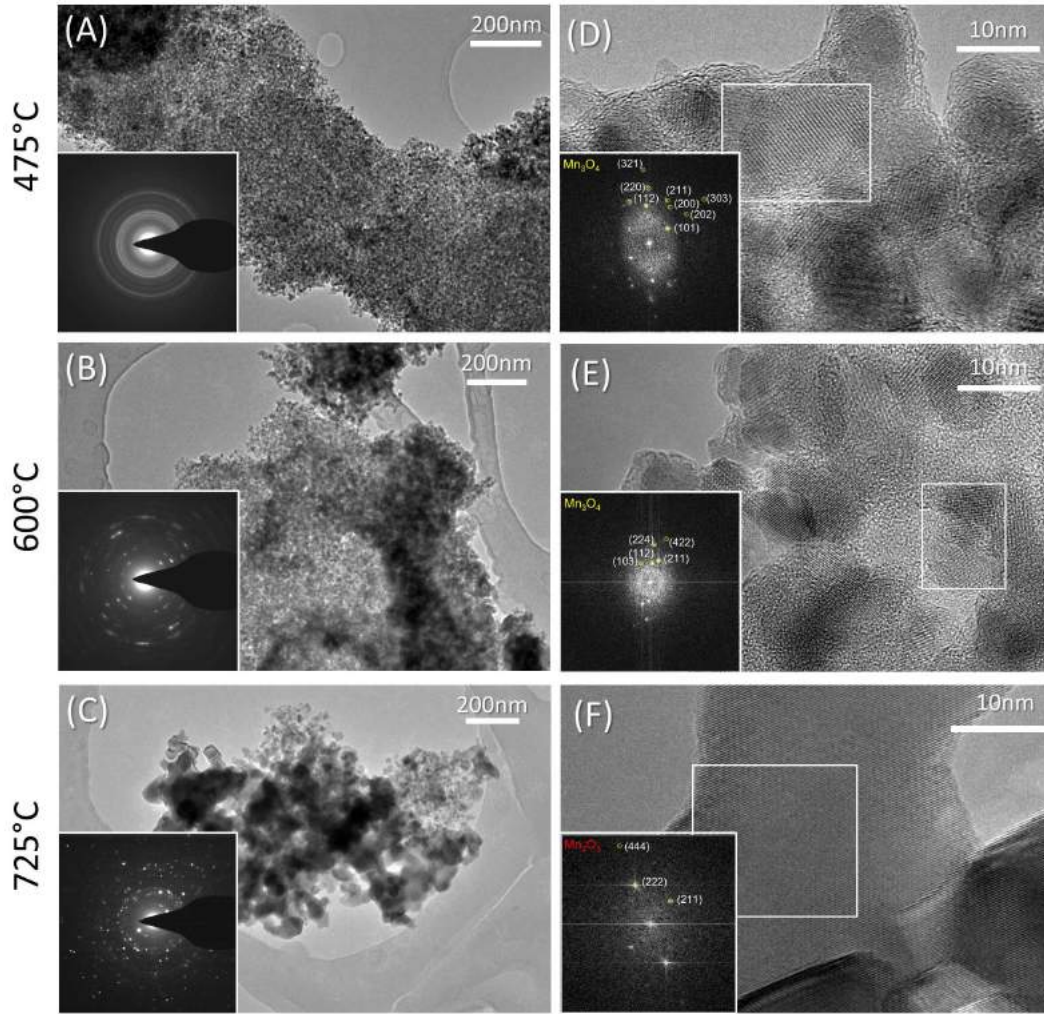
Fig. 4.6 TEM images of the manganese oxide nanofibers calcined at different final temperatures: (A) and (D) at 475 °C, (B) and (E) at 600°C, (C) and (F) at 725°C. In the first column (panels A, B, C), low magnification images and electron diffraction patterns put in evidence the change in the crystalline phase and morphology, as the calcination temperature increases. In the second column (panels D, E, F), higher magnifications and FFT of small regions, are reported. Adapted from [307].

4.3.3   Crystal formation and evolution

Based on the experimental observations, a possible mechanism for the formation of the Mn$_3$O$_4$ nanocrystals and their evolution into Mn$_2$O$_3$ can be derived [308, 307], as depicted in Fig. 4.7. At 75°C the 5%PEO+MnAc nanofibers are completely amorphous (step A in Fig. 4.7) as demonstrated by the XRD spectrum in Fig. 4.3. When the temperature is increased, Mn$_3$O$_4$ nanocrystals start to nucleate in the amorphous PEO polymeric matrix. At 125°C, the PEO acts as a support during the initial two steps (step B in Fig. 4.7), keeping isolated the growing nanocrystals.

After the complete degradation of the PEO, at 475°C, the nanofibers are constituted by Mn$_3$O$_4$ nanocrystals only, which are enough interconnected and sufficiently large to retain the 1D shape (step C in Fig. 4.7).

By further increasing the calcination temperature, Mn$_2$O$_3$ starts to nucleate between 575°C and 625°C following the reaction [315]:

$$4Mn_3O_4 + O_2 \rightarrow 6Mn_2O_3 \qquad (4.2)$$
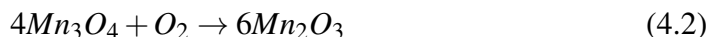
Based on the previous reaction, Mn$_3$O$_4$ is thermodynamically favored to be transformed into Mn$_2$O$_3$ in the presence of oxygen or air [315], as in this case. In fact, during the coordination with oxygen, Mn$_3$O$_4$ crystals coalesce, resulting in the formation of the Mn$_2$O$_3$, characterized by bigger crystals (stage D in Fig. 4.7).
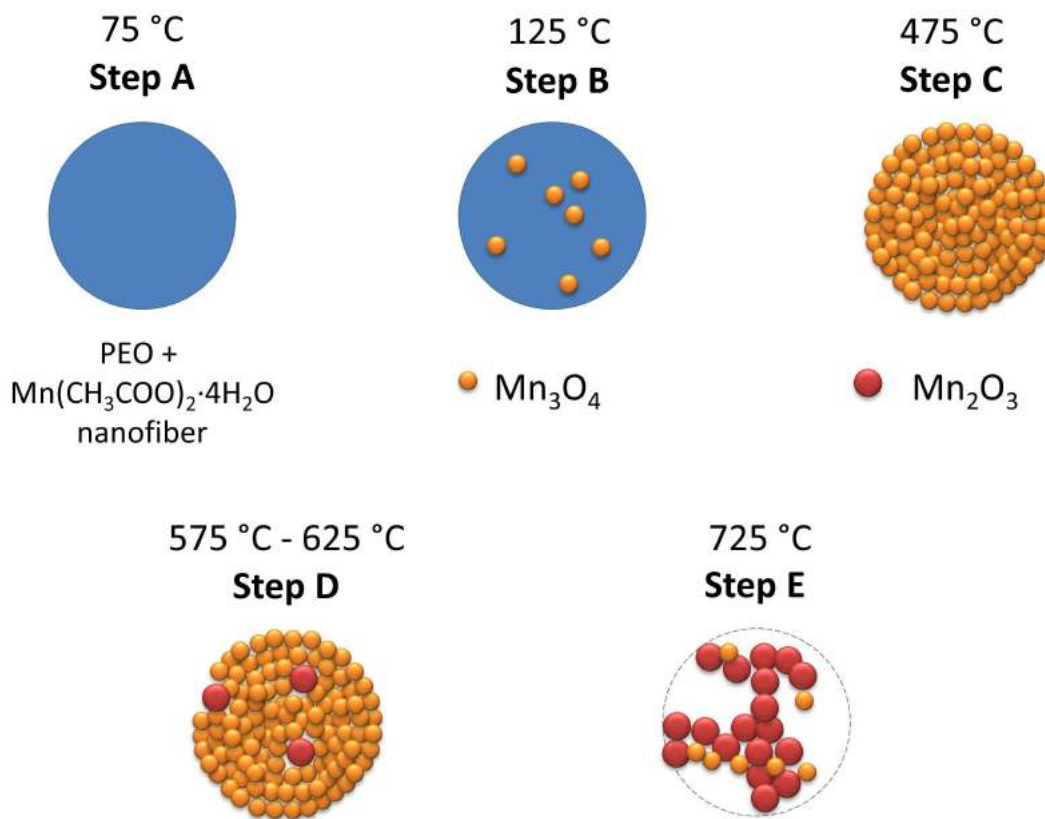
Fig. 4.7 Possible mechanism for the formation of the Mn$_3$O$_4$ nanocrystals inside the nanofibers and their evolution into Mn$_2$O$_3$. Adapted from [307].

Further increasing the temperature up to 725°C (stage E in Fig. 4.7), Mn$_3$O$_4$ continues to be converted. Moreover, Mn$_2$O$_3$ grows in crystal size, assuming a dendritic conformation and destroying the initial nanofibred shape, with only a residual small amount of the Mn$_3$O$_4$ in the sample. It is reasonable to suppose that,

with a further increase of temperature, all the Mn$_3$O$_4$ crystals would be completely converted in Mn$_2$O$_3$.

4.3.4 Electrochemical characterization

The catalytic performance of the different samples was evaluated through RRDE technique [307], whose results are reported in Fig. 4.8 (for more characterization details refer to App. A.4). As clearly evident, nanofibers calcined at 600°C, i.e. composed by a mixed phase composition, show reduced activity with respect to samples exhibiting pure phases. In fact, a valuable dependency on the potential can be observable for both electron transfer number and peroxide percentage curves, with values in the range (3.26 ÷ 3.46) and (27 ÷ 37)%, respectively. On the contrary, quite constant values were obtained for samples treated at 475°C (about 3.66 and 17 %) and at 725°C (about 3.69 and 16 %).
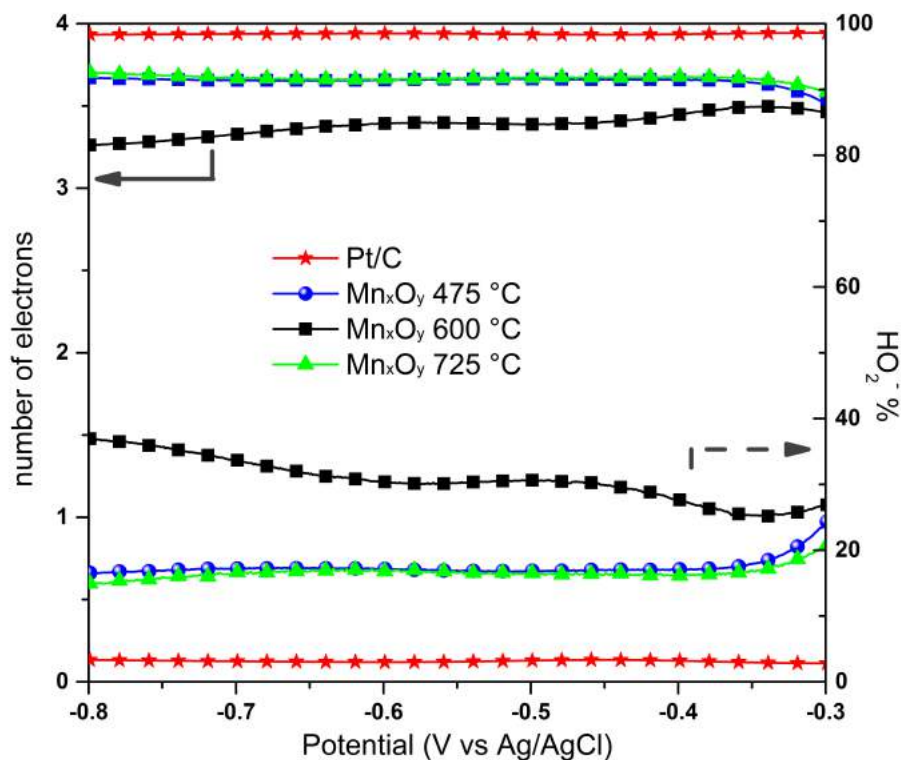
Fig. 4.8 Comparison of electron transfer number (left axis) and peroxide percentage (right axis) evaluated from RRDE measurements of the different manganese oxide-based samples and of the reference Pt/C catalyst. Adapted from [307].

Based on these results, it can be asserted that electrospun nanofibers show performances in line or even better with respect to Mn-based [316] or other cost-effective ORR catalysts recently proposed in the literature [317–319]. The nanofibers show indeed comparable performance with respect to expensive Pt-based materials,

as demonstrated in Fig. 4.8. In addition, it is worth nothing that, despite different phase compositions and morphologies, the catalytic activity of the samples calcined at 475°C and 725°C is rather similar. In order to cast light on this aspect, EIS analysis was carried out; Nyquist plots related to the three samples under investigation are reported in Fig.4.9.
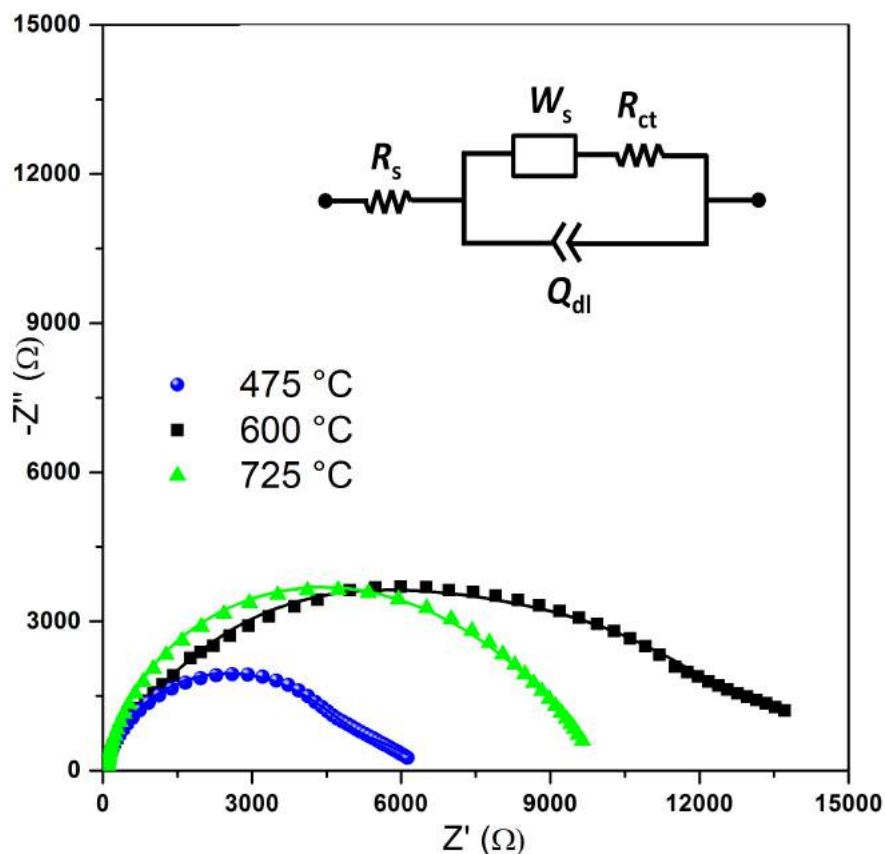
Fig. 4.9 Nyquist plot of the impedance of the different samples. The points are experimental data while the continuous lines are the curves obtained from a fitting procedure using the equivalent circuit shown in the inset. Reprinted from [307].

All the three spectra exhibit a high-frequency arc which is related to the charge transfer at the electrode/electrolyte interface, and a low-frequency side arc related to the diffusion of species; the displacement between the origin of axis and the beginning of high-frequency arc accounts for the electrolyte resistance [320]. Apart from mixed-phase nanofibers, characterized by largest impedance values, pure Mn$_3$O$_4$ sample exhibit reduced resistance with respect to Mn$_2$O$_3$ one; however, the latter is characterized by lower capacitive behavior, as manifest from the higher Z" values, roughly proportional to the inverse of capacitance [321]. In order to quantitatively evaluate resistances and capacitances associated with the pure and mixed phases

nanofiber samples, EIS data were fitted with the Randles' equivalent circuit [322] shown in the inset of Fig. 4.9.

In accordance with the above reported qualitative analysis, the following values were obtained for the charge transfer resistances R_{ct}: 6492 Ω, 14080 Ω and 10694 Ω for samples calcined at 475°C, 600°C and 725°C respectively. For what concerns double layer capacitances (here modeled through constant phase elements [323] with exponents β in the range (0.88 ÷ 0.91), values of 12.1, 6.4 and 6.1 s$^\beta$/Ω were obtained for the three samples. As discussed in the morphological characterization section, the sample calcined at 475°C is characterized by small Mn$_3$O$_4$ crystals and a good preservation of the fiber shape, thus offering a larger surface area exposed to the electrolyte while ORR takes place, if compared with the sample treated at 725°C (composed by big crystals of Mn$_2$O$_3$ and a partial loss of the fiber nanostructuration). This implies a higher number of active sites available for the reduction process in Mn$_3$O$_4$ with respect to the other sample (Mn$_2$O$_3$), and this could explain the observed lower value of the charge transfer resistance. On the other hand, larger exposed surface areas involve also larger capacitances, since double layer capacitor values are directly proportional to contact areas; this consideration is in agreement with the obtained results. Starting from the calculated electrical parameters, characteristic time constant associated to the charge transfer process can be obtained using the formula [324] $\tau = (R_{ct}Q_{dl})^{1/\beta}$: similar values equal to 0.51 and 0.48 s were obtained for pure Mn$_3$O$_4$ and pure Mn$_2$O$_3$ samples, respectively. Such results imply that even if the charge transfer resistance is reduced for the nanofibers calcined at lower temperature (475°C), the larger capacitive behavior exhibited by this sample is detrimental for the whole activity, leading to efficiencies which are comparable with that of Mn$_2$O$_3$ fibers/film. These findings once again support the hypothesis that the crystalline structure is not the only parameters to take into account when evaluating the catalytic activity of manganese oxide-based materials but also the morphology and nanostructuration of the crystals should be considered and optimized for the reduction reaction.

4.4 Mn$_x$O$_y$ NFs electrode integration

4.4.1 Electrode preparation

The previously discussed results evidence the good quality of the prepared catalysts. Among them, the catalyst selected is Mn$_3$O$_4$ calcined at 475°C, with the best compromise performance/sustainability, to prepare the cathodic electrode. By means of the electrospinning technique it is possible to integrate the Mn$_3$O$_4$ catalyst onto a commercial carbon based material (CP). In fact, Mn$_3$O$_4$ nanofibers have shown good catalytic performance, comparable with the sample calcined at 725°C, but obtained with a lower calcination temperature, 475°C. In order to prepare a sustainable and more green electrode, it is preferable to choose a thermal treatment at the lowest temperature, which gives the same catalytic results.
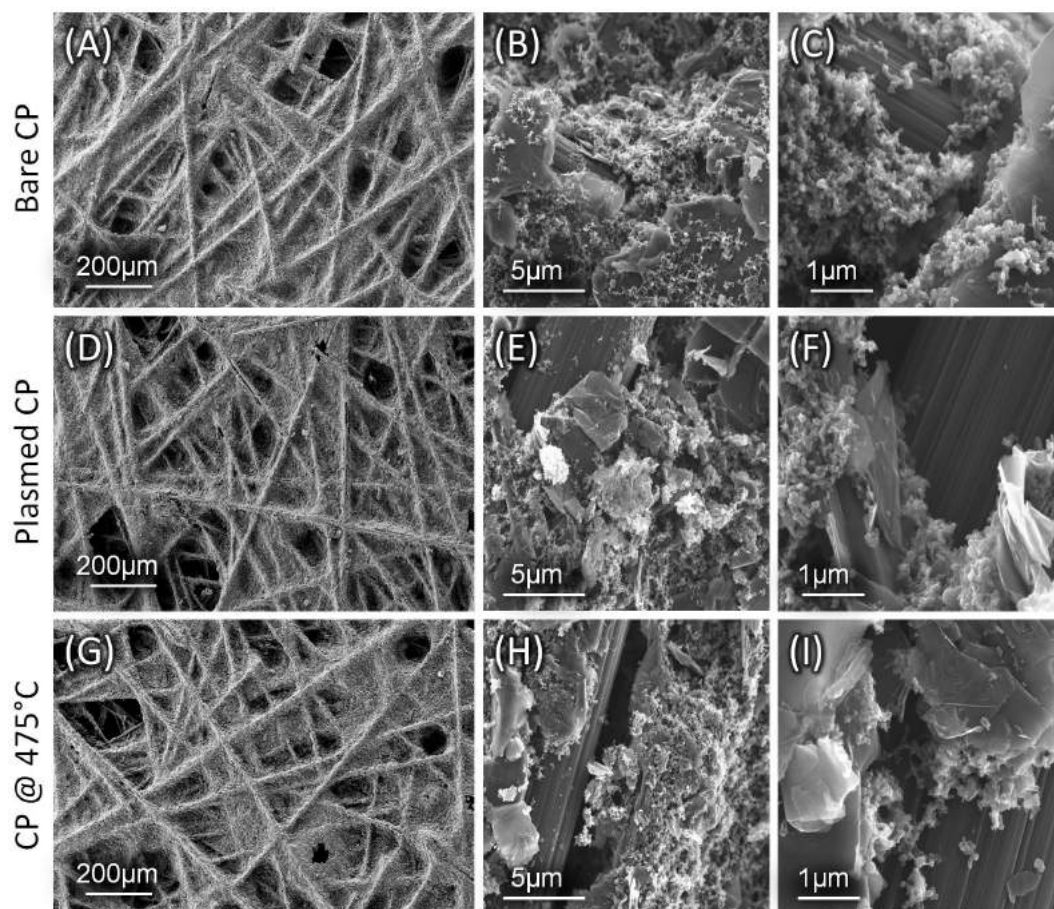
Fig. 4.10 FESEM images at different magnifications of: (A-C) bare CP, (D-F) CP after the plasma treatment and (G-I) CP after a thermal annealing at 475°C.

In Fig. 4.10A, a FESEM image of the CP substrate is showed at low magnification. It evident that the presence of big random carbon fibers embedded in a carbon-based binder, as highlighted in Fig. 4.10B and C. This substrate was selected first because is one of the standard materials used as MFC electrode, and also thank to its high electrical conductivity and thermal stability.

In order to enhance the wettability of the CP, and so improve the adhesion of the electrospun nanofibers on it, the substrates were firstly treated in pure O$_2$ plasma (Fempto) with a power of 30 W for 30 s (pressure 0.6 mbar). The plasma treated samples will be named as CPp. Fig. 4.10D-F show the FESEM images of the CPp, revealing no meaningful structural modification of the CP surface

Mn$_3$O$_4$ NFs were prepared starting from the same solution described in Sec. 4.2.1: a 3 ml of aqueous solution of 20 wt% manganese acetate tetrahydrate (Mn(CH$_3$COO)$_2$·4H$_2$O) and 9 ml of aqueous solution of 5 wt% PEO. The NFs were obtained at a working distance of 10 cm, feed rate of 0.1 ml/h and voltage

of 12.5 kV at 4 different deposition times: 5, 10, 15 and 20 minutes named , for simplicity, as NFs_5', NFs_10', NFs_15', NFs_20', respectively.

All obtained electrodes were then directly calcined in a tubular oven (Carbolite, VST 12/300/3216) for 3 h at 475°C in air (heating rate of 2.5°C/min) in order to obtain pure Mn$_3$O$_4$, as already discussed in Sec. 4.2.3 and 4.3.1, on CPp substrates. In order to demonstrate the thermal stability of the CPp, a piece of substrate was thermally annealed at 450°C in air, as showed by the Fig. 4.10G-I. Comparing these images with the former CP (4.10A-B) no significant modification of the CP substrate could be evidenced, confirming this material as a good candidate for the preparation of the electrode.

4.4.2   Morphological characterization
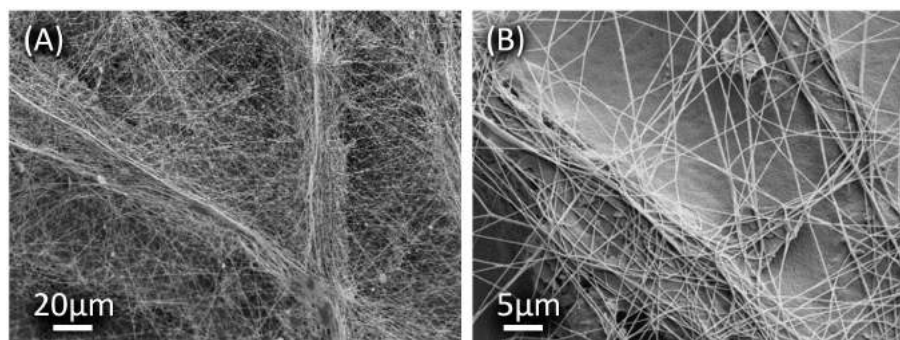
Fig. 4.11 FESEM images of the CP on which were electrospun the manganese acetate/PEO NFs (5 minutes) at two different magnifications.

Morphological characterizations of one not calcined sample and the four calcined electrodes are reported in Fig. 4.11, 4.13 and 4.14 at different magnifications. In particular, the samples in Fig. 4.13A-C, Fig. 4.13D-E, Fig. 4.14A-C and Fig. 4.14D-E report the nanostructuration of the electrodes NFs_5', NFs_10', NFs_15', NFs_20', respectively.

Focusing on Fig. 4.11, it may be noticed that the electrospinning deposition process is strongly influenced by the substrate morphology. In fact, it is quite evident that the CP induces a modification of the NFs deposition from what was observed in Fig. 4.4A, where it was possible to notice a NFs distribution uniform and randomly oriented. For greater clarity, in Fig. 4.12 a sketch depicting the nanofibers on top of the carbon paper, before and after calcination, is proposed. As already mentioned, the carbon paper is composed by carbon random fibers immersed in a carbon-based binder. Its roughness modules the local electric field between the needle and the substrate [325, 326]. In fact, the electric field lines are directed and concentrated onto the protrusions of the conductive fibers [325], indicating that, in these areas, the electrical field strength is stronger than other areas. This variation induces an accumulation of the NFs onto the protrusions, being the NFs electrically charged during the deposition process (Fig. 4.11).
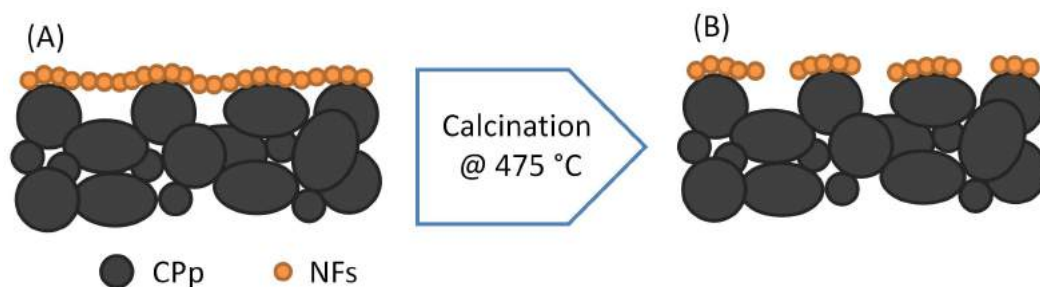
Fig. 4.12 Schematic representation, as a cross-section, of the nanofibred catalyst onto the CPp: (A) before and (B) after calcination.

After the calcination step, the nanofibers mat cracks due to the polymer degradation (see Fig. 4.12B), leaving the flakes onto the conductive electrode, that maintain the initial nanofibred structuration (see Fig. 4.13 and 4.14).

Comparing Fig. 4.13A and D it can be noticed that the amount of Mn_3O_4 NFs increases with the deposition time, while maintaining the distribution of the catalyst on all the electrode (white flakes in the images) quite uniform. In order to roughly evaluate the occupation percentage of the catalyst onto the CPp substrate, the FESEM images at lower magnification were graphically elaborated. By simply varying the brightness and contrast, it was possible to highlight in white the catalyst "flakes" from the black background (the CPp substrate). The occupation percentage is calculated by counting the white pixels with respect the pixels of the whole image. For the sample NFs_5' the occupation percentage is estimated as 16%, and rises to 20% in the case of the sample NFs_10'.

In Fig. 4.14A-C is reported the morphology of NFs_15', showing comparable occupation (18%) with respect to the NFs_10'. On the contrary, for NFs_20' electrode, in Fig. 4.14D-F, results a very low occupation percentage, less than 14%. The nanofibers appear more close-packed, being concentrated in big flakes, than the ones with shorter deposition times, due to the high amount of material deposited onto the CPp before calcination. As a first comment, in turns out that by increasing the deposition time, the nanofibers after calcination tend to aggregate in bigger flakes, resulting in a worse distribution of the catalyst on top of the CPp. Thus only the samples with the highest occupation and yield were selected to be tested as electrodes.
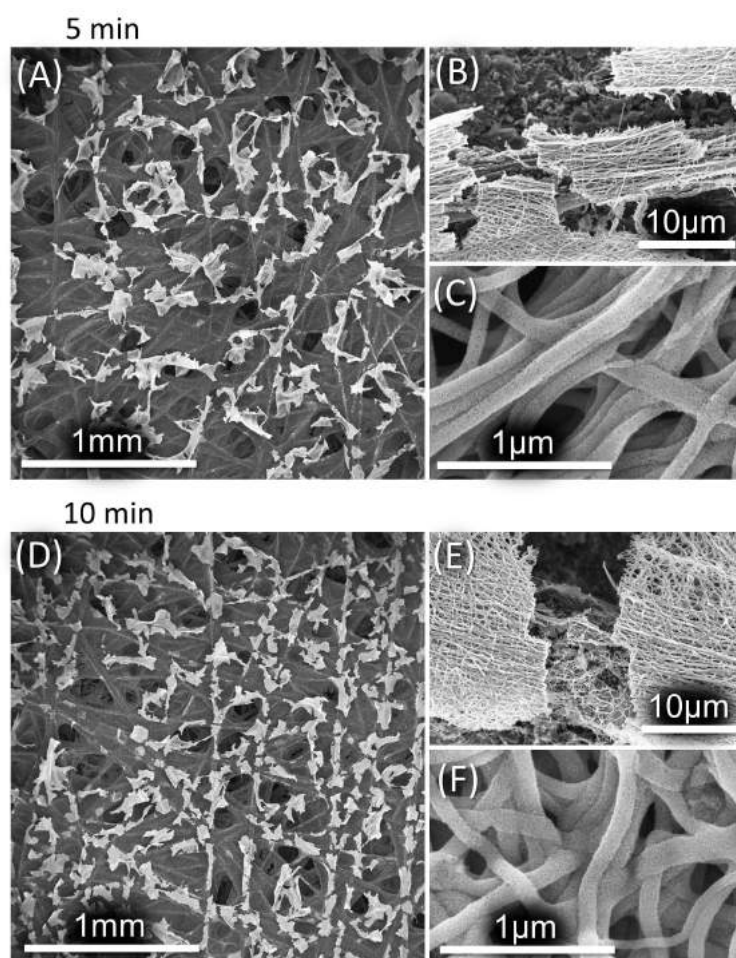
Fig. 4.13 FESEM images of the CP/catalyst assembly at three different magnifications: (A-C) NFs_5', (D-F) NFs_10'.
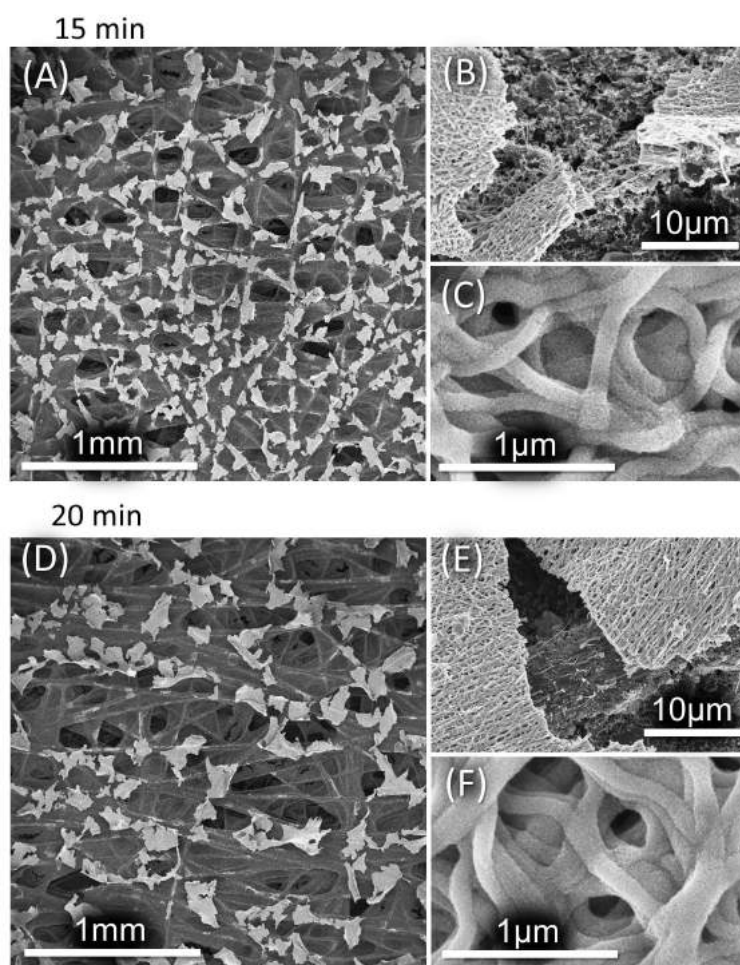
Fig. 4.14 FESEM images of the CP/catalyst assembly at three different magnifications: (A-C) NFs_15', (D-F) NFs_20'.

In Table 4.1 are summarized all the samples described, comparing the expected density (per unit of area) deposited and the qualitative experimental occupation percentage measured. The first value derives from calculation, done under some hypothesis, and it is proposed for sake of comparison of different samples:

(i) Uniform NFs distribution onto the deposited area;
(ii) Elliptical shape of the NFs mat, with *a* and *b* as minor axis and major axis, respectively;
(iii) Deposition mat ellipse do not increase in dimension by increasing the deposition time;
(iv) Oxide percentage residue is about 24%, after a thermal treatment at 475°, result obtained from the TGA analysis showed in Fig. 4.2.

The amount of deposited material is obtained by the electrospinning feed rate ($FR = 0.1$ ml/h) times the deposition time (t, 5 to 20 min). The value obtained is the amount of dried mat that is deposited uniformly in the ellipse. It should be multiplied by 24% (TGA%) in order to get the amount of manganese oxide (Mn$_3$O$_4$) onto the CPp. This number is expressed in *ml*, in order to obtain the result in g/cm^2, it should be multiplied by the oxide density ($d_{Mn_3O_4} = 4.8$ g/ml) and divided by the area ($A = 14$ cm^2). As summary, the calculation can be written as:

$$m_{dep} = FR \cdot t \cdot \frac{TGA\% \cdot d_{Mn_3O_4}}{100 \cdot A} \tag{4.3}$$

On the other side, the occupation percentage comes from the FESEM images elaboration at the same magnification (Fig. 4.13A and D, Fig. 4.14A and D), as already said. It has to be highlighted that m$_{dep}$ is the maximum amount of oxide that can be deposited onto CP, and it should be multiplied by the occupation percentage in order to get a plausible amount of catalyst on the substrate. It can be noticed that the samples NFs_5' and NFs_10' are the most efficient in terms of production process when compared to NFs_15' and NFs_20', leaving the highest amount of catalyst for shorter deposition times. For this reason, the following electrochemical characterizations have been performed only on the first two samples.

Mn$_x$O$_y$	Time [min]	Name	m$_{dep}$ [g/cm^{-2}]	Occupation %
	5	NFs_5'	$4.8 \cdot 10^{-4}$	16%
	10	NFs_10'	$9.6 \cdot 10^{-4}$	20%
NFs	15	NFs_15'	$1.4 \cdot 10^{-3}$	18%
	20	NFs_20'	$1.9 \cdot 10^{-3}$	14%

Table 4.1 Summary of the Mn$_x$O$_y$ NFs electrodes fabricated and described with their name, theoretical density of the catalyst deposited and experimental occupation percentage of the oxide onto CP.

4.4.3 Electrochemical characterizations

To study the catalytic activity of the prepared electrodes, RRDE measurements were performed, in order to evaluate the number of electrons exchanged in the reaction and comparing them to the standard Pt/C reference and the bare CP. Differently from what done for the catalyst alone, in this case the manganese oxide-based electrodes and the bare CP were not reduced in a paste, but they were "glued" of the RRDE glassy carbon disk by putting a drop of Nafion$^©$ solution, while the Pt/C paste was prepared as described in App. A.4.
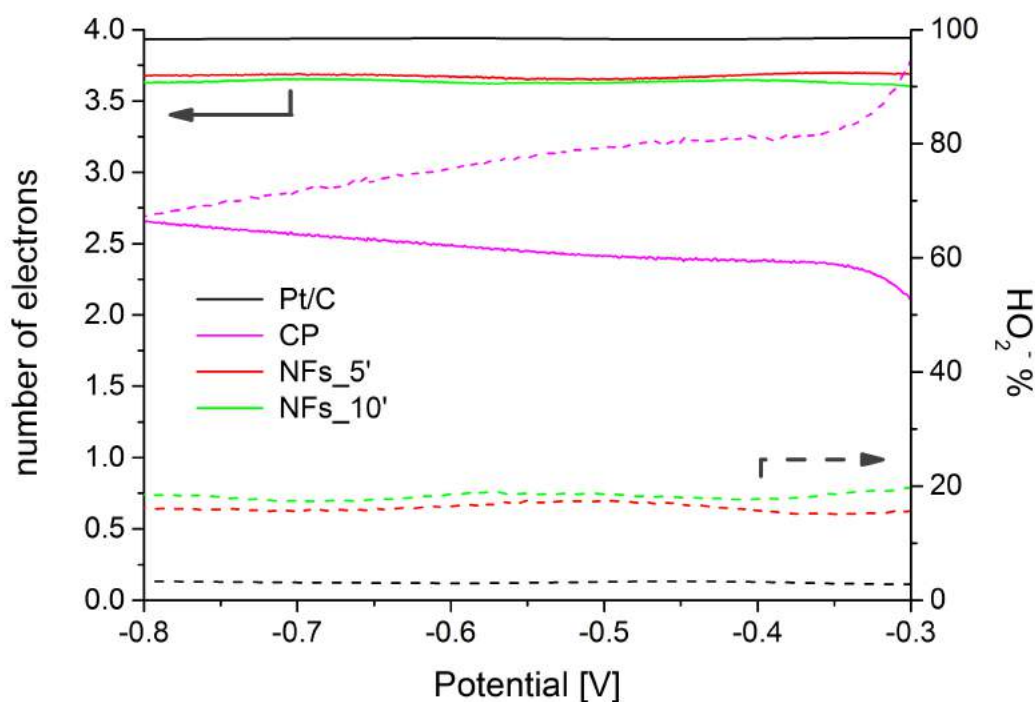
Fig. 4.15 Comparison of electron transfer number (straight lines, left axis) and peroxide percentage (dashed lines, right axis) evaluated from RRDE measurements of the samples NFs_5', NFs_10', bare carbon paper (CP) and reference Pt/C catalyst.

As clearly evident in Fig. 4.15, CP shows very low catalytic properties, as evidenced by both electron transfer number and peroxide percentage curves. On the other side, quite constant values were obtained for the electron transfer number related to Mn$_3$O$_4$–based electrodes: 3.68 for NFs_5' and 3.65 for NFs_10' (see also Table 4.2). Moreover, the percentages of peroxide species produced are below 20% for both the electrodes. Based on these results, it can be asserted that manganese oxide electrodes show performances in line with the Mn-based [316] or other cost-effective ORR catalysts recently proposed in the literature [317–319, 327].

In light of the results above reported, it may be appreciated that the NF_5' and NF_10' samples produces a comparable amount of peroxide species, with a gap around 1%. To better clarify the catalytic performance, electrochemical impedance spectroscopy (EIS) analysis was carried out.

Sample	n @ -0.55 V	HO$_2^-$ % @ -0.55 V
CP	2.4	78%
NFs_5'	3.65	17.5%
NFs_10'	3.62	18.6%
Pt/C	3.94	3%

Table 4.2 Values at -0.55 V of the electron transfer number (n) and peroxide percentage (HO$_2^-$) of the manganese oxide based electrodes, compared with the CP and the Pt/C reference.
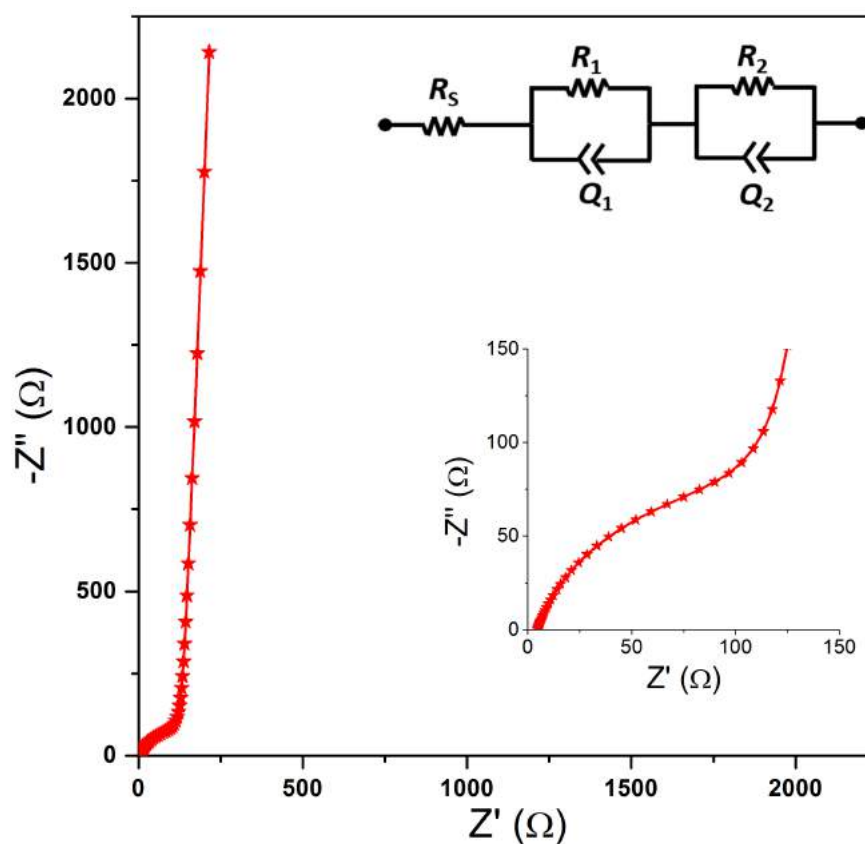
Fig. 4.16 Nyquist plot of the impedance of the ND_10' sample. The points are experimental data while the continuous lines are the curves obtained from a fitting procedure using the equivalent circuit shown in the inset. Q$_1$ and Q$_2$ are the constant phase elements (CPEs) associated to high frequency and low-frequency capacitances, respectively, with β_1 and β_2 are the CPEs indexes.

In Fig. 4.16, Nyquist plots related to NFs_10' sample is reported, which is the one that showed good RRDE results together with the highest amount of loaded catalyst. In the inset is reported magnification of the plot at low Z values. As it is clearly evident, the electrode exhibit a typical two-time constants spectrum, with a high-

frequency arc, which is related to the charge transport inside the electrode, and a low-frequency incomplete arc, related to the charge transfer at the electrode/electrolyte interface; a third feature related to charge diffusion cannot be appreciated due to instrumental frequency limitations [328]. By comparing the NFs_10' spectra with the one in Fig. 4.9, it is manifest that synthesized electrode is characterized by reduced impedance both in high frequency and low frequency part of the spectrum, as witnessed by the lower diameter of the two arcs (even the second incomplete one). This qualitative analysis was numerically confirmed by fitting the experimental data with the equivalent electrical circuit shown in the inset of Fig. 4.16: both charge transport R_1 and charge transfer R_2 resistance values were found to be lower for NFs_10' sample with respect to the bare NFs, as summarized in Table 4.3.

Electrode	R_s [Ω]	Q_1 (s^{β_1}/Ω)	β_1	R_1 [Ω]	Q_2 (s^{β_2}/Ω)	β_2	R_2 [Ω]
NFs_10'	4.7	$2.4 \cdot 10^{-4}$	0.91	127.4	$9.4 \, 10^{-4}$	0.97	24940

Table 4.3 Parameters extracted from the EIS analysis.

EIS revealed that NFs-based electrode is characterized by improved charge transport properties along the electrode, as well as enhanced electron transfer at electrode/electrolyte interface. These features can thus explain EIS results, and, on the whole, the improved catalytic performance of the sample. The direct electrode integration can be an efficient way to improve the electrode engineering, without using a paste or reduce the catalytic properties of the manganese oxide, and it could be a good choice for a test in device.

4.4.4 MFC test

Given the results discussed in the previous sections, the sample NFs_10' was selected to be tested in device, in particular, a squared single chamber MFC device (SCMFC), with an open air cathode configuration, represented in Fig. 4.17. The test devices were realized by a 3D printer (OBJET 30), being composed by 3 different compartments: the anodic part (i), the intermediate compartment (ii) and the cathodic side (iii - iv). Both the anodic and cathodic areas are equal to 6.25 cm^2, and the volume occupied by the electrolyte is 9 ml. The electrolyte is constituted by 12 mM of sodium acetate as carbon-energy source and by other compounds, such as 5.8 mM of ammonium chloride and phosphate buffer saline solution (PBS, pH=7.4, 140 mM of sodium chloride, 2.7 mM of potassium chloride and 10 mM of sodium phosphate buffer) to maintain a value of pH close to 7. An environmental sediment sample is selected as the inoculum source (from Valle D'Aosta river).

The performances of the NFs_10' electrode were compared with commercial carbon paper (CP) and with Pt/C paste deposited on CP. In the latter case, the cathode is obtained by depositing, onto CP, a layer made of platinum and Nafion$^{©}$, defined as catalyst layer (CL) [329]. The catalyst layer is obtained by mixing 0.5 mg/cm^2 of Pt, 5wt% of Nafion$^{©}$ with isopropanol. Nafion$^{©}$ and isopropanol are used to ensure the adhesion of platinum onto the cathode. Later, the CL is dried in air at
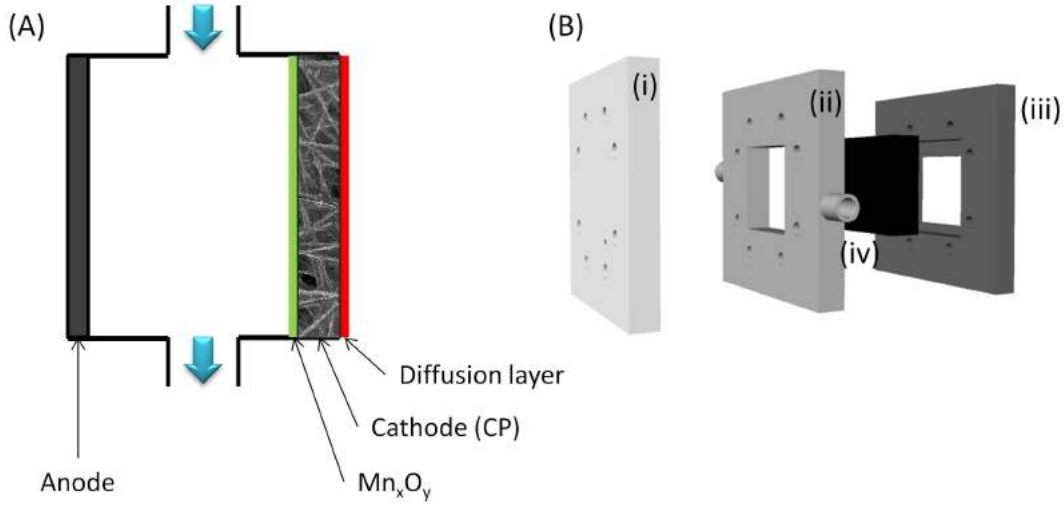
Fig. 4.17 (A) Cross-section of a single chamber microbial fuel cell (SCMFC). (B) 3D polymeric SCMFC composed by i) anodic side; ii) intermediate space and iii) cathodic side and iv) example of cathode electrode obtained cutting a piece 3x3 cm^2 of CP.

room temperature for 1 day. The anodes of the cells were based on commercial carbon based electrode. Titanium wires were used to ensure a good electrical contact, threaded in the carbon paper by a conductive paste made of carbon cement. An external load equal to 1000 Ω was applied to monitor the cells potentials and consequently to define the final performance of the SCMFCs.

In line with the aforementioned results, Linear Sweep Voltammetry (LSV) is performed on MFCs containing NFs_10' as cathode electrode, compared with the cathode electrode based on Pt/C on CP and with bare CP. More detailed description of the characterization setup can be found in App. A.4.3. In order to deeply investigate the key role played by catalysts, current and power output were normalized both for the electrode geometrical area (Fig. 4.18) and for the nominal weight of catalyst loaded (Fig. 4.19). In the case of NFs_10' sample, the weight of loaded catalyst m$_{cat}$ is calculated as in paragraph 4.4.2:

$$m_{cat} = m_{dep} \cdot \frac{\%Occupation}{100} \cdot A \qquad (4.4)$$

where A is the electrode geometrical area.

LSV results (see Fig. 4.18), in the case of area normalization, show that the maximum power density, depicted in Fig. 4.18 as dotted lines, reached by Pt/C paste, close to 89.2 mW/cm^2, higher than the one obtained with NFs_10' (27.6 mW/cm^2) and with CP (9.28 mW/cm^2). However the electrodes areas are equal for the three materials, what really changes is amount of catalyst loaded onto the CP. For this reason, the normalization was also calculated by the catalyst weight. In the case of bare CP, the curve is not normalized because there is no catalyst upon it.
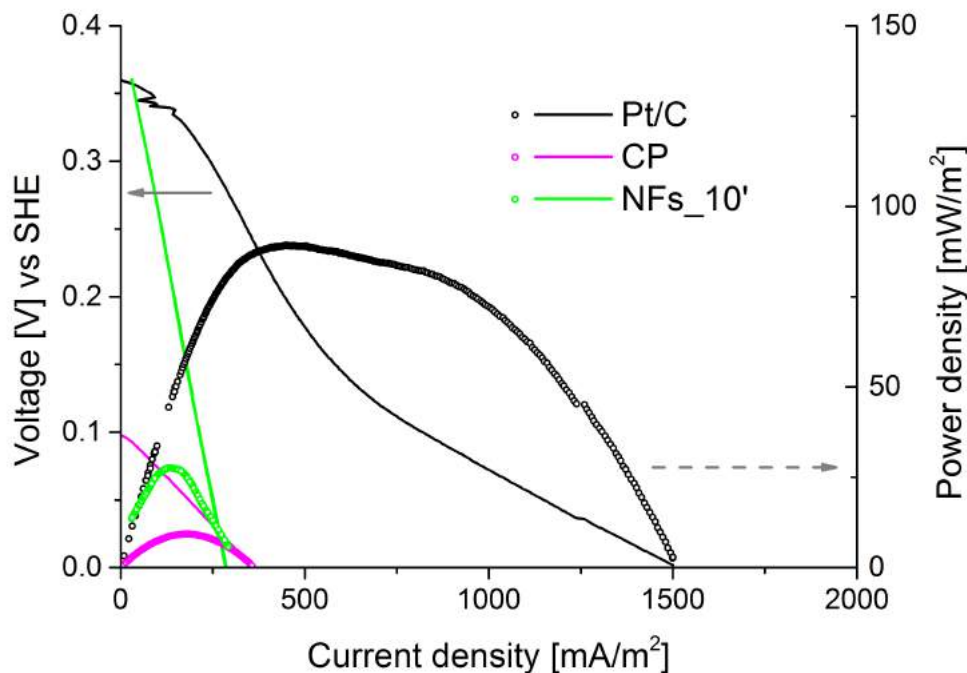
Fig. 4.18 I-V trend (straight lines) and power density (scatter) evaluated from LSV results of the different cathode electrodes and normalized by the electrode geometrical area: NFs_10' (green line and scatter), Pt/C (black line and scatter) and bare CP (pink line and scatter).

Fig. 4.19 shows the LSV results, after the catalyst weight normalization, confirming that the NFs_10' maximum power density (1.5 mW/g) reached by the MFC is close to the Pt/C (1.7 mW/g). It is also interesting to notice that power density of NFs_10' is two orders of magnitude higher than the one obtained by bare CP equal to 0.074 mW/g.

All the obtained results demonstrate that Mn$_3$O$_4$ NFs–based electrode provide a good catalytic behavior, ensuring an electron transfer number close to the ideal value of 4. Based on all these results, it is possible to conclude that this electrode preparation method is a good way to directly integrate the catalyst onto a substrate without destroying the initial nanostructuration. In fact, the evaluation of the overall performances of MFC demonstrate that the NFs_10' si a good MFC cathode electrode, characterized by a power density value comparable to the one obtained in MFC with a cathode made of Pt/C on CP.
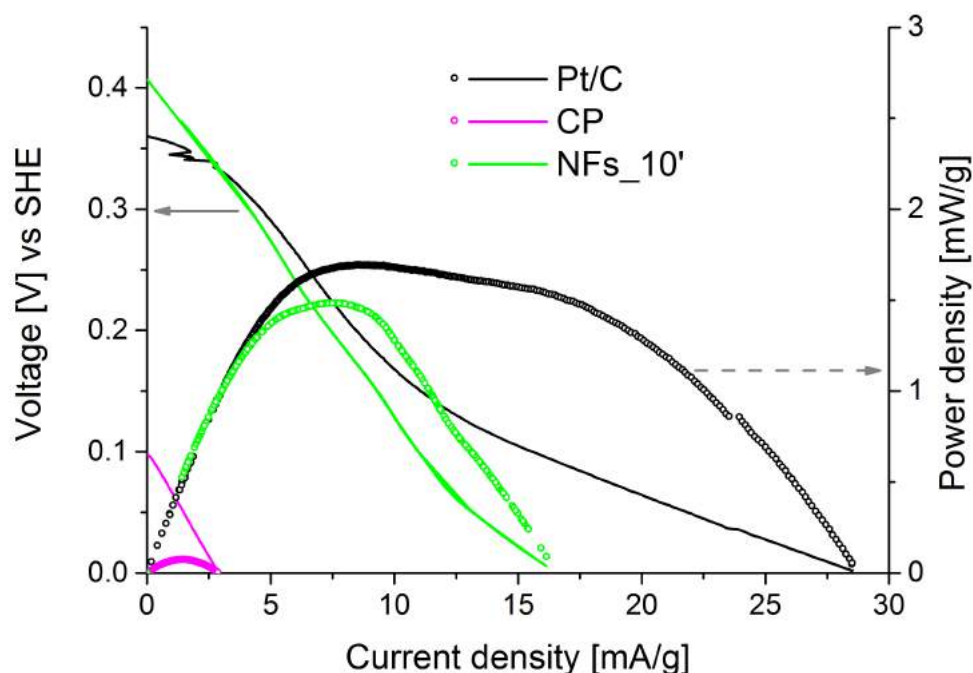
Fig. 4.19 I-V trend (straight lines) and power density (scatter) evaluated from LSV results of the different cathode electrodes and normalized by the catalyst mass: NFs_10' (blue line and scatter), Pt/C (black line and scatter) and bare CP (pink line and scatter).

4.5   Mn$_x$O$_y$ NDs-based electrode, a preliminary study

In order to test the role of the nanostructured catalyst on the CPp, a preliminary experiment was performed by varying the experimental parameters in the electro-spinner, obtaining thus an electrospraying regime. In the same apparatus, a voltage is applied between the nozzle and the substrate [330, 331], but the solution viscosity is reduced until reaching the electrospraying regime (see Sec. 3.1.5). Moreover, the nanometric dimension of the charged droplets prevent the earlier aggregation of the material, together with a fast solvent evaporation [332]. Some examples of applications of this deposition technique can be found in a wide variety of fields such as: fabrication of metal oxide and semiconductor devices [333–335], lithium batteries [336], micro-electromechanical systems [337] and micro- and nano- particle ceramic production [338].

The goal of this preliminary work is to show the catalytic capability of manganese oxide nanodrops (NDs) -based electrodes deposited on carbon paper. The preparation method will be similar to the one described in Sec. 4.4, and the same characterization techniques.

4.5.1   Electrode preparation

As for the the cathode prepared with Mn$_3$O$_4$ NFs, the nanodrops (NDs) were sprayed on commercial carbon based material (CP). As described in Sec. 4.4, the CP substrates were firstly treated in an O$_2$ plasma to enhance the carbon paper wettability, obtaining the substrate called CPp.

Mn$_3$O$_4$ NDs were obtained by mixing 9 ml of aqueous solution of 1 wt% of PEO with 3 ml of aqueous solution of 10 wt% manganese acetate tetrahydrate and stirred overnight. The low viscosity of this mixture gave the possibility to achieve the electrospray regime and to obtain nano-scaled drops during deposition. The NDs were obtained by electrospraying at a distance of 10 cm, feed rate of 0.1 ml/h and voltage of 18 kV at 2 different deposition times: 5 and 10 minutes named, for simplicity, as NDs_5' and NDs_10', respectively.

The two obtained samples were then directly calcined in a tubular oven (Carbolite, VST 12/300/3216) for 3 h at 475°C in air (heating rate of 2.5°C/min) in order to completely eliminate the polymeric component (PEO), and oxidize the precursor into manganese oxide.

4.5.2   Morphological characterization
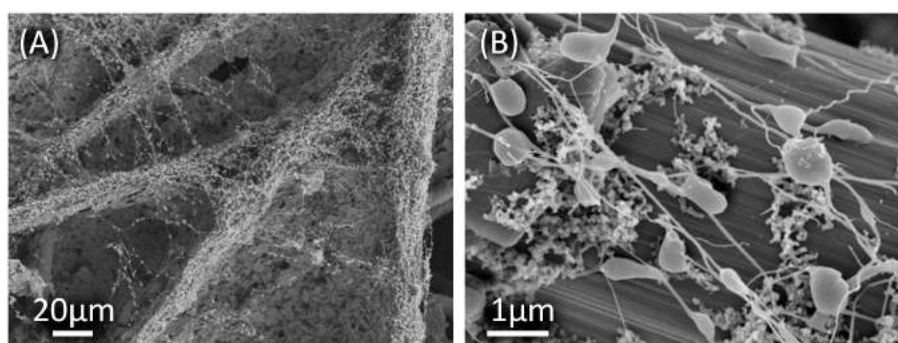
Fig. 4.20 FESEM images of the CP on which were electrospun the manganese acetate/PEO NDs (5 minutes) at two different magnifications.

Morphological characterizations of the not calcined and the two calcined electrodes are reported in Fig. 4.20 and 4.22 at different magnifications. In particular, the samples in Fig. 4.13A-C and Fig. 4.13D-E report the nanostructuration of the electrodes NDs_5' and NDs_10', respectively.

Differently from Fig. 4.11, in the NDs not calcined sample (Fig. 4.20), the nanofibred structuration is almost lost. In fact, only thin nanofibers join the not calcined nanodrops. This structure may recall a beaded structure [339], in which the beads dimensions are at least one order of magnitude higher than the nanofibers. As already stated for NFs, the electric field varies locally due to the substrate roughness, attracting most of the nanodrops/nanofibers structure onto the protrusions of the

conductive CP fibers [325], as shown in Fig. 4.20A. For greater clarity, in Fig. 4.21 a sketch depicting the NDs on top of the carbon paper, before and after calcination, is proposed. The thermal treatment fixes the NDs in their position (see Fig. 4.21B), with a density depending on the deposition time, as showed in the following Fig. 4.22, while the thin NFs are lost.
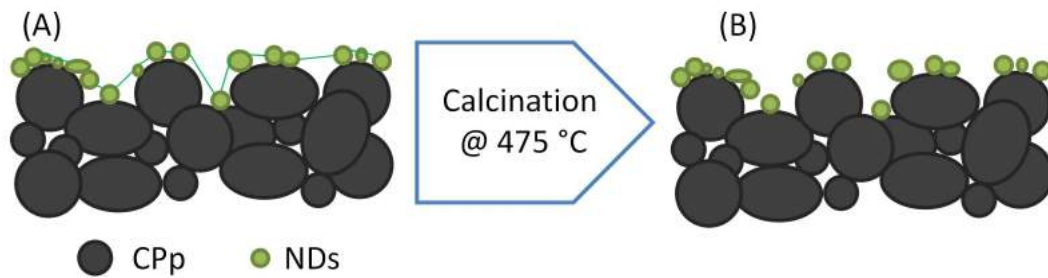
Fig. 4.21 Schematic representation, as a cross-section, of the nanodrop catalyst onto the CPs (A) before and (B) after calcination.

The morphologies of the calcined samples NDs_5' and NDs_10' evidence no substantial differences at lower magnifications (Fig. 4.22A an D). By increasing magnification, it can be noticed that denser NDs correspond to longer electrospraying times (Fig. 4.22B and E). As for the nanofibers, also in this case, it can be noticed an accumulation of the NDs onto the pointed areas, corresponding to the much more rough arts of the substrate [325, 326]. In Fig. 4.22C and F, the nanodrops show similar shape, with a diameter ranging from 200 nm up to 350 nm. Thanks to these last images, it can be noticed that the NDs are constituted by small crystals, as already noticed in the case of nanofibers calcined at the same temperature (see Fig. 4.5D). Thus, it may be reasonable to suppose that the NDs are composed by Mn$_3$O$_4$, however, to better understand the composition, TEM characterization should be performed onto a single ND.

In Table 4.4 are summarized the two NDs samples, comparing their expected density deposited m$_{dep}$, calculated with the same method of NFs. As already demonstrated by the FESEM images, the m$_{dep}$ rises with the deposition time. Unlike NFs, in the case of nanodrops it couldn't be possible to estimate the occupation percentage from the FESEM images elaboration due to their nanoscaled dimension. For this reason, the m$_{dep}$ value has to be considered as the maximum amount of Mn$_x$O$_y$ NDs that can be deposited onto the CPp, considering negligible the amount of thin nanofibers lost during calcination. When the weight normalizations will be applied, the resulting values should be considered as the minimum one.

Comparing the NDs morphology with the NFs, the differences are quite evident. In fact, the substrate-catalyst interaction is influenced by the dimension scales of the two synthesized oxides. Thus, because of the increased substrate catalyst interaction of the NDs with respect to the NFs, the NDs may exhibit shorter electron pathways, offering catalytic sites closer to the conductive electrode. Such interaction should be exploited by the reduced size of the Mn$_3$O$_4$ NDs and a much more uniform catalyst distribution on the CPp. This point will be more stressed in the following paragraph.
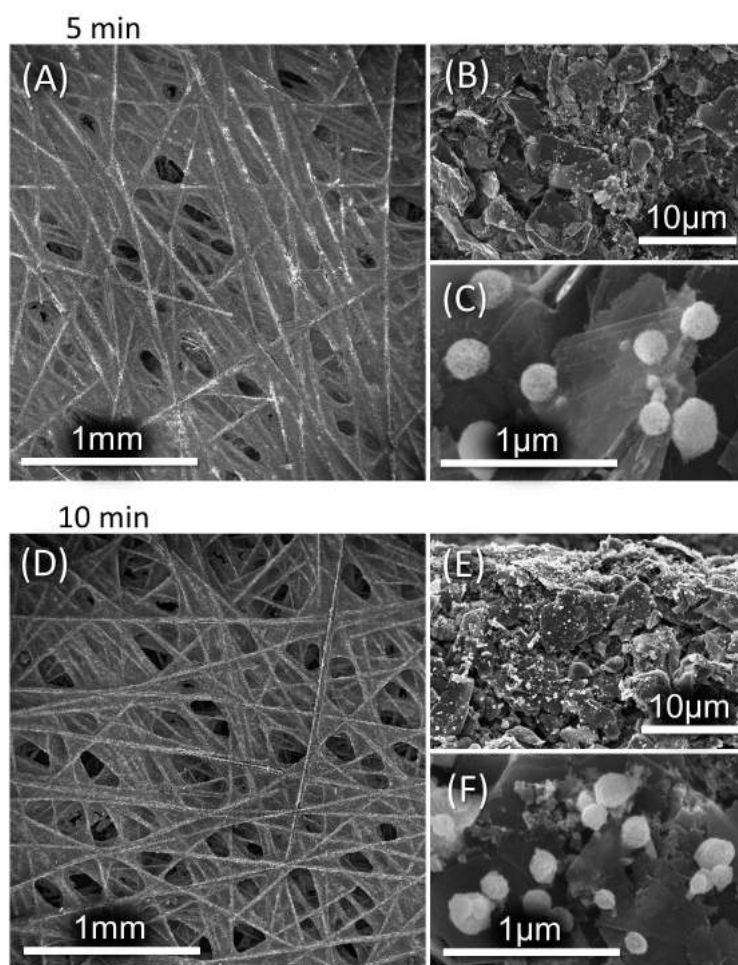
Fig. 4.22 FESEM images of the CP/NDs catalyst assembly at three different magnifications: (A-C) NDs_5', (D-F) NDs_10'.

Mn_xO_y	Time [min]	Name	m_{dep} [g/cm^{-2}]
NDs	5	NDs_5'	$2.4 \cdot 10^{-4}$
	10	NDs_10'	$4.8 \cdot 10^{-4}$

Table 4.4 Summary of the Mn_xO_y NDs electrodes fabricated and described with their names and the expected density (weight per unit area) of the catalyst deposited.

4.5.3 Electrochemical characterizations

To study the catalytic activities of the prepared electrodes, RRDE measurements were performed, in order to evaluate the number of electrons exchanged in the reaction and comparing them to the standard Pt/C reference and bare CP. As for NFs electrodes,

NDs electrodes and CP were "glued" on the glassy carbon disk employing a drop of Nafion$^©$ solution, while the Pt/C paste was prepared as described in App. A.4.
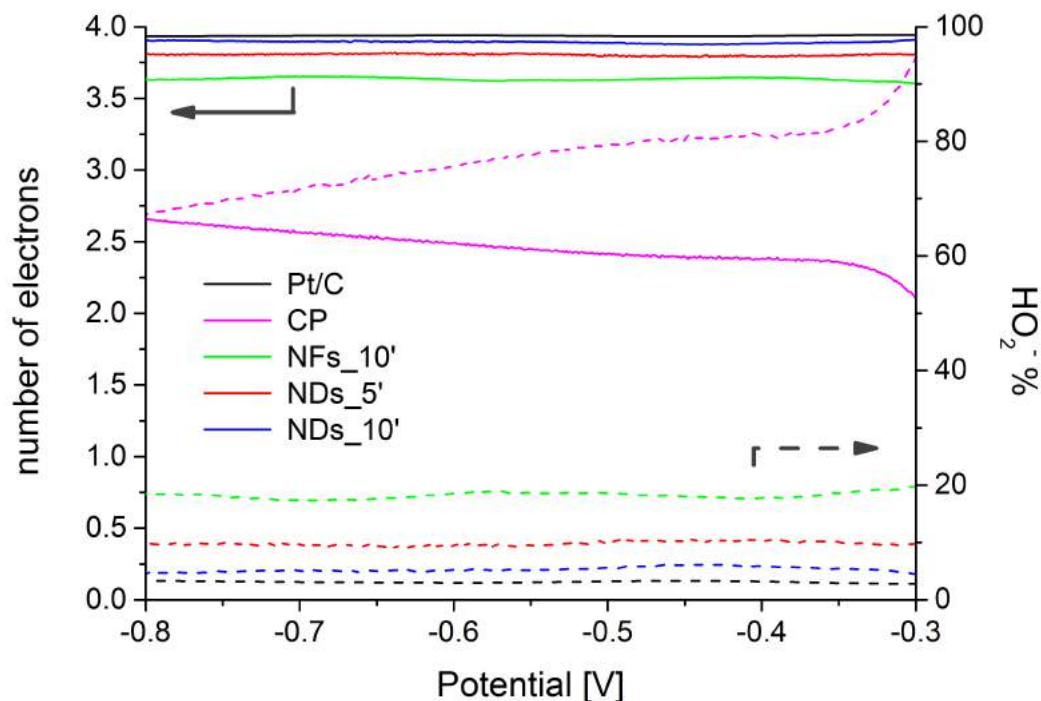
Fig. 4.23 Comparison of electron transfer number (straight lines, left axis) and peroxide percentage (dashed lines, right axis) evaluated from RRDE measurements of ND_5', ND_10', NFs_10' samples, bare carbon paper (CP) and reference Pt/C catalyst.

As clearly evident in Fig. 4.23, CP shows very low catalytic properties, evidenced by both electron transfer number and peroxide percentage curves. On the other side, quite constant values were obtained for the electron transfer number related to NDs–based electrodes: 3.81 for NDs_5' and 3.9 for NDs_10' (see also Table 4.5). Moreover, the percentages of peroxide species produced are impressively low, especially for the sample NDs_10' (about 5%), a value which is very close to the reference sample (about 3%). Based on these results, it can be asserted that NDs electrodes show performances in line or even better with respect to Mn-based [316] or other cost-effective ORR catalysts recently proposed in the literature [317–319, 327].

In light of the results above reported, a slight difference can be appreciated between NDs-based electrodes and the former NFs ones, both in morphology and catalytic performance. In order to clarify the reason of this difference, electrochemical impedance spectroscopy (EIS) analysis was carried out. In order to make a comparison with the NFs_10' sample, the NDs_10' was chosen, being also the most performing one in the RRDE analysis with higher n value and lower amount of peroxide produced.

In Fig. 4.24, Nyquist plots related to NDs_10' sample is reported and compared to the NF_10' one, which is the ones that perform best in RRDE analysis. As it is

Sample	n @ -0.55 V	HO_2^-% @ -0.55 V
CP	2.4	78%
NFs_10'	3.62	18.6%
NDs_5'	3.8	9.7%
NDs_10'	3.9	5.2%
Pt/C	3.94	3%

Table 4.5 Values at -0.55 V of the electron transfer number (n) and peroxide percentage (HO_2^-) of the manganese oxide based electrodes, compared with the CP and the Pt/C reference.
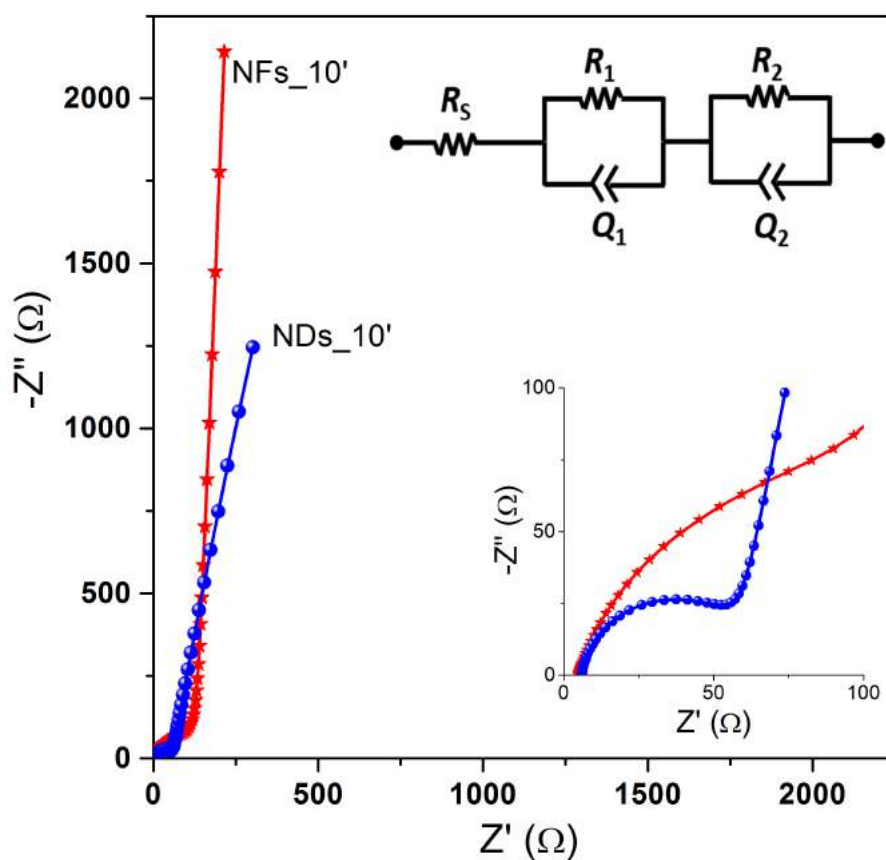
Fig. 4.24 Nyquist plot of the impedance of the NDs_10' (blue) and NFs_10' (red) samples. The points are experimental data while the continuous lines are the curves obtained from a fitting procedure using the equivalent circuit shown in the inset. Q_1 and Q_2 are the constant phase elements (CPEs) associated to high frequency and low-frequency capacitances, respectively, with β_1 and β_2 are the CPEs indexes.

evident, both electrodes exhibit a typical two-time constants spectrum, with a high-frequency arc, which is related to the charge transport inside the electrode, and a low-frequency incomplete arc, related to the charge transfer at the electrode/electrolyte

Electrode	R$_s$ [Ω]	Q$_1$ (s^{β_1}/Ω)	β_1	R$_1$ [Ω]	Q$_2$ (s^{β_2}/Ω)	β_2	R$_2$ [Ω]
NFs_10'	4.7	$2.4 \cdot 10^{-4}$	0.91	127.4	$9.4 \, 10^{-4}$	0.97	24940
NDs_10'	5.9	$7.2 \cdot 10^{-5}$	0.92	51.2	$1.2 \, 10^{-3}$	0.99	1369

Table 4.6 Parameters extracted from the EIS analysis.

interface; a third feature related to charge diffusion cannot be appreciated due to frequency limitations [328]. By comparing the two spectra, it is manifest that NDs_10' electrode is characterized by reduced impedance both in high frequency and low frequency part of the spectrum, as witnessed by the lower diameter of the two arcs (even the second incomplete one). This qualitative analysis was confirmed by performing a fitting procedure exploiting the equivalent electrical circuit shown in the inset of Fig. 4.24: both charge transport R$_1$ and charge transfer R$_2$ resistance values were found to be lower for NDs sample with respect to those of NFs, already reported, as summarized in Table 4.6.

EIS revealed that NDs-based electrodes were characterized by improved charge transport properties along the electrode, as well as enhanced electron transfer at electrode/electrolyte interface. Indeed, NDs electrode morphology, characterized by uniformly distributed nanodrops, can guarantee both a short high-resistive electron path (as anticipated above) and a more intimate contact with dissolved oxygen molecules, with respect to the clusters of nanofibers characterizing NFs-based electrode. These features can thus explain EIS results, and, on the whole, the improved catalytic performance of NDs-based samples.

4.5.4 MFC test

Given these preliminary results discussed in the previous sections, the sample NDs_10' was selected to be tested in SCMFC. Same setup and preparation procedure was followed in this case, as already described for the NFs case in Sec. 4.4.4.

In line with the NFs results, Linear Sweep Voltammetry (LSV) is performed on MFCs containing NDs_10' on CP as cathode electrode, compared with the cathode electrode based on Pt/C on CP and with bare CP. In order to deeply investigate the key role played by catalysts, current and power output were normalized both for the electrode geometrical area (Fig. 4.25) and for the weight of catalyst loaded (Fig. 4.26). In the case of NDs_10' sample, the weight of loaded catalyst is considered to be equal to m$_{cat}$· A, where A is the electrode geometrical area.

LSV results (see Fig. 4.18), in the case of area normalization, show that the maximum power density reached by Pt/C and NDs_10' are comparable, 89.2 mW/cm^2 and 88.6 mW/cm^2, respectively. They are both much higher than than the one obtained with bare CP (9.28 mW/cm^2). However the electrodes areas are equal for the three materials, what really changes is amount of catalyst loaded onto the CP. As for the NFs case, the normalization was also calculated by the catalyst weight.
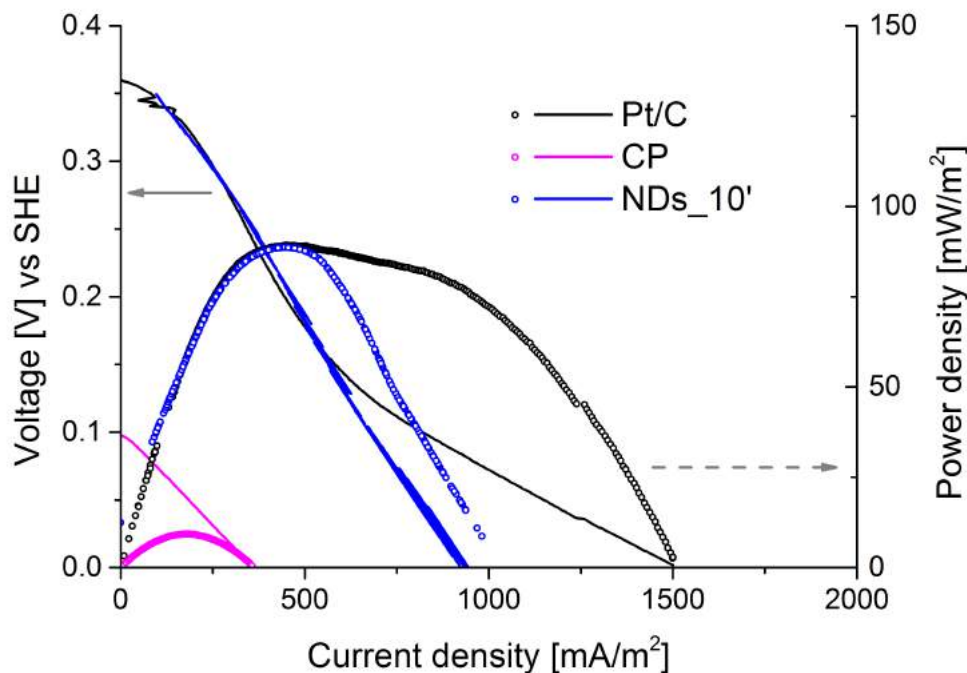
Fig. 4.25 I-V trend (straight lines) and power density (scatter) evaluated from LSV results of the different cathode electrodes and normalized by the electrode geometrical area: NDs_10' (green line and scatter), Pt/C (black line and scatter) and bare CP (pink line and scatter).

Fig. 4.25 shows the LSV results, after the catalyst weight normalization. It is evident that the NDs_10' maximum power density (3.0 mW/g) reached by the MFC is higher than the Pt/C one (1.7 mW/g). It is also interesting to notice that power density of NDs_10' is doubled with respect to the NFs_10' one (1.5 mW/g) and two orders of magnitude higher than the one obtained by bare CP equal to 0.074 mW/g.

All the obtained results demonstrate that NDs–based electrodes provide an impressive catalytic behavior, ensuring an electron transfer number close to the ideal value of 4. Moreover, it is interesting to notice that NDs exhibit shorter electron pathways with respect to NFs, offering catalyst sites closer to the conductive electrode and improving consequently their charge transport properties along the electrode, as confirmed by EIS analysis. Indeed, NDs electrode morphology, characterized by uniformly distributed nanodrops, guarantee both a short high-resistive electron path and a more intimate contact with dissolved oxygen molecules, with respect to the clusters of nanofibers characterizing NFs-based electrode. Based on all these results, the evaluation of the overall performances of MFCs demonstrate that the NDs_10' is a good MFC cathode, characterized by a power density value higher than the one obtained in MFC with a cathode made of Pt/C on CP.
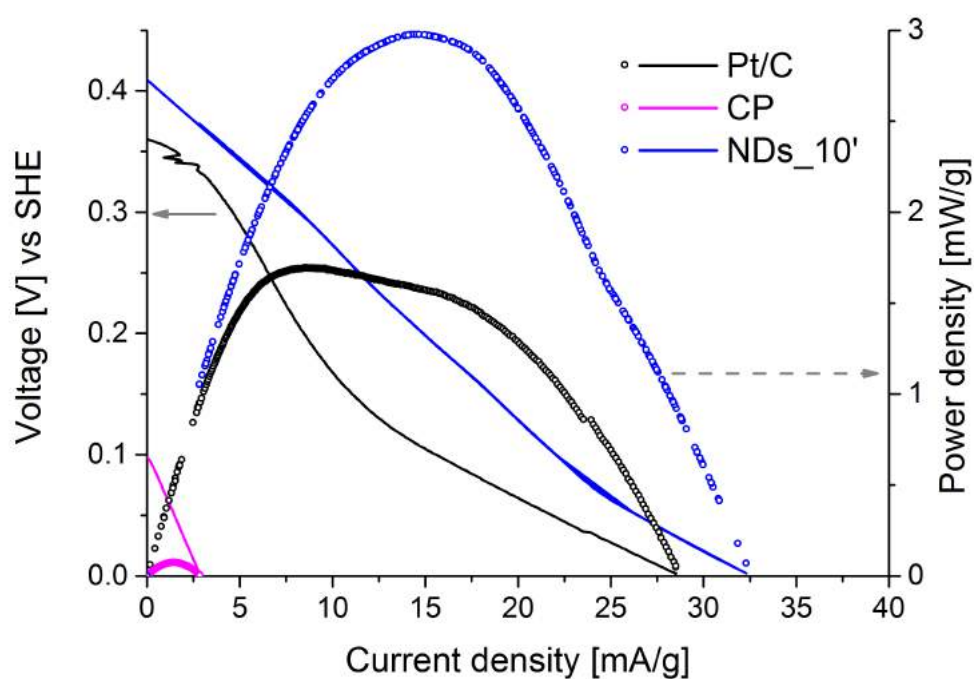
Fig. 4.26 I-V trend (straight lines) and power density (scatter) evaluated from LSV results of the different cathode electrodes and normalized by the catalyst mass: NDs_10' (blue line and scatter), Pt/C (black line and scatter) and bare CP (pink line and scatter).

Chapter 5

CO$_2$RR catalysts

Chapter abstract   *In Chapter 5 are analyzed titanium dioxide (TiO$_2$) and copper oxide (Cu$_x$O) -based nanostructures as CO$_2$RR catalysts. In Sec. 5.1 are listed the materials used in this chapter. In Sec. 5.2, TiO$_2$ NTs synthesis is described, followed by the material characterizations. In the same section, Cu and Cu$_x$O supported onto TiO$_2$ NTs are studied in terms of morphology, composition and electrocatalytic activity. In the last section, Sec. 5.3, Cu$_x$O NWs and TiO$_2$ supported onto Cu$_x$O NWs samples are described. Also in this case, the materials are characterized in terms of morphology, composition and electrocatalytic activity.*

5.1   Materials

5.1.1   TiO$_2$ nanotubes

A 250 μm thick titanium foils (99.97% purity, Sigma Aldrich) and a 250 μm platinum sheet (99.99% purity, Advent Research Materials) were employed as anode and cathode in a two-electrode configuration electrochemical cell, respectively. For the electrolytic solution, ammonium fluoride (NH$_4$F) and ethylene glycol were used, purchased from Sigma Aldrich and processed without any further purification. De-ionized water was used both for the electrolytic solution and for the samples rinsing.

5.1.2   Cu$_x$O nanowires

Copper foils with purity of 99.99+% and 250 μm thick were purchased from Goodfellow and employed for the thermal oxidation process.

Kapton$^{®}$ tape was purchased from 3M, in order to mask and electrically isolate the prepared samples.

5.2   TiO$_2$ NTs-based catalysts

5.2.1   TiO$_2$ NTs

The titanium foil was cut into rectangles (2x3 cm^2) and then cleaned in acetone and ethanol through an ultra-sonic bath for 5 minutes each. The TiO$_2$ NTs array was grown by anodic oxidation into a glass becker used as an electrochemical cell. In order to grow the NTs only in a selected area, Kapton$^®$ tape was used to mask the Ti foil, thus obtaining an electrode active area of 1 cm^2. In Fig. 5.1, the setup used in all the experiments is reported (Fig. 5.1A). A magnification of the two-electrode arrangement is presented in Fig. 5.1B.
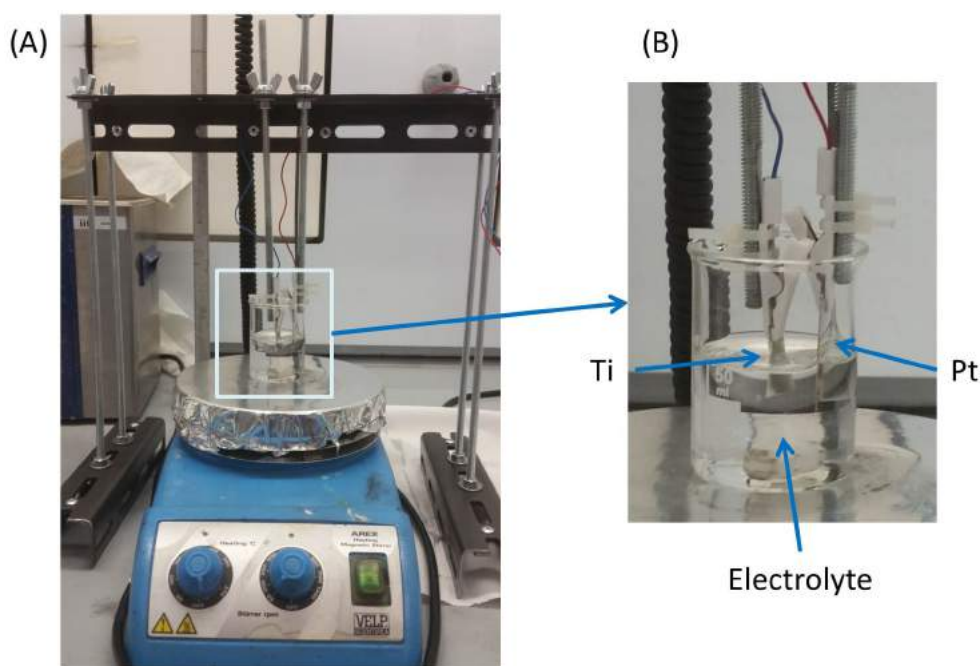
Fig. 5.1 Photograph of the anodic oxidation setup (A) used during the experiments and (B) magnification of the two-electrode configuration.

The electrolytic solution was prepared by mixing in ethylene glycol, 0.5 wt% of NH$_4$F and 2.5 vol% of deionized water, kept under stirring during the oxidation process. The electrochemical reaction was performed at a constant voltage of 60 V applied between the working electrode (Ti foil, WE) and the counter electrode (Pt foil, CE), put at a distance of about 1 cm. In order to obtain ordered TiO$_2$ NTs, a two-anodization process was employed [340]. The first anodization was performed for 7 minutes, followed by a strong ultra-sonication bath in de-ionized water in order to remove the NTs just grown and prepare a smooth honey-comb structure. Under identical parameters, a second anodization was performed for 5 minutes. After this, the Ti foil covered with NTs was rinsed in de-ionized water to remove the electrolyte residues.

Morphological characterization

In order to verify the quality of the synthesized NTs, morphological and compositional characterizations were conducted both before and after calcination of the catalyst.
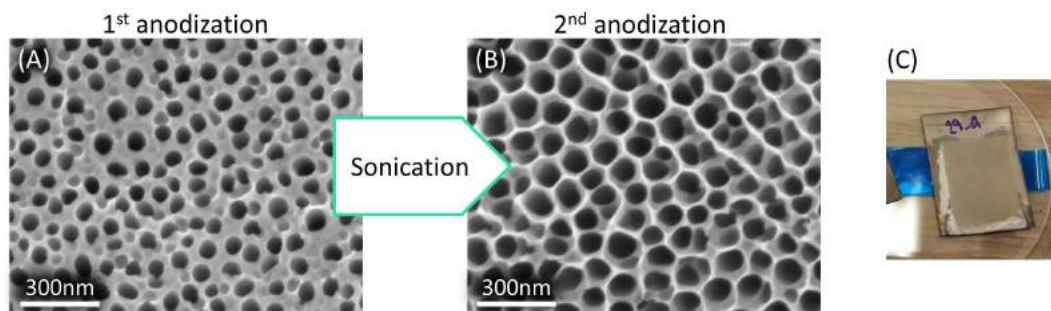
Fig. 5.2 Top view of the TiO$_2$ NTs after the first (A) and second (B) anodic oxidation steps on a Ti foil. (C) Example of the resulting TiO$_2$ nanotube sample (dimension 2x2.5 cm^2).

In Fig. 5.2 the FESEM images the top of the TiO$_2$ NTs after the first (Fig. 5.2A) and second anodic oxidation (Fig. 5.2B) are shown. Fig. 5.2A reveals a not-regular pattern of the array where both pits and nanotubes can be identified. After sonication and a second anodization (Fig. 5.2B), a more regular pattern is visible, composed by ordered NTs in a honey comb-like structure. The resulting sample is showed in the example in Fig. 5.2C, where the oxidized surface is the opaque rectangle.
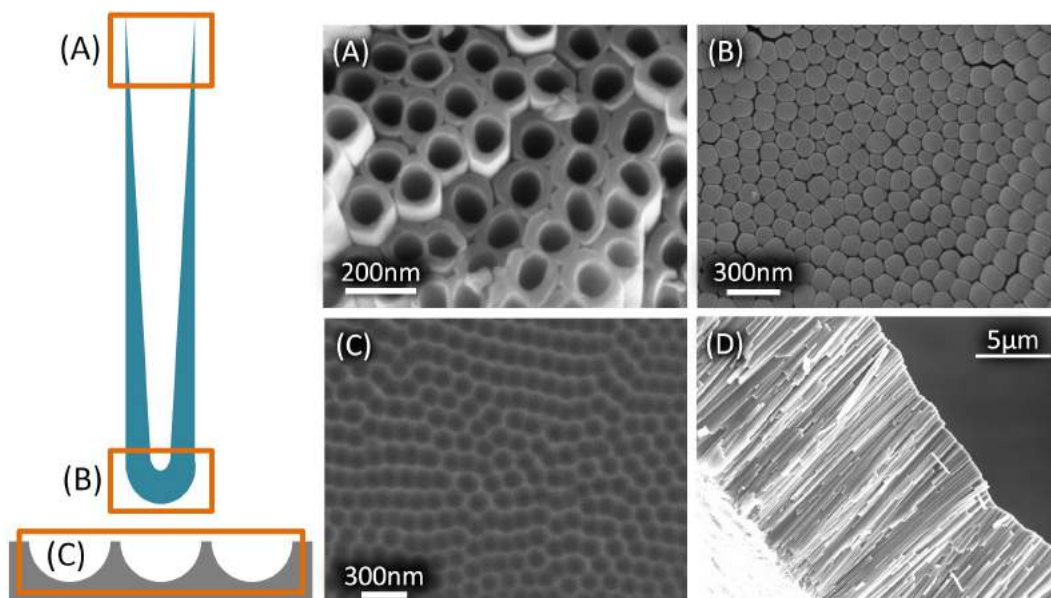
Fig. 5.3 Detailed FESEM images of the TiO$_2$ NTs sample: (A) top view, (B) bottom part of the nanotubes, (C) Ti foil surface after the ultra-sonication and removal of the NTs (depicted in grey in the drawing on the left side) and (D) vertical cross section of the NTs.

For a better comprehension, Fig. 5.3 shows the FESEM images of specific parts of the TiO$_2$ NTs sample. In particular, the hexagonally-packed assembly is clearly visible in Fig. 5.3A and B, which are the topmost and bottommost parts of the NTs, respectively. From the first panel, the average NTs wall thickness can be estimated to be about 30 nm, while the inner diameter is about 90 nm. The honey-comb structure can be found also on the surface of the Ti foil, after the sonication step, as showed in Fig. 5.3C. This structure permits the formation of a regular pattern during the second anodization, becoming the starting pits of the new nanotubes. Thanks to a 5 minute anodization, as already said, 15 μm TiO$_2$ nanotubes were obtained (see Fig. 5.3D), well aligned and with a smooth surface. When the anodization time was extended up to 1h, chemical etching of the outermost (formed earlier) tube parts took place, as showed in Fig. 5.4. This process drawback leads to substantial thinning and finally disintegration of the tube walls, revealing a "nanograss" appearance on the top of the tubes. From Fig. 5.4C, it can be noticed that the nanotube walls became so thin that they reached the electron transparency: in fact in some areas underlying walls can be identified.
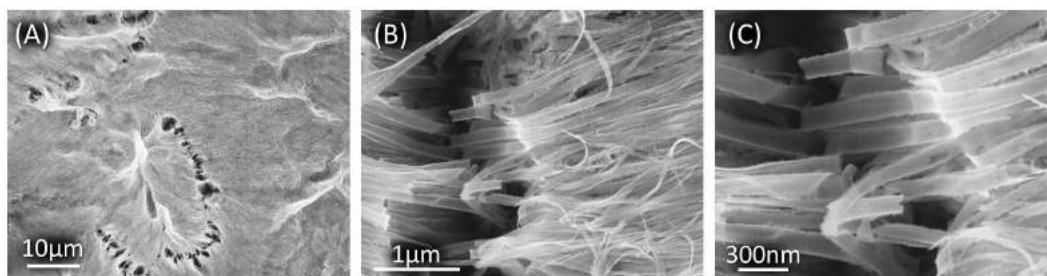
Fig. 5.4 FESEM images of 1h anodic oxidation with the "nanograss" formation.

Thanks to the two-step anodization process, the electrochemical growth of the NTs array is fast, leading to a more ordered distribution [341] due to the presence of holes (Fig. 5.3C) formed after the removal of the first anodized layer. Moreover, the length of the TiO$_2$ NTs array depends strongly on the anodization time with a well known linear trend [342]. For these reasons, this study focuses on titania nanotubes grown with short anodization times: less than ten minutes each in order to maintain the overall catalyst resistance low.

In order to obtain the TiO$_2$ crystallization, the prepared samples were annealed for 4 hours in air atmosphere (heating rate: 1°C/min) by means of a vertical furnace (Carbolite, VST 12/300/3216) at two different temperatures: 450°C and 600°C. The first one should lead to the formation of pure anatase phase, while the second to both anatase and rutile phases. In this thesis, the first set of samples will be referred as TiO$_2$_450, while the second as TiO$_2$_600. In Fig. 5.5 a comparison of the TiO$_2$ NTs samples before (Fig. 5.5A and D) and after the calcination step at 450°C (Fig. 5.5B and E) and 600°C (Fig. 5.5C and G) is shown.

By comparing the low magnification panels, it can be noticed that the calcination in air leads to the cracking of the TiO$_2$ array, while increasing temperature. This phenomenon may be due to the lattice rearrangement between the amorphous titanium
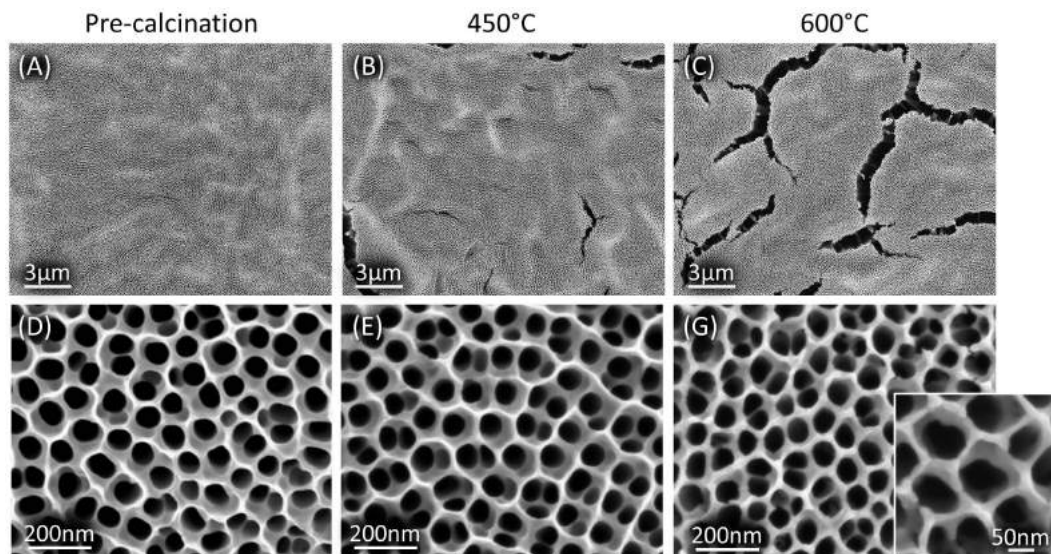
Fig. 5.5 FESEM images of the comparison between the TiO$_2$ NTs samples before (A and D) and after the calcination step at 450°C (TiO$_2$_450, B and E) and 600°C (TiO$_2$_600, C and G). The inset of (G) shows a magnification of the NTs top layer.

dioxide and crystalline one (both anatase and rutile). Comparing the higher magnification panels, no substantial difference can be identified between Fig. 5.5D and E. On the other side, Fig. 5.5G evidences the formation of cracks at the outermost part of the tubes, maybe related to the presence of a second phase.

Compositional characterization

In order to verify the composition of the calcined TiO$_2$ NTs, XRD characterization was performed on the two samples. Fig. 5.6 shows the spectra for the samples TiO$_2$_450 (black curve) and TiO$_2$_600 (red curve). As a general comment, diffraction peaks corresponding to titanium and TiO$_2$ in anatase phase can be identified in both samples. For more simplicity, in the XRD spectra, the anatase and rutile phases are indicated with the capital letters A and R, respectively.

In both samples, Ti related peaks appear at 2θ values of about 38.5°, 70.7°, 40.2°, 53°, 29.3°, 76.2°, 35.2°, 63°, 83.2° and 77.4° in order of decreasing intensity (JCPDS 89-5009). In the TiO$_2$_450, only the anatase-related peaks are present at 2θ values of about 38°, 25.5°, 54.1°, 48.2°, 37.1°, 69° and 55.4° (in order of decreasing intensity), corresponding to the (004), (101), (105), (200), (103), (116) and (211) planes (JCPDS 89-4221), respectively. On the contrary, in TiO$_2$_600 sample an other phase can be identified in addition to anatase, i.e. rutile. The peaks related to this phase appear at 2θ values of about 27.5°, 39.3°, 69°, 36° (in order of decreasing intensity), corresponding to the (110), (200), (301) and (101) planes (JCPDS 89-4202), respectively. From these results it is confirmed that the pure anatase phase is obtained at 450°C, while at higher calcination temperature, a second phases starts
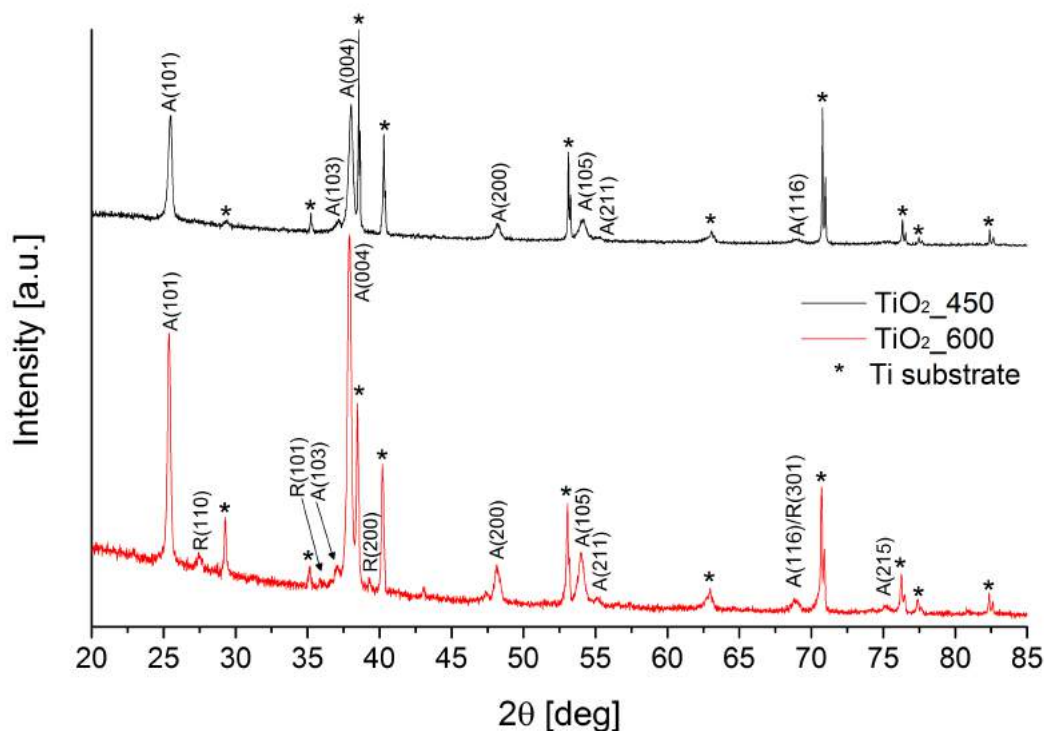
Fig. 5.6 XRD spectra of the calcined samples: TiO$_2$_450 (black curve) and TiO$_2$_600 (red curve). With the letter A is indicated the anatase phase, with R the rutile one.

to crystallize. In the case of the TiO$_2$_450 spectra, the TiO$_2$ peaks appear to be defined but a bit broad. This is related to the small size of the anatase crystals in the sample. Because of their low size, they are also not visible in the presented FESEM images, as already showed in Fig. 5.5E. When the calcination temperature is increased, TiO$_2$_600 sample, the anatase peaks rise in intensity and become more sharp. This means that the crystals became bigger than the previous sample, while the rutile crystals have a smaller size, indicated by the broad shape of the peaks. The anatase crystal growth may be the possible cause of the cracking of the NTs carpet.

Because of the better TiO$_2$ sample integrity and the presence of a pure phase, this work will be focused on the anatase samples calcined at 450°C from now on.

5.2.2   Cu and Cu$_x$O supported on TiO$_2$ NTs

In the photo-electrocatalysis, titania is the most studied semiconductor for both CO$_2$ reduction reaction and water splitting. However, it's efficiency is limited due to the large electron-hole recombination phenomena and the large band gap (3.2 eV) which limits the absorption spectra in the UV range. Moreover, when considering the CO$_2$RR in aqueous electrolytes, hydrogen formation is the preferential competitive process due to its high rate of formation if compared to the carbon dioxide reduction (see Sec. 2.4.2). The best strategy, in order to limit the H$_2$ production and shift the

selectivity toward CO$_2$ reduction, is coupling of TiO$_2$ with co-catalysts such as Pt, Ag, Au or Cu [343–346]. In spite of these recent advances, few studies have reported all the binary combinations (Metal + TiO$_2$) for CO$_2$RR. It has been proposed that the presence of copper and gold co-catalysts on TiO$_2$ increases the efficiency of the CO$_2$RR, producing mainly methane with a good selectivity, up to 44 μmol·h^{-1}·g^{-1} [344].

For these reasons, copper supported on TiO$_2$ has been chosen as first testing material for the carbon dioxide reduction. The as-prepared TiO$_2$ samples, after the annealing step, were coated with Cu by means of a sputter coater (Quorum Technologies, Q150T ES), as described in Sec. 3.3.4. The copper sputtering lasted 128 s and the prepared samples are named TiO$_2$_Cu.

A second set of samples, called TiO$_2$_Cu_450, are also presented in order to study a possible binary combination of oxides. These samples were prepared starting from TiO$_2$_Cu and calcining them at 450° in order to oxidize copper in air atmosphere (heating rate: 1°C/min) by means of a vertical furnace (Carbolite, VST 12/300/3216). In the following sections a complete characterization, in term of morphology, composition and catalytic activity, for both TiO$_2$_Cu and TiO$_2$_Cu_450 will be discussed. The samples described in the previous sections are summarized in Table 5.1, with their names and the main process steps.

Sample name	1st calcination	Cu deposition	2nd calcination
TiO$_2$	-	No	-
TiO$_2$_450	450°C	No	-
TiO$_2$_600	600°C	No	-
TiO$_2$_Cu	450°C	Yes	-
TiO$_2$_Cu_450	450°C	Yes	450°C

Table 5.1 Summary of the TiO$_2$ NTs -based samples.

Morphological characterization

FESEM images copper supported on titania samples, TiO$_2$_Cu, are presented in Fig. 5.7. From low magnification panels, the not uniformity of the metallic deposition can be noticed. In fact, copper tends to accumulate at the outer edges of the NTs, apparently not clogging the tubes nor penetrating into them (Fig. 5.7C and D). This means that the sample surface will be mostly constituted of TiO$_2$ because the exposed inner tube surface will be the prevailing one. Thanks to the low-current sputtering process, the Cu could grow forming small crystals and following the initial titania nanostructure, as demonstrated in Fig.5.7D.

In order to evaluate the elemental distribution after the deposition process, a qualitative EDX map was done as presented in Fig. 5.8. It can be observed that titanium and oxygen (cyan and yellow colors, respectively) have a quite uniform distribution all over the analyzed area. The uniformity can be appreciated in the
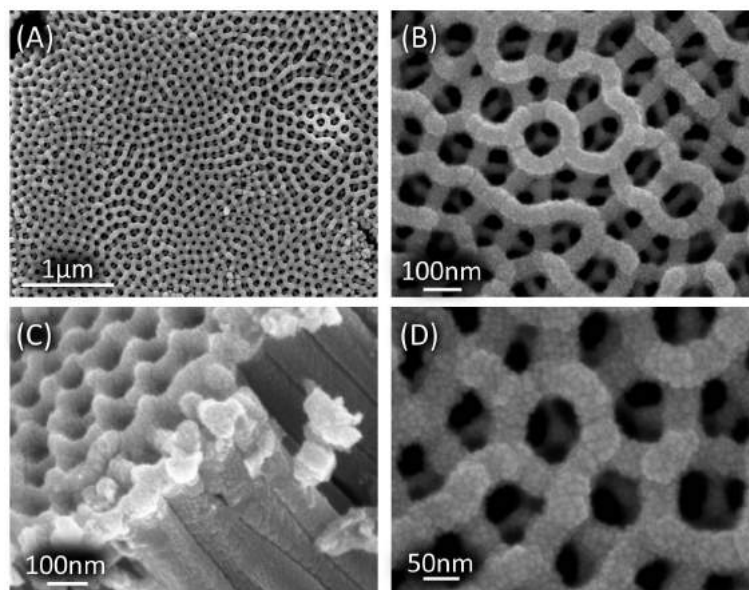
Fig. 5.7 FESEM images of TiO$_2$_Cu at different magnifications.

panel on right side (FESEM + O, Fig. 5.8), where oxygen can be detected all over the analyzed area. On the other side, copper (green color) shows a signal coming mostly from the outer edges of the TiO$_2$ NTs. The measured atomic percentages of the elements are about 4%, 35% and 61% for Cu, Ti and O, respectively. Unfortunately, as well known, this technique is not able to determine whether the oxygen is bond to only titanium or also to copper.

The same characterizations were performed also for the annealed samples called TiO$_2$_Cu_450, as showed in Fig. 5.9 and 5.10. In the FESEM images (Fig. 5.9) the deposited and oxidized layer show a not uniform distribution, as the TiO$_2$_Cu sample, with a prevailing copper oxide accumulation onto the outer edges of the NTs. Differently from the uncalcinated samples, the top of TiO$_2$ NTs appear to be more clogged due to the expansion of copper during its oxidation. Fig. 5.9C shows a slight penetration of the Cu$_x$O into the tubes of the order of 100 nm, not enough to cover the whole nanotube inner length, which is two orders of magnitude higher.

Fig. 5.10 shows the EDX map of the TiO$_2$_Cu_450. Differently from the previous sample, in this case both copper and oxygen (green and yellow colors, respectively) show a prevailing signal coming from the outer edges of the NTs, while titanium (cyan color) continues to be uniform all over the analyzed area. The not uniform distribution can be observed in the panel on right side (FESEM + O, Fig. 5.8), where the oxygen signal comes mostly from the outer edges of the TiO$_2$ NTs. In this case, copper could be assumed as oxidized, but it cannot be said with certainty if the oxide is formed. The measured atomic percentages of the elements are about 3%, 32% and 65% for Cu, Ti and O, respectively.

In order to study the crystalline evolution during the copper oxidation, STEM and TEM characterization were performed on a lamella cut from the sample TiO$_2$_Cu
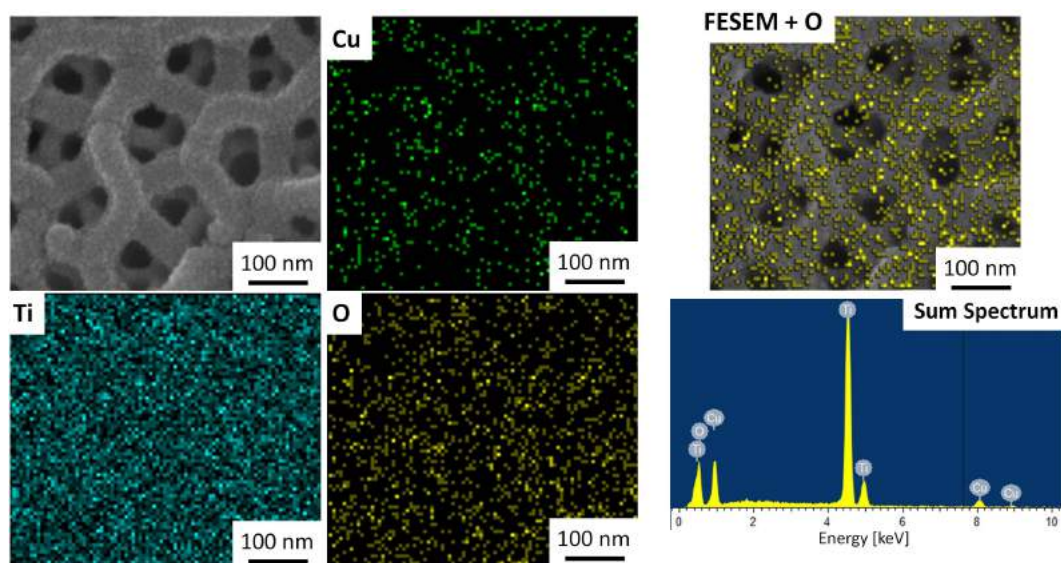
Fig. 5.8 Qualitative EDX map of TiO$_2$_Cu sample in false colors: green for Cu, cyan for Ti and yellow for O. On the right side a superimposition of FESEM and oxygen images is proposed. On the lower right it is reported the sum spectrum correspondent to the EDX map.
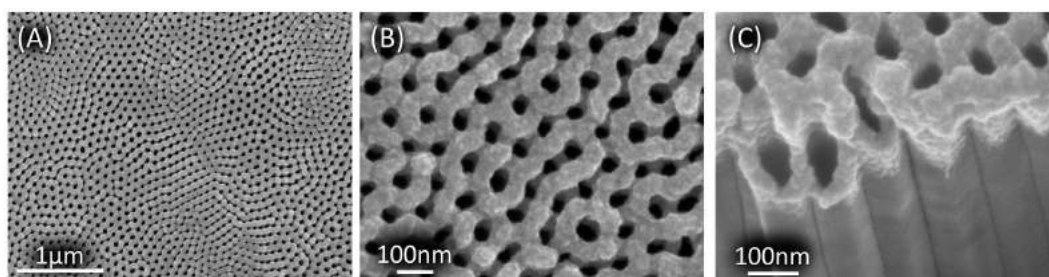
Fig. 5.9 FESEM images of TiO$_2$_Cu_450 at different magnifications.

with Focused Ion Beam. The specimen was prepared in order to be electron-transparent as described in App. A.1.1. The prepared lamella was analyzed and calcined by using a TEM sample holder (Denssolutions) for the ex-situ heating in air at the KAUST (King Abdullah University of Science and Technology, Saudi Arabia) as described in App. A.1. The calcination was performed in two steps 225°C and 450°C, to better follow the crystalline evolution, in air atmosphere (heating rate: 4 °C/min) for 30 minutes each temperature.

In Fig. 5.11 the STEM images of the sample TiO$_2$_Cu at room temperature (panels A, D, G), calcined at 225°C (panels B, E, H) and at 450°C (panels C, F, I) are reported.

In the STEM low-magnification images (Fig. 5.11A-C), 3 different layers can be evidenced: Ti on left, TiO$_2$ NTs in the middle and Pt on the right (present because of the lamella preparation). At high magnification, the well defined NTs structure can be appreciated both at the bottom of the tubes (Fig. 5.11D-F) and at the top (Fig.
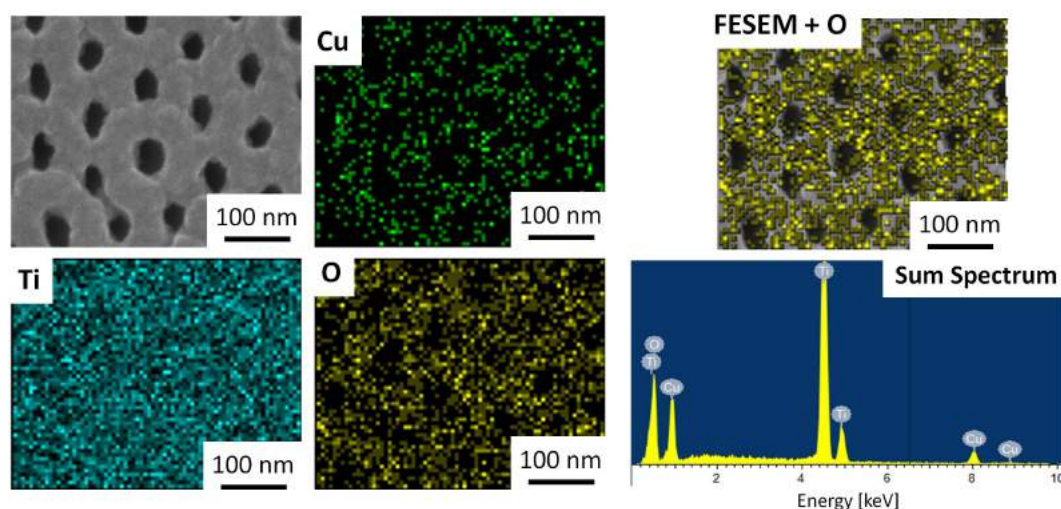
Fig. 5.10 EDX map of TiO$_2$_Cu_450 sample in false colors: green for Cu, cyan for Ti and yellow for O. On the right side a superimposition of FESEM and oxygen images is proposed. On the lower right it is reported the sum spectrum correspondent to the EDX map.

5.11G-I). By comparing the images collected for the amorphous (as prepared) and crystalline samples, it is possible to put in evidence a change in the contrast probably due to contribution of crystal edges, different crystalline orientation, or defects, that change the electron channelling across the different crystals. In particular, at the NTs bottom, it can be noticed a contrast change due to the calcination, evidencing the presence of a crystalline phase. In the topmost layer (Fig. 5.11G-I), the crystallization is more evident, especially at the highest temperature (panel I).

In Fig. 5.12 are presented three different TEM images at the position indicated in orange on the blue NT (left side), with their diffraction patterns (panels D-F) and an HRTEM (panel G). With yellow boxes, the area where diffraction patterns were performed are highlighted. As a general comment, it can be said that the NT is crystalline, after the thermal treatment. In fact, this is indicated by the presence of spots and rings in the diffraction patterns reported. However, in the three zones, A, B and C, the electron diffraction pattern is mostly related to the TiO$_2$ anatase. No clear evidence of copper oxide was found, also because of the partial superposition of same spots, even though the presence of Cu was confirmed by EDX.
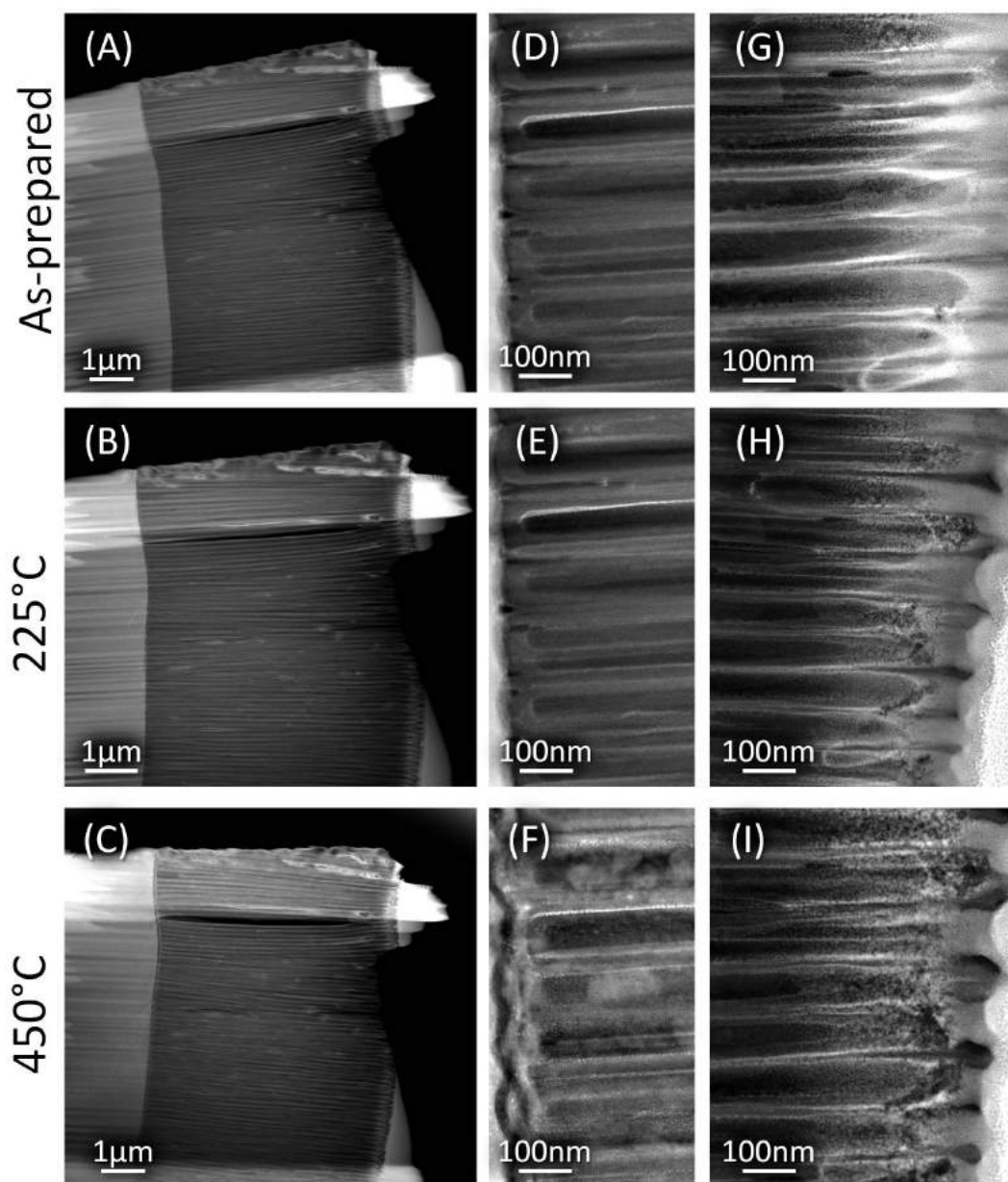
Fig. 5.11 STEM images of the sample TiO$_2$_Cu uncalcined (A, D, G), calcined at 225°C (B, E, H) and at 450°C (C, F, I) collected with an HAADF detector.
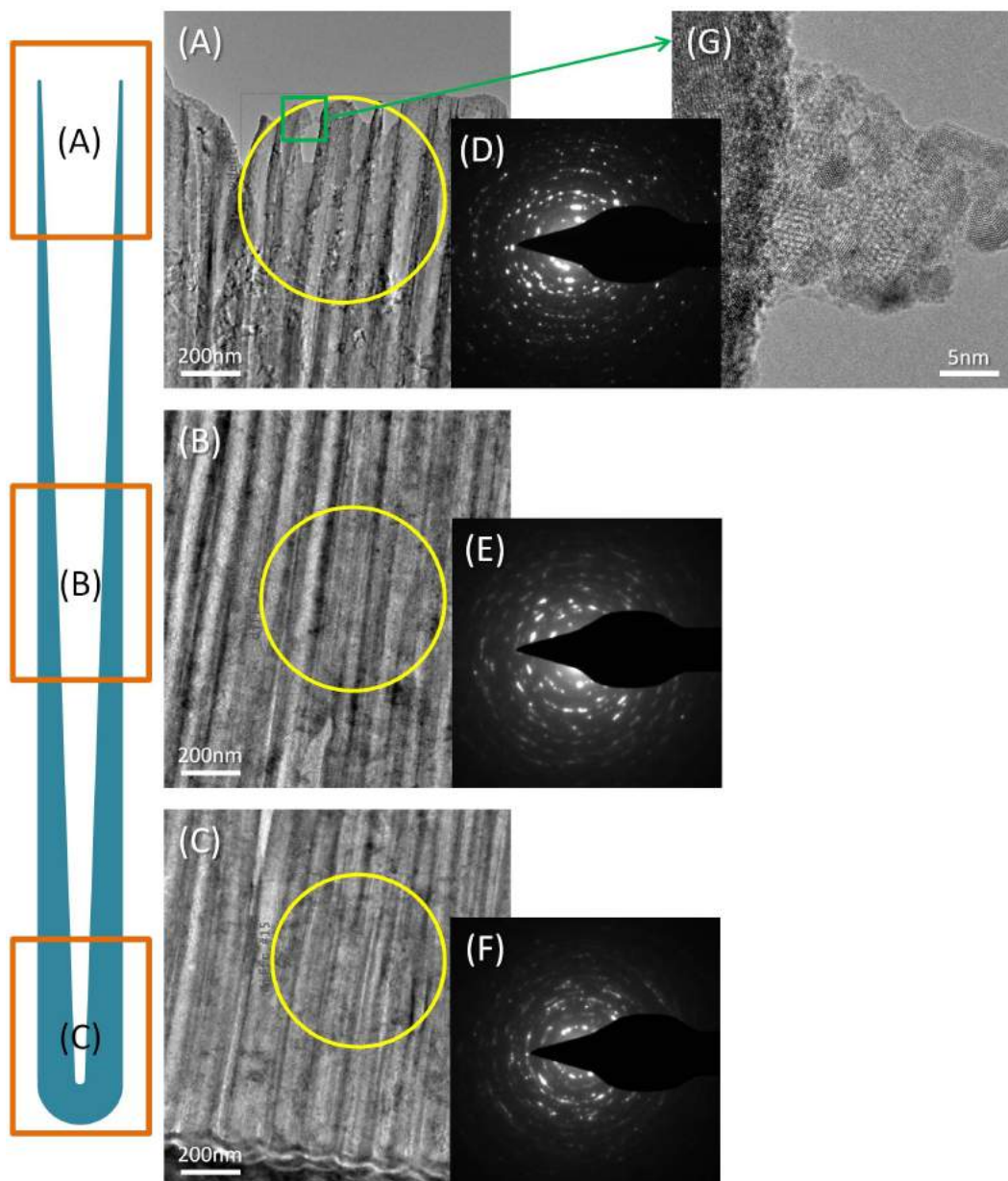
Fig. 5.12 Cross-sectional TEM image of the TiO$_2$_Cu_450 at different nanotube position: (A) top, (B) middle, (C) bottom, with their diffraction pattern D, E, F, respectively. Yellow circles in A, B, C panels indicate the areas in which electron diffraction was performed. (G) Higher magnification of the top NT region.

Compositional characterization

In order to verify the composition of the Cu and Cu$_x$O supported on TiO$_2$ NTs, XRD characterization was performed on both samples and compared with the TiO$_2$_450, as reference.

Fig. 5.13 shows the spectra for the samples TiO$_2$_Cu (black curve) and TiO$_2$_450 (red curve). Both samples show diffraction peaks corresponding to titanium (indicated with "*") and TiO$_2$ anatase phase (indicated with the letter "A"), but no evident peaks for Cu can be clearly identified probably because of the small quantity. Ti and TiO$_2$ peaks appear at the same 2θ positions of the ones reported in Sec. 5.2.1 and for this reason, they will not be reported here. As a main difference, it can be observed that the anatase-related peaks for the TiO$_2$_Cu sample are lower in intensity than the TiO$_2$_450 sample (all the samples were normalized for the more intense Ti peak, being the thickness of the different sample almost equal). Even if the copper is not visible in the XRD spectra, the copper presence was already demonstrated by the EDX maps presented in Fig. 5.8.
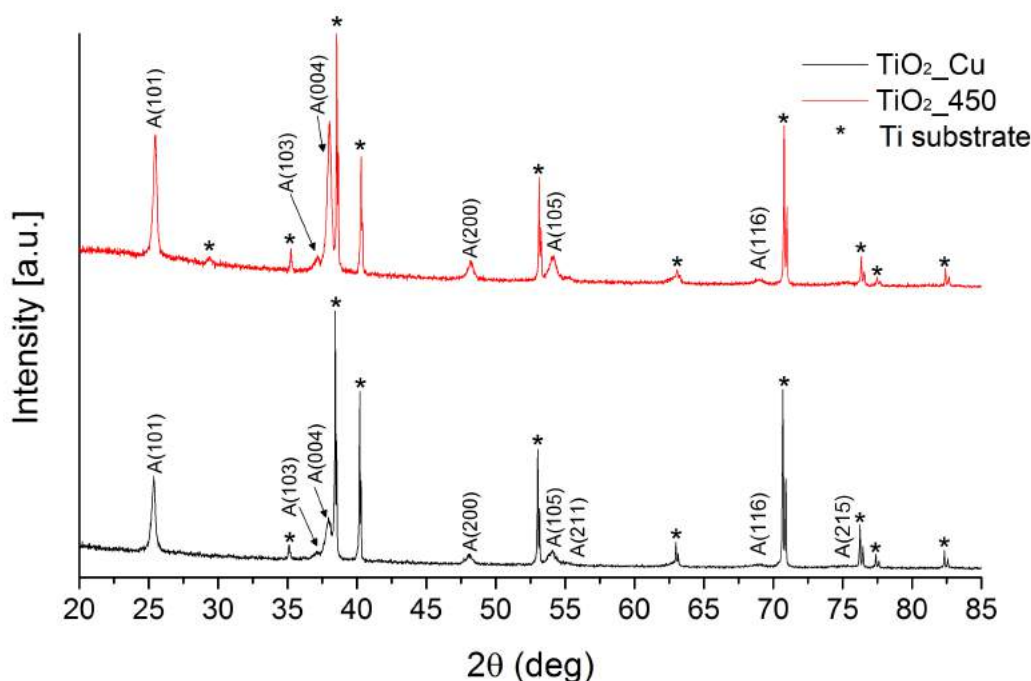
Fig. 5.13 XRD spectra of the TiO$_2$_Cu (black curve) and TiO$_2$_450 (red curve) samples. With the letter A is indicated the anatase phase.

The XRD spectrum of the TiO$_2$_Cu_450 sample is reported in Fig. 5.14 (black curve), compared with the TiO$_2$_450 (red curve), as reference. Also in this case, the presence of Ti and TiO$_2$ anatase phase may be identified, but they will not be reported (see. Sec. 5.2.1). In the new sample, the anatase phase is less intense that the TiO$_2$_450 sample, and, also in this case, the copper oxide presence cannot be reported, because of the lower amount with respect to the titania one. Nevertheless,

it is reasonable to suppose that a mixture of CuO and Cu_2O is present onto the NTs carpet because of the color change after the annealing (from metallic copper to black/brown) and because of the presence of Cu in the EDX spectra (Fig. 5.10).
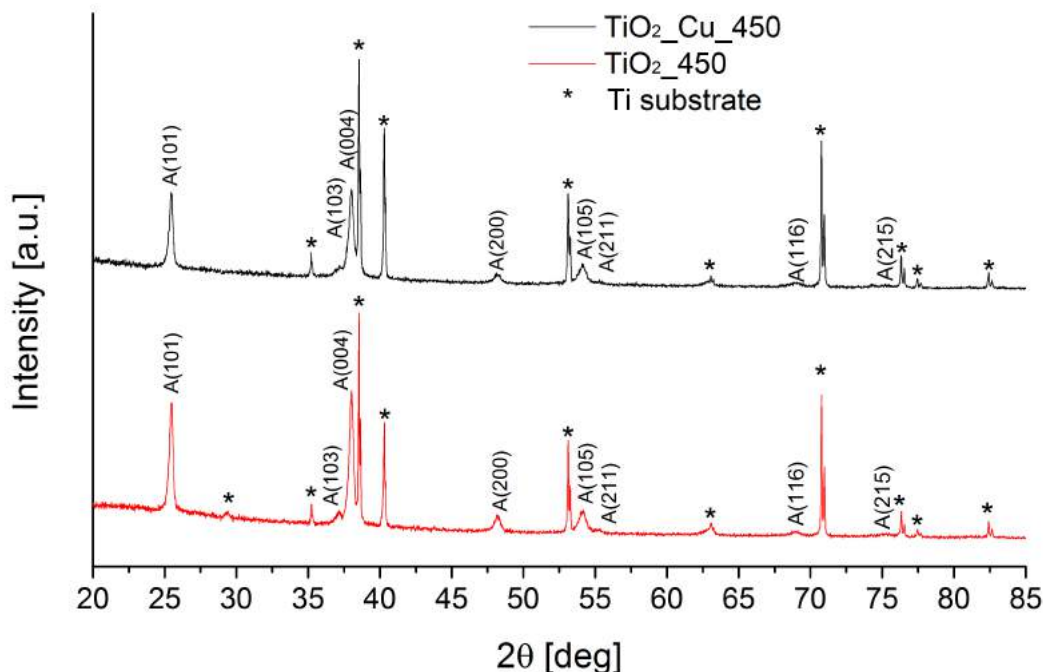
Fig. 5.14 XRD spectra of the $TiO_2\_Cu\_450$ (black curve) and TiO_2_450 (red curve) samples. With the letter A is indicated the anatase phase.

Electrochemical characterization

In order to verify the catalytic properties of the prepared samples, the electronic structure and band alignment should be investigated. In order to correctly draw the electronic band structure of a semiconducting material, *ab initio* or FEM simulations should be performed. These methods take into account the nanoscaled dimensions of the materials, starting from theoretical assumptions. In this thesis, only experimental observations and measures are performed, compared with the theoretic band alignments of the bulk materials; however, the energy levels may be shifted in case of nanometric or nanostructured materials. In Fig. 5.15 and 5.16 are drawn the theoretic band alignments of the TiO_2_Cu and $TiO_2\_Cu\_450$ samples, respectively, before and after thermal equilibrium under the hypothesis of bulk materials.

Focusing on Fig. 5.15B, it can be clearly noticed that the TiO_2 Conduction Band (CB) should be curved downward, when placed at thermal equilibrium with Cu. This should favor the accumulation of electrons e^- in the copper layer, therefore on the surface of the catalyst. The electrons can be generated both electrically (applying an external potential) and under light stimulation (sun illumination). On the other side,
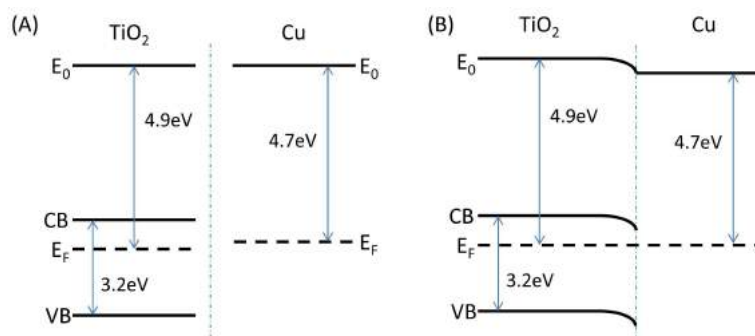
Fig. 5.15 Theoretic band alignment for a TiO$_2$/Cu bulk sample before (A) and after (B) thermal equilibrium.

the holes h$^+$ should flow in the opposite direction, toward the Valence Band of the TiO$_2$, ensuring a correct charge separation.
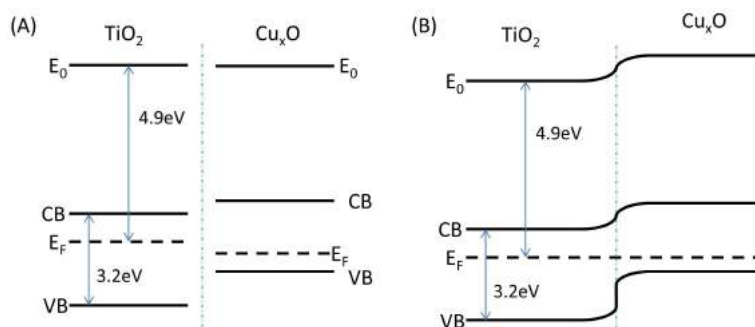
Fig. 5.16 Theoretic band alignment for a TiO$_2$/Cu$_x$O bulk sample before (A) and after (B) thermal equilibrium.

On the contrary, when Cu$_x$O is put at thermal equilibrium with TiO$_2$, the copper oxide CB lies above the titania one. This means that the e$^-$ are not energetically favored to reach the material surface unless an external force is applied. It can be, in fact, an external potential applied between an anode and a cathode (the TiO$_2$_Cu_450 sample), in magnitude higher than the flat band potential of the drawn p-n junction. This would ensure the correct charge separation, similar to the previous sample.

As a starting point, spectrophotometer measures were conducted as described in App. A.7 in order to calculate the samples' band gaps, by measuring the optical absorption spectra of the material. As it was reasonable to suppose, that it was possible to measure only the direct band gap of the TiO$_2$_Cu sample, as reported in the Tauc plot in Fig. 5.17. In fact, metallic copper gave no contribution to absorbance, having no band gap, and only one linear fit could be drawn, whose intercept with the x axis is the material's direct band gaps. The *Linear Fit* intercept is at about (3.03± 0.06) eV and may correspond to the TiO$_2$ direct band gap.

Considering the annealed sample, TiO$_2$_Cu_450, it could be possible to identify 3 linear parts in the Tauc plot in Fig. 5.18. Two fits might be drawn in direct Tauc
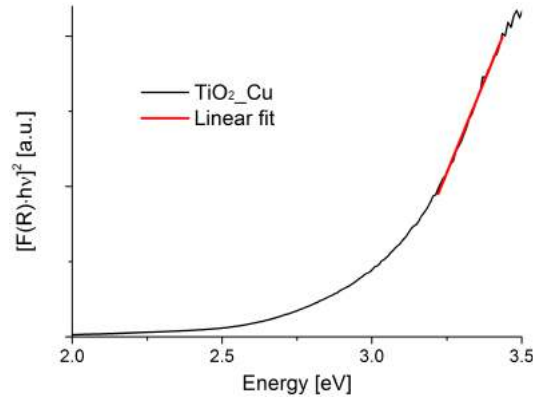
Fig. 5.17 Tauc plots of TiO$_2$_Cu sample for the direct band gap in black, linear fits applied in red.
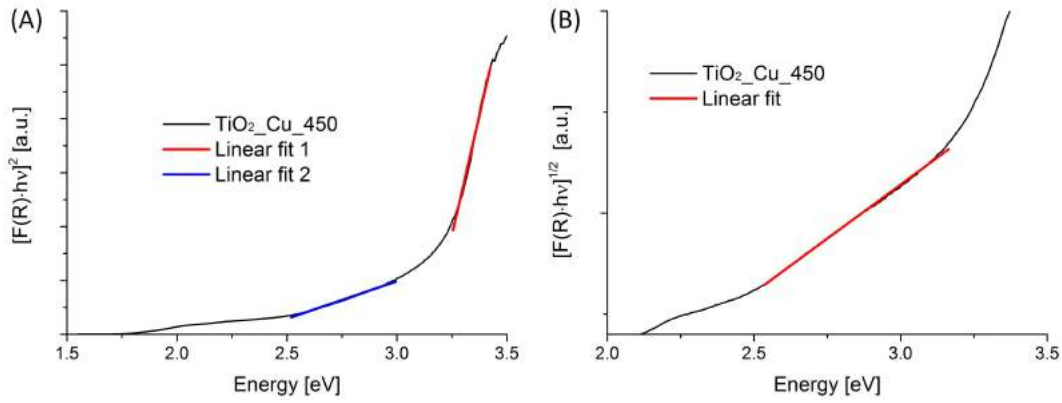
Fig. 5.18 Tauc plots of TiO$_2$_Cu_450 sample. (A) Tauc plot for the direct band gaps in black, linear fits applied in red and blue. (B) Tauc plot for the indirect band gap in black, linear fit applied in red.

plot and one in the indirect one. However, it has to be considered that the smallest band gap is the one that absorbs the majority of photons during the characterization. The other two gaps may be detected but with a much lower detection efficiency than the smallest, and so precision. Focusing on the Tauc plot for the direct band gap (Fig. 5.18A), two linear fits can be drawn, whose intercept with the x axis are at about (3.15 ± 0.10) eV and (2.29 ± 0.07) eV for the *Linear Fit 1* and *Linear Fit 2*, respectively. Instead, the *Linear Fit* of the Tauc plot for the indirect band gap (Fig. 5.18B) intercepts the x axis at about (1.48 ± 0.02) eV, attributable to the CuO indirect band gap with enough reliability, being the smallest gap value. The first two values, 3.15 eV and 2.29 eV, could be attributed to the TiO$_2$ and Cu$_2$O direct band gaps, being values similar to the bulk ones.

In general, it can be said that due to the nanostructuration and nanoscale dimension of the materials taken into account, the band gap values are slightly different from the bulk one. However, in order to calculate the nano-dimentions influence,

simulations should be done, as already stated. Knowing the band gap values gives the possibility of using the samples not only as electro-catalysts (as it will be further discussed), but also as photo-catalyst being able to select the proper absorption range, hopefully the visible one. This second possibility, however, was not exploited in this study.

In order to draw an approximation of the samples band diagram, the flat band potential V_{FB}, i.e. the difference between the Fermi levels of the catalysts material and the solution in which it is immersed, is needed. This kind of experiment can be done through the Mott-Schottky measure as it is described in App. A.4.5. Moreover, XPS (X-ray Photoelectron Spectroscopy) can provide data of the position of the conduction band of the catalysts. Knowing the energy levels position could give a more precise indication of the possible byproduct of the CO$_2$RR during working condition. In fact, knowing the position of the conduction band of the material in contact with the solution, it is possible to determine the correct reaction occurring on the catalyst surface (table 2.1).
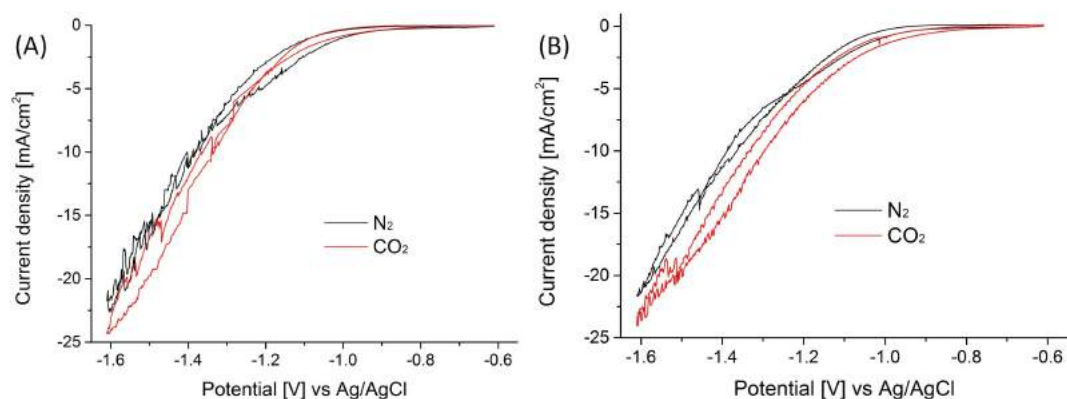
Fig. 5.19 CV of the samples: (A) TiO$_2$_Cu and (B) TiO$_2$_Cu_450. The black lines represent the CV under N$_2$, while the red lines under CO$_2$. Scan rate: 10 mV/s.

For a preliminary catalyst characterization, cyclic voltammetries were conducted to study the catalytic behavior of the three sets of sample as reported in Fig. 5.19, as described in App. A.4.4. As a general comment, both TiO$_2$_Cu (Fig. 5.19A) and TiO$_2$_Cu_450 (Fig. 5.19B) samples exhibit a quite similar CV shape for the nitrogen-saturated solution and for the carbon dioxide-saturated curves. For both samples it has to be taken into account that most of the exposed surface is composed of TiO$_2$, having no penetration of Cu or Cu$_x$O inside the tubes. This may lead to a less selectivity of the sample toward CO$_2$RR, while enhancing the HER. Having an high titanium dioxide contribution, the CV curves seem to be quite similar, showing the same current density at -1.6V.

In Table 5.2 are reported the results of the tests conducted on the samples TiO$_2$_Cu and TiO$_2$_Cu_450 at different potentials. The first set of tests were conducted by setting the potentials thanks to the chonoamperometric test, better explained in App. A.5.2, and done in order to study the kinetics of chemical reactions and determine the potential at which this reaction occurs. In the second set of tests,

the Faradaic Efficiencies (FE), reported with their absolute error, were calculated (see App. A.5.1) thanks to the measured gaseous byproducts by the μ-GC (see App. A.5).

Sample	Potential [V]	FE H$_2$ [%]	Δ(FE H$_2$) [%]	FE CO [%]	Δ(FE CO) [%]
TiO$_2$_Cu	-1.6	97	6	1	0.1
	-1.8	84	4	-	-
TiO$_2$_Cu_450	-1.6	101	8	1	0.1

Table 5.2 Summary of the quantity of byproducts measured for the TiO$_2$_Cu and TiO$_2$_Cu_450 samples through μ-GC test.

As a general comment, the experimental results at the different potentials are not so much encouraging for the samples TiO$_2$_Cu and TiO$_2$_Cu_450. In fact, at -1.6 V, the hydrogen production for both samples is close to 100%. While, at a lower potential, -1.8 V, the H$_2$ production lowers to 84% for TiO$_2$_Cu. The remaining 16% can be attributed to some liquid byproduct, but in any case it won't be analyzed being not efficient for CO$_2$RR. The possible explanation of such a bad behavior of the sample TiO$_2$_Cu is that the co-catalyst detached from TiO$_2$, thus not contributing to the catalytic process. Such hypothesis is partially confirmed by FESEM characterization in Fig. 5.7, showing the catalyst after the electrochemical test. Comparing these images with the former ones, Fig. 5.7, it is clearly evident that the copper detached from the underlying NTs, probably due to a not good adhesion of Cu on TiO$_2$ NTs.
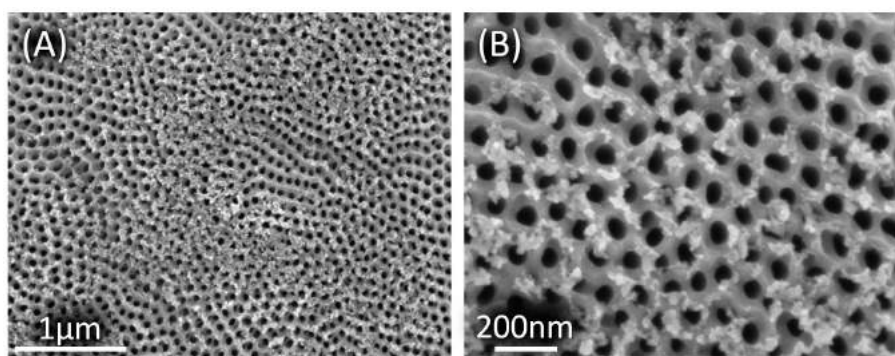
Fig. 5.20 FESEM image of the TiO$_2$_Cu sample after 50 min cycling.

5.3   Cu$_x$O NWs-based catalysts

5.3.1   Cu$_x$O NWs

Nanostrucured Cu$_x$O electrodes were synthesized from copper foils by thermal oxidation in air for 30 minutes at different temperatures, starting from pieces of (1x1.5) cm^2. The copper substrates were cleaned in acetone and ethanol under an ultrasonic bath for 5 min each. After drying by N$_2$ flow, they were loaded into a vertical furnace (Carbolite, VST 12/300/3216) with an heating rate of 5°C/min. Depending on the final oxidation temperature, 400°C, 500°C and 600°C, 3 sets of samples were obtained and named Cu_400, Cu_500 and Cu_600, respectively.

In order to obtain an electrode active area of 1 cm^2, Kapton® tape was used to mask the samples.

Morphological characterization

After the annealing step, it was expected [297] that the copper foils surface would be oxidized, resulting in a nanowire structuration on the surface. In Fig. 5.21 are shown three different magnifications of the Cu_400 sample obtained by FESEM. It can be noticed that rarely distributed NWs are present, together with a slight oxide nanostructuration of the sample surface. The nanowires diameter is around 10 nm, while length ranges from few tens of nm up to hundreds of nm, but not as dense as expected.
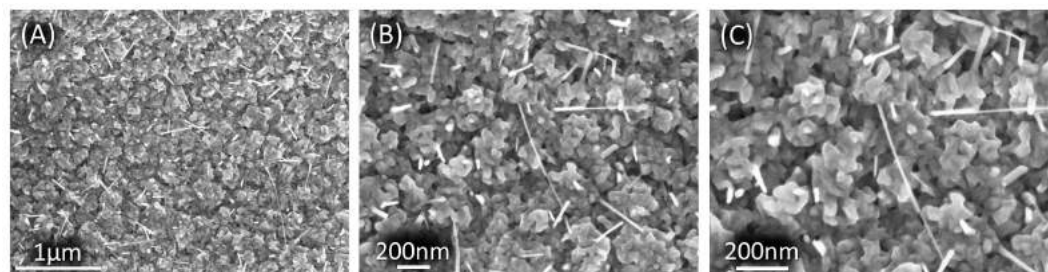
Fig. 5.21 FESEM images of Cu_400 at different magnifications.

FESEM images of the Cu_500 sample are presented in Fig. 5.22. The higher annealing temperature led to a denser distribution of the NWs if compared to Cu_400. Also in this case, a rough nastructutured surface is present under the NWs carpet. As can be seen from Fig. 5.22D, the NWs length is about 1 μm, with and average diameter of about 50 nm.

When the oxidation temperature is increased up to 600°C, the NWs are almost absent (see Fig. 5.23). The electrode surface, instead, is covered by a porous-like nanostructure, with larger grains. In fact, grain boundaries can be clearly seen in Fig. 5.23D (right side). The few NWs grown present a length between 400 - 700 nm.
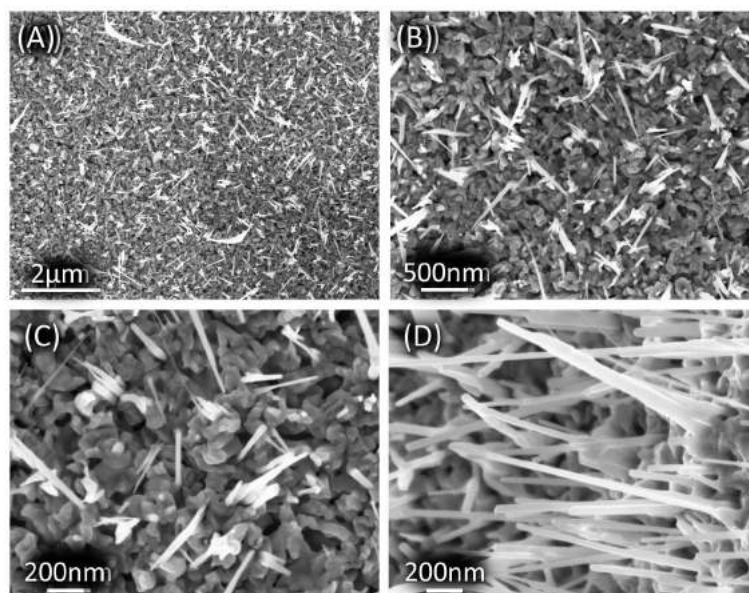
Fig. 5.22 FESEM images of Cu_500 at different magnifications.

However, their shape is quite different from the Cu_400 and Cu_500: they are bend with a rounded tip at the apex (see Fig. 5.23D).
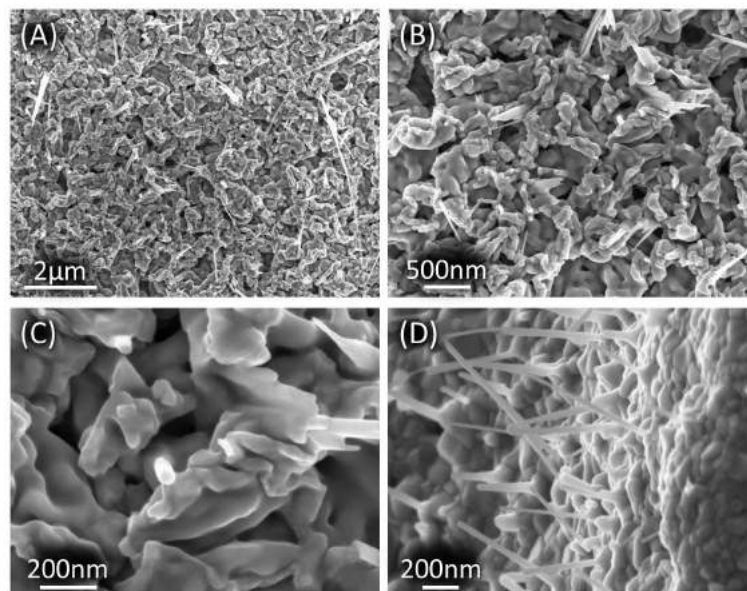
Fig. 5.23 FESEM images of Cu_600 at different magnifications.

Compositional characterization

In order to verify the composition of the oxidized Cu foils, XRD characterization was performed on the three samples. Fig. 5.24 shows the spectra for the samples Cu_400 (black curve), Cu_500 (red curve) and Cu_600 (green curve). As a first comment, diffraction peaks corresponding to both the copper oxides (CuO and Cu$_2$O) can be found, together with pure Cu phases (substrate).
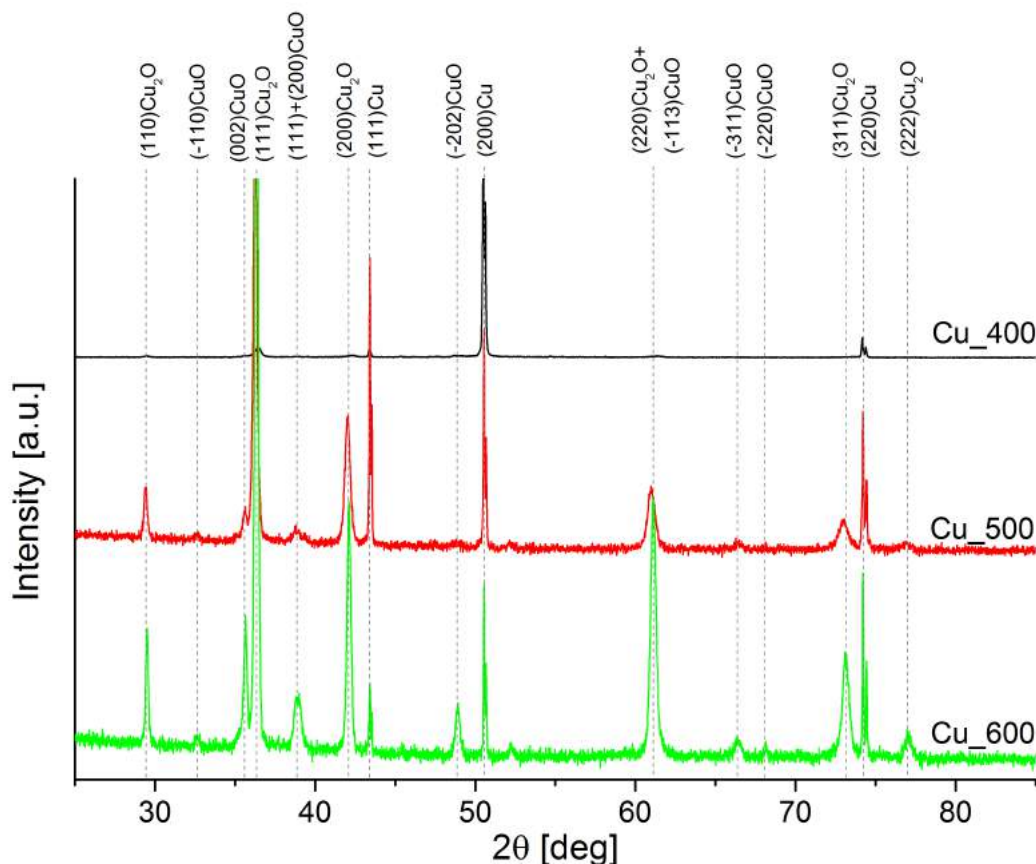
Fig. 5.24 XRD spectra of the thermally oxidized copper samples: Cu_400 (black curve), Cu_500 (red curve), Cu_600 (green curve).

Cu-related peaks appear at about 50.5°, 43.4° and 74.26° (in order of decreasing intensity), corresponding to the (200), (111), (220) planes (JCPDS 04-0836), respectively. With increasing oxidation temperature, the relative intensity of the metallic copper decreases due to the thickening of the oxide upper layer. In fact, both Cu$_2$O and CuO peaks increase in intensity. The Cu$_2$O peaks appear at about 36.2°, 42°, 29.3°, 61°, 72.8° and 76.8° (in order of decreasing intensity), corresponding to the (111), (200), (110), (220), (311) and (222) planes (JCPDS 05-0667), respectively. On the other side, the CuO peaks appear at about 35.6°, 61°, 38.8°, 48.9°, 66.5°, 32.6° and 68.3° (in order of decreasing intensity), corresponding to the (002), (-113), (111)/(200), (-202), (-311), (-110) and (-220) planes (JCPDS 45-0937), respectively.

In general it can be stated that the Cu$_2$O is the main oxidation product, with a small amount of CuO, and both increase with oxidation temperature. For the first oxide it can be noticed a sharpening of the related peaks, which means that the Cu$_2$O crystals increase their size from Cu_400 up to Cu_600. On the other side, most of the CuO peaks are present only in the samples oxidized at 500°C and 600°C, meaning that, at lower temperatures, its amount the oxide amount is very low compared to Cu and Cu$_2$O. These results may help to explain what found with FESEM characterization in the previous sections. In fact, literature [284, 285, 303–305] associates the NWs composition to CuO, while the observed nanostructured layer is composed by a three layered structure made of Cu, Cu$_2$O and CuO (from bulk to surface), as already explained in Sec. 3.2.2. The low NWs amount in sample Cu_400 (Fig. 5.21) is demonstrated by the low intensity of the CuO peaks, while for sample Cu_500 and Cu_600, the peaks are higher meaning that the NWs amount and density is increased with temperature.

Electrochemical characterization

As for TiO$_2$ decorated with Cu or copper oxide, in order to verify the catalytic properties of the prepared samples, the electronic structure and band alignment should be investigated. In order to correctly draw the electronic band structure of a semiconducting material, *ab initio* or FEM simulations should be performed. These methods take into account the nanoscaled dimensions of the materials, starting from theoretical assumptions. In this thesis, only experimental observations and measures are performed, compared with the theoretic band alignments of the bulk materials; however, the energy levels may be shifted in case of nanometric or nanostructured materials. In Fig. 5.25 is represented the theoretic band alignment of a copper oxide sample, under the hypothesis of bulk materials and based on XRD results. Under this constrain, the Cu$_2$O should have a larger band gap (about 2.2 eV, direct) if compared to the CuO (about 1.5 eV, indirect), exhibiting both a p-type behavior.
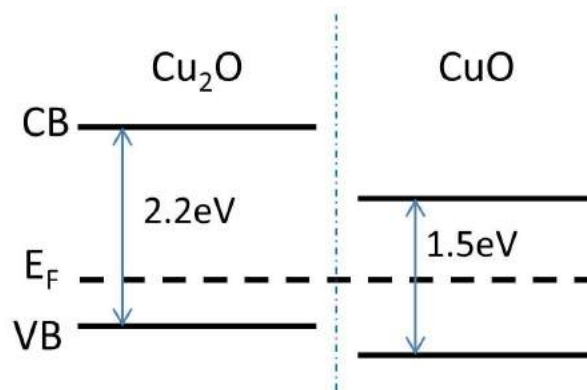
Fig. 5.25 Theoretic band gap alignment for a Cu$_2$O/CuO bulk sample.

In order to calculate the Cu_400, Cu_500, Cu_600 band gaps, spectrophotometer measures were conducted as described in App. A.7, in order to calculate the samples'

band gaps, by measuring the optical absorption spectra of the material. For all the samples it could be possible to identify two linear regions in the Tauc plots, one direct and one indirect. In Fig. 5.26 is reported an example of the Tauc plot for the Cu_500 sample that shows the two linearities. The blue *Linear Fit* (Fig. 5.26A) intercepts the x axis at about (2.27 ± 0.04) eV, while the red *Linear Fit* (Fig. 5.26B) at about (1.43 ± 0.02) eV. Being the second value smaller than the first one, 1.43 eV can be attributed to the CuO indirect band gap with enough reliability. On the other side, the energy gap value coming from the first fit, 2.27 eV, may be indicate the Cu$_2$O direct band gap, being a value similar to the bulk one. It has to be considered that the CuO band gap is the one that absorb the majority of photons, being the smallest, during the characterization.
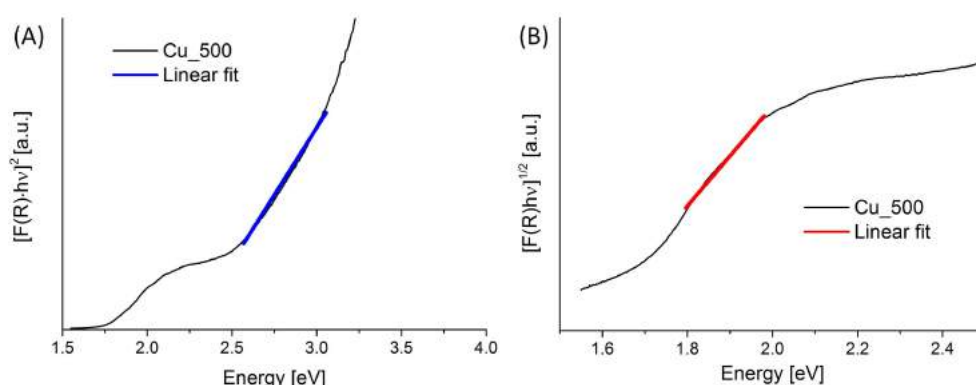
Fig. 5.26 Tauc plots of Cu_500 sample. (A) Tauc plot for the direct band gaps in black, linear fit applied in blue. (B) Tauc plot for the indirect band gap in black, linear fit applied in red.

In general, it can be said that due to the nanostructuration and nanoscale dimension of the materials prepared, the band gap values are slightly different from the bulk ones. However, in order to calculate the nano-scale influence, simulations should be done, as already stated. Knowing the gap values gives the possibility of using the samples not only as electro-catalysts (as it will be further discussed), but also as photo-catalyst being able to know the absorption range, hopefully the visible one. This second possibility, however, was not exploited in this study.

In order to draw an approximation of the samples band diagram, the flat band potential V_{FB}, i.e. the difference between the Fermi levels of the catalysts material and the solution in which it is immersed, is needed. This kind of experiment can be done through the Mott-Schottky measure as it is described in App. A.4.5. Moreover, XPS can provide data of the position of the conduction band of the catalysts. Knowing the energy levels position could give a more precise indication of the possible byproduct of the CO$_2$RR during working condition. In fact, knowing the position of the conduction band of the material in contact with the solution, it is possible to determine the correct reaction occurring on the catalyst surface (table 2.1).

Cyclic voltammetries were conducted to study the catalytic behavior of the three sets of sample as reported in Fig. 5.27, as described in App. A.4.4. As a general comment, all the samples exhibit a similar CV shape for the nitrogen-saturated

solution and for the carbon dioxide-saturated curves. Cu_400 (Fig. 5.27A) do not show any specific peak related to the catalytic activity of the material, for all the CV cycles. Coupling this result with low nanostructuration visible in the FESEM images (Fig. 5.21), the sample do not appears to be a promising catalyst for CO$_2$RR. On the other side, both Cu_500 (Fig. 5.27B) and Cu_600 (Fig. 5.27C) curves present a reduction phenomena in the first CV cycle of the of the CO$_2$-saturated test (shown in the insets of the figures). Previous studies [347] have identified that the peak at -0.8 V (inset in Fig. 5.27C) is related to reduction of Cu(II) oxide to Cu(I) oxide in the presence of CO$_2$ saturated solution of KHCO$_3$. Moreover, the broad peak at -1.2 V (inset in Fig. 5.27B) may be associated to the reduction of Cu(I) oxide to Cu(0), in the same conditions. In this second case, the peak is so broad that further peaks are really difficult to be identified. The reduction phenomena occur only at the first cycle, while, at the second cycle, the CO$_2$-saturated curves are more stable and more negative then the N$_2$-saturated, especially in the case of Cu_500. Both Cu_500 and Cu_600 samples were chosen to be tested as electrodes for CO$_2$RR, in two sets of experiment in order to analyze either gaseous or liquid byproducts.
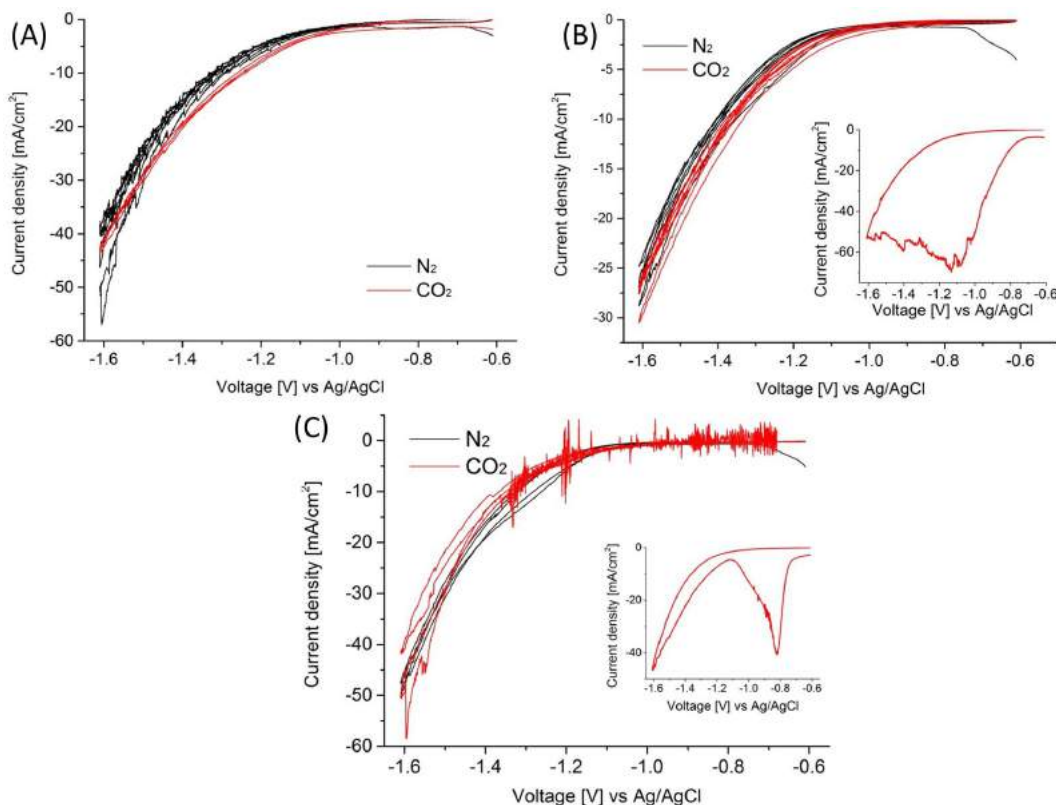
Fig. 5.27 CV of the thermally annealed Cu samples: (A) Cu_400, (B) Cu_500, (C) Cu_600. The black lines represent the CV under N$_2$, while the red lines under CO$_2$. The insets in (B) and (C) show the first CV cycle. Scan rate: 10 mV/s.

In Table 5.3 are reported the results of the tests conducted on the samples Cu_500 and Cu_600 at different potentials. The first set of tests were conducted by setting

the potentials thanks to the chonoamperometric test (explained in App. A.5.2). In this case, a liquid portion was taken, at the end of the previous tests, in order to quantify the amount of organic molecules present through the Chemical Oxygen Demand (COD) tests(explained in App. A.6). In the second set of tests, the Faradaic Efficiencies (FE), reported with their absolute error, were calculated (see App. A.5.1) thanks to the measured gaseous byproducts by the μ-GC (see App. A.5).

Sample	Potential [V]	FE H$_2$ [%]	Δ(FE H$_2$) [%]	FE CO [%]	Δ(FE CO) [%]	COD [mg/l of O$_2$]
Cu_500	-1.4	-	-	-	-	152
	-1.6	70	5	2	0.1	124
Cu_600	-1.2	-	-	-	-	116
	-1.4	49	2	5	0.2	80
	-1.6	-	-	-	-	52

Table 5.3 Summary of the quantity of byproducts measured for the Cu_500 and Cu_600 sample through μ-GC and COD tests.

Comparing the gaseous products of the two samples, it can be notice that a large amount of hydrogen is produced, with a faradaic efficiency (FE) of about 70% (@-1.6V) and 49% (@-1.4V) for Cu_500 and Cu_600, respectively. Even though are not the expected ones, these results seem to be encouraging, since they are better than the ones measured with the TiO$_2$ NTs-based catalysts. In fact, with these samples these is the 28% and 46% of FE is used to produce some byproducts in the liquid phase. COD analyzes gave good results especially for reductions at low potentials, even though it is not possible to determine the type of organic product. This kind of test was conducted in order to verify the presence of organic molecules (among methanol, formaldehyde and formic acid) due to the lack of HPLC (High-Performance Liquid Chromatography), that would have allowed to complete the validation.

By comparing the COD of the two samples, it turns out that Cu_500 exhibit an higher amount of oxidized organic molecules at lower potentials (152 mg/l of O$_2$ @ -1.4V), revealing a promising catalytic activity toward CO$_2$RR. The same test conducted onto Cu_600 confirmed the reduction of carbon dioxide, but with a lower amount of organic molecules produced (80 mg/l of O$_2$ @ -1.4V). This result should be interpreted as an higher selectivity of the Cu_500 sample toward methanol, formaldehyde and formic acid production with respect to Cu_600. In order to discriminate which one is the best performing sample, more potentials should be investigated together with a deep analysis of the liquid products of the reduction process by High-Performance Liquid Chromatography.

5.3.2 TiO$_2$ supported on Cu$_x$O NWs

In order to develop a good performing material, it was chosen to study the behavior of a p-n heterojunction made by coupling the thermally-oxidized Cu foils with TiO$_2$.

The idea of coupling this material with low band gap materials such as copper oxides should lead to the possibility of using the material not only as electro-catalyst, but also as photo-catalyst, with a much broader absorption region with respect to the bare titania.

This new material is obtained by a simple three-steps process. The first is the thermal oxidation of the Cu foil by means of a vertical furnace (Carbolite, VST 12/300/3216) up to 500°C for 30 minutes (heating rate of 5°/min), described in the previous section as Cu_500 sample. This temperature was chosen because of the promising results for CO_2 reduction into organic molecules. On the top of the Cu_500 substrate is then deposited Ti thanks to an Electron Beam Evaporator (see App. A.8) in order to obtain a film of a thickness of 100 nm. This sample will be named in text as Cu_500-100nm_Ti. The final step consists in a second thermal oxidation of the evaporated sample up to 450°C for 45 minutes (heating rate of 5°/min) in air atmosphere by means of the vertical furnace. The re-oxidized sample will be referred as Cu_500-100nm_TiO$_2$.
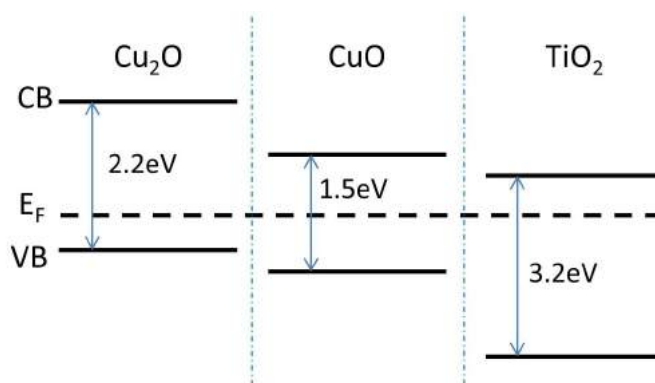
Fig. 5.28 Theoretic band alignment for a Cu$_2$O/CuO/TiO$_2$ bulk sample.

As already stated in previous studies [348], the energy levels of these prepared samples should be roughly arranged as drawn in Fig. 5.28. In this case, both Cu$_2$O and CuO play the role of p-type semiconductors, while TiO$_2$ of n-type of the considered junction. The conduction bands alignment should favor the accumulation of electrons e$^-$ in the titania layer, therefore on the surface of the catalyst. The electrons can be generated both electrically (applying an external potential) and under light stimulation (sun illumination). On the other side, the holes h$^+$ should flow in the opposite direction, toward the valence band of the Cu$_2$O, ensuring a correct charge separation. The surface e$^-$ accumulation is the key point in order to efficiently reduce the carbon dioxide into methane, ethane, methanol, ethanol, ...etc.

Morphological characterization

Morphological characterization of the material was conducted after the Ti evaporation (Fig. 5.29) and after the second thermal oxidation (Fig. 5.31). Energy Dispersive X-ray Analysis (EDX, see Sec. 3.3.3) were conducted in order to verify

the compositional uniformity of the material during the synthesis step (Fig. 5.30 and 5.32).
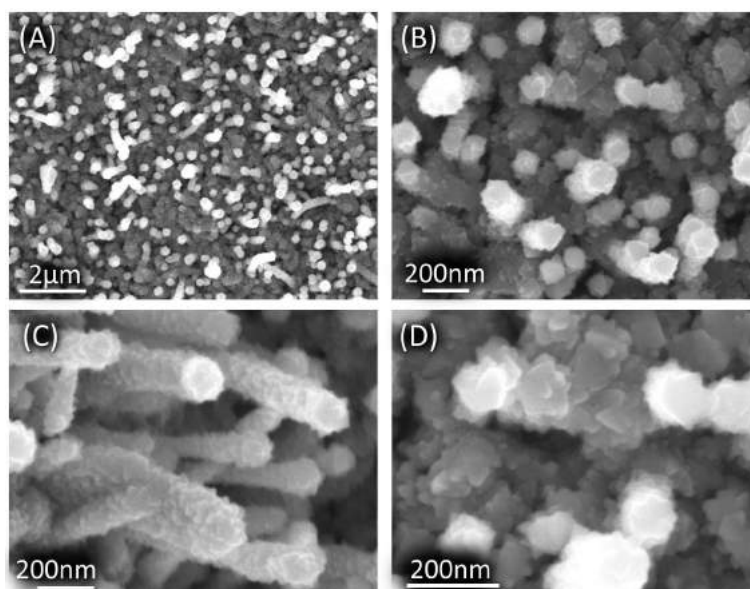
Fig. 5.29 FESEM images of Cu_500-100nm_Ti sample, after the titanium evaporation.
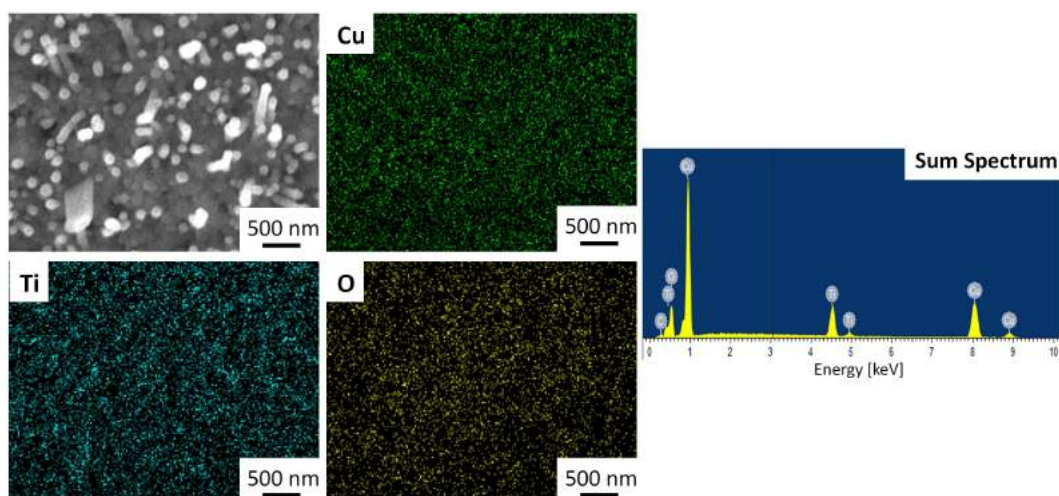
Fig. 5.30 EDX map of Cu_500-100nm_Ti sample in false colors: green for Cu, cyan for Ti and yellow for O. On the right side it is reported the sum spectrum correspondent to the EDX map.

In Fig. 5.29, FESEM images of the Cu_500-100nm_Ti sample are reported at different magnifications, as an example. The Cu$_x$O substrate appears to be uniformly covered by Ti (Fig. 5.29A and B), especially around the grown NWs (Fig. 5.29C and D). In fact, the metals evaporation ensured a quite uniform coverage of the substrate (Cu_500).
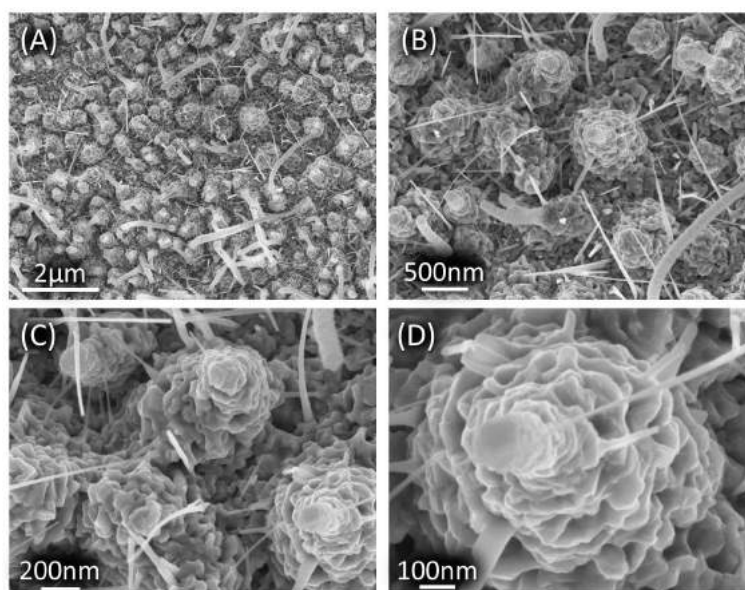
Fig. 5.31 FESEM images of Cu_500-100nm_TiO$_2$ sample, after the thermal oxidation.

From EDX maps (Fig. 5.30), the uniform elemental distribution can be appreciated. The measured atomic percentages are about 48%, 11.2% and 40.7% for Cu, Ti and O, respectively.

By looking at Fig. 5.31, FESEM images of the Cu_500-100nm_TiO$_2$ sample, it can be noticed that the NWs shape changed strongly due to the Ti oxidation in TiO$_2$, that increased the NWs diameter from about 150 nm up to more than 500 - 800 nm (measured at the bottom of the wires). Moreover, it can be reasonably supposed that the buried Cu$_x$O NWs kept on growing due to the overall annealing of the sample. This can be demonstrated by the presence of new CuO NWs (see Fig. 5.31B and C) similar to the one saw in Fig. 5.21C and Fig. 5.22C, but not present after the Ti evaporation (see Fig. 5.29B).

From the EDX map in Fig. 5.32, it can be pointed out the uniformity of the elemental distribution of Cu and Ti on the sample surface. On the other side, the oxygen map shows denser areas that correspond to presence of the two oxides (Cu$_x$O and TiO$_2$). The measured atomic percentages of the elements are about 44.4%, 2% and 53.6% for Cu, Ti and O, respectively. Due to the presence of different oxides, Cu$_2$O, CuO and TiO$_2$, it cannot be determined if the oxygen is bound to copper or titanium.
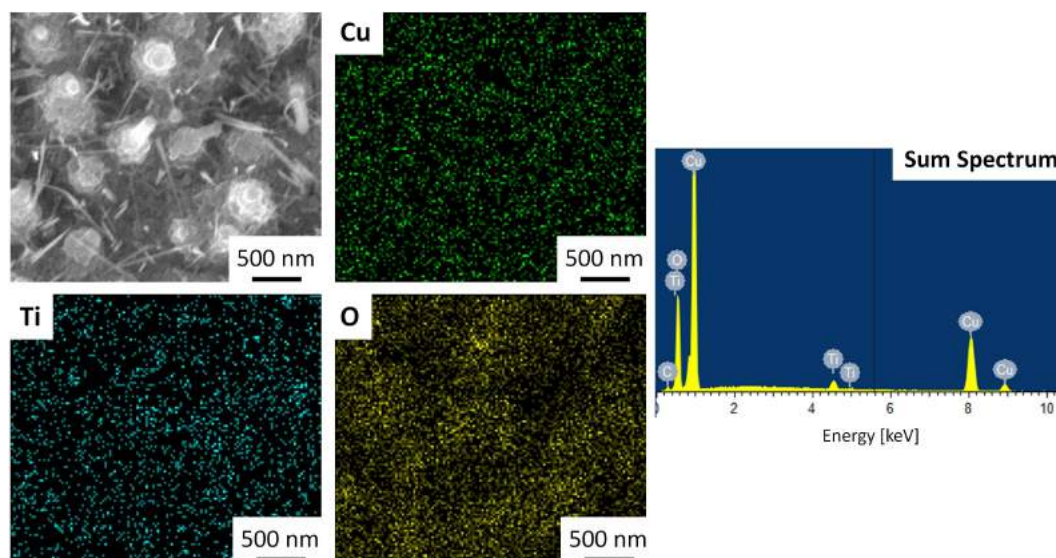
Fig. 5.32 EDX map of Cu_500-100nm_TiO$_2$ sample in false colors: green for Cu, cyan for Ti and yellow for O. On the right side it is reported the sum spectrum correspondent to the EDX map.

Compositional characterization

In order to verify the composition of the Cu_500-100nm_TiO$_2$ sample, XRD characterization was performed. Fig. 5.33 shows the XRD spectra for this sample (in red) compared with the Cu_500 (in green) curve, normalized by the copper most intense peak. As a first comment, diffraction peaks corresponding to both the copper oxides can be detected, together with pure Cu phases, but no evident peaks for TiO$_2$ can be clearly identified. Cu, Cu$_2$O, CuO peaks appear at the same 2θ positions of the ones reported in Sec. 5.3.1 and for this reason, they will not be reported here.

Comparing the two spectra, it can be noticed that both Cu$_2$O and CuO peaks increased in intensity. Such increase in intensity, together with a slight narrowing of the copper oxide peaks, can be related to the second oxidation process at 450°C, after the Ti evaporation. Concerning TiO$_2$, no evidence of its presence can be found in the XRD spectra, probably because of its low amount, even if it was detected by EDX.
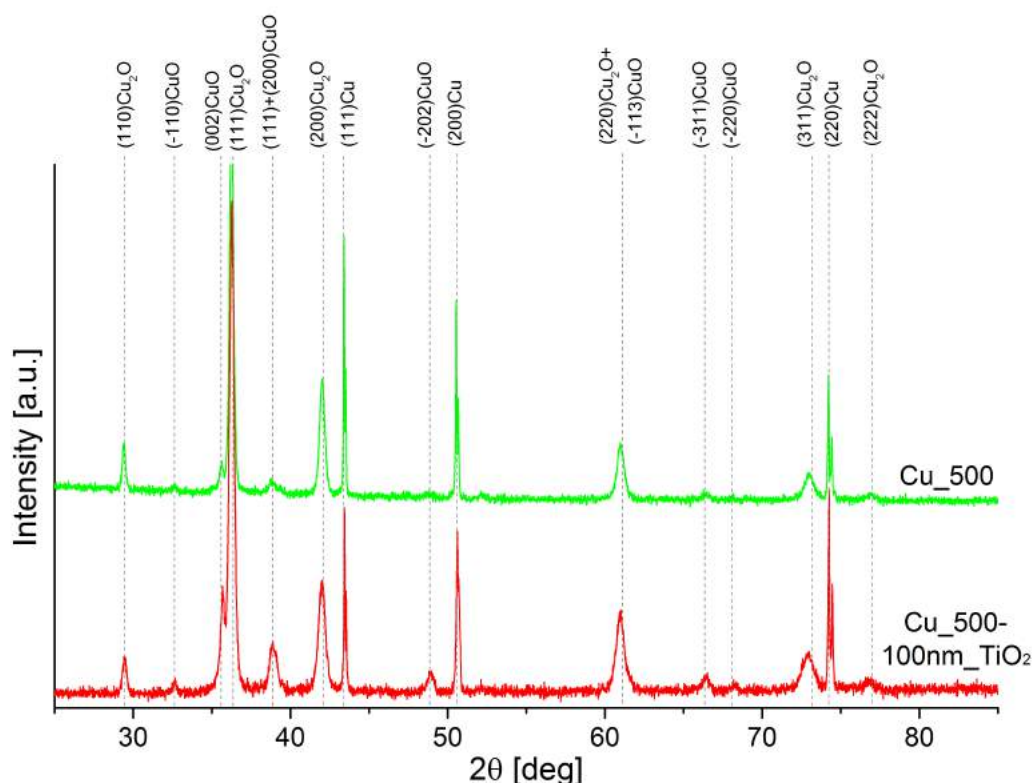
Fig. 5.33 XRD spectra of the thermally oxidized copper samples: Cu_500 (green curve) and Cu_500-100nm_TiO$_2$ (red curve).

Electrochemical characterization

As for thermally oxidized copper samples, in order to verify the catalytic properties of the prepared sample, the electronic structure and band alignment should be investigated. As already stated, the energy levels may be shifted in case of nanometric or nanostructured materials, as in this case. Spectrophotometer measures were conducted as described in App. A.7 and in Fig. 5.34, showing the Tauc plot for the direct and indirect band gap of the Cu_500-100nm_TiO$_2$.

In general, it could be possible to identify 3 linear parts in the Tauc plot in Fig. 5.34. Two fits might be drawn in direct Tauc plot and one in the indirect one. However, it has to be considered that the smallest band gap is the one that absorb the majority of photons during the characterization. The other two gaps may be detected but with a much lower efficiency than the smallest, and so precision. Focusing on the Tauc plot for the direct band gap (Fig. 5.34A), two linear fits can be drawn, whose intercept with the x axis are at about (3.12 ± 0.04) eV and (2.20 ± 0.04) eV for the *Linear Fit 1* and *Linear Fit 2*, respectively. Instead, the *Linear Fit* of the Tauc plot for the indirect band gap (Fig. 5.34B) intercepts the x axis at about (1.27 ± 0.02) eV, attributable to the CuO indirect band gap with enough reliability, being the smallest
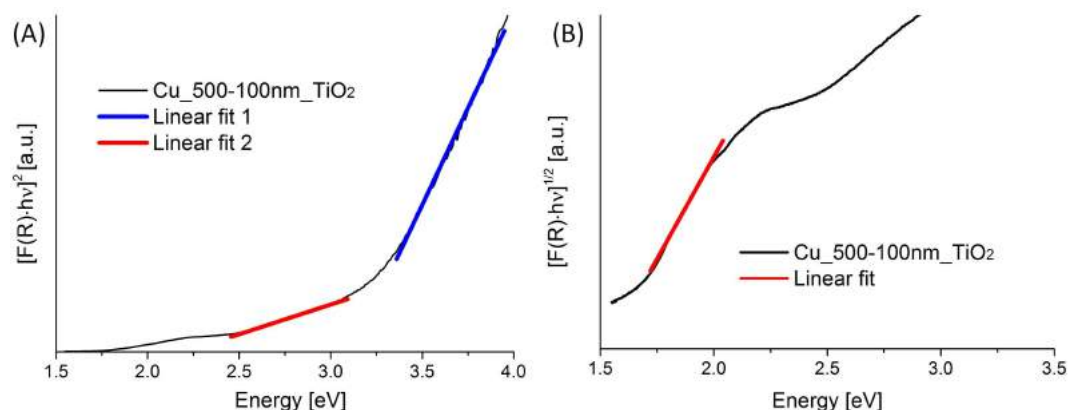
Fig. 5.34 Tauc plots of Cu_500-100nm_TiO₂ sample. (A) Tauc plot for the direct band gaps in black, linear fits applied in red and blue. (B) Tauc plot for the indirect band gap in black, linear fit applied in red.

gap value. The first two values, 3.12 eV and 2.20 eV, could be attributed to the TiO_2 and Cu_2O direct band gaps respectively, being values similar to the bulk ones.

In general, it can be said that due to the nanostructuration and nanoscale dimension of the materials prepared, the band gap values are slightly different from the bulk ones. However, in order to calculate the nano-scale influence, simulations should be done, as already stated. Differently from the Cu_500 sample, the Cu_500-100nm_TiO₂ possesses different value of band gaps. These slight variations can be related to the second oxidation step that changed the Cu_2O and CuO thicknesses, being dependent on the thermal treatment duration (see Sec. 3.2.2). Knowing the gap values gives the possibility of using the samples not only as electro-catalysts (as it will be further discussed), but also as photo-catalyst being able to know the absorption range, hopefully the visible one. This second possibility, however, was not exploited in this study.

In order to draw an approximation of the sample band diagram, the flat band potential V_{FB}, i.e. the difference between the Fermi levels of the catalyst material and the solution in which it is immersed, is needed. This kind of experiment can be done through the Mott-Schottky measure as it is described in App. A.4.5. Moreover, XPS can provide data of the position of the conduction band of the catalyst.

Cyclic voltammetry was conducted to study the catalytic behavior of the Cu_500-100nm_TiO₂ sample as reported in Fig. 5.35, as described in App. A.4.4. As a general comment, the sample current density is much lower than the one related to the oxidized copper foils (see Fig. 5.27), meaning that the sample is more resistive. Moreover, the current-voltage shape shows an hysteresis, meaning that Cu_500-100nm_TiO₂ has a capacitive behavior. This means that the catalyst may be a good candidate to be tested not only as electro-catalyst, but also as photo-catalyst. More specifically, the N₂-saturated curve shows an higher current density that the CO₂ one, possibly meaning that the HER has an higher conversion efficiency than the CO₂RR. On the other side, the CO₂-saturated curves (red and green in Fig. 5.27)
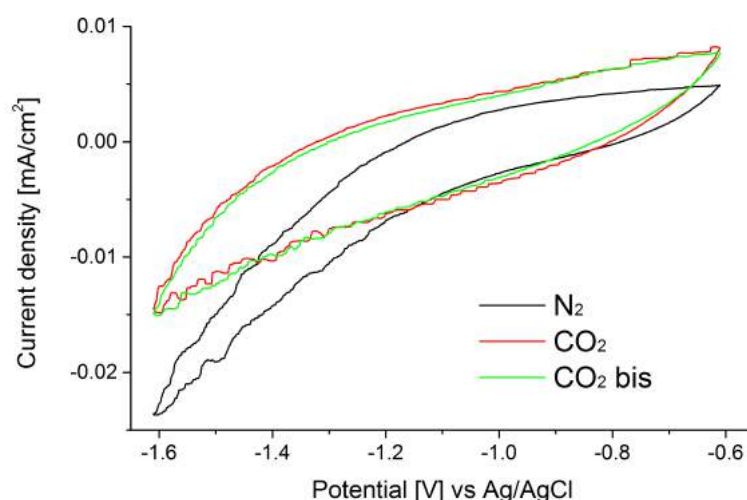
Fig. 5.35 CV of the Cu_500-100nm_TiO$_2$ sample. The black line represents the CV under N$_2$-saturated atmosphere, while the red and green curves under CO$_2$. Only the last cycle is reported for simplicity of reading, being all similar. Scan rate: 10 mV/s.

have a lower current, maybe due to the lower efficiency of the reaction coupled with the suppression of the hydrogen production. These curves, moreover, are repetition of the same test with different samples, demonstrating its repeatability, thanks to the simple production process.

Sample	Potential [V]	FE H$_2$ [%]	Δ(FE H$_2$) [%]	FE CO [%]	Δ(FE CO) [%]
	-1.2	91	6	2.0	0.1
Cu_500_TiO$_2$	-1.2 light	93	1	73	1
	-1.4	96	2	0	1

Table 5.4 Summary of the quantity of byproducts measured for the Cu_500-100nm_TiO$_2$ sample through μ-GC test. Where indicated, the test was performed under light condition, otherwise under dark conditions.

In Table 5.4 are reported the results of the tests conducted on the Cu_500-100nm_TiO$_2$ sample at different potentials and illumination condition. Unfortunately, the catalyst performance are very poor in all considered conditions, when compared to the former oxidized copper foils (Table 5.3). At -1.2 V and -1.4 V, with no light, the main product is hydrogen, while carbon monoxide is not present or detectable. The main reason may be related to the TiO$_2$ thickness which, in this case, may lowers the sample selectivity and increases the H$_2$ evolution. It is reasonable to suppose that different amount of titanium dioxide onto the NWs may lead to a CO$_2$RR enhancement. In the case of UV-vis lamp (Newport, Oriel apex illuminator), set at 8.5 cm from the electrode, the total FE rose to more than 160%, and, not being

scientifically significative, it was considered as an error. In these case, the COD were not done being the sum of the gaseous faradaic efficiencies almost 100%.

In conclusion, it can be said that the Cu_500-100nm_TiO$_2$ is not a promising electro-catalyst, but it could be as photo-catalyst, by repeating some experiments. Having also good performances, titania supported on Cu_600 could be a good alternative to the one just characterized. Moreover, Ti thicknesses should be tuned in order to lower the HER and favor the electron accumulation onto the catalyst surface.

Chapter 6

Conclusions and future work

Chapter abstract *In this thesis, I put in evidence the interconnection between nanotechnology and functional properties of materials, in particular in the framework of renewable energy electrochemical devices that produce energy (MFCs) or convert anthropogenic greenhouse gases (i.e. CO_2) into valuable products. In this context, I described two key reactions, the ORR and the CO_2RR, for these important applications, the microbial fuel cells (ORR at cathode) and CO_2 conversion into valuable products (CO_2RR at cathode). I proposed some examples of low-cost and green nanostructured catalysts, prepared with simple synthetic and processing routes. In the following sections I will summarize the main achievements and future perspectives of the studied devices, highlighting the newest contribution on which this Ph.D. study was focused.*

6.1 Mn_xO_y-based catalyst for ORR

Nanostructured manganese oxide nanofibers were synthesized starting from biocompatible and biodegradable precursors, by means of the electrospinning technique. Thanks to the thermal treatment optimization, reproducible samples of nanofibers composed by Mn_3O_4 and Mn_2O_3 were obtained, by selecting the proper calcination temperature. In particular, through morphological, thermogravimetric and in-situ X-ray diffraction analyses, it was possible to determine the structural and morphological characteristics of the electrospun nanofibers as a function of the calcination temperature. It was also possible to define the temperature conditions at which the two oxides start to crystallize, i.e. 125°C and about 600°C for Mn_3O_4 and Mn_2O_3, respectively. Moreover, it was found that, in the temperature range of 475°C - 575°C, the polymeric template completely degrades, leaving a nanostructured Mn_3O_4 single oxide catalyst in the form of nanofiber. As the calcination temperature increases, a coalescence phenomenon between crystals occurs during the transformation of Mn_3O_4 into Mn_2O_3. This process results to be detrimental for the initial nanofibred structure, that is transformed into a film with dendridic crystals, mostly composed of Mn_2O_3. Three calcination temperatures were selected to study the catalytic behavior

of both single and mixed manganese oxide phases; in particular were selected 475°C, 600°C and 725°C as the temperatures to obtain pure Mn_3O_4, mixed Mn_3O_4-Mn_2O_3 or pure Mn_2O_3, respectively.

All the nanostructured Mn_xO_y-based catalysts showed, in the form of paste, good catalytic performance for the oxygen reduction reaction. The number of exchanged electrons, n, was found to be between 3.6 and 3.7, at potentials lower than -0.4 V, which is in line with other cost-effective and green catalysts proposed in literature. Furthermore, the pure oxide phases (Mn_3O_4 and Mn_2O_3) resulted to have better results than the mixed one obtained at the calcination temperature of 600°C. Since the pure phases resulted both to be good candidates for ORR, the catalyst obtained with the lowest calcination temperature (475°C) was selected as the low-cost and green nanostructured catalyst at the cathode.

Thanks to the electrospinning versatility, it was possible to directly integrate of the Mn_3O_4 NFs onto a conductive substrate, a carbon paper, without the use of pastes or destroying the nanofibred structuration, obtaining in such a way a cathode for the oxygen reduction reaction for microbial fuel cells. To better optimize the cathode preparation, different electrospinning deposition times were tested, in particular 5, 10, 15 and 20 minutes. Moreover, by coupling the FESEM characterizations with the TGA results, it was possible to estimate and optimize the amount of NFs deposited onto the CP. Among the different deposition times, the nanofibers obtained at 5 and 10 minutes of electrospinning (NFs_5' and NFs_10') resulted to be the samples with the best compromise between catalyst loading and deposition time. Both of them showed good catalytic performance for the oxygen reduction reaction in form of electrodes, with n values of about 3.7 electrons (for Pt/C reference electrode n is 3.96), at potentials lower than -0.4 V, which again is in line with other cost-effective electrodes proposed in literature.

Single Chamber Microbial Fuel Cell tests gave encouraging results for the NFs_10' electrode, that showed a maximum power density of about 1.5 mW/g, comparable to the performance of the Pt/C reference electrode. Even though these results are promising, a deeper comprehension of the nanofibers deposition mechanism onto the electrode should be investigated, in order to further optimize the electrode performance, by simulating the effect of the conducting substrate roughness, carbon paper, on the electric field during the electrospinning process. This would lead to a better conductive substrate/catalyst integration, minimizing the manganese oxide load and improving the charge transfer toward the carbon paper. A final long-term test in MFCs should be done in order to study the aging of the electrode in working conditions.

To test the role of the nanostructuration of the catalyst in the cathode performances, a second set of samples has been prepared by turning the electrospinng process into an electrospray process, thus obtaining Mn_xO_y in the form of nanodrops on carbon paper, instead of nanofibers after the calcination process. The selected deposition times were 5 and 10 minutes, to be comparable with the nanofibers-based cathode.

The preliminary study gave impressive results, especially in terms of catalytic activity toward ORR. In fact, the sample NDs_10' showed an outstanding n value

of about 3.92, at potentials lower than -0.4 V. It is clear that this kind of nanostructuration is more effective that the fiber-based one to improve catalyst/electrode efficiency. With a lower amount of catalyst, the sample NDs_10' reached a maximum power density of the MFC very close to the Pt/C reference, and a power density two orders of magnitude higher than the bare CP. Also in this case, however, more light should be shed in order to understand deeply the deposition mechanism, the thermal evolution of the drops, the long term stability in working MFC, as already highlighted for NFs.

In conclusion, all the obtained results have demonstrated that the electrospun nanofibers and the electrosprayed nanodrops own good catalytic properties, revealing themselves as on of the most innovative and promising nanostructures for the design of cathodes in microbial fuel cells.

6.2 TiO$_2$ NTs-based catalysts for CO$_2$RR

Cathodes based on vertically aligned TiO$_2$ NTs were prepared in a reproducible way by anodic oxidation, starting from titanium foils, and they were characterized in terms of morphology and crystalline phase. They were synthesized in non-aqueous organic electrolytes, containing ammonium fluoride, with a simple two-step electrochemical process. XRD analyses confirmed the crystalline anatase phase after the thermal treatment at 450°C, while at higher temperatures, rutile phase starts to crystallize.

Copper and copper oxide were deposited in the form of thin film onto the TiO$_2$ NTs in order to enhance the material selectivity toward CO$_2$RR, as proposed in the literature. Morphological and compositional characterizations confirmed the presence of such films on top of the NTs. However, no evidence of crystalline Cu or copper oxide was found by X-ray diffraction, probably because of the small amount of material. Considering the electrochemical characterizations, unfortunately it results that neither TiO$_2$_Cu nor TiO$_2$_Cu_450 are good catalysts for carbon dioxide reduction. In fact, their main reaction product was hydrogen, reaching almost 100% in the case of TiO$_2$_Cu_450.

These results put in evidence that, even if theoretically the coupling of TiO$_2$_Cu or TiO$_2$_Cu_450 should be effective for CO$_2$RR, the Cu and Cu$_x$O interaction with TiO$_2$ is not optimized. In fact, an almost complete detach of the upper layers from the underlying titania during working conditions was observed. In conclusion, the samples TiO$_2$_Cu and TiO$_2$_Cu_450 revealed to be not suitable for CO$_2$RR. As a future perspective, other nanostructures or other materials should be used to decorate TiO$_2$ in order to improve the materials selectivity toward CO$_2$RR.

6.3 Cu$_x$O NWs-based catalysts for CO$_2$RR

Cathodes based on copper oxide nanostructures were obtained through reproducible, simple and convenient route, copper oxide NWs, starting from bare copper foils

and thermally treating them, and characterizing them in terms of morphology and crystalline phase. In this way, the catalyst material is grown directly on a conductive substrate, having as a final product an electrode, without the need of further catalyst deposition.

Depending of the final annealing temperature, density different nanostructures were obtained. In particular, the samples calcined at $500°C$ and $600°C$ (Cu_500 and Cu_600) were were composed of a thick Cu_2O and CuO nanostructured layer, on top of which, CuO nanowires could be found. Both of them were selected as cathodes for CO_2RR. As a result, at potential of about -1.6 V and -1.4 V, for both the samples hydrogen and liquid products were obtained, with different ratios. The sample calcined at $600°C$ resulted to be the better one, having a H_2 Faradic efficiency of about 49%, the lowest obtained among all the TiO_2-based or copper oxide-based cathodes. Unfortunately, because of long breakdown period of the HPLC, it was not possible to analyze the chemical composition of the liquid product. Even without these results, these samples might be considered as promising electrodes for CO_2RR.

As a first improvement, the nanostructured copper oxide was decorated with TiO_2, through Ti evaporation onto the copper oxide and further thermal oxidation, in order to modulate the absorption spectrum of the material. This solution was not giving the expected results, as the H_2 faradic efficiency increased up to 100%.

In conclusion, the cathodes based on nanostructured copper oxide catalyst can be considered as promising for the CO_2RR, while the possible decoration with other nanostructures should be further investigated.

References

[1] M.A. Fardin. On the rheology of cats. *Rheology Bulletin*, 83(2), 2014. http://www.rheology.org/sor/publications/rheology_b/RB2014Jul.pdf.

[2] K. Levecque, F. Anseel, A. De Beuckelaer, J. Van der Heyden, and L. Gisle. Work organization and mental health problems in PhD students. *Research Policy*, 46(4):868–879, 2017.

[3] L. Navarini, E. Nobile, F. Pinto, A. Scheri, and F. Suggi-Liverani. Experimental investigation of steam pressure coffee extraction in a stove-top coffee maker. *Appl. Therm. Eng.*, 29(5):998–1004, 2009.

[4] Q. Ma. Greenhouse gases: Refining the role of carbon dioxide. 1998. https://www.giss.nasa.gov/research/briefs/ma_01/.

[5] T.R. Karl and K.E. Trenberth. Modern global climate change. *Science*, 302(5651):1719–1723, 2003.

[6] UNFCCC. Historic Paris agreement on climate change—195 nations set path to keep temperature rise well below 2 degrees celsius. 1998. http://newsroom.unfccc.int/unfccc-newsroom/finale-cop21/.

[7] IPCC Climate Change. Mitigation of climate change. *Summary for Policymakers*, 10(5.4), 2007.

[8] H. Yang, Z. Xu, M. Fan, R. Gupta, R.B. Slimane, A.E. Bland, and I. Wright. Progress in carbon dioxide separation and capture: A review. *J. Environ. Sci.*, 20(1):14–27, 2008.

[9] International Energy Agency (IEA). Energy technology perspectives 2014 - harnessing electricity's potential. 2014. https://www.iea.org/media/news/2014/ETP14_factsheets.pdf.

[10] International Energy Agency (IEA). Energy technology perspectives 2012 - pathways to a clean energy system. 2012.

[11] R. Adib, H.E. Murdock, F. Appavou, A. Brown, B. Epp, A. Leidreiter, C. Lins, H.E. Murdock, E. Musolino, and K. Petrichenko et al. Renewables 2016 global status report. *Global Status Report RENEWABLE ENERGY POLICY NETWORK FOR THE 21st CENTURY (REN21)*, 2016.

[12] T.F. Stocker, D. Qin, G.K. Plattner, M. Tignor, S.K. Allen, J. Boschung, A. Nauels, Y. Xia, V. Bex, and P.M. Midgley. IPCC, 2013. *Climate change*, 2013.

[13] Exxon Mobil. The outlook of energy: A view to 2040, 2012. *Website: http://www. exxonmobil. com/corporate/files/news_pub_eo. pdf [accessed 20.09. 13]*, 2015.

[14] Z.W. Seh, J. Kibsgaard, C.F. Dickens, I. Chorkendorff, J.K. Nørskov, and T.F. Jaramillo. Combining theory and experiment in electrocatalysis: Insights into materials design. *Science*, 355(6321):eaad4998, 2017.

[15] G.A. Olah, A. Goeppert, and G.K.S. Prakash. *Beyond oil and gas: the methanol economy*. John Wiley & Sons, 2011.

[16] J.M. Campos-Martin, G. Blanco-Brieva, and J.L.G. Fierro. Hydrogen peroxide synthesis: an outlook beyond the anthraquinone process. *Angew. Chem. Int. Ed.*, 45(42):6962–6984, 2006.

[17] Y. Jiao, Y. Zheng, M. Jaroniec, and S.Z. Qiao. Design of electrocatalysts for oxygen- and hydrogen-involving energy conversion reactions. *Chem. Soc. Rev.*, 44(8):2060–2086, 2015.

[18] J.D. Benck, T.R. Hellstern, J. Kibsgaard, P. Chakthranont, and T.F. Jaramillo. Catalyzing the hydrogen evolution reaction (HER) with molybdenum sulfide nanomaterials. *ACS Catalysis*, 4(11):3957–3971, 2014.

[19] H.A. Gasteiger and N.M. Marković. Just a dream—or future reality? *Science*, 324(5923):48–49, 2009.

[20] H.A. Gasteiger, S.S. Kocha, B. Sompalli, and F.T. Wagner. Activity benchmarks and requirements for Pt, Pt-alloy, and non-Pt oxygen reduction catalysts for PEMFCs. *Appl. Catal., B*, 56(1):9–35, 2005.

[21] S. Siahrostami, A. Verdaguer-Casadevall, M. Karamad, D. Deiana, P. Malacrida, B. Wickman, M. Escudero-Escribano, E.A. Paoli, R. Frydendal, T.W. Hansen, et al. Enabling direct H_2O_2 production through rational electrocatalyst design. *Nat. Mater.*, 12(12):1137, 2013.

[22] D.T. Whipple and P.J.A. Kenis. Prospects of CO_2 utilization via direct heterogeneous electrochemical reduction. *J. Phys. Chem. Lett.*, 1(24):3451–3458, 2010.

[23] C.J.M. van der Ham, M.T.M. Koper, and D.G.H. Hetterscheid. Challenges in reduction of dinitrogen by proton and electron transfer. *Chem. Soc. Rev.*, 43(15):5183–5191, 2014.

[24] J. Zhang. PEM *fuel cell electrocatalysts and catalyst layers: fundamentals and applications*. Springer Science & Business Media, 2008.

[25] W. Bi, G.E. Gray, and T.F. Fuller. Pem fuel cell Pt/C dissolution and deposition in nafion electrolyte. *Electrochem. Solid State Lett.*, 10(5):B101–B104, 2007.

[26] F. Cheng and J. Chen. Metal–air batteries: from oxygen reduction electrochemistry to cathode catalysts. *Chem. Soc. Rev.*, 41(6):2172–2192, 2012.

[27] B. Peng and J. Chen. Functional materials with high-efficiency energy storage and conversion for batteries and fuel cells. *Coord. Chem. Rev.*, 253(23):2805–2813, 2009.

[28] Handbook of batteries. *D. Linden, T.B. Reddy*. McGraw-Hill: New York, 2002.

[29] K.M. Abraham and Z. Jiang. A polymer electrolyte-based rechargeable lithium/oxygen battery. *J. Electrochem. Soc.*, 143(1):1–5, 1996.

[30] G. Girishkumar, B. McCloskey, A.C. Luntz, S. Swanson, and W. Wilcke. Lithium- air battery: promise and challenges. *J. Phys. Chem. Lett.*, 1(14):2193–2203, 2010.

[31] J.S. Lee, S. Tai Kim, R. Cao, N.S. Choi, M. Liu, K. Lee, and J. Cho. Metal–air batteries with high energy density: Li–air versus Zn–air. *Adv. Energy Mater.*, 1(1):34–50, 2011.

[32] K. Kinoshita. *Electrochemical oxygen technology*, volume 30. John Wiley & Sons, 1992.

[33] R. Padbury and X. Zhang. Lithium–oxygen batteries—limiting factors that affect performance. *J. Power Sources*, 196(10):4436–4444, 2011.

[34] B.D. McCloskey, D.S. Bethune, R.M. Shelby, G. Girishkumar, and A.C. Luntz. Solvents' critical role in nonaqueous lithium–oxygen battery electrochemistry. *J. Phys. Chem. Lett.*, 2(10):1161–1166, 2011.

[35] S.V. Mohan, G. Velvizhi, J.A. Modestra, and S. Srikanth. Microbial fuel cell: critical factors regulating bio-catalyzed electrochemical process and recent advancements. *Renew. Sustainable Energy Rev.*, 40:779–797, 2014.

[36] S.V. Mohan, R. Saravanan, S.V. Raghavulu, G. Mohanakrishna, and P.N. Sarma. Bioelectricity production from wastewater treatment in dual chambered microbial fuel cell (MFC) using selectively enriched mixed microflora: effect of catholyte. *Bioresour. Technol.*, 99(3):596–603, 2008.

[37] S.V. Mohan, G. Mohanakrishna, and P.N. Sarma. Effect of anodic metabolic function on bioelectricity generation and substrate degradation in single chambered microbial fuel cell. *Environmental science & technology*, 42(21):8088–8094, 2008.

[38] B.E. Logan. Scaling up microbial fuel cells and other bioelectrochemical systems. *App.. Microbiol. Biotechnol.*, 85(6):1665–1671, 2010.

[39] S.V. Mohan, S.V. Raghavulu, and P.N. Sarma. Biochemical evaluation of bioelectricity production process from anaerobic wastewater treatment in a single chambered microbial fuel cell (MFC) employing glass wool membrane. *Biosens. Bioelectron.*, 23(9):1326–1332, 2008.

[40] S.V. Mohan, S.V. Raghavulu, S. Srikanth, and P.N. Sarma. Bioelectricity production by mediatorless microbial fuel cell under acidophilic condition using wastewater as substrate: Influence of substrate loading rate. *Curr. Sci.*, pages 1720–1726, 2007.

[41] M. Zhou, H. Wang, D.J. Hassett, and T. Gu. Recent advances in microbial fuel cells (MFCs) and microbial electrolysis cells (MECs) for wastewater treatment, bioenergy and bioproducts. *J. Chem. Technol. Biotechnol.*, 88(4):508–518, 2013.

[42] P. Chiranjeevi, R. Chandra, and S.V. Mohan. Ecologically engineered submerged and emergent macrophyte based system: an integrated eco-electrogenic design for harnessing power with simultaneous wastewater treatment. *Ecol. Eng.*, 51:181–190, 2013.

[43] S.V. Mohan, S. Srikanth, G. Velvizhi, and M.L. Babu. Microbial fuel cells for sustainable bioenergy generation: principles and perspective applications. In *Biofuel Technologies*, pages 335–368. Springer, 2013.

[44] K. Chandrasekhar and S.V. Mohan. Induced catabolic bio-electrohydrolysis of complex food waste by regulating external resistance for enhancing acidogenic biohydrogen production. *Bioresour. Technol.*, 165:372–382, 2014.

[45] S.V. Mohan and K. Chandrasekhar. Solid phase microbial fuel cell (SMFC) for harnessing bioelectricity from composite food waste fermentation: influence of electrode assembly and buffering capacity. *Bioresour. Technol.*, 102(14):7077–7085, 2011.

[46] K. P. Kuhl, E. R. Cave, D. N. Abram, and T. F. Jaramillo. New insights into the electrochemical reduction of carbon dioxide on metallic copper surfaces. *Energy Environ. Sci.*, 5(5):7050–7059, 2012.

[47] C. Zhao and J. Wang. Electrochemical reduction of CO_2 to formate in aqueous solution using electro-deposited sn catalysts. *Chem. Eng. J.*, 293:161–170, 2016.

[48] G. Centi, S. Perathoner, G. Winè, and M. Gangeri. Electrocatalytic conversion of CO_2 to long carbon-chain hydrocarbons. *Green Chem.*, 9(6):671–678, 2007.

[49] G. Centi, S. Perathoner, and Z.S. Rak. Gas-phase electrocatalytic conversion of CO_2 to fuels over gas diffusion membranes containing Pt or Pd nanoclusters. *Stud. Surf. Sci. Catal.*, 145:283–286, 2003.

[50] G. Centi and S. Perathoner. Reduction of greenhouse gas emissions by catalytic processes. In *Handbook of Climate Change Mitigation*, pages 1849–1890. Springer, 2012.

[51] G. Centi and S. Perathoner. Heterogeneous catalytic reactions with CO_2: status and perspectives. *Studies in surface science and catalysis*, 153:1–8, 2004.

[52] C. Oloman and H. Li. Electrochemical processing of carbon dioxide. *ChemSusChem*, 1(5):385–391, 2008.

[53] M. Fan, Z. Bai, Q. Zhang, C. Ma, X.D. Zhou, and J. Qiao. Aqueous CO_2 reduction on morphology controlled Cu_xo nanocatalysts at low overpotential. *RSC Adv.*, 4(84):44583–44591, 2014.

[54] J. Qiao, M. Fan, Y. Fu, Z. Bai, C. Ma, Y. Liu, and X.D. Zhou. Highly-active copper oxide/copper electrocatalysts induced from hierarchical copper oxide nanospheres for carbon dioxide reduction reaction. *Electrochim. Acta*, 153:559–565, 2015.

[55] O. Deutschmann, H. Knözinger, K. Kochloefl, and T. Turek. Heterogeneous catalysis and solid catalysts. *Ullmann's Encyclopedia of Industrial Chemistry*, 2009.

[56] A. K. Haghi. *Nanostructure, nanosystems, and nanostructured materials: theory, production and development*. Apple Academic Press, 2014.

[57] A. D. Pomogailo, A. S. Rozenberg, and I. E. Uflyand. Metal nanoparticles in polymers. *Khimiya*, page 672, 2000.

[58] A. I. Gusev. Nanomaterials, nanostructures, nanotechnologies. *Fizmatlit*, 416, 2005.

[59] I.P Suzdalev. Nanotechnology: Physicochemistry of nanoclusters, nanostructures and nanomaterials. *KD Librokom*, 2005.

[60] L. Zhang, J. Zhang, D.P. Wilkinson, and H. Wang. Progress in preparation of non-noble electrocatalysts for pem fuel cell reactions. *J. Power Sources.*, 156(2):171–182, 2006.

[61] C. Santoro, A. Serov, L. Stariha, M. Kodali, J. Gordon, S. Babanova, O. Bretschger, K. Artyushkova, and P. Atanassov. Iron based catalysts from novel low-cost organic precursors for enhanced oxygen reduction reaction in neutral media microbial fuel cells. *Energy Environ Sci.*, 9(7):2346–2353, 2016.

[62] S. Ratso, I. Kruusenberg, M. Käärik, M. Kook, R. Saar, M. Pärs, J. Leis, and K. Tammeveski. Highly efficient nitrogen-doped carbide-derived carbon materials for oxygen reduction reaction in alkaline media. *Carbon*, 113:159–169, 2017.

[63] Q. Zhou and G. Shi. Conducting polymer-based catalysts. *JACS*, 138(9):2868–2876, 2016.

[64] Y. Liang, Y. Li, H. Wang, J. Zhou, J. Wang, T. Regier, and H. Dai. Co_3O_4 nanocrystals on graphene as a synergistic catalyst for oxygen reduction reaction. *Nat. Mater.*, 10(10):780–786, 2011.

[65] E. Yeager. Dioxygen electrocatalysis: mechanisms in relation to catalyst structure. *JJ. Mol. Catal. Chem.*, 38(1-2):5–25, 1986.

[66] A. J. Bard, L. R. Faulkner, J. Leddy, and C. G. Zoski. *Electrochemical methods: fundamentals and applications*, volume 2. Wiley New York, 1980.

[67] J. Stacy, Y.N. Regmi, B. Leonard, and M. Fan. The recent progress and future of oxygen reduction reaction catalysis: A review. *Renew. Sustainable Energy Rev.*, 69:401–414, 2017.

[68] T.J. Schmidt, U.A. Paulus, H.A. Gasteiger, and R.J. Behm. The oxygen reduction reaction on a Pt/carbon fuel cell catalyst in the presence of chloride anions. *J. Electroanal. Chem.*, 508(1):41–47, 2001.

[69] O. T. Holton and J.W. Stevenson. The role of platinum in proton exchange membrane fuel cells. *Platin. Met. Rev.*, 57(4):259–271, 2013.

[70] H.A. Hansen, V. Viswanathan, and J.K. Nørskov. Unifying kinetic and thermodynamic analysis of 2 e–and 4 e–reduction of oxygen on metal surfaces. *J. Phys. Chem. C*, 118(13):6706–6718, 2014.

[71] C. Song and J. Zhang. Electrocatalytic oxygen reduction reaction. In *PEM fuel cell electrocatalysts and catalyst layers*, pages 89–134. Springer, 2008.

[72] A. Parthasarathy, S. Srinivasan, A. J. Appleby, and C. R. Martin. Temperature dependence of the electrode kinetics of oxygen reduction at the platinum/nafion® interface — a microelectrode investigation. *J. Electrochem. Soc.*, 139(9):2530–2537, 1992.

[73] N. Ramaswamy and S: Mukerjee. Fundamental mechanistic understanding of electrocatalysis of oxygen reduction on Pt and non-Pt surfaces: acid versus alkaline media. *Advances in Physical Chemistry*, 2012, 2012.

[74] V.S. Murthi, R.C. Urian, and S. Mukerjee. Oxygen reduction kinetics in low and medium temperature acid environment: correlation of water activation and surface properties in supported pt and pt alloy electrocatalysts. *J. Phys. Chem. B*, 108(30):11011–11023, 2004.

[75] B.E. Conway, J.O'M. Bockris, S.U.M. Khan, R.E. White, and E. Yeager. Kinetics and mechanisms of electrode processes. 1983.

[76] N.M. Marković, H.A. Gasteiger, and P.N. Ross. Oxygen reduction on platinum low-index single-crystal surfaces in alkaline solution: rotating ring diskpt (hkl) studies. *J. Phys. Chem.*, 100(16):6715–6721, 1996.

[77] O. Antoine and R. Durand. Rrde study of oxygen reduction on Pt nanoparticles inside Nafion®: H_2O_2 production in PEMFC cathode conditions. *J. Appl. Electrochem.*, 30(7):839–844, 2000.

[78] J. Cheng and P. Hu. Utilization of the three-dimensional volcano surface to understand the chemistry of multiphase systems in heterogeneous catalysis. *JACS*, 130(33):10868–10869, 2008.

[79] T. Bligaard, J.K. Nørskov, S. Dahl, J. Matthiesen, C.H. Christensen, and J. Sehested. The Brønsted–Evans–Polanyi relation and the volcano curve in heterogeneous catalysis. *J. Catal.*, 224(1):206–217, 2004.

[80] A. Stassi, C. D'urso, V. Baglio, A. Di Blasi, V. Antonucci, A.S. Arico, A.M.C. Luna, A. Bonesi, and W.E. Triaca. Electrocatalytic behaviour for oxygen reduction reaction of small nanostructured crystalline bimetallic Pt–M supported catalysts. *J. Appl. Electrochem.*, 36(10):1143–1149, 2006.

[81] K. Kimijima, A. Hayashi, S. Umemura, J. Miyamoto, K. Sekizawa, T. Yoshida, and I. Yagi. Oxygen reduction reactivity of precisely controlled nanostructured model catalysts. *J. Phys. Chem. C*, 114(35):14675–14683, 2010.

[82] A. Morozan, B. Jousselme, and S. Palacin. Low-platinum and platinum-free catalysts for the oxygen reduction reaction at fuel cell cathodes. *Energy Environ Sci.*, 4(4):1238–1254, 2011.

[83] D. Pillay, M.D. Johannes, Y. Garsany, and K.E. Swider-Lyons. Poisoning of Pt_3Co electrodes: A combined experimental and DFT study. *J. Phys. Chem. C*, 114(17):7822–7830, 2010.

[84] X. Yu and S. Ye. Recent advances in activity and durability enhancement of Pt/C catalytic cathode in PEMFC: Part ii: Degradation mechanism and durability enhancement of carbon supported platinum catalyst. *J. Power Sources*, 172(1):145–154, 2007.

[85] Y. Shao, G. Yin, and Y. Gao. Understanding and approaches for the durability issues of Pt-based catalysts for PEM fuel cell. *J. Power Sources*, 171(2):558–566, 2007.

[86] C.M. Sánchez-Sánchez, J. Solla-Gullón, F.J. Vidal-Iglesias, A. Aldaz, V. Montiel, and E. Herrero. Imaging structure sensitive catalysis on different shape-controlled platinum nanoparticles. *JACS*, 132(16):5622–5624, 2010.

[87] J. Yang, J.Y. Lee, Q. Zhang, W. Zhou, and Z. Liu. Carbon-supported pseudo-core–shell Pd–Pt nanoparticles for ORR with and without methanol. *J. Electrochem. Soc.*, 155(7):B776–B781, 2008.

[88] H.W. Liang, S. Liu, J.Y. Gong, S.B. Wang, L. Wang, and S.H. Yu. Ultrathin Te nanowires: an excellent platform for controlled synthesis of ultrathin platinum and palladium nanowires/nanotubes with very high aspect ratio. *Adv. Mater.*, 21(18):1850–1854, 2009.

[89] Z. Chen, M. Waje, W. Li, and Y. Yan. Supportless Pt and PtPd nanotubes as electrocatalysts for oxygen-reduction reactions. *Angew. Chem. Int. Ed.*, 46(22):4060–4063, 2007.

[90] L. Cademartiri and G.A. Ozin. Ultrathin nanowires—a materials chemistry perspective. *Adv. Mat.*, 21(9):1013–1020, 2009.

[91] C. Koenigsmann, W.P. Zhou, R.R. Adzic, E. Sutter, and S.S. Wong. Size-dependent enhancement of electrocatalytic performance in relatively defect-free, processed ultrathin platinum nanowires. *Nano Lett.*, 10(8):2806–2811, 2010.

[92] J. Greeley, I.E.L. Stephens, A.S. Bondarenko, T.P. Johansson, H.A. Hansen, T.F. Jaramillo, J. Rossmeisl, I.N.J.K. Chorkendorff, and J.K. Nørskov. Alloys of platinum and early transition metals as oxygen reduction electrocatalysts. *Nat. Chem.*, 1(7):552–556, 2009.

[93] R.A. Buchanan, I.S. Lee, and J.M. Williams. Surface modification of biomaterials through noble metal ion implantation. *Journal of Biomedical Materials Research Part A*, 24(3):309–318, 1990.

[94] S.B. Simonsen, I. Chorkendorff, S. Dahl, M. Skoglundh, J. Sehested, and S. Helveg. Direct observations of oxygen-induced platinum nanoparticle ripening studied by in situ TEM. *JACS*, 132(23):7968–7975, 2010.

[95] G. Zhang, Z.G. Shao, W. Lu, G. Li, F. Liu, and B. Yi. One-pot synthesis of Ir@ Pt nanodendrites as highly active bifunctional electrocatalysts for oxygen reduction and oxygen evolution in acidic medium. *Electrochem. Commun.*, 22:145–148, 2012.

[96] B. Lim, X. Lu, M. Jiang, P.H.C.Camargo, E.C. Cho, E.P. Lee, and Y. Xia. Facile synthesis of highly faceted multioctahedral Pt nanocrystals through controlled overgrowth. *Nano Lett.*, 8(11):4043–4047, 2008.

[97] M.H. Shao, K. Sasaki, and R.R. Adzic. Pd- Fe nanoparticles as electrocatalysts for oxygen reduction. *JACS*, 128(11):3526–3527, 2006.

[98] N.N. Kariuki, X. Wang, J.R. Mawdsley, M.S. Ferrandon, S.G. Niyogi, J.T. Vaughey, and D.J. Myers. Colloidal synthesis and characterization of carbon-supported Pd-Cu nanoparticle oxygen reduction electrocatalysts. *Chem. Mat.*, 22(14):4144–4152, 2010.

[99] C. Xu, Y. Zhang, L. Wang, L. Xu, X. Bian, H. Ma, and Y. Ding. Nanotubular mesoporous PdCu bimetallic electrocatalysts toward oxygen reduction reaction. *Chem. Mat.*, 21(14):3110–3116, 2009.

[100] R. Jasinski. A new fuel cell cathode catalyst. *Nature*, 201(4925):1212–1213, 1964.

[101] V.S. Bagotzky, M.R. Tarasevich, K.A. Radyushkina, O.A. Levina, and S.I. Andrusyova. Electrocatalysis of the oxygen reduction process on metal chelates in acid electrolyte. *J. Power Sources.*, 2(3):233–240, 1978.

[102] J. Zagal, M. Paez, A.A. Tanaka, J.R. Dos Santos, and C.A. Linkous. Electrocatalytic activity of metal phthalocyanines for oxygen reduction. *J. Electroanal. Chem.*, 339(1-2):13–30, 1992.

[103] Z. Odabaş, A. Altındal, A.R. Özkaya, B. Salih, and Ö. Bekaroğlu. Novel ball-type homo-and hetero-dinuclear phthalocyanines with four 1, 1'-methylenedinaphthalen-2-ol bridges: synthesis and characterization, electrical and gas sensing properties and electrocatalytic performance towards oxygen reduction. *Sensors Actuat. B-Chem.*, 145(1):355–366, 2010.

[104] Y.G. Wang, L. Cheng, F. Li, H.M. Xiong, and Y.Y. Xia. High electrocatalytic performance of Mn_3O_4/mesoporous carbon composite for oxygen reduction in alkaline solutions. *Chem. Mater.*, 19(8):2095–2101, 2007.

[105] F. Cheng, Y. Su, J. Liang, Z. Tao, and J. Chen. MnO_2-based nanostructures as catalysts for electrochemical oxygen reduction in alkaline media. *Chem. Mater.*, 22(3):898–905, 2009.

[106] W. Xiao, D. Wang, and X.W. Lou. Shape-controlled synthesis of MnO_2 nanostructures with enhanced electrocatalytic activity for oxygen reduction. *J. Phys. Chem. C*, 114(3):1694–1700, 2009.

[107] L. Mao, D. Zhang, T. Sotomura, K. Nakatsu, N. Koshiba, and T. Ohsaka. Mechanistic study of the reduction of oxygen in air electrode with manganese oxides as electrocatalysts. *Electrochim. Acta*, 48(8):1015–1021, 2003.

[108] F.H.B. Lima, M.L. Calegaro, and E.A. Ticianelli. Electrocatalytic activity of manganese oxides prepared by thermal decomposition for oxygen reduction. *Electrochim. Acta*, 52(11):3732–3738, 2007.

[109] Y.G. Wang and Y.Y. Xia. A direct borohydride fuel cell using MnO_2-catalyzed cathode and hydrogen storage alloy anode. *Electrochem. Commun.*, 8(11):1775–1778, 2006.

[110] D. Qu. Investigation of the porosity of electrolytic manganese dioxide and its performance as alkaline cathode material. *J. Power Sources*, 156(2):692–699, 2006.

[111] W. Sun, A. Hsu, and R. Chen. Carbon-supported tetragonal MnOOH catalysts for oxygen reduction reaction in alkaline media. *J. Power Sources*, 196(2):627–635, 2011.

[112] Y. Takasu, M. Suzuki, H. Yang, T. Ohashi, and W. Sugimoto. Oxygen reduction characteristics of several valve metal oxide electrodes in $HClO_4$ solution. *Electrochim. Acta*, 55(27):8220–8229, 2010.

[113] X. Pan, M.Q. Yang, X. Fu, N. Zhang, and Y.J. Xu. Defective TiO_2 with oxygen vacancies: synthesis, properties and photocatalytic applications. *Nanoscale*, 5(9):3601–3614, 2013.

[114] J.H. Kim, A. Ishihara, S. Mitsushima, N. Kamiya, and K.I. Ota. Catalytic activity of titanium oxide for oxygen reduction reaction as a non-platinum catalyst for PEFC. *Electrochim. acta*, 52(7):2492–2497, 2007.

[115] A. Ishihara, Y. Ohgi, K. Matsuzawa, S. Mitsushima, and K.I. Ota. Progress in non-precious metal oxide-based cathode for polymer electrolyte fuel cells. *Electrochim. Acta*, 55(27):8005–8012, 2010.

[116] S. Ferguson-Miller and G.T. Babcock. Heme/copper terminal oxidases. *Chem. Rev.*, 96(7):2889–2908, 1996.

[117] J.P. Collman, A. Dey, R.A. Decreau, Y. Yang, A. Hosseini, E.I. Solomon, and T.A. Eberspacher. Interaction of nitric oxide with a functional model of cytochrome c oxidase. *Proc. Natl. Acad. Sci. USA*, 105(29):9892–9896, 2008.

[118] E. Vayner, H. Schweiger, and A.B. Anderson. Four-electron reduction of O_2 over multiple Cu i centers: Quantum theory. *J. Electroanal. Chem.*, 607(1):90–100, 2007.

[119] N. Mano, J.L. Fernandez, Y. Kim, W. Shin, A.J. Bard, and A. Heller. Oxygen is electroreduced to water on a "wired" enzyme electrode at a lesser overpotential than on platinum. *JACS*, 125(50):15290–15291, 2003.

[120] J.A. Cracknell, K.A. Vincent, and F.A. Armstrong. Enzymes as working or inspirational electrocatalysts for fuel cells and electrolysis. *Chem. Rev.*, 108(7):2439–2461, 2008.

[121] J.P. Collman, N.K. Devaraj, R.A. Decréau, Y. Yang, Y.L. Yan, W. Ebina, T.A. Eberspacher, and C.E.D. Chidsey. A cytochrome c oxidase model catalyzes oxygen to water reduction under rate-limiting electron flux. *Science*, 315(5818):1565–1568, 2007.

[122] J. Qiao, Y. Liu, and J. Zhang. *Electrochemical Reduction of Carbon Dioxide: Fundamentals and Technologies*. Electrochemical Energy Storage and Conversion. CRC Press, 2016.

[123] J. Qiao, Y. Liu, F. Hong, and J. Zhang. A review of catalysts for the electroreduction of carbon dioxide to produce low-carbon fuels. *Chem. Soc. Rev.*, 43(2):631–675, 2014.

[124] Y. Hori, A. Murata, and R. Takahashi. Formation of hydrocarbons in the electrochemical reduction of carbon dioxide at a copper electrode in aqueous solution. *J. Chem. Soc., Faraday Trans. I*, 85(8):2309–2326, 1989.

[125] Y. Hori, R. Takahashi, Y. Yoshinami, and A. Murata. Electrochemical reduction of CO at a copper electrode. *J. Phys. Chem. B*, 101(36):7075–7081, 1997.

[126] D.A. Tryk, T. Yamamoto, M. Kokubun, K. Hirota, K. Hashimoto, M. Okawa, and A. Fujishima. Recent developments in electrochemical and photoelectrochemical CO_2 reduction: involvement of the $(CO_2)_2^{\bullet-}$-dimer radical anion. *Appl. Organomet. Chem.*, 15(2):113–120, 2001.

[127] Y.B. Vassiliev, V.S. Bagotsky, N.V.Osetrova, O.A. Khazova, and N.A. Mayorova. Electroreduction of carbon dioxide: Part i. the mechanism and kinetics of electroreduction of CO_2 in aqueous solutions on metals with high and moderate hydrogen overvoltages. *J. Electroanal. Chem.*, 189(2):271–294, 1985.

[128] R.P.S. Chaplin and A.A. Wragg. Effects of process conditions and electrode material on reaction pathways for carbon dioxide electroreduction with particular reference to formate formation. *J. Appl. Electrochem.*, 33(12):1107–1123, 2003.

[129] A.W.B. Aylmer-Kelly, A. Bewick, P.R. Cantrill, and A.M. Tuxford. Studies of electrochemically generated reaction intermediates using modulated specular reflectance spectroscopy. *Farad. Discuss.*, 56:96–107, 1973.

[130] W.M. Ayers. An overview of electrochemical carbon dioxide reduction. *Special Publication RSC*, 153(1):365–365, 1994.

[131] H. De Jesús-Cardona, C. Del Moral, and C.R. Cabrera. Voltammetric study of CO_2 reduction at Cu electrodes under different $KHCO_3$ concentrations, temperatures and CO_2 pressures. *J. Electroanal. Chem.*, 513(1):45–51, 2001.

[132] Y. Hori, A. Murata, R. Takahashi, and S. Suzuki. Electroreduction of carbon monoxide to methane and ethylene at a copper electrode in aqueous solutions at ambient temperature and pressure. *JACS*, 109(16):5022–5023, 1987.

[133] Y. Hori, H. Konishi, T. Futamura, A. Murata, O. Koga, H. Sakurai, and K. Oguma. "deactivation of copper electrode" in electrochemical reduction of CO_2. *Electrochim. Acta*, 50(27):5354–5369, 2005.

[134] S. Lee, J.D. Ocon, Y. Son, and J. Lee. Alkaline CO_2 electrolysis toward selective and continuous HCOO–production over SnO_2 nanocatalysts. *J. Phys. Chem. C*, 119(9):4884–4890, 2015.

[135] K. Hara, A. Kudo, and T. Sakata. Electrochemical reduction of carbon dioxide under high pressure on various electrodes in an aqueous electrolyte. *J. Electroanal. Chem.*, 391(1-2):141–147, 1995.

[136] S. Nakagawa, A. Kudo, M. Azuma, and T. Sakata. Effect of pressure on the electrochemical reduction of CO_2 on group VIII metal electrodes. *J. Electroanal. Chem. Interfacial Electrochem.*, 308(1-2):339–343, 1991.

[137] K. Hara, A. Kudo, and T. Sakata. Electrochemical reduction of high pressure carbon dioxide on Fe electrodes at large current density. *J. Electroanal. Chem.*, 386(1-2):257–260, 1995.

[138] M. Todoroki, K. Hara, A. Kudo, and T. Sakata. Electrochemical reduction of high pressure CO_2 at Pb, Hg and In electrodes in an aqueous $KHCO_3$ solution. *J. Electroanal. Chem.*, 394(1-2):199–203, 1995.

[139] H. Noda, S. Ikeda, Y. Oda, K. Imai, M. Maeda, and K. Ito. Electrochemical reduction of carbon dioxide at various metal electrodes in aqueous potassium hydrogen carbonate solution. *Bull. Chem. Soc. Jpn.*, 63(9):2459–2462, 1990.

[140] J.A. Ramos Sende, C.R. Arana, L. Hernandez, K.T. Potts, M. Keshevarz-K, and H.D. Abruna. Electrocatalysis of CO_2 reduction in aqueous media at electrodes modified with electropolymerized films of vinylterpyridine complexes of transition metals. *Inorg. Chem.*, 34(12):3339–3348, 1995.

[141] J. Wu, P.P. Sharma, B.H. Harris, and X.D. Zhou. Electrochemical reduction of carbon dioxide: IV dependence of the faradaic efficiency and current density on the microstructure and thickness of tin electrode. *J. Power Sources*, 258:189–194, 2014.

[142] Y. Oh, H. Vrubel, S. Guidoux, and X. Hu. Electrochemical reduction of CO_2 in organic solvents catalyzed by MoO_2. *ChemComm*, 50(29):3878–3881, 2014.

[143] J.H. Alstrum-Acevedo, M.K. Brennaman, and T.J. Meyer. Chemical approaches to artificial photosynthesis. 2. *Inorg. Chem.*, 44(20):6802–6827, 2005.

[144] Y. Tamaki and O. Ishitani. Supramolecular photocatalysts for the reduction of CO_2. *ACS Catalysis*, 7(5):3394–3409, 2017.

[145] Q. Lu and F. Jiao. Electrochemical CO_2 reduction: Electrocatalyst, reaction mechanism, and process engineering. *Nano Energy*, 29:439–456, 2016.

[146] C. Song. Global challenges and strategies for control, conversion and utilization of CO_2 for sustainable development involving energy, catalysis, adsorption and chemical processing. *Catal. today*, 115(1):2–32, 2006.

[147] H. Li and C. Oloman. Development of a continuous reactor for the electro-reduction of carbon dioxide to formate–part 2: Scale-up. *J. Appl. Electrochem.*, 37(10):1107–1117, 2007.

[148] Chuan Shi, Heine A Hansen, Adam C Lausche, and Jens K Nørskov. Trends in electrochemical CO_2 reduction activity for open and close-packed metal surfaces. *Phys. Chem. Chem. Phys.*, 16(10):4720–4727, 2014.

[149] B.R. Eggins and J. McNeill. Voltammetry of carbon dioxide: part i. a general survey of voltammetry at different electrode materials in different solvents. *J. Electroanal. Chem. Interfacial Electrochem.*, 148(1):17–24, 1983.

[150] G.M. Brisard, A.P.M. Camargo, F.C. Nart, and T. Iwasita. On-line mass spectrometry investigation of the reduction of carbon dioxide in acidic media on polycrystalline pt. *Electrochem. Commun.*, 3(11):603–607, 2001.

[151] K. Hara, A. Kudo, T. Sakata, and M. Watanabe. High efficiency electrochemical reduction of carbon dioxide under high pressure on a gas diffusion electrode containing pt catalysts. *J. Electrochem. Soc.*, 142(4):L57–L59, 1995.

[152] B. Hu, V. Stancovski, M. Morton, and S.L. Suib. Enhanced electrocatalytic reduction of CO_2/H_2O to paraformaldehyde at Pt/metal oxide interfaces. *Appl Catal A Gen.*, 382(2):277–283, 2010.

[153] X.Y. Wang, S.Q. Liu, K.L. Huang, Q.J. Feng, B. Liu, J.L. Liu, and G.H. Jin. Fixation of CO_2 by electrocatalytic reduction to synthesis of dimethyl carbonate in ionic liquid using effective silver-coated nanoporous copper composites. *Chin. Chem. Lett.*, 21(8):987–990, 2010.

[154] Y. Hori, A. Murata, R. Takahashi, and S. Suzuki. Enhanced formation of ethylene and alcohols at ambient temperature and pressure in electrochemical reduction of carbon dioxide at a copper electrode. *J. Chem. Soc., Chem. Commun.*, (1):17–19, 1988.

[155] R. Reske, H. Mistry, F. Behafarid, B. Roldan Cuenya, and P. Strasser. Particle size effects in the catalytic electroreduction of CO_2 on Cu nanoparticles. *JACS*, 136(19):6978–6986, 2014.

[156] L. Li, A.H. Larsen, N.A. Romero, V.A. Morozov, C. Glinsvad, F. Abild-Pedersen, J. Greeley, K.W. Jacobsen, and J.K. Nørskov. Investigation of catalytic finite-size-effects of platinum metal clusters. *J. Phys. Chem. Lett.*, 4(1):222–226, 2012.

[157] O. Ola and M.M. Maroto-Valer. Review of material design and reactor engineering on TiO_2 photocatalysis for CO_2 reduction. *J. Photochem. Photobiol. C*, 24:16–42, 2015.

[158] K.W. Frese. Electrochemical reduction of CO_2 at intentionally oxidized copper electrodes. *J. Electrochem. Soc.*, 138(11):3338–3344, 1991.

[159] T.Y. Chang, R.M. Liang, P.W. Wu, J.Y. Chen, and Y.C. Hsieh. Electrochemical reduction of CO_2 by Cu_2O-catalyzed carbon clothes. *Mat. Lett.*, 63(12):1001–1003, 2009.

[160] C.W. Li and M.W. Kanan. CO_2 reduction at low overpotential on cu electrodes resulting from the reduction of thick Cu_2O films. *JACS*, 134(17):7231–7234, 2012.

[161] M.A. Fox and M.T. Dulay. Heterogeneous photocatalysis. *Chem. Rev.*, 93(1):341–357, 1993.

[162] C. Creutz and E. Fujita. Carbon dioxide as a feedstock. *Carbon Management, The National Academic Press*, 2001.

[163] P. Li, H. Hu, J. Xu, H. Jing, H. Peng, J. Lu, C. Wu, and S. Ai. New insights into the photo-enhanced electrocatalytic reduction of carbon dioxide on MoS_2-rods/TiO_2 NTs with unmatched energy band. *Appl. Catal., B*, 147:912–919, 2014.

[164] J. Qu, X. Zhang, Y. Wang, and C. Xie. Electrochemical reduction of CO_2 on RuO_2/TiO_2 nanotubes composite modified Pt electrode. *Electrochim. Acta*, 50(16):3576–3580, 2005.

[165] N. Spataru, K. Tokuhiro, C. Terashima, T.N. Rao, and A. Fujishima. Electrochemical reduction of carbon dioxide at ruthenium dioxide deposited on boron-doped diamond. *J. Appl. Electrochem.*, 33(12):1205–1210, 2003.

[166] A. Monnier, J. Augustynski, and C. Stalder. On the electrolytic reduction of carbon dioxide at TiO_2 and TiO_2-Ru cathodes. *J. electroanal. chem. interfacial electrochem.*, 112(2):383–385, 1980.

[167] M. Koudelka, A. Monnier, and J. Augustynski. Electrocatalysis of the cathodic reduction of carbon dioxide on platinized titanium dioxide film electrodes. *J. Electrochem. Soc.*, 131(4):745–750, 1984.

[168] F. Köleli, T. Atilan, N. Palamut, A.M. Gizir, R. Aydin, and C.H. Hamann. Electrochemical reduction of CO_2 at Pb-and Sn-electrodes in a fixed-bed reactor in aqueous K_2CO_3 and $KHCO_3$ media. *J. Appl. Electrochem.*, 33(5):447–450, 2003.

[169] Y. Chen and M.W. Kanan. Tin oxide dependence of the CO_2 reduction efficiency on tin electrodes and enhanced activity for tin/tin oxide thin-film catalysts. *JACS*, 134(4):1986–1989, 2012.

[170] J. Wu, F.G. Risalvato, S. Ma, and X.D. Zhou. Electrochemical reduction of carbon dioxide III. the role of oxide layer thickness on the performance of Sn electrode in a full electrochemical cell. *J. Mater. Chem. A*, 2(6):1647–1651, 2014.

[171] E. Grabowska. Selected perovskite oxides: characterization, preparation and photocatalytic properties—a review. *Appl. Catal. B*, 186:97–126, 2016.

[172] P. Li, S. Ouyang, G. Xi, T. Kako, and J. Ye. The effects of crystal structure and electronic structure on photocatalytic H_2 evolution and CO_2 reduction over two phases of perovskite-structured $NaNbO_3$. *J. Phys. Chem. C*, 116(14):7621–7628, 2012.

[173] Y. Bi, M.F. Ehsan, Y. Huang, J. Jin, and T. He. Synthesis of cr-doped $SrTiO_3$ photocatalyst and its application in visible-light-driven transformation of CO_2 into CH_4. *Journal of CO2 Utilization*, 12:43–48, 2015.

[174] Z. Jiao, T. Chen, J. Xiong, T. Wang, G. Lu, J. Ye, and Y. Bi. Visible-light-driven photoelectrochemical and photocatalytic performances of Cr-doped $SrTiO_3/TiO_2$ heterostructured nanotube arrays. *Sci. Rep.*, 3, 2013.

[175] R.D.L. Smith and P.G. Pickup. Nitrogen-rich polymers for the electrocatalytic reduction of CO_2. *Electrochem. Commun.*, 12(12):1749–1751, 2010.

[176] F. Köleli, T. Röpke, and C.H. Hamann. The reduction of CO_2 on polyaniline electrode in a membrane cell. *Synth. Met.*, 140(1):65–68, 2004.

[177] P.K. Addo, R.L. Arechederra, A. Waheed, J.D. Shoemaker, W.S. Sly, and S.D. Minteer. Methanol production via bioelectrocatalytic reduction of carbon dioxide: role of carbonic anhydrase in improving electrode performance. *Electrochem. Solid State Lett.*, 14(4):E9–E13, 2011.

[178] D.R. Kauffman, D. Alfonso, C. Matranga, H. Qian, and R. Jin. Experimental and computational investigation of Au25 clusters and CO_2: a unique interaction and enhanced electrocatalytic activity. *JACS*, 134(24):10237–10243, 2012.

[179] E. Stojanovska, E. Canbay, E. S. Pampal, M. D. Calisir, O. Agma, Y. Polat, R. Simsek, N. A. S. Gundogdu, Y. Akgula, and A. Kilic. A review on non-electro nanofibre spinning techniques. *RSC. Adv.*, 6:83783–83801, 2016.

[180] V. M. Cepak and C. R. Martin. Preparation of polymeric micro- and nanostructures using a template-based deposition method. *Chem. Mater.*, 11(5):1363–1367, 1999.

[181] F. Cheng, Z. Tao, J. Liang, and J. Chen. Template-directed materials for rechargeable lithium-ion batteries. *Chem. Mater.*, 20(3):667–681, 2008.

[182] W. Gilbert. *De Magnete, Magneticisque Corporibus, et de Magno Magnete Tellure.* London: Peter Short, 1628.

[183] C. Boys. On the production, properties, and some suggested uses of the finest threads. *Proc. Phys. Soc. London*, 9:8–19, 1887.

[184] N .Bhardwaj and S. C. Kundu. Electrospinning: A fascinating fiber fabrication technique. *Biotechnol. Adv.*, 28:325–347, 2010.

[185] G. Taylor. Properties of liquid marbles. *Proc. R. Soc.*, 462(2067):973–999, 1964.

[186] G. Taylor. *Applied Mechanics*, chapter Conical free surfaces and fluid interfaces, pages 760–796. Springer, 1966.

[187] G. I. Taylor and J. R. Melcher. Electrohydrodynamics: a review of the role of interfacial shear stresses. *Annu. Rev. Fluid. Mech.*, 313:453–475, 1969.

[188] P. Baumgarted. Electrostatic spinning of acrylic microfibers. *J. Colloid Interface Sci.*, 36(1):71–79, 1971.

[189] S. Reznik, A. Therom, and E. Zussman. Transient and steady shapes of droplets attached to a surface in a strong electric field. *J. Fluid Mech.*, 516:349–377, 2004.

[190] M. Hohman, G. Ruletdge, and M. Brenner. Electrospinning and electrically forced jets. *Phys. Fluids*, 13(8):2221, 2001.

[191] G. Srinivasa and D. Reneker. Structure and morphology of small diameter electrospun aramid fibers. *Polymer International*, 36(2):195–201, 1995.

[192] D. Reneker and I. Chun. Nanometre diameter fibres of polymer, produced by electrospinning. *Nanotechnology*, 7(3):216–223, 1996.

[193] H. Fong, I. Chun, and D. Reneker. Beaded nanofibers formed during electrospinning. *Polymer*, 40(16):4585–4592, 1999.

[194] H. Hou and D. Reneker. Carbon nanotubes on carbon nanofibers: a novel structure based on electrospun polymer nanofibers. *Adv. Mat.*, 16(1):69–73, 2004.

[195] C. Thompson, G. Chase, and D. Reneker. Effects of parameters on nanofiber diameter determined from electrospinning model. *Polymer*, 48(23):6913–6922, 2007.

[196] W. E. Teo and S. Ramakrishna. A review on electrospinning design and nanofibre assemblies. *Nanotechnology*, 17:89–106, 2006.

[197] D. Li, G. Ouyang, J.T. McCann, and Y. Xia. Collecting electrospun nanofibers with patterned electrodes. *Nano Lett.*, 5(5):913–916, 2005.

[198] G. Taylor. Electrically driven jets. *Proc. R. Soc. Lond. A*, 313:453—-475, 1969.

[199] A.L. Yarin, S. Koombhongse, and D.H. Reneker. Bending instability in electrospinning of nanofibers. *J. Appl. Phys.*, 89(5):3018–3026, 2001.

[200] E. Adomavičiūtė and R. Milašius. The influence of applied voltage on poly (vinyl alcohol) (PVA) nanofibre diameter. *Fibres Text East Eur*, 15(5):64–65, 2007.

[201] A. Greiner and J. Wendorff. Functional self-assembled nanofibers by electrospinning in self assembled nanomaterials. *Adv. Polym. Sci.*, 219, 2007.

[202] A. Greiner and J.H. Wendorff. Electrospinning: a fascinating method for the preparation of ultrathin fibers. *Angew. Chem.*, 46(30):5670–5703, 2007.

[203] V. Kirichenko, Y. Filatov, and A. Budyka. Electrospinning of micro-and nanofibers: fundamentals in separation and filtration processes. *Int. J. Multiscale Comput. Eng.*, 8(4), 2010.

[204] S. Ramakrishna. *An introduction to electrospinning and nanofibers*. World Scientific, 2005.

[205] J.H. Wendorff, S. Agarwal, and A. Greiner. *Electrospinning: materials, processing, and applications*. John Wiley & Sons, 2012.

[206] D.H. Reneker and A.L. Yarin. Electrospinning jets and polymer nanofibers. *Polymer*, 49(10):2387–2425, 2008.

[207] A.L. Yarin, S. Koombhongse, and D.H. Reneker. Taylor cone and jetting from liquid droplets in electrospinning of nanofibers. *J. Appl. Phys.*, 90(9):4836–4846, 2001.

[208] M.M. Hohman, M. Shin, G. Rutledge, and M.P. Brenner. Electrospinning and electrically forced jets. i. stability theory. *Phys. Fluids*, 13(8):2201–2220, 2001.

[209] Y.M. Shin, M.M. Hohman, M.P. Brenner, and G.C. Rutledge. Experimental characterization of electrospinning: the electrically forced jet and instabilities. *Polymer*, 42(25):9955–9967, 2001.

[210] D.H. Reneker, A.L. Yarin, H. Fong, and S. Koombhongse. Bending instability of electrically charged liquid jets of polymer solutions in electrospinning. *J. Appl. Phys.*, 87(9):4531–4547, 2000.

[211] D.H. Reneker, A.L. Yarin, H. Fong, and S. Koombhongse. Bending instability of electrically charged liquid jets of polymer solutions in electrospinning. *J. Appl. Phys.*, 87(9):4531–4547, 2000.

[212] J.M. Deitzel, J. Kleinmeyer, D.E.A. Harris, and N.C.B. Tan. The effect of processing variables on the morphology of electrospun nanofibers and textiles. *Polymer*, 42(1):261–272, 2001.

[213] S. Earnshaw. On the nature of the molecular forces which regulate the constitution of the luminiferous ether. *Trans. Camb. Philos. Soc.*, 7:97–112, 1842.

[214] W.T. Scott. Who was earnshaw? *Am. J. Phys.*, 27(6):418–419, 1959.

[215] D.H. Reneker, A.L. Yarin, E. Zussman, and H. Xu. Electrospinning of nanofibers from polymer solutions and melts. *Adv. Appl. Mech.*, 41:43–346, 2007.

[216] L. Huangi, S.S. Manickam, and J.R. McCutcheon. Increasing strength of electrospun nanofiber membranes for water filtration using solvent vapor. *J. Membr. Sci*, 436:213–220, 2013.

[217] E.D. Boland, G.E. Wnek, D.G. Simpson, K.J. Pawlowski, and G.L. Bowlin. Tailoring tissue engineering scaffolds using electrostatic processing techniques: a study of poly (glycolic acid) electrospinning. *J. Macromol. Sci., Part A*, 38(12):1231–1243, 2001.

[218] J.A. Matthews, G.E. Wnek, D.G. Simpson, and G.L. Bowlin. Electrospinning of collagen nanofibers. *Biomacromolecules*, 3(2):232–238, 2002.

[219] Z.H. Huang, Y.-Z. Zhang, M. Kotaki, and S. Ramakrishna. A review on polymer nanofibers by electrospinning and their applications in nanocomposites. *Compos. Sci. Technol.*, 63(15):2223–2253, 2003.

[220] S.F. Fennessey and R.J. Farris. Fabrication of aligned and molecularly oriented electrospun polyacrylonitrile nanofibers and the mechanical behavior of their twisted yarns. *Polymer*, 45(12):4217–4225, 2004.

[221] R. Dersch, T. Liu, A.K. Schaper, A. Greiner, and J.K. Wendorff. Electrospun nanofibers: Internal structure and intrinsic orientation. *J. Polym. Sci., Part A: Polym. Chem.*, 41(4):545–553, 2003.

[222] A. Baji, Y.-W.Mai, S.-C. Wong, M. Abtahi, and P. Chen. Electrospinning of polymer nanofibers: effects on oriented morphology, structures and tensile properties. *Compos. Sci. Technol.*, 70(5):703–718, 2010.

[223] S.V. Fridrikh, H.Y. Jian, M.P. Brenner, and G.C. Rutledge. Controlling the fiber diameter during electrospinning. *Phys. Rev. Lett.*, 90(14):144502, 2003.

[224] S.A. Theron, E. Zussman, and A.L. Yarin. Experimental investigation of the governing parameters in the electrospinning of polymer solutions. *Polymer*, 45(6):2017–2030, 2004.

[225] Q.P. Pham, U. Sharma, and A.G. Mikos. Electrospinning of polymeric nanofibers for tissue engineering applications: a review. *Tissue Eng.*, 12(5):1197–1211, 2006.

[226] S. Rafiei, S. Maghsoodloo, B. Noroozi, V. Mottaghitalab, and A.K. Haghi. Mathematical modeling in electrospinning process of nanofibers: a detailed review. *Cellul. Chem. Technol.*, 47:323–338, 2013.

[227] C.S. Ki, D.H. Baek, K.D. Gang, K.H. Lee, I.C. Um, and Y.K. Park. Characterization of gelatin nanofiber prepared from gelatin–formic acid solution. *Polymer*, 46(14):5094–5102, 2005.

[228] W.K. Son, J.H. Youk, T.S. Lee, and W.H. Park. The effects of solution properties and polyelectrolyte on electrospinning of ultrafine poly (ethylene oxide) fibers. *Polymer*, 45(9):2959–2966, 2004.

[229] Sachin Talwar, Juan Hinestroza, Benham Pourdeyhimi, and Saad A Khan. Associative polymer facilitated electrospinning of nanofibers. *Macromolecules*, 41(12):4275–4283, 2008.

[230] V.J. Chen and P.X. Ma. Nano-fibrous poly (L-lactic acid) scaffolds with interconnected spherical macropores. *Biomaterials*, 25(11):2065–2073, 2004.

[231] M.M. Demir, I. Yilgor, E.E.A. Yilgor, and B. Erman. Electrospinning of polyurethane fibers. *Polymer*, 43(11):3303–3309, 2002.

[232] P. Gupta, C. Elkins, T.E. Long, and G.L. Wilkes. Electrospinning of linear homopolymers of poly (methyl methacrylate): exploring relationships between fiber formation, viscosity, molecular weight and concentration in a good solvent. *Polymer*, 46(13):4799–4810, 2005.

[233] J. Zeng, H. Haoqing, A. Schaper, J.H. Wendorff, and A. Greiner. Poly-L-lactide nanofibers by electrospinning–influence of solution viscosity and electrical conductivity on fiber diameter and fiber morphology. *e-Polymers*, 3(1):102–110, 2003.

[234] H. Jiang, D. Fang, B.S. Hsiao, B. Chu, and W. Chen. Optimization and characterization of dextran membranes prepared by electrospinning. *Biomacromolecules*, 5(2):326–333, 2004.

[235] T.J. Sill and H.A. von Recum. Electrospinning: applications in drug delivery and tissue engineering. *Biomaterials*, 29(13):1989–2006, 2008.

[236] W. Zuo, M. Zhu, W. Yang, H. Yu, Y. Chen, and Y. Zhang. Experimental study on relationship between jet instability and formation of beaded fibers during electrospinning. *Polym. Eng. Sci.*, 45(5):704–709, 2005.

[237] C. Mit-uppatham, M. Nithitanakul, and P. Supaphol. Ultrafine electrospun polyamide-6 fibers: effect of solution conditions on morphology and average fiber diameter. *Macromol. Chem. Phys*, 205(17):2327–2338, 2004.

[238] C.L. Casper, J.S. Stephens, N.G. Tassi, D.B. Chase, and J.F. Rabolt. Controlling surface morphology of electrospun polystyrene fibers: effect of humidity and molecular weight in the electrospinning process. *Macromolecules*, 37(2):573–578, 2004.

[239] D. Li and Y. Xia. Electrospinning of nanofibers: reinventing the wheel? *Adv. Mat.*, 16(14):1151–1170, 2004.

[240] S. Thenmozhi, N. Dharmaraj, K. Kadirvelu, and H.Y. Kim. Electrospun nanofibers: New generation materials for advanced applications. *Mater. Sci. Eng. B*, 217:36–48, 2017.

[241] and D.N. Heo S.J. Lee, J.H. Mooni, W.K. Ko, J.B. Lee, M.S. Bae, S.W. Park, J.E. Kim, D.H. Lee, E.C. Kim, et al. Electrospun chitosan nanofibers with controlled levels of silver nanoparticles. preparation, characterization and antibacterial activity. *Carbohydr. Polym.*, 111:530–537, 2014.

[242] A.R. Unnithan, G. Gnanasekaran, Y. Sathishkumar, Y.S.Lee, and C.S. Kim. Electrospun antibacterial polyurethane–cellulose acetate–zein composite mats for wound dressing. *Carbohydr. Polym.*, 102:884–892, 2014.

[243] P. Tonglairoum, T. Ngawhirunpat, T. Rojanarata, R. Kaomongkolgit, and P. Opanasopit. Fabrication of a novel scaffold of clotrimazole-microemulsion-containing nanofibers using an electrospinning process for oral candidiasis applications. *Colloids Surf., B*, 126:18–25, 2015.

[244] X. Zong, K. Kim, D. Fang, S. Ran, B.S. Hsiao, and B. Chu. Structure and process relationship of electrospun bioabsorbable nanofiber membranes. *Polymer*, 43(16):4403–4412, 2002.

[245] C.J. Buchko, L.C. Chen, Y. Shen, and D.C. Martin. Processing and microstructural characterization of porous biocompatible protein polymer thin films. *Polymer*, 40(26):7397–7407, 1999.

[246] G. Yang, J. Wang, Y. Wangi, L. Li, X. Guo, and S. Zhou. An implantable active-targeting micelle-in-nanofiber device for efficient and safe cancer therapy. *ACS nano*, 9(2):1161–1174, 2015.

[247] X. Fang, H. Ma, S. Xiao, M. Shen, R. Guo, X. Cao, and X. Shi. Facile immobilization of gold nanoparticles into electrospun polyethyleneimine/polyvinyl alcohol nanofibers for catalytic applications. *J. Mater. Chem.*, 21(12):4493–4501, 2011.

[248] A. Das, M. Gupta, S. Rajagopalan, and A.K. Tyagi. Selective capacitive sensor for ammonia hydroxide at room temperature. *IEEE Sens. J.*, 13(7):2757–2762, 2013.

[249] M. Breitwieser, C. Klose, M. Klingele, A. Hartmann, J. Erben, H. Cho, J. Kerres, R. Zengerle, and S. Thiele. Simple fabrication of 12 μm thin nanocomposite fuel cell membranes by direct electrospinning and printing. *J. Power Sources*, 337:137–144, 2017.

[250] S. Jayaraman, V. Aravindan, P. Suresh Kumar, W. Chui Ling, S. Ramakrishna, and S. Madhavi. Exceptional performance of $TiNb_2O_7$ anode in all one-dimensional architecture by electrospinning. *ACS Appl. Mater. Interfaces*, 6(11):8660–8666, 2014.

[251] J.C. Kim and D.W. Kim. Electrospun Cu/Sn/C nanocomposite fiber anodes with superior usable lifetime for lithium-and sodium-ion batteries. *Chem. Asian J.*, 9(11):3313–3318, 2014.

[252] R. Ramaseshan, S. Sundarrajan, Y. Liu, R.S. Barhate, N.L. Lala, and S. Ramakrishna. Functionalized polymer nanofibre membranes for protection from chemical warfare stimulants. *Nanotechnology*, 17(12):2947, 2006.

[253] P. Zhang, X. Zhao, X. Zhang, Y. Lai, X. Wang, J. Li, G. Wei, and Z. Su. Electrospun doping of carbon nanotubes and platinum nanoparticles into the β-phase polyvinylidene difluoride nanofibrous membrane for biosensor and catalysis applications. *ACS Appl. Mater. Interfaces*, 6(10):7563–7571, 2014.

[254] A. Mahapatra, B.G. Mishra, and G. Hota. Studies on electrospun alumina nanofibers for the removal of chromium (VI) and fluoride toxic ions from an aqueous system. *Ind. Eng. Chem. Res.*, 52(4):1554–1561, 2013.

[255] O.K. Varghese, M. Paulose, T.J. LaTempa, and C.A. Grimes. High-rate solar photocatalytic conversion of CO_2 and water vapor to hydrocarbon fuels. *Nano Lett.*, 9(2):731–737, 2009.

[256] M. Paulose, O.K. Varghese, G.K. Mor, C.A. Grimes, and K.G. Ong. Unprecedented ultra-high hydrogen gas sensitivity in undoped titania nanotubes. *Nanotechnology*, 17(2):398, 2005.

[257] K. Shankar, G.K. Mor, H.E. Prakasam, S. Yoriya, M. Paulose, O.K. Varghese, and C.A. Grimes. Highly-ordered TiO_2 nanotube arrays up to 220 μm in length: use in water photoelectrolysis and dye-sensitized solar cells. *Nanotechnology*, 18(6):065707, 2007.

[258] G.K. Mor, K. Shankar, M. Paulose, O.K. Varghese, and C.A. Grimes. Use of highly-ordered TiO_2 nanotube arrays in dye-sensitized solar cells. *Nano Lett.*, 6(2):215–218, 2006.

[259] L. Peng, A.D. Mendelsohn, T.J. LaTempa, S. Yoriya, C.A. Grimes, and T.A. Desai. Long-term small molecule and protein elution from TiO_2 nanotubes. *Nano Lett.*, 9(5):1932–1936, 2009.

[260] G.F. Ortiz, I. Hanzu, T. Djenizian, P. Lavela, J.L. Tirado, and P. Knauth. Alternative li-ion battery electrode based on self-organized titania nanotubes. *Chem. Mat.*, 21(1):63–67, 2008.

[261] X. Lu, G. Wang, T. Zhai, M. Yu, J. Gan, Y. Tong, and Y. Li. Hydrogenated TiO_2 nanotube arrays for supercapacitors. *Nano Lett.*, 12(3):1690–1696, 2012.

[262] K.C. Popat, M. Eltgroth, T.J. LaTempa, C.A. Grimes, and T.A. Desai. Decreased staphylococcus epidermis adhesion and increased osteoblast functionality on antibiotic-loaded titania nanotubes. *Biomaterials*, 28(32):4880–4888, 2007.

[263] J.H. Jung, H. Kobayashi, K.J.C. van Bommel, S. Shinkai, and T. Shimizu. Creation of novel helical ribbon and double-layered nanotube TiO_2 structures using an organogel template. *Chem. Mat.*, 14(4):1445–1447, 2002.

[264] H.H. Ou and S.L. Lo. Review of titania nanotubes synthesized via the hydrothermal treatment: fabrication, modification, and application. *Sep. Purif. Technol.*, 58(1):179–191, 2007.

[265] M. Paulose, H.E. Prakasam, O.K. Varghese, L. Peng, K.C. Popat, G.K. Mor, T.A. Desai, and C.A. Grimes. TiO_2 nanotube arrays of 1000 μm length by anodization of titanium foil: phenol red diffusion. *J. Phys. Chem. C*, 111(41):14992–14997, 2007.

[266] Q. Cai, M. Paulose, O.K. Varghese, and C.A. Grimes. The effect of electrolyte composition on the fabrication of self-organized titanium oxide nanotube arrays by anodic oxidation. *J. Mater. Res.*, 20(1):230–236, 2005.

[267] A. Valota, D.J. LeClere, P. Skeldon, M. Curioni, T. Hashimoto, S. Berger, J. Kunze, P. Schmuki, and G.E. Thompson. Influence of water content on nanotubular anodic titania formed in fluoride/glycerol electrolytes. *Electrochim. Acta*, 54(18):4321–4327, 2009.

[268] A. Lamberti, N. Garino, A. Sacco, S. Bianco, A. Chiodoni, and C. Gerbaldi. As-grown vertically aligned amorphous TiO_2 nanotube arrays as high-rate li-based micro-battery anodes with improved long-term performance. *Electrochim. Acta*, 151:222–229, 2015.

[269] A. Sacco, A. Lamberti, S. Bianco, and M.E. Tresso. Anodically grown TiO_2 nanotube membranes: Synthesis, characterization, and application in dye-sensitized solar cells. *Handbook of Nanoelectrochemistry: Electrochemical Synthesis Methods, Properties and Characterization Techniques*, pages 1–23, 2016.

[270] D. Pugliese, A. Lamberti, F. Bella, A. Sacco, S. Bianco, and M.E. Tresso. TiO_2 nanotubes as flexible photoanode for back-illuminated dye-sensitized solar cells with hemi-squaraine organic dye and iodine-free transparent electrolyte. *Org. Electron.*, 15(12):3715–3722, 2014.

[271] A. Lamberti, N. Garino, A. Sacco, S. Bianco, D. Manfredi, and C. Gerbaldi. Vertically aligned TiO_2 nanotube array for high rate li-based micro-battery anodes with improved durability. *Electrochim. Acta*, 102:233–239, 2013.

[272] G. Filipič and U. Cvelbar. Copper oxide nanowires: a review of growth. *Nanotechnology*, 23(19):194001, 2012.

[273] A.E. Rakhshani. Preparation, characteristics and photovoltaic properties of cuprous oxide-a review. *Solid-State Electron.*, 29(1):7–17, 1986.

[274] M. Izaki, T. Shinagawa, K.T. Mizuno, Y. Ida, M. Inaba, and A. Tasaka. Electrochemically constructed $p − Cu_2O/n − ZnO$ heterojunction diode for photovoltaic device. *J. Phys. D*, 40(11):3326, 2007.

[275] M. Schreier, F. Héroguel, L. Steier, S. Ahmad, J.S. Luterbacher, M.T. Mayer, J. Luo, and M. Grätzel. Solar conversion of CO_2 to CO using earth-abundant electrocatalysts prepared by atomic layer modification of CuO. *Nat. Energy*, 2(EPFL-ARTICLE-228911), 2017.

[276] N.D. Hoa, N. Van Quy, H. Jung, D. Kim, H. Kim, and S.K. Hong. Synthesis of porous CuO nanowires and its application to hydrogen detection. *Sens. Actuator B-Chem.*, 146(1):266–272, 2010.

[277] Y.M. Zhu, T. Yu, F.C. Cheong, X.J. Xu, C.T. Lim, V.B.C. Tan, J.T.L. Thong, and C.H. Sow. Large-scale synthesis and field emission properties of vertically oriented CuO nanowire films. *Nanotechnology*, 16(1):88, 2004.

[278] Z. Chen, T.F. Jaramillo, T.G. Deutsch, A. Kleiman-Shwarsctein, A.J. Forman, N. Gaillard, R. Garland, K. Takanabe, C. Heske, M. Sunkara, et al. Accelerating materials development for photoelectrochemical hydrogen production: Standards for methods, definitions, and reporting protocols. *J. Mater. Res.*, 25(1):3–16, 2010.

[279] Y.J. Ma, F. Zhou, L. Lu, and Z. Zhang. Low-temperature transport properties of individual SnO_2 nanowires. *Solid State Commun.*, 130(5):313–316, 2004.

[280] C. Xu, Y. Liu, G. Xu, and G. Wang. Preparation and characterization of CuO nanorods by thermal decomposition of CuC_2O_4 precursor. *Mater. Res. Bull.*, 37(14):2365–2372, 2002.

[281] D. Chen, G. Shen, K. Tang, and Y. Qian. Large-scale synthesis of CuO shuttle-like crystals via a convenient hydrothermal decomposition route. *J. Cryst. Growth*, 254(1):225–228, 2003.

[282] C.T. Hsieh, J.M. Chen, H.H. Lin, and H.C. Shih. Synthesis of well-ordered CuO nanofibers by a self-catalytic growth mechanism. *Appl. Phys. Lett.*, 82(19):3316–3318, 2003.

[283] M. Cao, C. Hu, Y. Wang, Y. Guo, C. Guo, and E. Wang. A controllable synthetic route to Cu, Cu_2O, and CuO nanotubes and nanorods. *Chem. Commun.*, (15):1884–1885, 2003.

[284] M. Kaur, K.P. Muthe, S.K. Despande, S. Choudhury, J.B. Singh, N. Verma, S.K. Gupta, and J.V. Yakhmi. Growth and branching of CuO nanowires by thermal oxidation of copper. *J. Cryst. Growth*, 289(2):670–675, 2006.

[285] L. Yuan, Y. Wang, R. Mema, and G. Zhou. Driving force and growth mechanism for spontaneous oxide nanowire formation during the thermal oxidation of metals. *Acta Mater.*, 59(6):2491–2500, 2011.

[286] M. Ma, K. Djanashvili, and W.A. Smith. Selective electrochemical reduction of CO_2 to CO on CuO-derived Cu nanowires. *Phys. Chem. Chem. Phys.*, 17(32):20861–20867, 2015.

[287] L. Young. *Anodic oxide films*. London; New York: Academic Press, 1961.

[288] F. Keller, M.S. Hunter, and D.L. Robinson. Structural features of oxide coatings on aluminum. *J. Electrochem. Soc.*, 100(9):411–419, 1953.

[289] J.M. Macak, H. Tsuchiya, A. Ghicov, K. Yasuda, R. Hahn, S. Bauer, and P. Schmuki. TiO_2 nanotubes: Self-organized electrochemical formation, properties and applications. *Curr. Opin. Solid State Mater. Sci.*, 11(1-2):3–18, 2007.

[290] D. Gong, C.A. Grimes, O.K. Varghese, W. Hu, R.S. Singh, Z. Chen, and E.C. Dickey. Titanium oxide nanotube arrays prepared by anodic oxidation. *J. Mater. Res.*, 16(12):3331–3334, 2001.

[291] S. Rani, S.C. Roy, M. Paulose, O.K. Varghese, G.K. Mor, S. Kim, S. Yoriya, T.J. LaTempa, and C.A. Grimes. Synthesis and applications of electrochemically self-assembled titania nanotube arrays. *Phys. Chem. Chem. Phys.*, 12(12):2780–2800, 2010.

[292] P. Roy, S. Berger, and P. Schmuki. TiO_2 nanotubes: synthesis and applications. *Angew. Chem. Int. Ed.*, 50(13):2904–2939, 2011.

[293] R.E. Bedworth and N.B. Pilling. The oxidation of metals at high temperatures. *J. Inst. Met.*, 29(3):529–582, 1923.

[294] H. Habazaki, M. Uozumi, H. Konno, K. Shimizu, S. Nagata, K. Takayama, Y. Oda, P. Skeldon, and G.E. Thompson. Influence of film composition on the structure and dielectric properties of anodic films on $Ti-W$ alloys. *J. Electrochem. Soc.*, 152(8):B263–B270, 2005.

[295] P. Skeldon, G.E. Thompson, S.J. Garcia-Vergara, L. Iglesias-Rubianes, and C.E. Blanco-Pinzon. *Electrochem. Solid-State Lett., 9*, 8:415, 2006.

[296] D. Chen, G. Shen, K. Tang, and Y. Qian. Large-scale synthesis of CuO shuttle-like crystals via a convenient hydrothermal decomposition route. *J. Cryst. Growth*, 254(1):225–228, 2003.

[297] A. Kumar, A.K. Srivastava, P. Tiwari, and R.V. Nandedkar. The effect of growth parameters on the aspect ratio and number density of CuO nanorods. *J. Phys.: Condens. Matter*, 16(47):8531, 2004.

[298] R.S. Wagner and W.C. Ellis. Vapor-liquid-solid mechanism of single crystal growth. *Appl. Phys. Lett.*, 4(5):89–90, 1964.

[299] V.A.L. Roy, A.B. Djurišić, W.K. Chan, J. Gao, H.F. Lui, and C. Surya. Luminescent and structural properties of ZnO nanorods prepared under different conditions. *Appl. Phys. Lett.*, 83(1):141–143, 2003.

[300] C.H. Xu, C.H. Woo, and S.Q. Shi. Formation of CuO nanowires on Cu foil. *Chem. Phys. Lett.*, 399(1):62–66, 2004.

[301] A.M.B. Gonçalves, L.C. Campos, A.S. Ferlauto, and R.G. Lacerda. On the growth and electrical characterization of CuO nanowires by thermal oxidation. *J. Appl. Phys.*, 106(3):034303, 2009.

[302] C.H. Bamford, C.F.H. Tipper, and R.G. Compton. Reactions of solids with gases, vol. 21, 1984.

[303] J.T. Chen, F. Zhang, J. Wang, G.A. Zhang, B.B. Miao, X.Y. Fan, D. Yan, and P.X. Yan. CuO nanowires synthesized by thermal oxidation route. *J. Alloys Compd.*, 454(1):268–273, 2008.

[304] X. Jiang, T. Herricks, and Y. Xia. CuO nanowires can be synthesized by heating copper substrates in air. *Nano Lett.*, 2(12):1333–1338, 2002.

[305] J. Liang, N. Kishi, T. Soga, and T. Jimbo. Cross-sectional characterization of cupric oxide nanowires grown by thermal oxidation of copper foils. *Appl. Surf. Sci.*, 257(1):62–66, 2010.

[306] L. Delmondo, G.P. Salvador, J.A. Muñoz-Tabares, A. Sacco, N. Garino, M. Castellino, M. Gerosa, G. Massaglia, A. Chiodoni, and M. Quaglio. Nanostructured Mn_xO_y for oxygen reduction reaction (ORR) catalysts. *Applied Surface Science*, 388:631–639, 2016.

[307] L. Delmondo, J.A.M. Tabares, A. Sacco, N. Garino, G. Massaglia, M. Castellino, G.P. Salvador, C.F. Pirri, M. Quaglio, and A.M. Chiodoni. Thermal evolution of Mn_xO_y nanofibres as catalysts for oxygen reduction reaction. *Phys. Chem. Chem. Phys.*, 19:28781–28787, 2017.

[308] G. Yang, W. Yan, J. Wang, and H. Yang. Fabrication and formation mechanism of Mn_2O_3 hollow nanofibers by single-spinneret electrospinning. *CrystEngComm*, 16(30):6907–6913, 2014.

[309] X. Li, G. Wang, X. Wang, X. Li, and J. Ji. Flexible supercapacitor based on MnO_2 nanoparticles via electrospinning. *J. Mater. Chem. A*, 1(35):10103–10106, 2013.

[310] Y. Du, X. Zhao, Z. Huang, Y. Li, and Q. Zhang. Freestanding composite electrodes of MnO_x embedded carbon nanofibers for high-performance supercapacitors. *RSC Adv.*, 4(74):39087–39094, 2014.

[311] B. Liu, X. Hu, H. Xu, W. Luo, Y. Sun, and Y. Huang. Encapsulation of MnO nanocrystals in electrospun carbon nanofibers as high-performance anode materials for lithium-ion batteries. *Sci. Rep.*, 4, 2014.

[312] M.A. Mohamed and S.A. Halawy. Kinetic and mechanistic study of the non-isothermal decomposition of manganese (II) acetate tetrahydrate. *Thermochim. acta*, 242:173–186, 1994.

[313] A.K.N. Nohman, H.M. Ismail, and G.A.M. Hussein. Thermal and chemical events in the decomposition course of manganese compounds. *J. Anal. Appl. Pyrolysis*, 34(2):265–278, 1995.

[314] A. Chandra, R.C. Agrawal, and Y.K. Mahipal. Ion transport property studies on PEO–PVP blended solid polymer electrolyte membranes. *. Phys. D: Appl. Phys.*, 42(13):135107, 2009.

[315] A.N. Grundy, B. Hallstedt, and L.J. Gauckler. Assessment of the Mn-O system. *J. Phase Equilib.*, 24(1):21–39, 2003.

[316] S. Bag, K. Roy, C.S. Gopinath, and C.R. Raj. Facile single-step synthesis of nitrogen-doped reduced graphene oxide-Mn_3O_4 hybrid functional material for the electrocatalytic reduction of oxygen. *ACS Appl. Mater. Interfaces*, 6(4):2692–2699, 2014.

[317] E.A. González, M. Gulppi, M.A. Páez, and J.H. Zagal. O_2 reduction on electrodes modified with nitrogen doped carbon nanotubes synthesized with different metal catalysts. *Diamond and Related Materials*, 64:119–129, 2016.

[318] X. Liu and W. Hu. Iron oxide/oxyhydroxide decorated graphene oxides for oxygen reduction reaction catalysis: a comparison study. *RSC Adv.*, 6(35):29848–29854, 2016.

[319] S.A. Wohlgemuth, R.J. White, M.G. Willinger, M.M. Titirici, and M. Antonietti. A one-pot hydrothermal synthesis of sulfur and nitrogen doped carbon aerogels with enhanced electrocatalytic activity in the oxygen reduction reaction. *Green Chem.*, 14(5):1515–1523, 2012.

[320] A. Sacco, A. Lamberti, M. Gerosa, C. Bisio, G. Gatti, F. Carniato, N. Shahzad, A. Chiodoni, E. Tresso, and L. Marchese. Toward quasi-solid state dye-sensitized solar cells: effect of $\gamma - Al_2O_3$ nanoparticle dispersion into liquid electrolyte. *Solar Energy*, 111:125–134, 2015.

[321] A. Sacco. Electrochemical impedance spectroscopy: Fundamentals and application in dye-sensitized solar cells. *Renew. Sustainable Energy Rev.*, 79:814–829, 2017.

[322] J.E.B. Randles. Kinetics of rapid electrode reactions. *Discuss. Faraday Soc.*, 1:11–19, 1947.

[323] B.T. Mark, E. Orazem, et al. Electrochemical impedance spectroscopy. *John Willey & Sons, Hoboken, New Jersey*, 2008.

[324] F. Bella, E.D. Ozzello, A. Sacco, S. Bianco, and R. Bongiovanni. Polymer electrolytes for dye-sensitized solar cells prepared by photopolymerization of peg-based oligomers. *Int. J. Hydrogen Energy*, 39(6):3036–3045, 2014.

[325] S. Zhao, Q. Zhou, Y.Z. Long, G.H. Sun, and Y. Zhang. Nanofibrous patterns by direct electrospinning of nanofibers onto topographically structured non-conductive substrates. *Nanoscale*, 5(11):4993–5000, 2013.

[326] Z. Ding, A. Salim, and B. Ziaie. Selective nanofiber deposition through field-enhanced electrospinning. *Langmuir*, 25(17):9648–9652, 2009.

[327] K.A. Stoerzinger, M. Risch, B. Han, and Y. Shao-Horn. Recent insights into manganese oxides in catalyzing oxygen reduction kinetics. *ACS Catal.*, 5(10):6021–6031, 2015.

[328] N. Garino, A. Sacco, M. Castellino, J.A. Muñoz-Tabares, A. Chiodoni, V. Agostino, V. Margaria, M. Gerosa, G. Massaglia, and M. Quaglio. Microwave-assisted synthesis of reduced graphene oxide/SnO_2 nanocomposite for oxygen reduction reaction in microbial fuel cells. *ACS Appl. Mater. Interfaces*, 8(7):4633–4643, 2016.

[329] S. Cheng, H. Liu, and B.E. Logan. Increased performance of single-chamber microbial fuel cells using an improved cathode structure. *Electrochem. Commun.*, 8(3):489–494, 2006.

[330] A. Jaworek. Electrospray droplet sources for thin film deposition. *J. Mater. Sci.*, 42(1):266–297, 2007.

[331] A. Jaworek and A.T. Sobczyk. Electrospraying route to nanotechnology: An overview. *J. Electrostat.*, 66(3):197–219, 2008.

[332] A. Varea, O. Monereo, E. Xuriguera, J.D. Prades, and A. Cirera. Electrospray as a suitable technique for manufacturing carbon-based devices. *J. Phys. D: Applied Physics*, 50(31):315301, 2017.

[333] R.L. Hoffman, B.J. Norris, and J.F. Wager. Zno-based transparent thin-film transistors. *Appl. Phys. Lett.*, 82(5):733–735, 2003.

[334] M. Gürbüz, G. Günkaya, and A. Doğan. Lpg sensing characteristics of electrospray deposited SnO_2 nanoparticles. *Appl. Surf. Sci.*, 318:334–340, 2014.

[335] S.N. Jayasinghe, M.J. Edirisinghe, and T. De Wilde. A novel ceramic printing technique based on electrostatic atomization of a suspension. *Mater. Res. Innovations*, 6(3):92–95, 2002.

[336] A.A. Van Zomeren, E.M. Kelder, J.C.M. Marijnissen, and J. Schoonman. The production of thin films of $LiMn_2O_4$ by electrospraying. *J. Aerosol Sci*, 25(6):1229–1235, 1994.

[337] K. Somroop, R. Pornprasertsuk, and S. Jinawath. Fabrication of Y_2O_3-doped $BaZrO_3$ thin films by electrostatic spray deposition. *Thin Solid Films*, 519(19):6408–6412, 2011.

[338] A. Jaworek. Micro-and nanoparticle production by electrospraying. *Powder technol.*, 176(1):18–35, 2007.

[339] H. Fong, I. Chun, and D.H. Reneker. Beaded nanofibers formed during electrospinning. *Polymer*, 40(16):4585–4592, 1999.

[340] G. Ali, C. Chen, S.H. Yoo, J.M. Kum, and S.O. Cho. Fabrication of complete titania nanoporous structures via electrochemical anodization of Ti. *Nanoscale research letters*, 6(1):332, 2011.

[341] Y. Shin and S. Lee. Self-organized regular arrays of anodic TiO_2 nanotubes. *Nano Lett.*, 8(10):3171–3173, 2008.

[342] G. Liu, K. Wang, N. Hoivik, and H. Jakobsen. Progress on free-standing and flow-through TiO_2 nanotube membranes. *Sol. Energ. Mat. Sol. C.*, 98:24–38, 2012.

[343] S. Neatu, J.A. Maciá-Agulló, and H. Garcia. Solar light photocatalytic CO_2 reduction: general considerations and selected bench-mark photocatalysts. *Int. J. Mol. Sci.*, 15(4):5246–5262, 2014.

[344] S. Neatu, J.A. Maciá-Agulló, P. Concepción, and H. Garcia. Gold–copper nanoalloys supported on TiO_2 as photocatalysts for CO_2 reduction by water. *JACS*, 136(45):15969–15976, 2014.

[345] W.N. Wang, W.J. An, B. Ramalingam, S. Mukherjee, D.M. Niedzwiedzki, S. Gangopadhyay, and P. Biswas. Size and structure matter: enhanced CO_2 photoreduction efficiency by size-resolved ultrafine Pt nanoparticles on TiO_2 single crystals. *JACS*, 134(27):11276–11281, 2012.

[346] Y. Izumi. Recent advances in the photocatalytic conversion of carbon dioxide to fuels with water and/or hydrogen using solar energy and beyond. *Coord. Chem. Rev.*, 257(1):171–186, 2013.

[347] L. Wang, K. Gupta, J.B.M. Goodall, J.A. Darr, and K.B. Holt. In situ spectroscopic monitoring of CO_2 reduction at copper oxide electrode. *Faraday Discuss.*, 197:517–532, 2017.

[348] S.M. Park, A. Razzaq, Y.H. Park, S. Sorcar, Y. Park, C.A. Grimes, and S.I. In. Hybrid $Cu_xO − TiO_2$ heterostructured composites for photocatalytic CO_2 reduction into methane using solar irradiation: Sunlight into fuel. *ACS Omega*, 1(5):868–875, 2016.

[349] R.W. Cheary and A.A. Coelho. Axial divergence in a conventional x-ray powder diffractometer. ii. realization and evaluation in a fundamental-parameter profile fitting procedure. *J. Appl. Cryst.*, 31(6):862–868, 1998.

[350] A. Sacco, N. Garino, A. Lamberti, C.F. Pirri, and M. Quaglio. Anodically-grown TiO_2 nanotubes: Effect of the crystallization on the catalytic activity toward the oxygen reduction reaction. *Appl. Surf. Sci.*, 412:447–454, 2017.

[351] B.E. Logan. *Microbial fuel cells*. John Wiley & Sons, 2008.

List of Figures

List of Tables

Appendix A

Characterization and deposition techniques

A.1 Transmission Electron Microscopy - TEM

The manganese oxides nanofibers Transmission Electron Microscopy (TEM) observations were performed with a FEI Tecnai F20ST (at CSFT - IIT - Italian Institute of Technology), equipped with a field emission gun (FEG), operating at 200 kV. Samples for TEM were prepared by suspending a small quantity of scratched nanofibers in ethanol, subsequently immersed in ultrasonic bath. A drop of the suspension droplet was then drawn and put on a standard TEM holey carbon copper grid, analyzing the specimen after the complete evaporation of the solvent.

TEM and STEM at KAUST (King Abdullah University of Science and Technology) were performed with an aberration corrected TITAN operating at 300 kV. The images were collected in STEM mode with an HAADF detector. The Z-contrast helped to put in evidence the regions where the substrate, the oxide and the protective Pt layer were. By comparing the images collected for the amorphous and crystalline samples, it was possible to observe a contribution of crystal edges, different crystalline orientation, or defects to the contrast, because of the change in the electron channelling across the different crystals. Furthermore, the STEM measurement put in evidence in the calcined samples the nucleation and growth of small crystals that in the amorphous phase were not present.

A.1.1 Lamella preparation

TiO_2_Cu TEM specimen cross-sections was prepared by using a Zeiss Dual Beam Auriga. Trench milling and thinning to 1 μm were carried out at 30 kV and 4–2 nA, respectively. The final milling steps were performed by using 30 kV and 50 pA, damage removal, while thinning to transparency were performed at 20 kV and 20 pA, respectively. In the end, a cleaning step was performed with a voltage of 2 kV and 20 pA, in order to achieve the final thickness and minimize the incidence of

implanted gallium ions and the subsequent formation of an amorphous layer of the surface.

A.2   X-Ray Diffraction - XRD

X-ray diffraction (XRD) with Bragg–Brentano symmetric geometry was performed with a PANalytical X'Pert Pro instrument using Cu-Kα (40 kV and 40 mA) radiation. Continuous scan mode was used to collect XRD data in a range of 20° to 90° and 0.02° as step size.

A.3   In situ XRD

In situ X-ray diffraction was performed in order to investigate the temperature dependence of the oxidation process during the calcination of the manganese acetate. The spectra were recorded in Bragg–Brentano symmetric geometry by using a PANalytical X'Pert Pro instrument (Cu-K radiation, 40 kV and 40 mA) equipped with an X'Celerator detector and a XRK 900 Reactor Chamber used as furnace heater. The samples were heated in air up to different final temperatures at a heating rate of 2.5°C/min, acquiring the spectra at steps of 50°C (continuous scan mode) in the range of 10° to 68° and 0.02° as step size. Rietveld analysis was performed in order to analyze each spectrum by using Topas Academic software (version 4.1). Convolution-based method was used where the source emission profiles with full axial instrument contributions was modeled [349], while the background was fitted with a Chebyshev polynomial function with eight parameters. Average crystallite size was assumed to be isotropic in all cases and modeled by applying the integral breadth based method, whereas lattice strain was assumed to be zero because of the small crystal size found during the early refinement steps.

A.4   Electrochemical measurements

The electrochemical measurements were carried out through a CHInstrument 760D electrochemical workstation and an ALS RRDE-3A rotating ring disk electrode apparatus in a four-electrodes electrochemical cell, constituted by a glassy carbon disk/Pt ring working electrode, a Pt counter electrode and a Ag/AgCl reference electrode; 0.1 M KOH aqueous solution was used as electrolyte.

A.4.1   Roataing Ring Disk Electrode - RRDE

Manganese oxide catalysts were deposited on the glassy carbon disk according to the following method: 2 mg of catalyst were dispersed in a solution containing 25 μl of

water, 175 μl of Nafion$^{©}$ solution and 100 μl of 2-propanol (from Sigma-Aldrich), then the mixture was ultrasonicated for 2 minutes in order to obtain a uniform black dispersion; 10 μl of this formulation were cast-coated onto the disk surface and then let drying at room temperature for one day. Commercial Pt/C paste (Sigma-Aldrich) was used as reference catalyst; the deposition was carried out as already described. For all the analysed materials, the final catalyst loading was 0.5 mg/cm^2.

RRDE measurements were performed by cathodically scanning the disk electrode in the range -0.2 ÷ -0.8 V vs Ag/AgCl, with fixed scan rate (5 mV/s) and rotating speed (2500 RPM), while maintaining the ring electrode potential at 0.2 V, and simultaneously acquiring ring I_R and disk I_D currents. Electron transfer number n and peroxide percentages HO_2^-% were calculated according to the formulas [350]:

$$n = 4 \cdot \frac{I_D}{I_D + I_R/N} \tag{A.1}$$

$$HO_2^-\% = 200 \cdot \frac{I_R/N}{I_D + I_R/N} \tag{A.2}$$

where N is the current collection efficiency of the Pt ring.

A.4.2 Electrochemical Impedance Spectroscopy - EIS

Electrochemical Impedance Spectroscopy (EIS) measurements were carried out with the same electrochemical workstation previously described at -0.3 V vs Ag/AgCl potential and 2500 rpm rotating speed, with a AC signal of 10 mV amplitude and 10^{-2} - 10^4 Hz frequency range.

A.4.3 Linear Sweep Voltammetry - LSV

Linear Sweep Voltammetry (LSV) is performed on the Single Chamber Microbial Fuel Cells (SCMFC) containing the cathode electrodes based on Mn_xO_y on CP, compared with the cathode based on Pt/C on CP and bare CP, used as reference anode material. The LSV estimates the polarization curves, by measuring the current density variations due to the application of different values of voltage [351]. The cells are set up in Open Circuit Voltage (OCV) configuration for some hours before the characterization beginning to ensures that the devices reached the steady state conditions. By the LSV characterization, the power density curve is then calculated, providing the maximum power density value achievable. This measure is performed by the VSP biologic potentiostat that ranges the voltage values during time, from the OCV value up to the short circuit one, with a slope of 0.1 mV/s and measures the current.

A.4.4   Cyclic Voltammetry - CV

Cyclic Voltammetry (CV) is performed in a 3-electrode electrochemical cell consisting of: a working electrode (the sample), a counter electrode (Pt wire), a reference electrode (Ag/AgCl) and an electrolytic solution containing 0.1M of $KHCO_3$. The tests are firstly conducted in N_2-saturated solution and, then, in a new solution CO_2-saturated, always maintaining ambient temperature and pressure. In this kind of measure, the voltage is swept linearly between from -0.61 V to -1.61 V and vice versa, and a current is measured. This interval is repeated for several cycles to verify the stability of the measurement by using a potentiostat (CH Instruments - Electrochemical Workstation CHI760D). For all the experiments conducted, the scan rate used was 0.01 V/s.

A.4.5   Mott-Schottky

The Mott-Schottky measures are done in a three-electrode system containing a 0.1M solution of $KHCO_3$. A variable drive potential is applied and superimposed to a sinusoidal potential wave with amplitude 25 mV and variable frequency (1kHz, 5kHz, 10 KHz). A current is measured as output of the measuring system and the corresponding capacity C is calculated.

In order to calculate the flat band potential between the semiconductor (the considered catalyst) and the electrolyte, the Mott-Schottky equation has to be considered:

$$\frac{1}{C^2} = \frac{2}{\varepsilon A^2 e N_d}\left(V - V_{FB} - \frac{k_B T}{e}\right) \tag{A.3}$$

where ε is the dielectric constant, A is the electrode area, N_d is the doping density, V_{FB} is the flat band potential, e is the electron charge, V is the applied potential, k_B is the Boltzmann constant and T is the temperature. The Eq. A.3 can be rewritten as:

$$\frac{1}{C^2} = \frac{2}{\varepsilon A^2 e N_d}V + \frac{2}{\varepsilon A^2 e N_d}\left(-V_{FB} - \frac{k_B T}{e}\right) = aV + B \tag{A.4}$$

where a is the slope of the fitting curve of the graph that is obtained from measurements and gives as a result, the doping of the semiconductor:

$$a = \frac{2}{\varepsilon A^2 e N_d} \rightarrow N_d = \frac{2}{\varepsilon A^2 e a} \tag{A.5}$$

B is the intercept of the fitting curve with the x axis and provides the V_{FB}, flat band potential:

$$B = a\left(-V_{FB} - \frac{k_B T}{e}\right) \rightarrow V_{FB} = -\frac{B}{a} - \frac{k_B T}{e} \tag{A.6}$$

In the experiments, the temperature was considered as 25°C, ambient temperature.

A.5 Micro Gas Chromatograph - μ-GC

The gas analysis setup is constituted by a CO_2 reactor, with custom design in Teflon by Hysytech and provided with a quartz window that allows the frontal illumination of the catalyst for performing both electro- and photo-catalytic tests and a μ-GC setup as described in the following. A CO_2 cylinder is connected to a mass flow controller (Bronkhorst EL-FLOW model F-201CV) in order to regulate the flow rate of the gas into the reactor. The CO_2 inlet is directly bubbled (at 1 atm) into the electrolytic solution, containing 0.1M of $KHCO_3$, which is kept under continuous magnetic stirring (400 rpm). A potentiostat (Biologic, VS.P-300) applies the wanted potential between the electrode containing the catalyst (WE) and the reference electrode (Radiometer Analytical, REF421 saturated calomel electrode), while the Pt foil acts as a counter electrode. The outlet of the reactor reaches the GC (Inficon, Micro GC Fusion Gas Analyzer), which measures the reaction product concentrations. Before each tests, the GC has been calibrated for CO, H_2, CH_4, CO_2 and N_2, in order to have a precise result. During the GC measurements, chronoamperometry tests were conducted by applying different potentials in series (e.g. -1.6 V, -1.4 V vs. SHE) to monitor the stability of the material under working conditions.

A.5.1 Faradaic Efficiency - FE

The faradaic efficiency (FE) gives information about the efficiency with which charges are transferred to a given system to facilitate an electrochemical system reaction. It is calculated as:

$$FE = 100\frac{nF\,\text{mol}}{It} = 100\frac{Q_{exp}}{Q_{theo}} \tag{A.7}$$

where Q_{exp} is the charge associated to a specific reaction, Q_{theo} is the total charge exchanged during the process, n is the number of the electrons needed for a specific CO_2 reduction, F is the Faraday constant, I is the current obtained at equilibrium from chronoamperometry and mol is the moles of gas produced. The number of electrons associated with reduction n can be 2,8,12,14 for the formation of CO, methane, ethylene and ethane, respectively. The μ-GC gives as output the ppm of the gas (products of the reduction reaction) that flows, giving the possibility to directly calculate the fraction mol/t as:

$$\frac{\text{mol}}{t} = \frac{\text{ppm} \cdot 10^{-6} f_{CO_2}}{V_{1mol}} = [mol/s] \tag{A.8}$$

where f_{CO_2} is the carbon dioxide flux set in the μ-GC and $V_{1mol} = 24.4$ @ 25°C/1 atm from gas perfect law.

A.5.2 ChronoAmperometry - CA

Chronoamperometry analysis is measure of current versus time at constant applied potential for 90 minutes. The potentials are chosen in order to determine the best electrocatalyst at a defined potential, by comparing different materials. The first potential is applied after the CO_2 saturation of the solution (0.1M of $KHCO_3$): corresponds to an average value of 1600 mg/l at 20 °C (registered with a dissolved CO_2 sensor). The saturation value at equilibrium decreases by increasing the potential: the maximum decrease occurs at -1.6 V vs. SHE, with a reduction of about 8-10 % with respect to the original saturation value.

A.6 Chemical Oxygen Demand - COD

The Chemical Oxygen Demand is a measure of the quantity of organic molecules, in a liquid solution, expressed as the amount of oxygen that is needed to completely oxidize the molecules among: methanol, formaldehyde, formic acid. It is commonly expressed in mass of oxygen consumed over volume of solution (mg/l). The COD of liquid samples coming from the GC tests, are determined by silver-catalyzed oxidation with potassium dichromate / sulfuric acid at 148°C during a two hour period (NANOCOLOR® COD 40). The measure range is 2 - 40 mg/l of O_2: for samples that would give an higher result, a dilution with Di-H_2O is done.

A.7 Spectrophotometer

The spectrophotometric or UV-Vis spectroscopy characterization were conducted in the range 200 - 800 nm with a Cary 5000 (UV-Vis-NIR spectrophotometer, Varian). Diffuse reflectance is acquired thanks to integrating sphere in order to obtain the whole reflectance of the bulk sample. Absorbance spectra are obtained from Kubelka Munk theory.

Due to the high S/N ratio for low wavelengths, the Tauc plots are reported by using spectra only in the range 300 - 800 nm and linearly fitted in order to ontain the band gap of the measured material. In general Tauc plots show the optical absorption spectrum of the analyzed material by plotting $(\alpha h \nu)^2$ (for allowed direct band gap transitions) or $(\alpha h \nu)^{(1/2)}$ (for allowed indirect band gap transitions) versus $h\nu$, the light energy.

A.8   Electron Beam Evaporator

The deposition of the titanium layers were done by using an Electron Beam Evaporator (Ulvac model EBX-14D), with a growth rate of 0.2 nm/s. A 120 mA electron beam current was used for the melting of the titanium source (Ti ingots, 6mm x 12mm, 99.95% pure purchased by Umicore) The process chamber was pumped at a vacuum in the $1 \cdot 10^{-7}$ Torr range during the deposition process, by means of a cryogenic pump.